

# **Magnetic Nanocrystals as MRI Contrast Agents: Role of Size, Shape, and Surface Coating**

By Jake Villanova

Sc.M., Biomedical Engineering, Brown University, Providence, RI, 2021

M.A., Christian Apologetics, Liberty University, Lynchburg, VA, 2017

B.S., Chemistry (ACS), Iona College, New Rochelle, NY, 2016

A DISSERTATION SUBMITTED IN PARTIAL FULFILLMENT OF THE REQUIREMENTS FOR THE  
DEGREE OF DOCTOR OF PHILOSOPHY IN THE DEPARTMENT OF CHEMISTRY AT BROWN  
UNIVERSITY

Providence, RI

February 2023

© Copyright 2023 by Jake Villanova

This dissertation by Jake Villanova is accepted in its present form by the Department of Chemistry as satisfying the dissertation requirement for the degree of Doctor of Philosophy.

Date: \_\_\_\_\_

Vicki L. Colvin, Advisor

Recommended to the Graduate Council

Date: \_\_\_\_\_

Ou Chen, Reader

Date: \_\_\_\_\_

Anita Shukla, Reader

Approved by the Graduate Council

Date: \_\_\_\_\_

Thomas A. Lewis, Dean of the Graduate School

## Curriculum Vitae

Originally from New York, Jake Villanova attended Mahopac High School. There, he had his first introduction to, and became interested in, the physical and life sciences – biology, chemistry, and physics. Seeking to continue his STEM education, Jake attended Iona College in New Rochelle, New York, where many in his family also studied. There, he majored in chemistry, became interested in nanoscience, and participated in surface and colloidal chemistry research under Profs. Sunghee Lee and Joseph Ryan. After graduating, Jake studied Christian apologetics at Liberty University to explore broader interests in philosophy and theology. There, he learned a lot about the principles of research, albeit in a non-STEM context. Finally, Jake came to Brown University to study chemistry (Ph.D.) and biomedical engineering (Sc.M.) and participate in nano-chemistry research under Prof. Vicki Colvin. His future plans include attending medical school and eventually continuing research in nanomedicine.

## Publications

1. **Villanova J.\***; Cho M.\*; Lee S. S.; Ines D.; Xiao Z.; Guo X.; Dunn J. A.; Stueber D. D.; Decuzzi P.; Colvin V. L., The Role of Surface Coating in Designing Highly Sensitive T2 MRI Contrast Agents, *in submission*.
2. **Villanova J.\***; Taheri N.\*; Bohloul A.; Bi Y.; Ines D.; Guo X.; Xiao Z.; Dunn J. A.; Avendano C.; Decuzzi P.; Pautler R. G.; Colvin V. L., The T1 Relaxivity of Gadolinium Nanoparticles in Biologically Relevant Media: The Role of Ionic Strength and Protein Association, *in preparation*.
3. **Villanova J.\***; Taheri N.\*; Stinnett G.\*; Bohloul A.; Guo X.; Esposito E. P.; Xiao Z.; Stueber D.; Avendano C.; Decuzzi P.; Pautler R. G.; Colvin V. L., 2D Gadolinium Oxide Nanoplates as T1 Magnetic Resonance Imaging Contrast Agents, *Advanced Healthcare Materials* **2021**, 10(11), 2001780.
4. Stueber D. D.; **Villanova J.**; Aponte I.; Xiao Z.; Colvin V. L., Magnetic Nanoparticles in Biology and Medicine: Past, Present, and Future Trends, *Pharmaceutics* **2021**,13(7), 943.
5. Xiao Z.; Zhang Q.; Guo X.; **Villanova J.**; Hu Y.; Kulaots I.; Garcia-Rojas D.; Guo W.; Colvin V. L., Libraries of Uniform Magnetic Multicore Nanoparticles with Tunable Dimensions for Biomedical and Photonic Applications, *ACS Applied Materials & Interfaces* **2020**, 12, 41932–41941.
6. Xiao, Z.; **Villanova, J.**; Lee, M. J.; Stueber, D. D.; Zhang, Q.; Colvin, V. L., Magnetic Nanocrystal Chains with Large Magnetic Susceptibilities and Anisotropic Coercivity, *in preparation*.

7. Xiao, Z.; **Villanova, J.**; Koval, P.; Stueber, D. D.; Colvin, V. L., Magnetically Induced Nanoheaters: from Biomedicine to the Remediation of Emerging Contaminants in Drinking Water, *in preparation*.
8. Xiao, Z.; Guo, X.; **Villanova, J.**; Bi, Y.; Avidan, S.; Effman, S.; Zhang, Q.; Colvin, V. L., Portable Heating and Environmental Remediation Using the Giant Susceptibilities of Manganese-Doped Ferrite Clusters, *in preparation*.
9. Hu, Y.; Atherton, E.; Zhang, Q.; Garcia, D.; Masteron, C.; Bi, Y.; Xiao, Z.; Guo, X.; **Villanova, J.**; Dunn, J.; Borton, D.; Colvin, V. L., Augmenting the Antioxidant Capacity of Ceria Nanoparticles with Catechol-grafted Poly(ethylene glycols), *in submission*.
10. Hu, Y.; Xiao, Z.; Guo, X.; Ling, V.; Bi, Y.; Atherton, E.; **Villanova, J.**; Masteron, C.; Dunn, J.; Colvin, V. L., Challenges and Solutions for Quantifying the Antioxidant Capacity of Inorganic Nanoparticles, *in preparation*.
11. Kim, H.; Guo, X.; Benoit, J.; Walden, E.; Rehak, P.; Nagaoka, Y.; **Villanova, J.**; Xiao, Z.; Shamoo, Y.; Hafner, J.; Kral, P.; Chen, O.; Colvin, V. L., Co-Crystallizing Diverse Proteins with Nanoparticle-Polymer Conjugates, *in preparation*.
12. Walden, E.; Guo, X.; Kim, H.; **Villanova, J.**; Xiao, Z.; Tariq, S.; D'Ordine, A.; Jogl, G.; Colvin, V. L., Opening up the Bottleneck: Designing Materials that Can Crystallize Biomolecules, *in preparation*.

\* These authors contributed equally.

# Acknowledgements

To Brown University, thank you for the educational opportunity. To my advisor and mentors, thank you for your time, patience, and guidance. To my coworkers and the staff/faculty, thank you for your friendly assistance. To my friends and family, thank you for your love and support. Above all, to my God, thank you for everything – I would not be here without you.

# Contents

<b>Curriculum Vitae</b> .....	iv
<b>Publications</b> .....	v
<b>Acknowledgements</b> .....	vii
<b>List of Figures</b> .....	xiii
<b>List of Tables</b> .....	xix
<b>Chapter 1 Magnetic Nanoparticles in Biology and Medicine: Past, Present, and Future</b>	
<b>Trends</b> .....	2
1.1. Abstract.....	2
1.2. Introduction .....	3
1.3. Treatment .....	7
1.3.1. Iron Oxide Catalyzed Cancer Therapies .....	7
1.3.2. Drug and Gene Delivery .....	9
1.3.3. Magnetothermal Heating.....	15
1.4. Imaging.....	17
1.4.1. Magnetic Resonance Imaging (MRI) Contrast Agents .....	17
1.4.2. Magnetic Particle Imaging (MPI) Tracers .....	25
1.5. Movement.....	29



1.5.1. Cell Separation .....	29
1.5.2. Soft Robotics .....	31
1.6. Diagnostics .....	33
1.6.1. Immunoassays.....	33
1.7. Conclusion.....	37
1.8. References .....	39

**Chapter 2 Two-Dimensional Gadolinium Oxide Nanoplates as T1 Magnetic Resonance**

<b>Imaging Contrast Agents .....</b>	<b>55</b>
2.1. Abstract.....	55
2.2. Introduction .....	55
2.3. Results and Discussion.....	60
2.3.1. Synthesis of Gadolinium Oxide Nanoplates.....	60
2.3.2. Surface Modification of Gadolinium Oxide Nanoplates .....	64
2.3.3. Relaxivity Measurements.....	66
2.3.4. Pharmacokinetics and Biodistribution .....	72
2.3.5. Cellular Uptake, Cytotoxicity, and Gadolinium Dissolution .....	76
2.3.6. Differentiation of Non-Alcoholic Fatty Liver Disease.....	79
2.4. Conclusion.....	84

2.5. Experimental Section .....	85
2.6. Supporting Information .....	97
2.7. References .....	109
<b>Chapter 3 The Role of Surface Coating in Designing Highly Sensitive T<sub>2</sub> MRI Contrast Agents</b> .....	121
3.1. Abstract.....	121
3.2. Introduction .....	122
3.3. Results and Discussion.....	125
3.3.1. Synthesis of Surface Coated Iron Oxide Nanocrystals .....	125
3.3.2. Colloidal Stability.....	128
3.3.3. T <sub>2</sub> Relaxation Dynamics .....	130
3.3.4. Size- and Surface Coating-Dependent Cytotoxicity .....	142
3.4. Conclusion.....	143
3.5. Experimental Section .....	144
3.6. Supporting Information .....	154
3.7. References .....	162
<b>Chapter 4 The T<sub>1</sub> Relaxivity of Gadolinium Nanoparticles in Biologically Relevant Media: The Role of Ionic Strength and Protein Association .....</b>	171

4.1. Abstract.....	171
4.2. Introduction.....	172
4.3. Results and Discussion.....	174
4.4. Conclusion.....	192
4.5. Experimental Section.....	193
4.6. Supporting Information.....	202
4.7. References.....	214
<b>Chapter 5 Clustered Magnetic Nanomaterials as MRI Contrast agents: Iron Oxide</b>	
<b>Nanoworms and Ferrite Clusters.....</b>	<b>227</b>
5.1. Abstract.....	227
5.2. Introduction.....	227
5.3. Results and Discussion.....	230
5.3.1. Iron Oxide Clusters.....	230
5.3.2. Nanoworms.....	236
5.3.3. Ferrite Clusters.....	243
5.4. Conclusion.....	250
5.5. Experimental Section.....	250
5.6. Supporting Information.....	261

5.7. References .....	272
-----------------------	-----

## List of Figures

<b>Figure 1.1</b> Biomedical applications of magnetic particles.....	5
<b>Figure 1.2</b> Schematic of magnetic drug delivery.....	9
<b>Figure 1.3</b> T <sub>1</sub> -weighed MRA of small and large animal models using IOP .....	21
<b>Figure 1.4</b> T <sub>2</sub> -weighted cell tracking MRI applications using IOP.....	22
<b>Figure 1.5</b> Brain tumor MRI applications using IOP .....	24
<b>Figure 1.6</b> MPI applications using IOP .....	28
<b>Figure 1.7</b> Magnetic batch separation for cell separation .....	29
<b>Figure 1.8</b> Soft robotics application of IOP .....	32
<b>Figure 1.9</b> Representative electron microscopy images of Dynabeads™ .....	34
<b>Figure 2.1</b> GONP core characterization .....	61
<b>Figure 2.2</b> GONP surface characterization .....	63
<b>Figure 2.3</b> Relaxometric characterization of GONP .....	70
<b>Figure 2.4</b> Biodistribution and pharmacokinetics of GONP in mice .....	73
<b>Figure 2.5</b> Cell uptake and viability of GONP .....	77
<b>Figure 2.6</b> Ex vivo T <sub>1</sub> -weighted MRI of mice using GONP .....	82
<b>Figure S2.1</b> Reaction condition size dependence .....	97
<b>Figure S2.2</b> TEM images of GONP. ....	98
<b>Figure S2.3</b> Chemical structure of PAMPS-LA .....	99

<b>Figure S2.4</b> GONP sample uniformity.....	100
<b>Figure S2.5</b> High field strength $T_1$ relaxation plot of GONP .....	101
<b>Figure S2.6</b> $T_1$ relaxivity of Magnevist and GONP with different surface coatings.....	102
<b>Figure S2.7</b> Cell uptake capacity of GONP.....	104
<b>Figure S2.8</b> $T_1$ - and $T_2$ -weighted MR phantom images .....	105
<b>Figure S2.9</b> In vitro cytotoxicity studies .....	106
<b>Figure S2.10</b> Three-day Gadolinium release experiment .....	107
<b>Figure S2.11</b> Twenty-day Gadolinium release experiments .....	108
<b>Figure 3.1</b> IONC core characterization .....	126
<b>Figure 3.2</b> IONC surface coating characterization.....	127
<b>Figure 3.3</b> $T_2$ relaxivity dependence of IONCs.....	134
<b>Figure 3.4</b> $T_2$ relaxivity hydrodynamic diameter dependence of IONCs.....	135
<b>Figure 3.5</b> Surface coating dependent diffusion constants.....	139
<b>Figure 3.6</b> Surface coating-dependent relaxometric stability and cell viability of IONC .....	141
<b>Figure S3.1</b> TEM images of IONC.....	154
<b>Figure S3.2</b> $T_2$ -weighted MR phantom images of IONCs.....	156
<b>Figure S3.3</b> Plots of $1/T_2$ values of iron oxide nanocrystals .....	157
<b>Figure S3.4</b> IONC magnetization .....	158
<b>Figure S3.5</b> MALDI-TOF of PAMPS-LA .....	160

<b>Figure S3.6</b> IONC surface coating grafting density.....	161
<b>Figure 4.1</b> Characterization of Gd <sub>2</sub> O <sub>3</sub> nanoplates cores and surface coating.....	176
<b>Figure 4.2</b> Characterization of Gd <sub>2</sub> O <sub>3</sub> nanoplates cores and surface coating.....	181
<b>Figure 4.3</b> T <sub>1</sub> relaxivity of PAMPS-LA and PAA-LA coated Gd <sub>2</sub> O <sub>3</sub> nanoplates in various concentrations of HSA and salt .....	183
<b>Figure 4.4</b> T <sub>1</sub> relaxivity of PAMPS-LA and PAA-LA coated Gd <sub>2</sub> O <sub>3</sub> nanoplates in FBS and water .....	185
<b>Figure 4.5</b> Size exclusion chromatography profiles for PAMPS-LA and PAA-LA coated Gd <sub>2</sub> O <sub>3</sub> nanoplates in HSA and FBS solution.....	187
<b>Figure 4.6</b> T <sub>1</sub> relaxation rates of PAMPS-LA and PAA-LA coated Gd <sub>2</sub> O <sub>3</sub> nanoplates at different FBS:nanocrystal concentration ratios .....	190
<b>Figure 4.7</b> Cell viability of PAMPS-LA and PAA-LA coated Gd <sub>2</sub> O <sub>3</sub> nanoplates.....	192
<b>Figure S4.1</b> Transmission electron microscopy (TEM) of Gd <sub>2</sub> O <sub>3</sub> nanoplates.....	202
<b>Figure S4.2</b> X-ray diffraction pattern of Gd <sub>2</sub> O <sub>3</sub> nanoplates.....	203
<b>Figure S4.3</b> Raman spectroscopy for Gd <sub>2</sub> O <sub>3</sub> nanoplates .....	203
<b>Figure S4.4</b> Thermogravimetric analysis (TGA) of Gd <sub>2</sub> O <sub>3</sub> nanoplates .....	204
<b>Figure S4.5</b> Fourier transform infrared (FTIR) spectroscopy of polymer coatings .....	204
<b>Figure S4.6</b> T <sub>1</sub> relaxation rates for Gd <sub>2</sub> O <sub>3</sub> samples in water, protein, and salt solution .....	205

<b>Figure S4.7</b> $T_1$ relaxation rates for $Gd_2O_3$ samples in different concentration solutions of protein and salt .....	206
<b>Figure S4.8</b> Dependence of surface coated $Gd_2O_3$ nanoplates hydrodynamic size on solution ionic strength.....	207
<b>Figure S4.9</b> $T_1$ relaxivity ( $r_1$ ) of PAMPS-LA coated nanoplates in water, salt, protein, and serum solutions .....	207
<b>Figure S4.10</b> $T_1$ relaxation rates for PAMPS-LA coated $Gd_2O_3$ nanoplates in water, salt, and protein solution .....	208
<b>Figure S4.11</b> Time-dependent size exclusion chromatograms for surface coated $Gd_2O_3$ nanoplates in HSA solution.....	209
<b>Figure S4.12</b> Time-dependent size exclusion chromatograms for surface coated $Gd_2O_3$ nanoplates in FBS solutions.....	210
<b>Figure S4.13</b> Concentration-dependent size exclusion chromatograms for surface coated $Gd_2O_3$ nanoplates in FBS solution .....	211
<b>Figure S4.14</b> Dependence of surface coated $Gd_2O_3$ nanoplates hydrodynamic size on BCS solution concentration .....	212
<b>Figure S4.15</b> Dissolution of gadolinium from coated and uncoated $Gd_2O_3$ particles in water and pH 4.5 solution .....	213
<b>Figure 5.1</b> Synthesis of the iron oxide nanoclusters .....	230



<b>Figure 5.2</b> Transmission electron microscopy (TEM) images and size distributions for iron oxide clusters of different size .....	231
<b>Figure 5.3</b> Cluster surface functionalization and colloidal stability .....	234
<b>Figure 5.4</b> T <sub>2</sub> weighted MR images and relaxivity of iron oxide clusters .....	235
<b>Figure 5.5</b> Schematic of forces governing nanoworm formation .....	237
<b>Figure 5.6</b> Role of applied magnetic field in the formation of nanoworms.....	238
<b>Figure 5.7</b> Nanoworm length dependence on applied field strength.....	240
<b>Figure 5.8</b> T <sub>1</sub> and T <sub>2</sub> relaxivities of silica coated Fe <sub>3</sub> O <sub>4</sub> clusters nanoworms .....	243
<b>Figure 5.9</b> Morphology, composition, and magnetic properties of MFCs .....	245
<b>Figure 5.10</b> Transmission electron microscopy (TEM) images of MFCs of different dimensions and composition .....	247
<b>Figure 5.11</b> T <sub>1</sub> and T <sub>2</sub> relaxivities of Fe <sub>3</sub> O <sub>4</sub> and ferrite clusters .....	249
<b>Figure S5.1</b> Transmission electron microscopy (TEM) images iron oxide clusters with different cluster (D <sub>c</sub> ) and primary particle (d <sub>p</sub> ) sizes .....	261
<b>Figure S5.2</b> Dependence of cluster dimensions on reaction conditions.....	262
<b>Figure S5.3</b> X-ray diffraction (XRD) patterns of iron oxide clusters .....	263
<b>Figure S5.4</b> Raman spectra of iron oxide clusters .....	264
<b>Figure S5.5</b> Magnetization curves of iron oxide clusters .....	264
<b>Figure S5.6</b> Fourier transform infrared (FTIR) spectra of iron oxide clusters .....	265
<b>Figure S5.7</b> Characterization of poly(AA-co-AMPS) .....	266

<b>Figure S5.8</b> Colloidal stability of nanoworms.....	266
<b>Figure S5.9</b> Dependence of nanoworm formation on cluster size and surface coating.....	267
<b>Figure S5.10</b> The chain length distribution of the nano-worm samples.....	268
<b>Figure S5.11</b> Magnetization curves of nanoworms .....	268
<b>Figure S5.12</b> Image of MFC ferrofluid .....	269
<b>Figure S5.13</b> Transmission electron microscopy (TEM) images of Gd- and Eu-ferrite clusters .....	270
<b>Figure S5.14</b> Photoluminescence emission spectra of Fe <sub>3</sub> O <sub>4</sub> and Eu-Fe <sub>3</sub> O <sub>4</sub> clusters.....	271

## List of Tables

<b>Table 1.1</b> Commercial iron oxide particles for clinical magnetic resonance imaging.....	19
<b>Table 2.1</b> Relaxivity values for PAMPS-LA-GONP and Magnevist in DI water at 1.4 T. ....	68
<b>Table 2.2</b> Plasma kinetics of Magnevist and Gadolinium oxide nanocrystals .....	74
<b>Table S2.1</b> Properties of Magnevist and GONP with various surface coatings at 1.4 T. ....	103
<b>Table 3.1</b> T2 relaxivity ( $r_2$ ) and hydrodynamic diameter (HD) of iron oxide nanocrystals with different sizes and phase transfer coatings. ....	128
<b>Table 3.2</b> Summary of relevant physiochemical, magnetic, and relaxometric parameters for IONCs reported here and the highest performing, single core, spherical iron oxide nanocrystal T <sub>2</sub> MRI contrast agents found in the literature.....	138
<b>Table S3.1</b> Hydrodynamic size of iron oxide nanocrystals with single layer surface coatings. ....	155
<b>Table S3.2</b> Molecular weight and grafting densities of iron oxide nanocrystals with different surface coatings.....	159

<b>Table 4.1</b> $T_1$ relaxivities of Magnevist and polymer-coated $Gd_2O_3$ nanoplates in various media. .....	180
<b>Table S4.1</b> Hydrodynamic diameters (HD) and zeta potentials for coated GONPs in varying pH solution.....	205
<b>Table 5.1</b> Summary nanoworm physical and magnetic properties. ....	241
<b>Table S5.1</b> MFC dimensions based on changing concentration of water.....	269
<b>Table S5.2</b> MFC dimensions based on changing reaction temperature. ....	270
<b>Table S5.3</b> MFC composition based on changing Mn/Fe salt ratio.....	270

## Chapter 1

### Magnetic Nanoparticles in Biology and Medicine: Past, Present, and Future

#### Trends<sup>†</sup>

† Reprinted (adapted) with permission from Stueber D. D.; Villanova J.; Aponte I.; Xiao Z.; Colvin V. L., Magnetic Nanoparticles in Biology and Medicine: Past, Present, and Future Trends, *Pharmaceutics* **2021**,13(7), 943.

# Chapter 1 Magnetic Nanoparticles in Biology and Medicine: Past, Present, and Future Trends

## 1.1. Abstract

The use of magnetism in medicine has changed dramatically since its first application by the ancient Greeks in 624 BC. Now, by leveraging magnetic nanoparticles, investigators have developed a range of modern applications that use external magnetic fields to manipulate biological systems. Drug delivery systems that incorporate these particles can target therapeutics to specific tissues without the need for biological or chemical cues. Once precisely located within an organism, magnetic nanoparticles can be heated by oscillating magnetic fields, which results in localized inductive heating that can be used for thermal ablation or more subtle cellular manipulation. Biological imaging can also be improved using magnetic nanoparticles as contrast agents; several types of iron oxide nanoparticles are US Food and Drug Administration (FDA)-approved for use in magnetic resonance imaging (MRI) as contrast agents that can improve image resolution and information content. New imaging modalities, such as magnetic particle imaging (MPI), directly detect magnetic nanoparticles within organisms, allowing for background-free imaging of magnetic particle transport and collection. “Lab-on-a-chip” technology benefits from the increased control that magnetic nanoparticles provide over separation, leading to improved cellular separation. Magnetic separation is also becoming important in next-generation immunoassays, in which particles are used to both increase sensitivity and enable multiple analyte detection. More recently, the ability to manipulate material motion with external fields has been applied in magnetically actuated soft robotics that are designed for biomedical interventions. In this review article, the origins of these

various areas are introduced, followed by a discussion of current clinical applications, as well as emerging trends in the study and application of these materials.

## 1.2. Introduction

Magnetism has been linked to medicine for thousands of years. It is thought that the Greek scientist and astronomer, Thales of Miletus, was the first person to apply magnetic materials to organisms as early as 624–547 BC. His work led to a cultural belief in the healing powers of lodestones that persisted for centuries.<sup>1</sup> In the 14th century, the Swiss doctor and alchemist, Paracelsus, wrote the *Volumen Medicinae Paramirum* which detailed how to manipulate the health of a body using magnets. After seeing the way that magnets could attract iron, he hypothesized that magnets could be used to attract diseases from the body in the same way.<sup>1</sup> Several hundred years later, in 1892, the first definitive study of magnets on organisms was completed. Five humans and one dog were exposed to magnetic fields of roughly several thousand gauss or several thousand times the earth's magnetic field, but no measurable effect was observed.<sup>2</sup> The first modern discussion of the prospects for magnetism in medicine was published in 1962 by Freeman et al., who predicted that magnetism would emerge as a powerful tool for biochemical analysis and medical diagnosis.<sup>3</sup>

By the 1970s, the significance of magnetism in medicine was a reality in diagnostic imaging, but broader applications remained elusive until the development of nanotechnology. Magnetic resonance imaging (MRI) transitioned from the laboratory into the clinic in the early 1970s, and it was soon widely applied for detecting cancerous tumors.<sup>4</sup> Because of MRI scanners, doctors, for the first time, had access to instruments

capable of applying large magnetic fields ( $B_0 > 2 \text{ T}$ ) and this inspired many to explore how magnetism could be used for more than just imaging. Unfortunately, this avenue of research resulted in little new applications and conventional MRI imaging remained the dominant use of magnetism in medicine. However, with the advent of nanotechnology in the 1980s, native tissue could be transformed into magnetically responsive material using magnetic nanoparticles. This opened the door to a much wider set of potential medical applications. With appropriate surface functionality, magnetic nanoparticles, being typically less than a few hundred nanometers in dimension, could be used to label cells and biomolecules, thereby endowing tissues and other biological molecules with useful magnetic properties. The early applications of this new capability included the magnetic guidance of catheters for the treatment of bradycardic arrhythmia, movement of unerupted teeth in dentistry, and even magnetic intrauterine devices (IUD) for contraception.<sup>1</sup>

Since the 1990s, there has been an explosion of research seeking to develop diverse medical applications for magnetic nanoparticles. In all cases, external magnetic fields interact with ferrimagnetic nanoparticles that can associate or interact with tissue, cells, or biomolecules allowing for applications from molecular imaging to magnetothermal heating (**Figure 1.1**). Superparamagnetic iron oxide nanocrystals (SPIONs) are central to these technologies; these materials (**Figure 1.1**) are made from iron oxide, but, because of their small dimensions, they do not exhibit any magnetization unless they are in an external magnetic field.<sup>5</sup> This is especially desirable for biological applications due to the decreased potential for aggregation in the absence of applied fields.<sup>6</sup> **Figure 1.1** presents



a loose classification of this large set of scientific literature based on the underlying goals of the technology: treatment, imaging, directed movement, and diagnostics. MRI imaging is a mature area of clinical practice, and the US Food and Drug Administration (FDA) has approved magnetic nanoparticles for use as MRI contrast agents, but most have been discontinued commercially.<sup>7</sup> Also notable is the widespread use of magnetic nanoparticles, typically referred to as “beads” by the analytical community, to facilitate immunoassays and other medical diagnostics. Emerging applications include cancer therapies, drug delivery, and magnetothermal schemes for disease therapy, as well as the controlled movement and direction of magnetic particles within organisms. While some

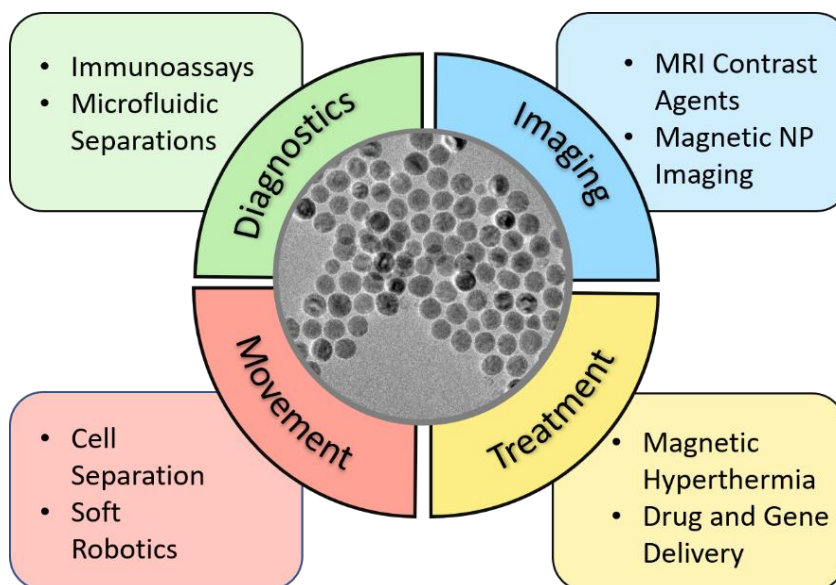


**Figure 1.1 Biomedical applications of magnetic particles.** The applications of magnetic particles can be classified into four categories depending on the aim of the technology. Imaging and in vitro diagnostics are mature areas that have clinical relevance, while research into magnetic particles to treat disease or affect controlled motion of larger organelles, cells and biomaterials is at the pre-clinical stage. Abbreviations: Magnetic Resonance Imaging (MRI), Magnetic Nanoparticle (NP) Imaging Inset picture provided by Zhen Xiao, iron oxide (magnetite) nanocrystals  $d = 23 \pm 2$  nm.

of these examples have reached Phase 1 clinical trials, widespread clinical application has not yet been achieved.<sup>8-10</sup>

To take full clinical advantage of these applications, it is vital to have practical systems for applying magnetic fields as well as highly responsive magnetic particles. Generating magnetic fields inside organisms that are large enough to affect particle movement is a challenge; particles move along the spatial gradient of a magnetic field and, often, field strengths are reduced to zero just a few millimeters away from a permanent magnet.<sup>11, 12</sup> New designs for magnetic field application may make it possible to create larger field gradients that allow for the movement of materials far deeper in the body.<sup>13, 14</sup> Additionally, clinical applications will demand models that can effectively predict magnetic particle movement in complex in vivo settings as such data are a necessary requisite for any clinical application. Finally, the clinical success of these new systems and models will require minimally toxic magnetic particles that are highly sensitive to even small external magnetic fields.

Here, four broad applications of magnetic nanoparticles in biology and medicine are surveyed: treatment, imaging, movement, and diagnostics (**Figure 1.1**). For treatment, magnetic nanoparticles are used to efficiently deliver various therapeutics, whether it is drugs, genes, or the particles themselves for magnetothermal heat treatment or as therapeutic catalysts. In clinical and preclinical imaging, magnetic nanoparticles are used as image-enhancing agents in MRI and magnetic particle imaging (MPI). Biomedically-relevant movement via the external field actuation of magnetic particles make the clinical translation of cell separation techniques and soft robotics more feasible. Finally, magnetic

nanoparticles can be used to boost the diagnostic performance and throughput efficiencies of various immunoassays. Across these four broad fields, particular focus is given to iron oxide-based magnetic nanomaterials, because of their biocompatibility, versatility, and wide range of use. In each section, novel trends of magnetic nanoparticles are examined considering their history and common uses within that field.

### 1.3. Treatment

#### 1.3.1. Iron Oxide Catalyzed Cancer Therapies

Cancer treatment is one of the largest fields of biomedical research. Doxorubicin, gold, silver, and ferrite nanoparticles have all been studied for their cancer killing abilities, and they have been clinically applied to varying degrees. These therapies work through the increased generation and tuning of reactive oxygen species (ROS) in tumor regions that can induce apoptosis and cellular death.<sup>15</sup> Ferrite nanoparticles, specifically iron oxide nanoparticles, can be used for this purpose, due to their intrinsic peroxidase-like activity. By catalyzing the Fenton reaction of  $H_2O_2$ , highly toxic hydroxyl groups, a type of ROS, are overproduced and cell death occurs. This was first discovered by Yan et al. in 2007 and, when combined with the magnetic targeting properties of these particles, it created considerable promise for the field.<sup>16</sup> Six years later, Zhang et al. took this knowledge and demonstrated the use of magnetic nanoparticles in tumor treatment.<sup>17</sup> Research has continued in this field focusing on the tunability of this characteristic through both manipulation of the particle itself and the external field acting upon it. While it is well studied that the catalytic activity can be tuned through particle size, composition, and morphology, recent trends in this field are focused on combining the biological and

chemical properties through surface coatings and targeting molecules. For example, Thoidingjam et al. was able to synthesize phyllanthus emblica-coated iron oxide nanoparticles, which allowed for the stabilization of very small iron oxide nanoparticles (~6 nm), which are ideal for the overproduction of ROS in lung cancer cells.<sup>18</sup> Likewise, Pandey et al. synthesized poly-L-lysine-coated Fe<sub>3</sub>O<sub>4</sub>@FePt particles for the targeting of mitochondria through its pH responsiveness offering a targeted multimodal therapy for glioblastoma.<sup>19</sup> The next step for these treatments lies in optimizing their catalytic efficiency to increase the potential adoption into the clinical.

External electromagnetic fields, when absorbed by the ferrite material, can be used to boost the catalytic activity, thus increasing ROS production, and decreasing the amount of ferrite material needed. Electromagnetic fields that are commonly studied for this purpose are alternating magnetic fields (AMFs) and X-ray.<sup>16</sup> AMFs were utilized by Wu et al., as they developed a magnetic hydrogel that is activated by a non-invasive external AMF to increase the production of ROS.<sup>20</sup> Similarly, Liu et al. synthesized novel graphene oxide- grafted iron oxide nanorings that have high magnetothermal properties. A significant increase in the ROS generation was observed when an AMF was applied.<sup>21</sup> The use of X-rays was studied when Klein et al. fabricated high stability, functionalized co-ferrite and superparamagnetic magnetite particles that, when exposed to X-ray radiation, released either Fe<sup>2+</sup> or Co<sup>2+</sup> ions, leading to ROS production and cancer cell apoptosis.<sup>22</sup> As research continues in the area of tuning particle physical properties, external field manipulation advancements are a compounding asset in the fight against cancer.

### 1.3.2. Drug and Gene Delivery

Magnetic nanoparticles can be used to direct the delivery of drug and gene therapies in the body. A major challenge in pharmacology is the specific delivery of an agent to the disease site; most widely prescribed drugs that are taken orally or via intravenous injection are not targeted.<sup>23</sup> Consequently, it is estimated that less than 10% of the dose makes it to the organ of interest and even less to cellular targets.<sup>24</sup> The most common solution is to increase the delivered dose to assure sufficient drug concentration at the

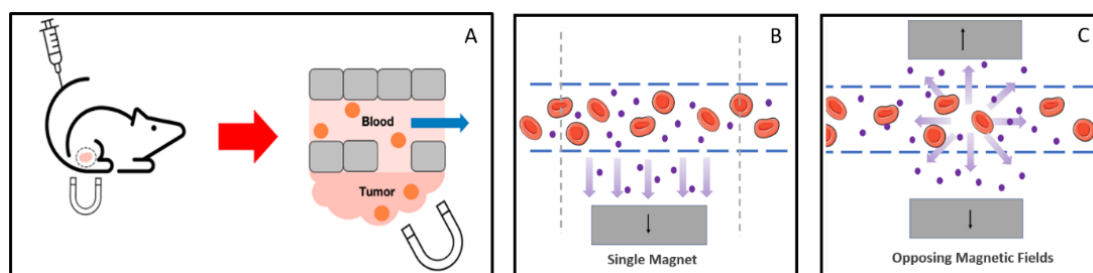


**Figure 1.2 Schematic of magnetic drug delivery.** (A) After a tail vein injection of magnetic nanoparticles, the materials collect at a site with a large external field gradient. Particles (shown in orange) extravasate into extracellular space where they are collected in regions of high magnetic field gradient. Adapted with permission from Al-Jamal K.T., *Nano Letters*; published by American Chemical Society, 2016. (B) Applied single magnets only pull in one direction towards the magnet versus dual magnets that can maintain a more constant gradient resulting in a constant outward radial force. (C) Magnetic set-up from Liu et al. using two oppositely polarized magnets to enhance magnetic drug targeting in deep tissues. Current methods use a single applied magnet resulting in limited use to surface level depths compared to dual magnets. The magnetic gradient of a single magnet falls off very quickly as distance increases compared to the pro-posed dual magnet device, which maintains the magnetic field with an increase in distance. Adapted with permission from Liu et al, *ACS Nano*; published by American Chemical Society, 2020 Modeled using art modified from Servier Medical Art, licensed under a Creative Commons Attribution 3.0 Generic License, date accessed (20, April 2021). <http://smart.servier.com/>.

target site.<sup>3, 25</sup> This inefficiency leads to off-target effects and toxicity, which can limit the clinical use of promising treatments. Additionally, non-selective delivery can also lead to negative immune responses at the site of administration.

Introducing selectivity into drug delivery is a general goal for all of pharmacology because of its broad relevance. One approach to increasing drug selectivity is by using nanoscale delivery systems, such as liposomes and polymeric nanoparticles, which possess cell-specific surface ligands. Several recent reviews have highlighted the common challenges that are faced by these non-magnetic biological and chemical targeting strategies.<sup>26-36</sup> Of these challenges, the most intractable is the body's own physiological response to these foreign nanoscale systems, which quickly removes, metabolizes, and/or excretes them. Even with stealthy surface coatings that have only minimal protein interactions, nanoscale particles are still recognized and eliminated by the innate immune system.<sup>37</sup> As such, even with the most efficient targeted nanoscale delivery systems, only 2% of the drug payload is released at the target site.<sup>24</sup>

This modest targeting performance could be vastly exceeded with magnetic drug delivery systems. Early investigators envisioned applied magnetic fields that were positioned around an organism capturing magnetic nanoparticles within tissue (**Figure 1.2**).<sup>14, 38</sup> As an example, an intravenous injection of a magnetic nanoparticles yields bloodborne particles that could be captured or collected in a solid tumor that was subjected to large magnetic field gradients. Such gradients could be generated by a magnetic system external to the animal or by permanent magnets inserted into the target tissue. The reliance on the physical separation of magnetic materials within a biological system for

targeting delivery is a fundamentally different approach to targeting than the chemical and biological strategies that were introduced earlier. If successful, this approach could increase the efficacy of delivery, limit off-target effects, and reduce the overall amount and time course of treatments.<sup>39</sup>

Magnetic nanoparticles that have been explored for targeted drug delivery have had to meet many stringent demands. Their dimensions and surface treatments must balance particle circulation time, drug distribution, drug release, accumulation, and, if needed, cellular uptake.<sup>25</sup> For most exposure routes (e.g., intravenous, oral, etc.), investigators aim for hydrodynamic diameters between 10 and 200 nm.<sup>37</sup> The application of polyethylene glycol (PEG) as a surface coating can prolong the circulation of intravenously injected materials, even with some degree of targeting functionality.<sup>40</sup> Iron oxide-based magnetic nanomaterials are of particular interest, because various SPION formulations have been approved by the US Food and Drug Administration (FDA) for various applications, including as MRI contrast agents.<sup>41</sup> While these materials are not widely adopted by radiologists due to the difficulty in interpreting T<sub>2</sub> contrast signals, they have found success off-label as treatments for iron deficiency.<sup>42</sup> Other challenges for the clinical translation of magnetic drug delivery systems include the reproducibility and scale of particle production, the economic feasibility of the application, and the practicality and safety of effective external magnetic field application. Magnetic drug delivery is also limited by the fact that particles are not retained at a target site once the external field is removed, which precludes many longer and chronic drug delivery applications.<sup>43</sup>

In addition to tackling these clinical obstacles, investigators are also broadening the appeal and reach of magnetic drug delivery.<sup>34,35,82</sup> One avenue of exploration is to increase the benefits of magnetic drug delivery through the integration of multiple delivery and imaging modalities. For example, Hervault et al. developed magnetic nanocomposites (MNCs) that included both a hyperthermic agent as well as a drug carrier for applications of multimodal cancer therapy.<sup>44</sup> By combining pH and thermo-responsive behavior, they could spatially and temporally control the release of Doxorubicin, which is a common chemotherapeutic agent. Chen et al. demonstrate that multifunctional envelope-type mesoporous silica nanoparticles (MEMSN) can increase the specificity of drug delivery and enhance the contrast of magnetic resonance imaging (MRI).<sup>45</sup> This is achieved through a release system that is initiated in acidic environments via the reactivity of immobilized surface acetals. This acid-catalyzed surface coating results in burst release of the target drug, Doxorubicin, in the slightly acidic tumor microenvironment allowing for efficient and targeted delivery of an otherwise highly toxic anticancer therapeutic. When addressing the treatment of glioblastoma, specifically with Doxorubicin, passage through the blood brain barrier must be considered. Norouzi et al. developed a Doxorubicin loaded magnetic combination therapy that displayed a dramatic increase in passage through the blood brain barrier. This 2.8-fold increase is due to the use of cadherin binding peptides, which transiently open the tight junctions of the blood brain barrier, combined with the use of an external magnetic field to draw the particles to the target region.<sup>46</sup> This work, like many others in the field, shows the promising impactful change that magnetic combination therapies can have.



Dual drug delivery and imaging nanoscale delivery systems, which are often termed theranostics, can be useful for both therapeutic and diagnostic purposes. Luque-Michel et al. developed theranostic polymeric nanoparticles loaded with SPIONs and doxorubicin to treat glioma-bearing mice.<sup>47</sup> They found significant particle accumulation when the animal is under static magnetic field and the accumulation was easily imaged using MRI. Theranostics are the logical next step for magnetic nanoparticle applications since the same material can be used in multiple ways. Currently, researchers are forming hybrid magnetic nanoparticles to optimize the optical or chemical properties. This can be the addition of gold, manganese, sulfides of copper, or tungsten, which increases the particles' magnetism and relaxivity when compared with non-doped SPIONs.<sup>48</sup> By combining different material characteristics, more effective and less toxic theranostics can be developed.

Magnetic gene delivery is also of ongoing interest to researchers because of its broad significance. Often referred to as magnetofection, this type of magnetic drug delivery attaches magnetic carriers to a viral vector carrying a therapeutic gene; in some cases, more rarely, the nucleic acid is directly linked to a magnetic nanoparticle via ionic interactions.<sup>11</sup> In 2002, Scherer et al. presented the first example of magnetofection in vitro and demonstrated that transfection efficiency could be increased by the application of a localized external magnetic field.<sup>49</sup> Nearly two decades later, research into magnetofection is focused on reducing the time for magnetic transfection, minimizing the vector dose, and expanding gene delivery to in vivo transfection in lung epithelium and blood vessel endothelial cells.<sup>50-52</sup> The current challenges facing application of this

delivery system in vivo are the potential for magnetic nanoparticle agglomeration and poor transfection efficiency if the viral carrier is removed.<sup>51</sup> Indeed, magnetofection has high transfection efficiency when compared to other methods, and it is a commonly used technique for in vitro applications.

Finally, any use of external magnetic fields to manipulate particles in vivo requires efficient systems for applying them. Until recently, single electromagnetic coils or permanent magnets were used for this purpose. Clinical applications would require much larger magnetics, increasing power demands, the need for efficient cooling systems, and cost. Originally, large magnetic field gradients generated inside of electromagnetic coils directed magnetic particle movement, but only towards the magnet instead of holding them at the region of interest. Nacev et al. used multiple focusing magnets to address this issue and to extend the reach of external fields to areas that are deeper within the body.<sup>53</sup> They used fast magnetic pulses to trap ferromagnetic rods at specific locations, resulting in inward-pointing magnetic forces. These forces were, in effect, focused, and lead to a larger field gradient and more specific and localized targeting. Although they did not apply their methodology to drug delivery, this more specific and targeted approach has the potential to overcome some of the largest barriers to entry for clinical applications. In another example, Liu et al. positioned permanent magnets in an opposing square (a simplified model is shown in **Figure 1.2C** to improve the accumulation and penetration of magnetic nanocarriers into solid tumors.<sup>54</sup> They demonstrated a five-fold increase of penetration and a three-fold increase in the accumulation of magnetic nanoparticles when compared to passive accumulation alone. Moreover, the system could reach

deeper into tissue than approaches that rely on a single permanent magnet that can only collect materials at superficial depths, typically only a few millimeters for a rare earth permanent magnet. This two-magnet configuration is just one example of emerging magnet designs that improve the efficacy, accumulation, and movement control of magnetic nanoparticles, bringing magnetically driven drug targeting closer to the clinic.

### 1.3.3. Magnetothermal Heating

The magnetothermal heating of magnetic particles was first observed in 1954, where it was used to selectively destroy cancer metastases in lymph nodes that might have been previously missed in surgery.<sup>55</sup> Briefly, magnetothermal heating occurs when magnetic particles are subjected to alternating magnetic fields (AMFs). Through magnetic induction, nanoparticles in AMFs are selectively heated, providing for localized increases in temperature. The effect can be used in drug delivery schemes that apply thermally sensitive coatings to nanoparticles, which result in the release of chemotherapeutic agents in addition to the thermal ablation of the cancer cells.<sup>56, 57</sup> Magnetothermal treatments have been approved in the European Union (EU), and they were also approved by the US Food and Drug Administration (FDA) in 2006 for phase I clinical trials in the treatment of prostate cancer. Ongoing clinical applications have been limited by the need for precise placement of large AMFs within the human body.<sup>81</sup> Conventionally, the organism is placed within an electromagnetic coil, but this can be difficult with larger animals. The duration of heat treatment and the strength of the AMFs are also important parameters to control with existing methods.

Magnetothermal heating can be very heterogeneous, leading to insufficient and unpredictable heating, because of tumor vasculature and extracellular matrix structure. Silva et al. combined magnetic nanoparticles with green fluorescent protein to form “nanothermometers” that use feedback to minimize heterogeneous heating.<sup>58</sup> While the early days of magnetothermal heating were concerned with heating tissue to high temperatures (>45 °C) to kill cells, recent interest has centered on using mild heating to influence biological processes with great precision. Christiansen et al. used the localized heating of magnetic nanoparticles to actuate neuronal ion channels from a distance using magnetic nanoparticles.<sup>56</sup> Other researchers have also used AMF heating to open and close an ion channel without affecting the health of cells.<sup>12</sup> Radio-frequency magnetic fields can also remotely activate cation channels in cells deep within tissue, thereby offering an alternative to the limited depth penetration of photothermal therapies. However, a more recent trend attempts to pair photothermal and magnetothermal together to give a secondary “activation” force to carry out the necessary heating even deeper within the body for applications from arterial inflammation to cancer therapies.<sup>34, 59</sup> This combination therapy is ten times more effective at heating the target region than the individual use of these therapies.<sup>60</sup> This combination of photothermal and magnetothermal therapies can be used to apply hyperthermia treatment and release drug to the region of interest. This is demonstrated by Lu et al. and their work with modified iron oxide composite nanoparticles loaded with cetuximab. Combination thermal heating was used for both applying hyperthermia treatment and to thermally release drug.<sup>61</sup>

However, more stable, and sensitive magnetic particles are needed to make the clinical translation of magnetothermal therapy more feasible. Some investigators have also reported challenges with superparamagnetic iron oxide nanocrystals (SPION) aggregation. Therefore, without proper surface engineering, the use of SPION in magnetothermal applications like tumor treatment could be limited.<sup>62</sup> More recently, these challenges are being met in a variety of ways, and several recent review papers cover these advances with respect to magnetothermal heating.<sup>28, 32, 34, 36</sup> The responsiveness of magnetic particles to smaller AMFs can be optimized by altering their composition and shape to increase their magnetic susceptibility.<sup>28</sup> Doped ferrites are a promising approach for increasing susceptibility, and therefore sensitivity, without complicating their surface engineering.<sup>63</sup> Different nanoparticle shapes, such as the magnetic nanoplates proposed by Alhasan et al., allow for more efficient heating with lower AMFs.<sup>62</sup>

## 1.4. Imaging

### 1.4.1. Magnetic Resonance Imaging (MRI) Contrast Agents

A common medical application for magnetic nanoparticles is their use as contrast agents for magnetic resonance imaging (MRI). MRI is a non-invasive and high-resolution imaging modality that has become the clinical standard for visualizing anatomical structures. Despite its wide clinical use, MRI has low signal intensity and sensitivity, which makes rapid and accurate diagnoses difficult.<sup>64</sup> Consequently, approximately 40–50% of MRI procedures require contrast agents for image enhancement.<sup>65</sup> Gadolinium chelates (GCs) are the current clinical standard for MRI because of their low toxicity, short circulation

half-life, and positive contrast enhancement.<sup>7, 66, 67</sup> However, concerns have been raised regarding potential toxicity, non-specific biodistribution, poor cellular uptake and retention, and the sub-optimal contrast enhancement of GCs.<sup>7, 68, 69</sup> As a result, many improvements and alternatives to GCs have been developed.<sup>7, -77</sup>

Being developed as gadolinium-free alternatives to GCs, iron oxide particles (IOP) garnered clinical interest as MRI contrast agents because of their useful magnetic properties, unique biodistribution and pharmacokinetic profiles, targeting potential, and biocompatibility.<sup>78</sup> Early successes with superparamagnetic iron oxide nanocrystals (SPIONs,  $D_H > 50$  nm) and ultrasmall SPIONs (USPIONs,  $D_H < 50$  nm) led to the development of IOP with more robust synthetic approaches and a range of physiochemical, magnetic, biodistribution, and pharmacokinetic properties (**Table 1.1**).<sup>7,</sup>

<sup>66, 70-72, 79-84</sup> These materials have demonstrated preclinical and clinical potential, but many have been commercially discontinued for MRI and are only used in non-MRI clinical applications (**Table 1.1**).

The notable failure of iron oxide particles (IOP) to become standard tools in clinical MRI is generally ascribed to two distinct challenges. First is the reluctance of healthcare providers to use IOP in their regular practice. This is due, in part, to toxicity concerns that are amplified by black box warnings issued by the US Food and Drug Administration (FDA) after studies showed small, but measurable, risks of serious adverse events (0–1%) and anaphylaxis (0.02–0.2%) after ferumoxytol administration.<sup>66, 85</sup> Additionally, radiologists are not as experienced in interpreting the dark contrast provided by IOP in transverse water relaxation time ( $T_2$ )-enhanced MR images.<sup>85, 86</sup> Dark contrast enhancement and

susceptibility artifacts from IOP can result in misdiagnosis and an overestimation of lesion margins.<sup>70, 85-87</sup> A second issue has been the reluctance of pharmaceutical companies to produce IOP contrast agents. The demand for IOP is low because of healthcare provider

**Table 1.1** Commercial iron oxide particles for clinical magnetic resonance imaging.

IOP Name	IOP Type	Core Size/D <sub>H</sub> (nm)	r <sub>1</sub> /r <sub>2</sub> (mM <sup>-1</sup> s <sup>-1</sup> )	B <sub>0</sub> (T)	t <sub>1/2</sub> (h)	MRI Applications	Commercial Status	Clinical Approval	References
<b>Ferristene (Abdoscan)</b>	MIOP	-/~3500	-	-	oral	GI	discontinued (2000)	-	71,80,7
<b>Ferumoxsil (AMI-121, GastroMARK, Lumirem)</b>	MIOP	-/300	3.4, 2/3.8, 47	1, 1.5	oral	GI	discontinued (2012)	1996 US/EU (GI MRI)	71,72,80,7
<b>Ferumoxides (AMI-25, Feridex, Endorem)</b>	SPION	4.5–5.6/50–100	40, ~10/~120–160	0.47, 1.5	2	L, S, BM, CTL, BT	discontinued (2008)	1996 US (L and S MRI)	71,72,80,7,79,66,70,81,82
<b>Ferrixan (SHU 555A, Resovist, Clivvist)</b>	SPION	~10/60–80	25.4, 9.7/~150–190	1.5	2.4–3.6	L, S, MRA, CTL	available in limited countries	2001 EU/JP/AU (L MRI)	71,72,80,7,79,66,70,82
<b>Ferumoxtran-10 (AMI-227, Combidex, Sinerem)</b>	USPION	4–6/20–50	23, ~10–20/53, ~65–88	0.47, 1.5	24–36	L, LN, S, MRA, M, CTL, BT	discontinued (2007)	-	71,72,80,7,66,70,82
<b>Ferumoxytol (AMI-7228, Feraheme, Rienso)</b>	USPION	6.7/20–30	38, 15	0.47, 1.5	10–14	L, LN, MRA, M, I, CTL, BT, BL, S	available	2009 US, 2013 EU (iron deficiency treatment)	71,72,80,7,66,70,81,83,84
<b>Ferucarbotran C (SHU 555C, Supravist)</b>	USPION	3–5/20–25	24, 10.7/60, 38	0.47, 1.5	6–8	MRA, CTL, M	discontinued	-	71,80,72,66,70
<b>Feruglose (NC100150, PEG-feron, Clariscan)</b>	USPION	5–7/11–15	20	0.5	2–6	L, LN, P, MRA	discontinued (early 2000s)	-	71,72,80,7,70,66,82
<b>VSOP-C184</b>	USPION	4–5	20.1, 14	0.94, 1.5	0.6–1.3	L, MRA, CTL, M	stopped development	-	71,72,80,7,70

Abbreviations: iron oxide particle (IOP), micron-sized iron oxide particle (MIOP), superparamagnetic iron oxide nanocrystal (SPION), ultrasmall superparamagnetic iron oxide nanocrystal (USPION), hydrodynamic diameter (D<sub>H</sub>), longitudinal water relaxivity (r<sub>1</sub>), transverse water relaxivity (r<sub>2</sub>), external magnetic field strength (B<sub>0</sub>), circulation half-life (t<sub>1/2</sub>), magnetic resonance imaging (MRI), United States (US), European Union (EU), Japan (JP), Australia (AU), gastrointestinal (GI), liver (L), spleen (S), magnetic resonance angiography (MRA), bone marrow (BM), lymph node (LN), macrophage (M), cell tracking and labeling (CTL), perfusion (P), brain tumor (BT), inflammation (I), sarcoma (S), and brain lesions (BL).

hesitancy, niche application (e.g., liver-, spleen-, and lymph node-related imaging and patients with renal deficiency), and ongoing concerns regarding their diagnostic utility when compared to conventional contrast agents.<sup>88, 102, 91</sup>

In response to these issues, researchers have continued to develop IOP to reduce toxicity concerns, optimize magnetic properties and contrast performance, and apply them in novel and significant ways.<sup>65, 66, 72-75, 86, 88</sup> Here, we focus on the latter, and examine the current trends in IOP-based MRI. IOP have been mostly relegated to mononuclear phagocyte system (MPS)-related imaging (e.g., liver, spleen, and lymph nodes) and cellular tracking applications.<sup>70</sup> To overcome radiologists' concerns about the dark contrast resulting from  $T_2$  manipulation, IOPs are being developed as longitudinal water relaxation time ( $T_1$ ) contrast agents.<sup>86, 88</sup> This provides the desirable white contrast in images, and  $T_1$  enhanced magnetic nanoparticles are typically smaller, and they yield greater signal-to-noise (tissue  $T_1 > T_2$ ) and better spatial resolution than those developed for  $T_2$  applications. This makes the materials relevant for a wider variety of applications. For instance, Wei et al. developed a zwitterion-coated exceedingly small SPION (ZES-SPION,  $D_H = 4.7$  nm) for magnetic resonance angiography (MRA) in small animals (**Figure 1.3A–C**).<sup>87</sup> These ZES-SPIONs are biocompatible, renally cleared (unlike commercial USPIO), and possess  $T_1$  contrast and blood circulation times that are comparable to commercial GCs.<sup>67, 87</sup> Lu et al. used slightly larger polyethylene glycol (PEG)-coated USPIOs (PEG-IONC,  $D_H = \sim 12$  nm) to study the toxicity and potential of IOP as  $T_1$  MRI contrast agents in larger animal models (**Figure 1.3D–G**).<sup>89</sup> PEG-IONCs demonstrated no significant toxicity, and they were successfully used for full-body MRA; notably they were



able to identify ischemia in cerebral angiograms. More recently, Kang et al. used similar USPIO in rats to monitor the remodeling of cerebral vasculature after ischemic stroke.<sup>90</sup> Cellular tracking and labeling are another common trend in preclinical and clinical IOP-based MRI.<sup>79, 91</sup> Because  $T_1$  imaging can be significantly impacted by compartmentalization of nanoparticles in cells, applications usually use  $T_2$ -weighted

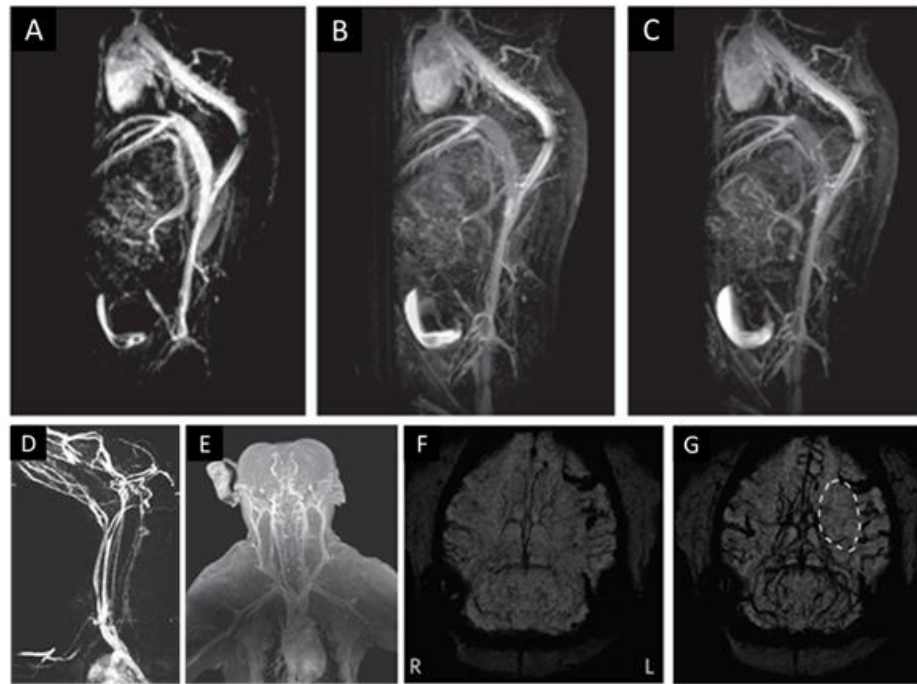


**Figure 1.3  $T_1$ -weighed MRA of small and large animal models using IOP.**  $T_1$ -weighed MRA of a mouse at (A) 4, (B) 12, and (C) 20 min post injection with ZES-SPIOs. MRA of (D) canine (beagle) and (E) non-human primate (macaque) animal models post PEG-IONC injection. Dynamic susceptibility contrast perfusion-weighted images of left cerebral ischemia in a macaque (F) before and (G) after bolus injection of PEG-IONC. (A–C) Reproduced with permission with modifications from Wei et al., Proceedings of the National Academy of Sciences of the United States of America; published by National Academy of Science, 2017. (D–G) Reproduced with permission with modifications from Lu Y. et al., Nature Biomedical Engineering; published by Springer Nature, 2017.

MRI.<sup>66</sup> Guldris et al. developed glucosamine-modified polyacrylic acid-coated USPIOs (USPIO-PAA-GlcN,  $D_H = 40$  nm) for enhanced cellular uptake and biocompatibility and use in long-term MRI tracking of intra-arterially injected stem cells in healthy rat brains (**Figure 1.4C**).<sup>92</sup> When compared to PAA-coated SPIONs and USPIOs, USPIO-PAA-GlcN demonstrate greater promise for potential in vivo applications in tracking the stem cell treatment of cerebral ischemia. However, there are concerns that IOP can adversely impact the functions of labeled cells.<sup>85, 93</sup> Wierzbinski et al. labeled human skeletal

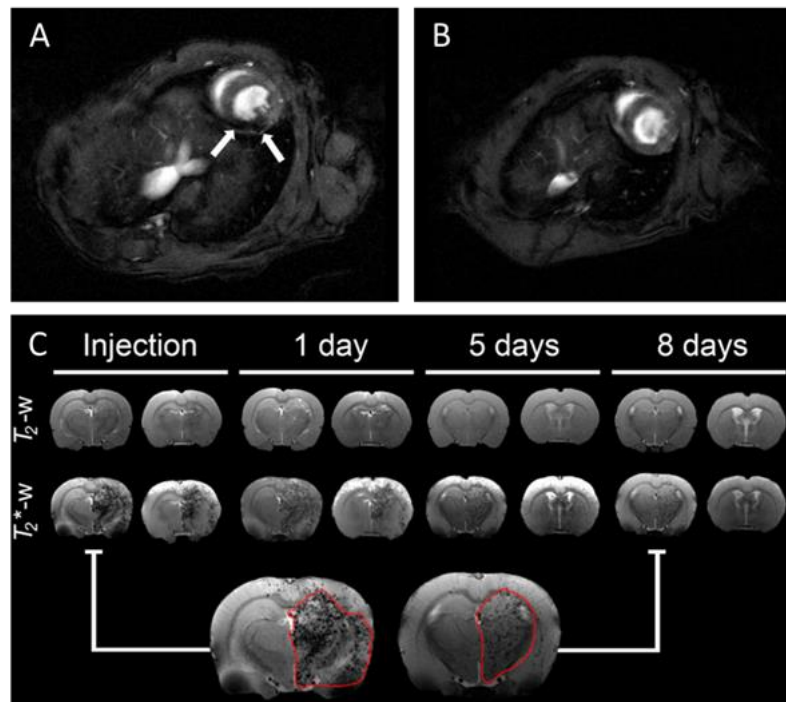


**Figure 1.4 T<sub>2</sub>-weighted cell tracking MRI applications using IOP.** T<sub>2</sub>-weighted MR image of mouse (A) without and (B) with intracardially implanted SPION-labeled myoblasts. (C) T<sub>2</sub>/T<sub>2</sub>\*-weighted cerebral MR images of mice intra-arterially injected with USPIO-PAA-GlcN-labeled mesenchymal stem cells after 1 h, 24 h, 5 days, and 8 days. (A, B) Reproduced with permission with modifications from Wierzbinski, K. R. et al., *Scientific Reports*; published by Nature Research, 2018. (C) Reproduced with permission from Guldris, N. et al., *Bioconjugate Chemistry*; published by American Chemical Society, 2017.

myoblasts with carboxylic acid-coated USPIO (DMSA-USPIO, core size = ~10 nm) to track integration after implantation into the left heart ventricle of mice (**Figure 1.4A, B**).<sup>94</sup> DMSA-USPIOs had no significant functional or cytotoxic effect on myoblasts. Moreover, the work demonstrated the potential for clinically tracking the integration and progress of skeletal myoblast transplants into postinfarction scars. Ultimately, the adverse effects on labeled cells can be reduced with more biocompatible and responsive IOP to enable a lower effective nanoparticle dose.

IOP are also being used in a wide variety of passive and active targeting-based molecular MRI applications.<sup>64</sup> Sherwood et al. developed bovine serum albumin (BSA)-USPIO clusters (core sizes <4 nm, cluster size = ~200 nm) for MR image-guided drug delivery to subcutaneous tumor-bearing mice.<sup>95</sup> This is possible because tumors often exhibit molecular features that can cause porous vasculature and poor lymphatic drainage, which results in the passive accumulation of nanoscale materials—often called the enhanced permeability and retention (EPR) effect.<sup>96, 97</sup> Others have developed pH responsive USPIO clusters to take advantage of, and target, the slightly lower pH (pH 5.6–6.8) of the tumor microenvironment.<sup>98, 99</sup> In the presence of the slightly acidic tumor microenvironment, pH-sensitive cluster crosslinkers disassociate, causing the release of smaller USPIO, which allows for greater accumulation, signal-to-noise, and T<sub>1</sub> contrast enhancement (**Figure 1.5B**). IOP contrast agents can also be used for the molecular imaging of the inflammation that is associated with pain because of the greater presence of MPS cells—which preferentially uptake foreign nanoscale objects.<sup>67</sup> A few recent clinical studies highlight the advantages of molecular imaging by comparing USPIO- and

GC-enhanced MRI for assessing a variety of disease states that are associated with inflammation as well as tumors.<sup>86,87,103,104</sup> In all cases, T<sub>1</sub>- and or T<sub>2</sub>-weighted USPIO-enhanced MRI provided equal or greater diagnostic utility when used alone or in

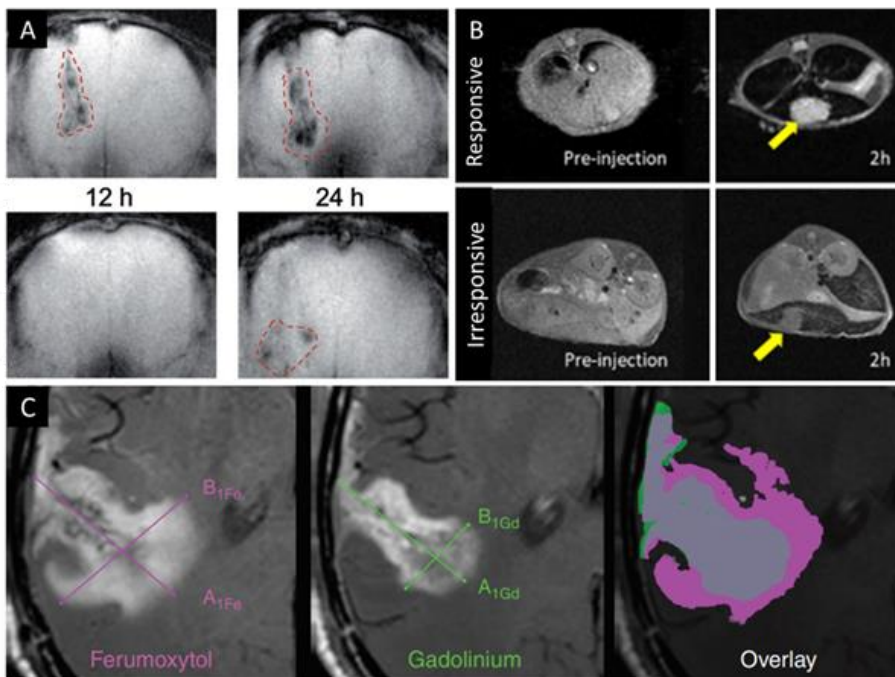


**Figure 1 5 Brain tumor MRI applications using IOP.** (A) T2-weighted MR images of a U-87 MG (human glioblastoma) tumor in the brain of a nude mouse using iron oxide nanocubes (top) with B6 peptide and (bottom) without at 12 and 24 h intervals after intravenous injection. (B) T1-weighted MR images of orthotopic hepatocellular carcinoma mouse models before and 2 h after injection with pH-responsive (top) and pH-irresponsive (bottom) USPIO clusters. (C) Representative ferumoxytol- and GC-enhanced MR images of a patient with glioblastoma and an overlay of the two demonstrating the mismatch used to distinguish between pseudoprogression and true progression. (A) Reproduced with modifications with permission from Lu, Z. et al., *Advanced Functional Materials*; published by John Wiley and Sons; 2017. (B) Reproduced with modifications with permission from Lu, J. et al., *Journal of the American Chemical Society*; published by American Chemical Society, 2018. (C) Reproduced with modifications with permission from Barajas, R. F. et al., *Neuro-Oncology*; published by Oxford University Press, 2019.

conjunction with T<sub>1</sub>-weighted GC-enhanced MRI. Notably, Barajas et al. demonstrated that dual ferumoxytol- and GC-enhanced MRI could reliably differentiate between true progression (recurrence) and pseudoprogression (therapy-associated tissue damage and inflammation) by observing biodistribution-associated mismatch in their imaging enhancement (**Figure 1.5C**).<sup>100</sup>

In response to critiques of EPR-based passive accumulation, actively targeted IOP are being used to further increase the specificity and sensitivity of molecular MRI.<sup>96, 101</sup> Because transferrin receptors (TfR) are overexpressed in glioma, Lu et al. attached a TfR-specific peptide (B6) to a SPION-based drug delivery system (CARD-B6) for targeted T<sub>2</sub> imaging of glioma.<sup>102</sup> When compared to non-targeted CARD, CARD-B6 demonstrated much greater accumulation inside the tumor margins (Figure 5A). Husain et al. targeted excess matrix metalloproteinase (MMP-12) that was associated with inflammation to image molecular features associated with neuropathic pain in rats.<sup>103</sup> Even with these IOP-based molecular MRI techniques, sensitivity is a concern, because accumulation can often be too low to achieve meaningful contrast enhancement.<sup>85</sup> Current efforts focus on enhancing the magnetic properties of IOP to decrease the effective dose, reducing the associated toxicity and imaging artifacts.<sup>5, 73, 104</sup>

#### 1.4.2. Magnetic Particle Imaging (MPI) Tracers

Magnetic particle imaging (MPI) is a novel imaging technique that was first proposed in 2001.<sup>105</sup> MPI detects signals from superparamagnetic nanomaterials, also referred to as MPI tracers, which are generated by a fast-moving magnetic field-free region (FFR).<sup>105, 106</sup> In 2005, Gleich et al. demonstrated that this signal can be processed to reflect tracer

spatial location and concentration, thereby offering an opportunity for quantitative imaging with high spatial resolution ( $\sim 1$  mm) and sensitivity ( $\sim 100$   $\mu\text{mol Fe/L}$ ).<sup>107</sup> Additionally, since superparamagnetic tracers are not naturally present in the body, MPI has nearly zero background, as compared to the clinical contrast-enhanced MRI. Following the development of early preclinical prototypes in the late 2000s, Weizenecker et al. performed the first in vivo three-dimensional MPI experiment examining the beating heart of a mouse in real-time.<sup>105, 108</sup> Despite this success, the clinical translation of MPI depends on the development of much larger scanners and highly responsive tracers to further enhance spatial resolution and sensitivity.<sup>109, 110, 113, 114</sup> MPI tracer performance is dependent on its ability to reverse its magnetic moment in the FFR; the larger the change in magnetic moment, the larger the MPI signal. As with any nanomedicine, the colloidal stability, pharmacokinetics, biodistribution, and biocompatibility of the magnetic nanoparticles for MPI are also important considerations.

As tracer technology continues to develop, MPI can be applied in a wide range of biomedical applications.<sup>109</sup> Zhou et. al. performed the first in vivo MPI of lung perfusion in rats (**Figure 1.6A, B**).<sup>110</sup> Here, micron-sized bovine serum albumin (BSA)-conjugated SPION aggregates (MAA-SPION,  $\sim 25$   $\mu\text{m}$ ) were used to target the narrow capillary bed of the lungs ( $6$   $\mu\text{m}$ ) after their first pass through the heart. When compared to standard diagnostic techniques for assessing pulmonary embolism, this preliminary study on healthy rats demonstrates the potential of MAA-SPION-based MPI as a convenient and ionizing radiation-free alternative to other diagnostic options. The first-pass pulmonary trapping of micron-sized objects, while useful for lung imaging, presents a problem for

the intravenous therapeutic delivery of mesenchymal stem cells (MSC). To better understand the biological fate of cellular therapies, Zheng et al. used quantitative MPI to assess the biodistribution and pharmacokinetics of tracer tagged MSCs (**Figure 1.6C, D**).<sup>111</sup> MPI can also be used to visualize and assess disease states. For instance, Yu et al. used subtraction MPI to quantify the extent of gastrointestinal (GI) bleeding in a mouse model that was predisposed to developing GI polyps (**Figure 1.6E, F**).<sup>112</sup> MPI offers a non-invasive, non-ionizing, and rapidly administered alternative compared to traditional approaches for assessing GI bleeds (e.g., colonoscopy and radionuclide scintigraphy). As with nanoparticle magnetic resonance imaging (MRI) contrast agents, MPI tracers can also take advantage of the enhanced permeability and retention (EPR) effect and passive accumulation to image tumors when possible.<sup>113</sup>

Apart from simple tumor imaging, MPI can be used for therapeutic purposes. For example, Zhu et. al. used quantitative MPI to monitor in vivo drug release in tumor-bearing mice.<sup>114</sup> Their unique MPI tracer is a pH-sensitive SPION-drug cluster that, when introduced to the acidic tumor microenvironment, releases SPION and doxorubicin. Increased SPION Brownian motion after release enhances the MPI signal, and it provides an indirect, but accurate, measure of drug release. Likewise, Tay et. al. used SPION tracers for MPI-guided magnetic hyperthermia therapy on a tumor bearing mouse (**Figure 1.6G–J**).<sup>115</sup> MPI is used to map the distribution of SPION, the FFR is moved to the region of interest (tumor), and a second alternating magnetic field is then applied for magnetic hyperthermia in that region only. The ability to precisely monitor the location and

magnitude of therapy applied (e.g., drug release or magnetic hyperthermia) would allow for more accurate dosing and tracking of therapeutic efficacy, thus optimizing treatments.

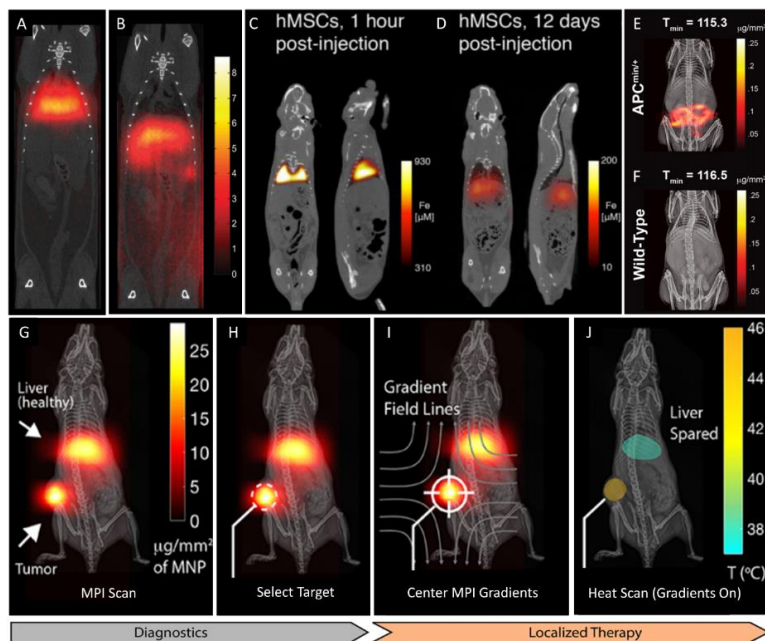


**Figure 1.6 MPI applications using IOP.** MPI of intravenously administered (A) MAA-SPION and (B) SPION in healthy rats. The larger MAA-SPION target the lungs while smaller SPION distribute primarily to the liver. MPI of tracer labeled human MSCs (C) 1 h and (D) 12 days after intravenous administration in healthy rats. Labeled MSCs move from the lungs to the liver and spleen over the course of 12 days. The subtraction MPI of (E) GI polyp/bleed and (F) normal mouse models about 2 h post intravenous administration. Signal evident in the intestines for mice with GI bleed. (G–J) Procedure for MPI-guided localization and magnetic hyperthermia therapy. The diagnostic stage involves (G) the initial MPI scan of the tumor-bearing mouse model and (H) selecting the target. The localized therapy stage involves (I) centering the FFR on the target followed by (J) the therapeutic heat scan. (A, B) Reproduced with permission with Zhou, X. Y. et al., *Physics in Medicine & Biology*; published by Institute of Physics and Engineering in Medicine, 2017. (C, D) Reproduced with permission from Zheng, B. et al., *Theranostics*; published by Ivyspring International Publisher, 2016. (E, F) Reproduced with permission from Yu, E. Y., et al., *ACS Nano*; American Chemical Society, 2017. (G–J) Reproduced with permission from Tay, Z. W., et al., *Nano Letters*; published by American Chemical Society, 2018.



## 1.5. Movement

### 1.5.1. Cell Separation

The magnetic separation of biological material using particles was first applied in the 1970s to sorting cells and, since then, “magnetophoresis”, as it has been termed, is widely used to separate specific cells from a biofluid or trim down cell populations (**Figure 1.7**).<sup>116, 117</sup> The speed and ability to batch process biological samples make magnetic-activated cell sorting (MACS) an especially appealing option for cell sorting in flow cytometry instruments.<sup>117</sup> The current limitations of magnetic separation for this

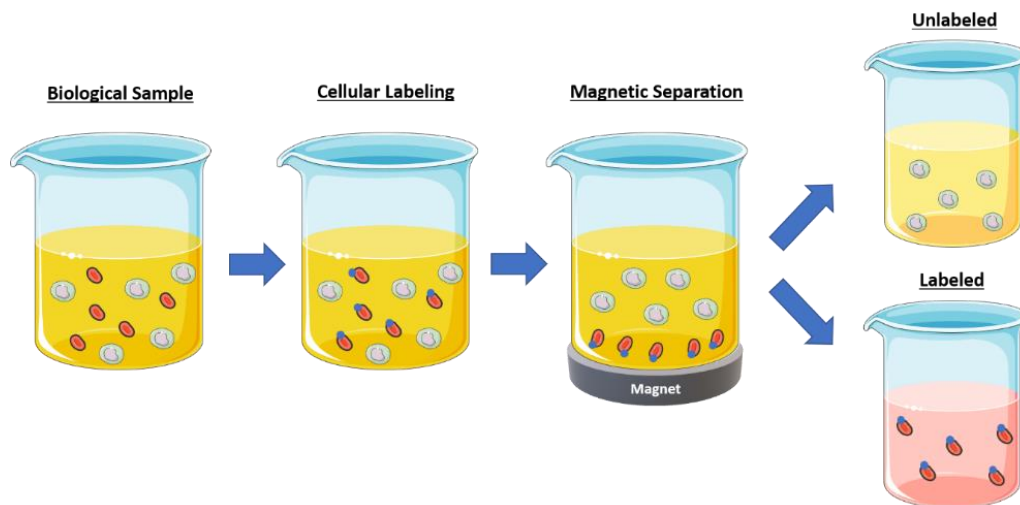


**Figure 1.7 Magnetic batch separation for cell separation.** Initially cells are suspended and then the desired cell population is labeled with magnetic nanoparticles. The final step depends on the selection methodology: labeled or unlabeled selection. In unlabeled selection, the desired cells remain in the supernatant and the labeled cells are magnetically captured via a permanent magnet (also known as negative selection). Alternatively, the cells of interest can be labeled and magnetically captured, and the supernatant can be discarded (also known as positive selection). Art modified from Servier Medical Art, licensed under a Creative Common Attribution 3.0 Generic License accessed (20 April 2021). <http://smart.servier.com/>.

application include high sample processing cost, limited sample throughput, low processing speeds, and loss of cellular function or viability.<sup>117</sup> However, magnetophoresis in the scaled-down environment of microfluidic systems faces fewer of these issues and remains an expanding area of research.

One area of focus for research in this area has been single cell capture as it relates to cancer diagnostics. The internal capture of circulating tumor cells, for example, is possible using an intravascular magnetic wire implanted into a patient, and magnetic particles offer less invasive, but similar, opportunities.<sup>118</sup> External use of microfluidics, often termed “lab on a chip”, can be applied to the analysis of small drops of biofluids in which magnetic nanoparticles can be used to separate cells using antibodies or proteins as markers.<sup>119-124</sup> Alternatively, Robert et al. was able to sort monocytes and macrophages by exploiting the different internalization rates of iron oxide nanoparticles.<sup>125</sup> The macrophages were sorted into five different groups, depending on the nanoparticle load using on-chip free-flow magnetophoresis. Monocytes had a much lower capacity to internalize particles and, as a result, were far less magnetic, thereby providing an excellent on-chip example of negative selection. Zhang Q. et al. demonstrated an immuno-magnetic sorting procedure using four types of immuno-magnetic nanoparticles for the separation of different T cells.<sup>126</sup> They found that selectivity could be preserved, even at processing volumes as high as four liters of processed blood sample but noted that increased throughput did degrade the selectivity of the separation process. While many examples of magnetic cell-sorting have been developed for the research laboratory, there is some promise that the technology could be relevant to consumers. Tran et al.

demonstrated a supraparticle assembly of magnetic nanoparticles for selective cell separation and counting using a smartphone-based imaging platform.<sup>127</sup> The integration of magnetic particles with “lab on a chip” technology has been advantageous in many biomedical applications.

### 1.5.2. Soft Robotics

Soft robotics is one of the most novel applications of magnetic nanoparticles in the field of directed motion. Soft robotics refers to systems that are built with flexible and stretchable materials to mimic living, moving tissue.<sup>128</sup> Being inspired by natural systems, nanoparticles can be incorporated into soft robotics to facilitate actuation of movement on a macro-scale and, if biocompatible, demonstrate promise for biomedical applications. Soft robots have been introduced into surgery, diagnosis, drug delivery, wearable and assistive devices, prostheses, and even artificial organs.<sup>129</sup> Most soft robots are quite large—on the order of millimeters—and their movement mechanisms are often electrically actuated. Magnetically actuated microrobots, while being more difficult to design, are of great interest, as they can be controlled at a distance without the need for a connection to a power source.<sup>130</sup> Magnetic microrobots that are subjected to applied magnetic fields can exhibit a wide range of deformations allowing for multiple types of movement, including rolling, walking, crawling, and jumping.<sup>131</sup> Magneto-elastic soft millimeter-scale robots offer greater movement due to their higher degrees of mobility, and they have been even shown to be able to transit between different liquid and solid terrains as well as switching between different locomotive modes. Although not at the nanoscale, Gu et al. developed magneto-elastic microrobots that mimic natural cilia—the

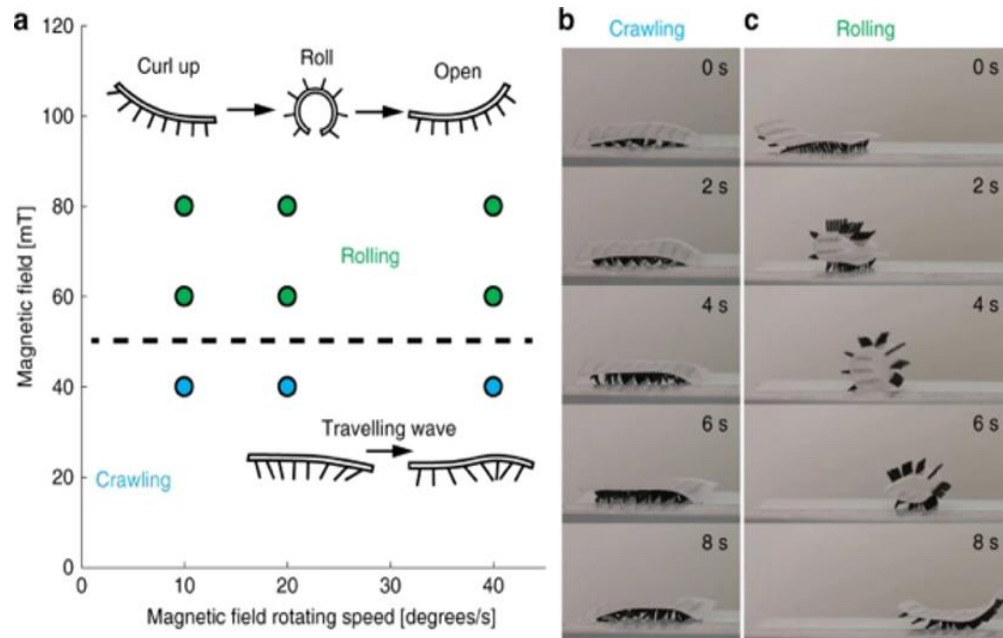


**Figure 1.8 Soft robotics application of IOP.** (A) Work from Gu H. et al. displays different modes of locomotion possible using magnetically actuated cilia including crawling and rolling. (B) Metachronal waves of the cilia structures leads to a crawling motion (C) When the magnetic field is larger than 60 mT the strong magnetic torque leads the soft robot to roll. Reprinted without changes with permission through the Creative Commons License 4.0 International License from Gu H. et al., Nature Communication; published by Springer Nature Limited, 2020.

hair-like structures that are found on microorganisms. The programmable robots can generate metachronal waves, making them able to crawl and roll, depending on the strength of the magnetic field, as seen in **Figure 1.8**.<sup>132</sup>

The limitations of current magnetically actuated soft robots include their difficulty navigating unknown obstacles, poor response to environmental change, and large millimeter sizes that limit clinical application.<sup>132</sup> Iron oxide nanoparticles can be incorporated into elastomeric matrices that can be shaped into sub-micron objects to reduce the size of these soft robots. Bayaniahangar et al. 3D printed helical coils using a

ferrofluid-siloxane mixture that could be actuated via external magnetic field.<sup>133</sup> Gouda et al. and Breger et al. created “micro-grippers” by embedding superparamagnetic iron oxide nanocrystals (SPIONs) into biodegradable matrices, so that the programmable 3D structures could be non-invasively triggered via external field. These magnetic structures were biodegradable, thereby eliminating the need for a second surgery for removal.<sup>134,</sup>  
<sup>135</sup> Hwang et al. demonstrated that multifunctional soft robots responsive to external magnetic fields can efficiently, and precisely, destroy biofilms. They built catalytic antimicrobial robots (CARs) that generate bactericidal free radicals that break down biofilms, and then remove the fragmented biofilm via magnetically directed processes. Such concepts may find applications in areas that range from wound care to dentistry.<sup>136</sup> Current trends focus on increasing the magnetic sensitivity of the embedded particles as well as exploring the wide space of combined chemical and mechanical activity.<sup>116, 137, 138</sup>

## 1.6. Diagnostics

### 1.6.1. Immunoassays

The attraction of magnetic nanoparticles towards externally applied fields is the basis of their use for diverse biological detection problems. Research in this area dates back to 1976, when a Norwegian scientist, John Ugelstad, exploring the synthesis of uniform polymer spheres for chromatography, first precipitated iron oxide nanoparticles into the porous colloids.<sup>139</sup> This yielded polymer particles, typically 20–30 w/w% iron oxide, which could be readily captured via rare earth, handheld magnets. Later research revealed that the materials were nanoscale maghemite, superparamagnetic, and well dispersed throughout the micron-sized polymer beads (**Figure 1.9**).<sup>140</sup> Among their first applications

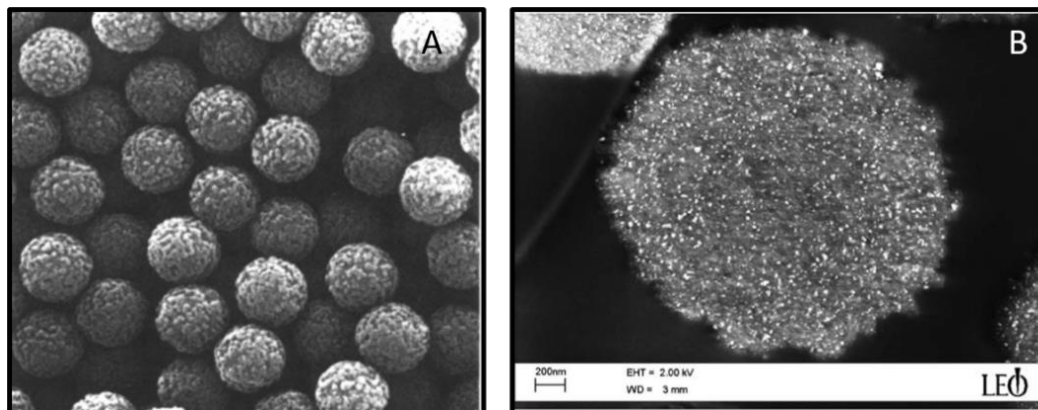


**Figure 1.9 Representative electron microscopy images of Dynabeads™.** (A) Polystyrene beads of average diameter 2.8 microns containing 12 w/w% iron in their pores. (B) SEM of a M-280 bead from Dynabeads™. The nanoparticles in the bead are visualized as bright points and were determined to be ~8 nm in diameter. (B) Reproduced with permission from Ugelstad et al., *Progress in Polymer Science*; published by Elsevier, 1992. Reproduced with permission from Fonnum et al., *Journal of Magnetism and Magnetic Materials*; published by Elsevier, 2005.

was the treatment of pediatric neuroblastomas in which the magnetic beads were used to separate tumor cells from patient's bone marrow prior to autologous transplantation.<sup>141, 142</sup> By decorating the surface of the particles with an antibody to known tumor cell antigens, investigators found that they could reduce the population of tumor cells in aspirates by three orders of magnitude. Through appropriate surface design, researchers throughout the early 1990s extended this flexible platform beyond cell-based separations to include the isolation and detection of proteins, nucleic acids, viruses, and bacteria.<sup>143-145</sup>

Commercial entities quickly capitalized on these magnetic beads for applications in biomedical research enabling the development of clinical applications. Such effort required reliable and reproducible materials and companies, such as Dynabeads™, were

able to meet the need for high quality nanoparticles. By 1996, there was a robust commercial business that provided researchers with magnetic beads, in both small (1  $\mu\text{m}$ ) and large (2.5  $\mu\text{m}$ ) diameter formats, with an array of different surface coatings. Biomedical researchers used benchtop magnetic separators and these beads as alternatives to tedious, multi-step purification protocols for various biomolecules, while clinical researchers began to explore bead-based analysis for disease detection, as described in Section 4.1. In one example, investigators correlated the success of kidney transplantation to the number of circulating epithelial cells that were recovered via immunomagnetic capture.<sup>146</sup> Magnetic beads were also used to analyze the DNA retrieved from patients with meningitis, to confirm its bacterial origins.<sup>147</sup>

The past five years have seen continued growth in magnetic bead technology for diagnostics, as their application has expanded substantially into the in vitro diagnostics of both protein and nucleic acids. Bead technology, and specifically magnetic beads, are now viewed as an increasingly attractive alternative to the enzyme-linked immunosorbent assay (ELISA) platform. This interest is driven, in part, by the pressing need for automation and simplified sample and liquid handling. Magnetic beads are well suited to such an environment, as they can be held fixed in place while robotic systems introduce reagents and eluent buffers. Several companies now sell commercial versions (MagPix<sup>TM</sup>) of systems that utilize these advantages, and the immunoassays perform at least as well, or even better, than the conventional ELISA systems.<sup>148, 149</sup> The simplified handling of magnetic particles is also of great value in the preparation of samples for quantitative

polymerase chain reaction (qPCR), as was demonstrated in the sensitive detection of Tuberculosis pathogens using a magnetic bead to gather sample DNA (e.g., amplicons).<sup>150</sup>

Multianalyte detection is a major theme in modern clinical diagnostic research, and magnetic beads are poised to play a central role. The rich abundance of proteomic and genomic information now readily available has established a growing need for the simultaneous detection of multiple biomarkers, ideally without extra cost or time. Commercial schemes leverage the capability to form libraries of beads, each being “barcoded” with optically distinct molecular fluorophore signatures, and each tailored with a unique surface targeting different biomolecules. Early versions of this technology used flow-based optical read-out to interrogate non-magnetic beads one-by-one, like conventional flow cytometry.<sup>151, 152</sup> The latest systems use magnetic beads that can be draw down into a monolayer; high resolution optical cameras can then image the bead barcodes as well as level of analyte bound over a field. In one case, such multiplex bead-based technology was as effective as sequential ELISA immunoassays for measuring up to ten biomarker proteins for bladder cancer in urine.<sup>153</sup> Also important is the development of magnetic bead-based assays for low resource settings. Paper-based immunoassays using functionalized magnetic beads to replace costly sample preparation steps are the subject of intense study.<sup>154</sup> Such accessible technology is particularly important for the multiplex detection of malaria antibodies for which magnetic bead technology is particularly well suited.<sup>155-157</sup>

Although commercial magnetic beads are largely unchanged from those applied forty years ago, new magnetic nanoparticles and their composites offer improved performance



and new types of applications. Investigators have used ferrites, typically Co-Fe<sub>2</sub>O<sub>4</sub>, instead of iron oxide as a magnetic material, beads are more responsive to applied fields, leading to faster separations.<sup>158-160</sup> Control over the dimensions of the magnetic nanoparticles also presents the opportunity to use different field strengths for multiplexed separations. By incorporating gold nanoparticles onto magnetic beads, several investigators have demonstrated more sensitive detection in immunoassays by leveraging particle-generated chemiluminescence or gold particle dissolution.<sup>161, 162</sup> Alternatively, immunomagnetic separation events can be confirmed through the precipitation of gold nanoparticles at bead surfaces.<sup>163</sup> Quantum dots can also be incorporated into magnetic nanoparticle composites yielding spectrally encoded beads for multiplexed analysis and have recently been used for malaria detection.<sup>164, 165</sup>

## 1.7. Conclusion

The use of magnetism in medicine has come a long way since the days of the ancient Greeks. It is the miniature lodestones of today, magnetic nanoparticles (e.g., SPIONs), which make their dream of healing the human body with magnetic fields a modern reality. SPIONs are unique, in that they are therapeutic agents themselves, through their intrinsic ability to catalyze Fenton reactions, but they also have the capacity to deliver specific drugs, gene fragments, or magnetothermal heating to specific areas of interest. Current trends improve this prospective by offering multifunctional particles, more effective magnetic field application systems, and even more magnetically sensitive particles. Researchers working to apply magnetic particles in MRI imaging have been successful in synthesizing SPION contrast agents with no notable toxicity, a higher blood circulation

time, and both passive and active targeting capabilities. This new generation of magnetic nanoparticles for both MRI and MPI may ultimately make their use in clinical imaging a reality. Finally, the integration of magnetic particles into “lab on a chip” and other diagnostic settings is both meeting the practical needs for faster and cheaper analysis, while also expanding the possibilities for multiple analyte sensing. Even the emerging area of soft robotics stands to benefit from advances in the magnetic nanomaterials that allow for more responsive and functional systems. Progress in both the development of the magnetic nanoparticles, as well as their expanding biomedical applications, has been swift since Ugelstad’s first report of magnetic polymer particles in 1976. One can only imagine what their continued study over the next four decades will have to offer to both science and medicine.

## 1.8. References

1. Häfeli, U., The History of Magnetism in Medicine. In *Magnetism in Medicine*, 2006; pp 1-25.
2. Peterson, F.; Kennelly, A. E., *Some physiological experiments with magnets at the Edison Laboratory*. D. Appleton: 1892.
3. Freeman, M. W.; Arrott, A.; Watson, J. H. L., Magnetism in Medicine. *Journal of Applied Physics* **1960**, *31* (5), S404-S405.
4. Damadian, R., TUMOR DETECTION BY NUCLEAR MAGNETIC RESONANCE. *Science* **1971**, *171* (3976), 1151-&.
5. Xiao, Z.; Zhang, Q.; Guo, X.; Villanova, J.; Hu, Y.; Külaots, I.; Garcia-Rojas, D.; Guo, W.; Colvin, V. L., Libraries of Uniform Magnetic Multicore Nanoparticles with Tunable Dimensions for Biomedical and Photonic Applications. *ACS Applied Materials & Interfaces* **2020**, *12* (37), 41932-41941.
6. Wu, K.; Su, D.; Liu, J.; Saha, R.; Wang, J.-P., Magnetic nanoparticles in nanomedicine: a review of recent advances. *Nanotechnology* **2019**, *30* (50), 502003-502003.
7. Wahsner, J.; Gale, E. M.; Rodriguez-Rodriguez, A.; Caravan, P., Chemistry of MRI Contrast Agents: Current Challenges and New Frontiers. *Chem. Rev.* **2019**, *119* (2), 957-1057.
8. Johannsen, M.; Gneveckow, U.; Taymoorian, K.; Thiesen, B.; Waldofner, N.; Scholz, R.; Jung, K.; Jordan, A.; Wust, P.; Loening, S. A., Morbidity and quality of life during thermotherapy using magnetic nanoparticles in locally recurrent prostate cancer: Results of a prospective phase I trial. *International Journal of Hyperthermia* **2007**, *23* (3), 315-323.
9. Lubbe, A. S., Preclinical experiences with magnetic drug targeting: Tolerance and efficacy and clinical experiences with magnetic drug targeting: A phase I study with 4'-epidoxorubicin in 14 patients with advanced solid tumors - Reply. *Cancer Research* **1997**, *57* (14), 3064-3065.
10. Merle, P.; Ahmed, S. S.; Habersetzer, F.; Abergel, A.; Taieb, J.; Bonyhay, L.; Costantini, D.; Dufour-Lamartinie, J.; Trepo, C., Phase 1 study of intra-arterial hepatic (IAH) delivery of doxorubicin-transdrug (R) (DT) for patients with advanced hepatocellular carcinoma (HCC). *Journal of Clinical Virology* **2006**, *36*, S179-S179.
11. Pankhurst, Q. A.; Connolly, J.; Jones, S. K.; Dobson, J., Applications of magnetic nanoparticles in biomedicine. *Journal of Physics D-Applied Physics* **2003**, *36* (13), R167-R181.
12. Huang, H.; Delikanli, S.; Zeng, H.; Ferkey, D. M.; Pralle, A., Remote control of ion channels and neurons through magnetic-field heating of nanoparticles. *Nature Nanotechnology* **2010**, *5* (8), 602-606.

13. Henriksen, A. D.; Rozlosnik, N.; Hansen, M. F., Geometrical optimization of microstripe arrays for microbead magnetophoresis. *Biomicrofluidics* **2015**, *9* (5), 14.
14. Liu, J. F.; Lan, Z. Y.; Ferrari, C.; Stein, J. M.; Higbee-Dempsey, E.; Yan, L.; Amirshaghghi, A.; Cheng, Z. L.; Issadore, D.; Tsourkas, A., Use of Oppositely Polarized External Magnets To Improve the Accumulation and Penetration of Magnetic Nanocarriers into Solid Tumors. *ACS Nano* **2020**, *14* (1), 142-152.
15. Liou, G.-Y.; Storz, P., Reactive oxygen species in cancer. *Free Radical Research* **2010**, *44* (5), 479-496.
16. Yu, S.; Zhang, H.; Zhang, S.; Zhong, M.; Fan, H., Ferrite Nanoparticles-Based Reactive Oxygen Species-Mediated Cancer Therapy. *Frontiers in Chemistry* **2021**, *9* (184).
17. Zhang, D.; Zhao, Y.-X.; Gao, Y.-J.; Gao, F.-P.; Fan, Y.-S.; Li, X.-J.; Duan, Z.-Y.; Wang, H., Anti-bacterial and in vivo tumor treatment by reactive oxygen species generated by magnetic nanoparticles. *Journal of Materials Chemistry B* **2013**, *1* (38), 5100-5107.
18. Thoidingjam, S.; Tiku, A. B., Therapeutic efficacy of Phyllanthus emblica-coated iron oxide nanoparticles in A549 lung cancer cell line. *Nanomedicine* **2019**, *14* (17), 2355-2371.
19. Pandey, A.; Singh, K.; Subramanian, S.; Korde, A.; Singh, R.; Sawant, K., Heterogeneous surface architected pH responsive Metal-Drug Nano-conjugates for mitochondria targeted therapy of Glioblastomas: A multimodal intranasal approach. *Chemical Engineering Journal* **2020**, *394*, 124419.
20. Wu, H.; Liu, L.; Song, L.; Ma, M.; Gu, N.; Zhang, Y., Enhanced Tumor Synergistic Therapy by Injectable Magnetic Hydrogel Mediated Generation of Hyperthermia and Highly Toxic Reactive Oxygen Species. *ACS Nano* **2019**, *13* (12), 14013-14023.
21. Liu, X.; Yan, B.; Li, Y.; Ma, X.; Jiao, W.; Shi, K.; Zhang, T.; Chen, S.; He, Y.; Liang, X.-J.; Fan, H., Graphene Oxide-Grafted Magnetic Nanorings Mediated Magnetothermodynamic Therapy Favoring Reactive Oxygen Species-Related Immune Response for Enhanced Antitumor Efficacy. *ACS Nano* **2020**, *14* (2), 1936-1950.
22. Klein, S.; Kızaloğlu, M.; Portilla, L.; Park, H.; Rejek, T.; Hümmer, J.; Meyer, K.; Hock, R.; Distel, L. V. R.; Halik, M.; Kryschi, C., Enhanced In Vitro Biocompatibility and Water Dispersibility of Magnetite and Cobalt Ferrite Nanoparticles Employed as ROS Formation Enhancer in Radiation Cancer Therapy. *Small* **2018**, *14* (21), 1704111.
23. Patra, J. K.; Das, G.; Fraceto, L. F.; Campos, E. V. R.; Rodriguez-Torres, M. D. P.; Acosta-Torres, L. S.; Diaz-Torres, L. A.; Grillo, R.; Swamy, M. K.; Sharma, S.; Habtemariam, S.; Shin, H. S., Nano based drug delivery systems: recent developments and future prospects. *Journal of Nanobiotechnology* **2018**, *16*, 33.

24. Torrice, M., Does Nanomedicine Have a Delivery Problem? *Acs Central Science* **2016**, 2 (7), 434-437.
25. Wen, H.; Jung, H. J.; Li, X. H., Drug Delivery Approaches in Addressing Clinical Pharmacology-Related Issues: Opportunities and Challenges. *Aaps Journal* **2015**, 17 (6), 1327-1340.
26. Rizvi, S. A. A.; Saleh, A. M., Applications of nanoparticle systems in drug delivery technology. *Saudi Pharmaceutical Journal* **2018**, 26 (1), 64-70.
27. Fang, R. H.; Kroll, A. V.; Gao, W. W.; Zhang, L. F., Cell Membrane Coating Nanotechnology. *Advanced Materials* **2018**, 30 (23), 34.
28. Wang, Y.; Miao, Y.; Li, G.; Su, M.; Chen, X.; Zhang, H.; Zhang, Y.; Jiao, W.; He, Y.; Yi, J.; Liu, X.; Fan, H., Engineering ferrite nanoparticles with enhanced magnetic response for advanced biomedical applications. *Materials Today Advances* **2020**, 8, 16.
29. Poon, W.; Kingston, B. R.; Ouyang, B.; Ngo, W.; Chan, W. C. W., A framework for designing delivery systems. *Nature Nanotechnology* **2020**, 15 (10), 819-829.
30. Riley, R. S.; Day, E. S., Gold nanoparticle-mediated photothermal therapy: applications and opportunities for multimodal cancer treatment. *Wiley Interdisciplinary Reviews-Nanomedicine and Nanobiotechnology* **2017**, 9 (4), 16.
31. Her, S.; Jaffray, D. A.; Allen, C., Gold nanoparticles for applications in cancer radiotherapy: Mechanisms and recent advancements. *Advanced Drug Delivery Reviews* **2017**, 109, 84-101.
32. Srinivasan, S. Y.; Paknikar, K. M.; Gajbhiye, V.; Bodas, D., Magneto-Conducting Core/Shell Nanoparticles for Biomedical Applications. *Chemnanomat* **2018**, 4 (2), 151-164.
33. Dai, Y. L.; Xu, C.; Sun, X. L.; Chen, X. Y., Nanoparticle design strategies for enhanced anticancer therapy by exploiting the tumour microenvironment. *Chemical Society Reviews* **2017**, 46 (12), 3830-3852.
34. Nikazar, S.; Barani, M.; Rahdar, A.; Zoghi, M.; Kyzas, G. Z., Photo- and Magneto-thermally Responsive Nanomaterials for Therapy, Controlled Drug Delivery and Imaging Applications. *Chemistryselect* **2020**, 5 (40), 12590-12609.
35. Rosenblum, D.; Joshi, N.; Tao, W.; Karp, J. M.; Peer, D., Progress and challenges towards targeted delivery of cancer therapeutics. *Nature Communications* **2018**, 9, 12.
36. Noh, S. H.; Moon, S. H.; Shin, T. H.; Lim, Y.; Cheon, J., Recent advances of magneto-thermal capabilities of nanoparticles: From design principles to biomedical applications. *Nano Today* **2017**, 13, 61-76.

37. Kudr, J.; Haddad, Y.; Richtera, L.; Heger, Z.; Cernak, M.; Adam, V.; Zitka, O., Magnetic Nanoparticles: From Design and Synthesis to Real World Applications. *Nanomaterials* **2017**, *7* (9), 29.
38. Al-Jamal, K. T.; Bai, J.; Wang, J. T. W.; Protti, A.; Southern, P.; Bogart, L.; Heidari, H.; Li, X. J.; Cakebread, A.; Asker, D.; Al-Jamal, W. T.; Shah, A.; Bals, S.; Sosabowski, J.; Pankhurst, Q. A., Magnetic Drug Targeting: Preclinical in Vivo Studies, Mathematical Modeling, and Extrapolation to Humans. *Nano Letters* **2016**, *16* (9), 5652-5660.
39. Arruebo, M.; Fernandez-Pacheco, R.; Ibarra, M. R.; Santamaria, J., Magnetic nanoparticles for drug delivery. *Nano Today* **2007**, *2* (3), 22-32.
40. Owens, D. E.; Peppas, N. A., Opsonization, biodistribution, and pharmacokinetics of polymeric nanoparticles. *International Journal of Pharmaceutics* **2006**, *307* (1), 93-102.
41. Thakor, A. S.; Jokerst, J. V.; Ghanouni, P.; Campbell, J. L.; Mittra, E.; Gambhir, S. S., Clinically Approved Nanoparticle Imaging Agents. *Journal of Nuclear Medicine* **2016**, *57* (12), 1833-1837.
42. Chen, F.; Ward, J.; Robinson, P. J., MR imaging of the liver and spleen: A comparison of the effects on signal intensity of two superparamagnetic iron oxide agents. *Magnetic Resonance Imaging* **1999**, *17* (4), 549-556.
43. Anderson, S. D.; Gwenin, V. V.; Gwenin, C. D., Magnetic Functionalized Nanoparticles for Biomedical, Drug Delivery and Imaging Applications. *Nanoscale Research Letters* **2019**, *14*, 16.
44. Hervault, A.; Dunn, A. E.; Lim, M.; Boyer, C.; Mott, D.; Maenosono, S.; Thanh, N. T. K., Doxorubicin loaded dual pH- and thermo-responsive magnetic nanocarrier for combined magnetic hyperthermia and targeted controlled drug delivery applications. *Nanoscale* **2016**, *8* (24), 12152-12161.
45. Chen, Y.; Ai, K. L.; Liu, J. H.; Sun, G. Y.; Yin, Q.; Lu, L. H., Multifunctional envelope-type mesoporous silica nanoparticles for pH-responsive drug delivery and magnetic resonance imaging. *Biomaterials* **2015**, *60*, 111-120.
46. Norouzi, M.; Yathindranath, V.; Thliveris, J. A.; Kopec, B. M.; Siahaan, T. J.; Miller, D. W., Doxorubicin-loaded iron oxide nanoparticles for glioblastoma therapy: a combinational approach for enhanced delivery of nanoparticles. *Scientific Reports* **2020**, *10* (1).
47. Luque-Michel, E.; Lemaire, L.; Blanco-Prieto, M. J., SPION and doxorubicin-loaded polymeric nanocarriers for glioblastoma theranostics. *Drug Delivery and Translational Research*.
48. Shetty, A.; Chandra, S., Inorganic hybrid nanoparticles in cancer theranostics: understanding their combinations for better clinical translation. *Materials Today Chemistry* **2020**, *18*.

49. Scherer, F.; Anton, M.; Schillinger, U.; Henkel, J.; Bergemann, C.; Kruger, A.; Gansbacher, B.; Plank, C., Magnetofection: enhancing and targeting gene delivery by magnetic force in vitro and in vivo. *Gene Therapy* **2002**, *9* (2), 102-109.
50. Gersting, S. W.; Schillinger, U.; Lausier, J.; Nicklaus, P.; Rudolph, C.; Plank, C.; Reinhardt, D.; Rosenecker, J., Gene delivery to respiratory epithelial cells by magnetofection. *Journal of Gene Medicine* **2004**, *6* (8), 913-922.
51. Bono, N.; Ponti, F.; Mantovani, D.; Candiani, G., Non-Viral in Vitro Gene Delivery: It is Now Time to Set the Bar! *Pharmaceutics* **2020**, *12* (2), 23.
52. Krotz, F.; Sohn, H. Y.; Gloe, T.; Plank, C.; Pohl, U., Magnetofection potentiates gene delivery to cultured endothelial cells. *Journal of Vascular Research* **2003**, *40* (5), 425-434.
53. Nacev, A.; Weinberg, I. N.; Stepanov, P. Y.; Kupfer, S.; Mair, L. O.; Urdaneta, M. G.; Shimoji, M.; Fricke, S. T.; Shapiro, B., Dynamic Inversion Enables External Magnets To Concentrate Ferromagnetic Rods to a Central Target. *Nano Letters* **2015**, *15* (1), 359-364.
54. Liu, Y. L.; Chen, D.; Shang, P.; Yin, D. C., A review of magnet systems for targeted drug delivery. *Journal of Controlled Release* **2019**, *302*, 90-104.
55. Gilchrist, R. K.; Medal, R.; Shorey, W. D.; Hanselman, R. C.; Parrott, J. C.; Taylor, C. B., SELECTIVE INDUCTIVE HEATING OF LYMPH NODES. *Annals of Surgery* **1957**, *146* (4), 596-606.
56. Christiansen, M. G.; Senko, A. W.; Chen, R.; Romero, G.; Anikeev, P., Magnetically multiplexed heating of single domain nanoparticles. *Applied Physics Letters* **2014**, *104* (21), 5.
57. Curley, S., Thermal Cancer Ablation Therapies Using Nanoparticles. In *Encyclopedia of Nanotechnology*, Bhushan, B., Ed. Springer Netherlands: Dordrecht, 2012; pp 2697-2704.
58. Silva, P. L.; Savchuk, O. A.; Gallo, J.; Garcia-Hevia, L.; Banobre-Lopez, M.; Nieder, J. B., Mapping intracellular thermal response of cancer cells to magnetic hyperthermia treatment. *Nanoscale* **2020**, *12* (42), 21647-21656.
59. Liu, J. C.; Guo, X.; Zhao, Z.; Li, B.; Qin, J. B.; Peng, Z. Y.; He, G. J.; Brett, D. J. L.; Wang, R. H.; Lu, X. W., Fe<sub>3</sub>S<sub>4</sub> nanoparticles for arterial inflammation therapy: Integration of magnetic hyperthermia and photothermal treatment. *Applied Materials Today* **2020**, *18*, 13.
60. Yang, F.; Skripka, A.; Tabatabaei, M. S.; Hong, S. H.; Ren, F. Q.; Benayas, A.; Oh, J. K.; Martel, S.; Liu, X. Y.; Vetrone, F.; Ma, D. L., Multifunctional Self-Assembled Supernanoparticles for Deep-Tissue Bimodal Imaging and Amplified Dual-Mode Heating Treatment. *Acs Nano* **2019**, *13* (1), 408-420.
61. Lu, Q. L.; Dai, X. Y.; Zhang, P.; Tan, X.; Zhong, Y. J.; Yao, C.; Song, M.; Song, G. L.; Zhang, Z. H.; Peng, G.; Guo, Z. R.; Ge, Y. Q.; Zhang, K. Z.; Li, Y. T., Fe<sub>3</sub>O<sub>4</sub>@Au

- composite magnetic nanoparticles modified with cetuximab for targeted magneto-photothermal therapy of glioma cells. *International Journal of Nanomedicine* **2018**, *13*, 2491-2505.
62. Alhasan, A. H.; Fardous, R. S.; Alsudir, S. A.; Majrashi, M. A.; Alghamd, W. M.; Alsharaeh, E. H.; Almalik, A. M., Polymeric Reactor for the Synthesis of Superparamagnetic-Thermal Treatment of Breast Cancer. *Molecular Pharmaceutics* **2019**, *16* (8), 3577-3587.
  63. Pardo, A.; Pelaz, B.; Gallo, J.; Banobre-Lopez, M.; Parak, W. J.; Barbosa, S.; del Pino, P.; Taboada, P., Synthesis, Characterization, and Evaluation of Superparamagnetic Doped Ferrites as Potential Therapeutic Nanotools. *Chemistry of Materials* **2020**, *32* (6), 2220-2231.
  64. Smith, B. R.; Gambhir, S. S., Nanomaterials for In Vivo Imaging. *Chem. Rev.* **2017**, *117* (3), 901-986.
  65. Shen, Z. Y.; Wu, A. G.; Chen, X. Y., Iron Oxide Nanoparticle Based Contrast Agents for Magnetic Resonance Imaging. *Mol. Pharm.* **2017**, *14* (5), 1352-1364.
  66. Daldrup-Link, H. E., Ten Things You Might Not Know about Iron Oxide Nanoparticles. *Radiology* **2017**, *284* (3), 616-629.
  67. Shen, S.; Ding, W.; Ahmed, S.; Hu, R.; Opalacz, A.; Roth, S.; You, Z.; Wotjkiewicz, G. R.; Lim, G.; Chen, L.; Mao, J.; Chen, J. W.; Zhang, Y., Ultrasmall Superparamagnetic Iron Oxide Imaging Identifies Tissue and Nerve Inflammation in Pain Conditions. *Pain Med* **2018**, *19* (4), 686-692.
  68. Choi, J. W.; Moon, W. J., Gadolinium Deposition in the Brain: Current Updates. *Korean J. Radiol.* **2019**, *20* (1), 134-147.
  69. Pasquini, L.; Napolitano, A.; Visconti, E.; Longo, D.; Romano, A.; Toma, P.; Espagnet, M. C. R., Gadolinium-Based Contrast Agent-Related Toxicities. *CNS Drugs* **2018**, *32* (3), 229-240.
  70. Fortin, M.-A., Magnetic Nanoparticles Used as Contrast Agents in MRI: Relaxometric Characterisation. In *Magnetic Characterization Techniques for Nanomaterials*, Kumar, C. S. S. R., Ed. Springer: Berlin, 2017; pp 511-555.
  71. Laurent, S.; Elst, L. V.; Muller, R. N., Superparamagnetic Iron Oxide Nanoparticles for MRI. In *The Chemistry of Contrast Agents in Medical Magnetic Resonance Imaging*, 2013; pp 427-447.
  72. Laurent, S. H., C.; Stanicki, D.; Boutry, S.; Lipani, E.; Belaid, S.; Muller, R. N.; Elst, L. V., *MRI Contrast Agents: From Molecules to Particles*. 1 ed.; Springer: Singapore, 2017; p 125.
  73. Ni, D. L.; Bu, W. B.; Ehlerding, E. B.; Cai, W. B.; Shi, J. L., Engineering of inorganic nanoparticles as magnetic resonance imaging contrast agents. *Chem. Soc. Rev.* **2017**, *46* (23), 7438-7468.



74. Stanicki, D.; Vander Elst, L.; Muller, R. N.; Laurent, S.; Felder-Flesch, D.; Mertz, D.; Parat, A.; Begin-Colin, S.; Cotin, G.; Greneche, J.-M.; Ersen, O.; Pichon, B.; Socoliuc, V.; Kuncser, V.; Turcu, R.; Ladislau, V.; Foster, P.; Bartha, R., Chapter 4 Iron-oxide Nanoparticle-based Contrast Agents. In *Contrast Agents for MRI: Experimental Methods*, The Royal Society of Chemistry: 2018; pp 318-447.
75. Zeng, L. Y.; Wu, D.; Zou, R. F.; Chen, T. X.; Zhang, J. C.; Wu, A. G., Paramagnetic and Superparamagnetic Inorganic Nanoparticles for T1-Weighted Magnetic Resonance Imaging. *Curr. Med. Chem.* **2018**, *25* (25), 2970-2986.
76. Cho, M. J.; Sethi, R.; Narayanan, J. S. A.; Lee, S. S.; Benoit, D. N.; Taheri, N.; Decuzzi, P.; Colvin, V. L., Gadolinium oxide nanoplates with high longitudinal relaxivity for magnetic resonance imaging. *Nanoscale* **2014**, *6* (22), 13637-13645.
77. Stinnett, G.; Taheri, N.; Villanova, J.; Bohoulou, A.; Guo, X.; Esposito, E. P.; Xiao, Z.; Stueber, D.; Avendano, C.; Decuzzi, P.; Pautler, R. G.; Colvin, V. L., 2D Gadolinium Oxide Nanoplates as T1 Magnetic Resonance Imaging Contrast Agents. *Advanced Healthcare Materials n/a* (n/a), 2001780.
78. Caspani, S.; Magalhães, R.; Araújo, J. P.; Sousa, C. T., Magnetic Nanomaterials as Contrast Agents for MRI. *Materials (Basel)* **2020**, *13* (11), 2586.
79. Bernsen, M. R.; Guenoun, J.; Tiel, S. T. v.; Krestin, G. P., Nanoparticles and clinically applicable cell tracking. *The British Journal of Radiology* **2015**, *88* (1054), 20150375.
80. Liu, H.; Zhang, J.; Chen, X.; Du, X. S.; Zhang, J. L.; Liu, G.; Zhang, W. G., Application of iron oxide nanoparticles in glioma imaging and therapy: from bench to bedside. *Nanoscale* **2016**, *8* (15), 7808-7826.
81. Weissig, V.; Pettinger, T. K.; Murdock, N., Nanopharmaceuticals (part I): products on the market. *Int. J. Nanomed.* **2014**, *9*, 4357-4373.
82. Wang, Y.-X. J., Superparamagnetic iron oxide based MRI contrast agents: Current status of clinical application. *Quant. Imaging. Med. Surg.* **2011**, *1* (1), 35-40.
83. Langsjoen, J.; Neuwelt, A.; Eberhardt, S.; Mlady, G.; Shukla, U.; Murali, S.; Pizanis, C.; Sillerud, L. O., A comparison of ferumoxytol with gadolinium as contrast agents for the diagnostic magnetic resonance imaging of osteomyelitis. *Magn. Reson. Imaging* **2020**, *71*, 45-54.
84. Siedek, F.; Muehe, A. M.; Theruvath, A. J.; Avedian, R.; Pribnow, A.; Spunt, S. L.; Liang, T.; Farrell, C.; Daldrup-Link, H. E., Comparison of ferumoxytol- and gadolinium chelate-enhanced MRI for assessment of sarcomas in children and adolescents. *Eur Radiol* **2020**, *30* (3), 1790-1803.
85. Wang, Y. X. J.; Idee, J. M., A comprehensive literatures update of clinical researches of superparamagnetic resonance iron oxide nanoparticles for magnetic resonance imaging. *Quant. Imaging. Med. Surg.* **2017**, *7* (1), 88-122.

86. Jeon, M.; Halbert, M. V.; Stephen, Z. R.; Zhang, M., Iron Oxide Nanoparticles as T1 Contrast Agents for Magnetic Resonance Imaging: Fundamentals, Challenges, Applications, and Prospectives. *Adv. Mater.* **2020**, 1-18.
87. Wei, H.; Bruns, O. T.; Kaul, M. G.; Hansen, E. C.; Barch, M.; Wisniowska, A.; Chen, O.; Chen, Y.; Li, N.; Okada, S.; Cordero, J. M.; Heine, M.; Farrar, C. T.; Montana, D. M.; Adam, G.; Ittrich, H.; Jasanoff, A.; Nielsen, P.; Bawendi, M. G., Exceedingly small iron oxide nanoparticles as positive MRI contrast agents. *Proc. Natl. Acad. Sci. U. S. A.* **2017**, *114* (9), 2325-2330.
88. Bao, Y.; Sherwood, J. A.; Sun, Z., Magnetic iron oxide nanoparticles as T-1 contrast agents for magnetic resonance imaging. *J. Mater. Chem. C* **2018**, *6* (6), 1280-1290.
89. Lu, Y.; Xu, Y.-J.; Zhang, G.-b.; Ling, D.; Wang, M.-q.; Zhou, Y.; Wu, Y.-D.; Wu, T.; Hackett, M. J.; Hyo Kim, B.; Chang, H.; Kim, J.; Hu, X.-T.; Dong, L.; Lee, N.; Li, F.; He, J.-C.; Zhang, L.; Wen, H.-Q.; Yang, B.; Hong Choi, S.; Hyeon, T.; Zou, D.-H., Iron oxide nanoclusters for T1 magnetic resonance imaging of non-human primates. *Nature Biomedical Engineering* **2017**, *1* (8), 637-643.
90. Kang, M.; Jin, S.; Lee, D.; Cho, H., MRI Visualization of Whole Brain Macro- and Microvascular Remodeling in a Rat Model of Ischemic Stroke: A Pilot Study. *Scientific Reports* **2020**, *10* (1), 4989.
91. Shapiro, E. M., Biodegradable, polymer encapsulated, metal oxide particles for MRI-based cell tracking. *Magnetic Resonance in Medicine* **2015**, *73* (1), 376-389.
92. Guldris, N.; Argibay, B.; Gallo, J.; Iglesias-Rey, R.; Carbó-Argibay, E.; Kolen'ko, Y. V.; Campos, F.; Sobrino, T.; Salonen, L. M.; Bañobre-López, M.; Castillo, J.; Rivas, J., Magnetite Nanoparticles for Stem Cell Labeling with High Efficiency and Long-Term in Vivo Tracking. *Bioconjugate Chemistry* **2017**, *28* (2), 362-370.
93. Ohki, A.; Saito, S.; Fukuchi, K., Magnetic resonance imaging of umbilical cord stem cells labeled with superparamagnetic iron oxide nanoparticles: effects of labelling and transplantation parameters. *Scientific Reports* **2020**, *10* (1), 13684.
94. Wierzbinski, K. R.; Szymanski, T.; Rozwadowska, N.; Rybka, J. D.; Zimna, A.; Zalewski, T.; Nowicka-Bauer, K.; Malcher, A.; Nowaczyk, M.; Krupinski, M.; Fiedorowicz, M.; Bogorodzki, P.; Grieb, P.; Giersig, M.; Kurpisz, M. K., Potential use of superparamagnetic iron oxide nanoparticles for in vitro and in vivo bioimaging of human myoblasts. *Scientific Reports* **2018**, *8* (1), 3682.
95. Sherwood, J.; Rich, M.; Lovas, K.; Warram, J.; Bolding, M. S.; Bao, Y., T(1)-Enhanced MRI-visible nanoclusters for imaging-guided drug delivery. *Nanoscale* **2017**, *9* (32), 11785-11792.
96. Danhier, F., To exploit the tumor microenvironment: Since the EPR effect fails in the clinic, what is the future of nanomedicine? *J Control Release* **2016**, *244* (Pt A), 108-121.

97. Matsumura, Y.; Maeda, H., A new concept for macromolecular therapeutics in cancer chemotherapy: mechanism of tumorotropic accumulation of proteins and the antitumor agent smancs. *Cancer Res* **1986**, *46* (12 Pt 1), 6387-92.
98. Zu, G. Y.; Kuang, Y.; Dong, J. J.; Cao, Y.; Zhang, T. T.; Liu, M.; Luo, L. Q.; Pei, R. J., Gadolinium(III)-based Polymeric Magnetic Resonance Imaging Agents for Tumor Imaging. *Current Medicinal Chemistry* **2018**, *25* (25), 2910-2937.
99. Li, F. Y.; Liang, Z. Y.; Liu, J. N.; Sun, J. H.; Hu, X.; Zhao, M.; Liu, J. X.; Bai, R. L.; Kim, D.; Sun, X. L.; Hyeon, T.; Ling, D. S., Dynamically Reversible Iron Oxide Nanoparticle Assemblies for Targeted Amplification of T1-Weighted Magnetic Resonance Imaging of Tumors. *Nano Lett.* **2019**, *19* (7), 4213-4220.
100. Barajas, R. F.; Hamilton, B. E.; Schwartz, D.; McConnell, H. L.; Pettersson, D. R.; Horvath, A.; Szidonya, L.; Varallyay, C. G.; Firkins, J.; Jaboin, J. J.; Kubicky, C. D.; Raslan, A. M.; Dogan, A.; Cetas, J. S.; Ciporen, J.; Han, S. J.; Ambady, P.; Muldoon, L. L.; Woltjer, R.; Rooney, W. D.; Neuwelt, E. A., Combined iron oxide nanoparticle ferumoxytol and gadolinium contrast enhanced MRI define glioblastoma pseudoprogression. *Neuro-Oncology* **2019**, *21* (4), 517-526.
101. Richard, S.; Boucher, M.; Lalatonne, Y.; Meriaux, S.; Motte, L., Iron oxide nanoparticle surface decorated with cRGD peptides for magnetic resonance imaging of brain tumors. *Biochim. Biophys. Acta-Gen. Subj.* **2017**, *1861* (6), 1515-1520.
102. Lu, Z.; Li, Y.; Shi, Y.; Li, Y.; Xiao, Z.; Zhang, X., Traceable Nanoparticles with Spatiotemporally Controlled Release Ability for Synergistic Glioblastoma Multiforme Treatment. *Advanced Functional Materials* **2017**, *27* (46), 1703967.
103. Husain, S. F.; Lam, R. W. M.; Hu, T.; Ng, M. W. F.; Liao, Z. Q. G.; Nagata, K.; Khanna, S.; Lam, Y.; Bhakoo, K.; Ho, R. C. M.; Wong, H. K., Locating the Site of Neuropathic Pain In Vivo Using MMP-12-Targeted Magnetic Nanoparticles. *Pain Res Manag* **2019**, *2019*, 9394715.
104. Zhou, Y. F.; Xiong, S. C.; Zhang, K. K.; Feng, L.; Chen, X. L.; Wu, Y. H.; Huang, X. L.; Xiong, Y. H., Quantum bead-based fluorescence-linked immunosorbent assay for ultrasensitive detection of aflatoxin M-1 in pasteurized milk, yogurt, and milk powder. *Journal of Dairy Science* **2019**, *102* (5), 3985-3993.
105. Bulte, J. W. M., Superparamagnetic iron oxides as MPI tracers: A primer and review of early applications. *Advanced Drug Delivery Reviews* **2019**, *138*, 293-301.
106. Du, Y. M.; Lai, P. T.; Leung, C. H.; Pong, P. W. T., Design of Superparamagnetic Nanoparticles for Magnetic Particle Imaging (MPI). *International Journal of Molecular Sciences* **2013**, *14* (9), 18682-18710.
107. Gleich, B.; Weizenecker, J., Tomographic imaging using the nonlinear response of magnetic particles. *Nature* **2005**, *435* (7046), 1214-1217.

108. Weizenecker, J.; Gleich, B.; Rahmer, J.; Dahnke, H.; Borgert, J., Three-dimensional real-time in vivo magnetic particle imaging. *Physics in Medicine and Biology* **2009**, *54* (5), L1-L10.
109. Talebloo, N.; Gudi, M.; Robertson, N.; Wang, P., Magnetic Particle Imaging: Current Applications in Biomedical Research. *Journal of Magnetic Resonance Imaging* **2020**, *51* (6), 1659-1668.
110. Zhou, X. Y.; Jeffris, K. E.; Yu, E. Y.; Zheng, B.; Goodwill, P. W.; Nahid, P.; Conolly, S. M., First in vivo magnetic particle imaging of lung perfusion in rats. *Phys Med Biol* **2017**, *62* (9), 3510-3522.
111. Zheng, B.; von See, M. P.; Yu, E.; Gunel, B.; Lu, K.; Vazin, T.; Schaffer, D. V.; Goodwill, P. W.; Conolly, S. M., Quantitative Magnetic Particle Imaging Monitors the Transplantation, Biodistribution, and Clearance of Stem Cells In Vivo. *Theranostics* **2016**, *6* (3), 291-301.
112. Yu, E. Y.; Chandrasekharan, P.; Berzon, R.; Tay, Z. W.; Zhou, X. Y.; Khandhar, A. P.; Ferguson, R. M.; Kemp, S. J.; Zheng, B.; Goodwill, P. W.; Wendland, M. F.; Krishnan, K. M.; Behr, S.; Carter, J.; Conolly, S. M., Magnetic Particle Imaging for Highly Sensitive, Quantitative, and Safe in Vivo Gut Bleed Detection in a Murine Model. *ACS Nano* **2017**, *11* (12), 12067-12076.
113. Yu, E. Y.; Bishop, M.; Zheng, B.; Ferguson, R. M.; Khandhar, A. P.; Kemp, S. J.; Krishnan, K. M.; Goodwill, P. W.; Conolly, S. M., Magnetic Particle Imaging: A Novel in Vivo Imaging Platform for Cancer Detection. *Nano Lett* **2017**, *17* (3), 1648-1654.
114. Zhu, X.; Li, J.; Peng, P.; Hosseini Nassab, N.; Smith, B. R., Quantitative Drug Release Monitoring in Tumors of Living Subjects by Magnetic Particle Imaging Nanocomposite. *Nano Letters* **2019**, *19* (10), 6725-6733.
115. Tay, Z. W.; Chandrasekharan, P.; Chiu-Lam, A.; Hensley, D. W.; Dhavalikar, R.; Zhou, X. Y.; Yu, E. Y.; Goodwill, P. W.; Zheng, B.; Rinaldi, C.; Conolly, S. M., Magnetic Particle Imaging-Guided Heating in Vivo Using Gradient Fields for Arbitrary Localization of Magnetic Hyperthermia Therapy. *ACS Nano* **2018**, *12* (4), 3699-3713.
116. Cohn, D.; Zarek, M.; Elyashiv, A.; Abu Sbitan, M.; Sharma, V.; Ramanujan, R. V., Remotely triggered morphing behavior of additively manufactured thermoset polymer-magnetic nanoparticle composite structures. *Smart Materials and Structures* **2021**, *30* (4), 9.
117. Shields, C. W.; Reyes, C. D.; Lopez, G. P., Microfluidic cell sorting: a review of the advances in the separation of cells from debulking to rare cell isolation. *Lab on a Chip* **2015**, *15* (5), 1230-1249.
118. Vermesh, O.; Aalipour, A.; Ge, T. J.; Saenz, Y.; Guo, Y.; Alam, I. S.; Park, S. M.; Adelson, C. N.; Mitsutake, Y.; Vilches-Moure, J.; Godoy, E.; Bachmann, M. H.; Ooi, C. C.; Lyons, J. K.; Mueller, K.; Arami, H.; Green, A.; Solomon, E. I.; Wang, S. X.; Gambhir, S. S., An intravascular magnetic wire for the high-throughput

- retrieval of circulating tumour cells in vivo. *Nature Biomedical Engineering* **2018**, 2 (9), 696-705.
119. Haghghi, A. H.; Faghieh, Z.; Khorasani, M. T.; Farjadian, F., Antibody conjugated onto surface modified magnetic nanoparticles for separation of HER2+breast cancer cells. *Journal of Magnetism and Magnetic Materials* **2019**, 490, 11.
  120. Liang, W. F.; Liu, J.; Yang, X. L.; Zhang, Q.; Yang, W. G.; Zhang, H. M.; Liu, L. Q., Microfluidic-based cancer cell separation using active and passive mechanisms. *Microfluidics and Nanofluidics* **2020**, 24 (4), 19.
  121. Saei, A.; Asfia, S.; Kouchakzadeh, H.; Rahmandoust, M., Antibody-modified magnetic nanoparticles as specific high-efficient cell-separation agents. *Journal of Biomedical Materials Research Part B-Applied Biomaterials* **2020**, 108 (6), 2633-2642.
  122. Wilson, R. E.; O'Connor, R.; Gallops, C. E.; Kwizera, E. A.; Noroozi, B.; Morshed, B. I.; Wang, Y. M.; Huang, X. H., Immunomagnetic Capture and Multiplexed Surface Marker Detection of Circulating Tumor Cells with Magnetic Multicolor Surface-Enhanced Raman Scattering Nanotags. *Acs Applied Materials & Interfaces* **2020**, 12 (42), 47220-47232.
  123. Zhang, H.; Ding, W. P.; Li, S. B.; Ya, S. N.; Li, F. F.; Qiu, B. S., On-chip analysis of magnetically labeled cells with integrated cell sorting and counting techniques. *Talanta* **2020**, 220, 9.
  124. Korangath, P.; Ivkov, R., Magnet-assisted Flow Cytometry of in vivo Tumors to Quantitate Cell-specific Responses to Magnetic Iron Oxide Nanoparticles. *Bio-Protocol* **2020**, 10 (22), 9.
  125. Robert, D.; Pamme, N.; Conjeaud, H.; Gazeau, F.; Iles, A.; Wilhelm, C., Cell sorting by endocytotic capacity in a microfluidic magnetophoresis device. *Lab on a Chip* **2011**, 11 (11), 1902-1910.
  126. Zhang, Q.; Yin, T.; Xu, R. R.; Gao, W. J.; Zhao, H.; Shapter, J. G.; Wang, K.; Shen, Y. L.; Huang, P.; Gao, G.; Wu, Y. F.; Cui, D. X., Large-scale immuno-magnetic cell sorting of T cells based on a self-designed high-throughput system for potential clinical application. *Nanoscale* **2017**, 9 (36), 13592-13599.
  127. Tran, M. V.; Susumu, K.; Medintz, I. L.; Algar, W. R., Supraparticle Assemblies of Magnetic Nanoparticles and Quantum Dots for Selective Cell Isolation and Counting on a Smartphone-Based Imaging Platform. *Analytical Chemistry* **2019**, 91 (18), 11963-11971.
  128. Schmitt, F.; Piccin, O.; Barbe, L.; Bayle, B., Soft Robots Manufacturing: A Review. *Frontiers in Robotics and Ai* **2018**, 5, 17.
  129. Cianchetti, M.; Laschi, C.; Menciassi, A.; Dario, P., Biomedical applications of soft robotics. *Nature Reviews Materials* **2018**, 3 (6), 143-153.

130. Cao, Q. L.; Fan, Q.; Chen, Q.; Liu, C. T.; Han, X. T.; Li, L., Recent advances in manipulation of micro- and nano-objects with magnetic fields at small scales. *Materials Horizons* **2020**, *7* (3), 638-666.
131. Hu, W. Q.; Lum, G. Z.; Mastrangeli, M.; Sitti, M., Small-scale soft-bodied robot with multimodal locomotion. *Nature* **2018**, *554* (7690), 81-85.
132. Gu, H. R.; Boehler, Q.; Cui, H. Y.; Secchi, E.; Savorana, G.; De Marco, C.; Gervasoni, S.; Peyron, Q.; Huang, T. Y.; Pane, S.; Hirt, A. M.; Ahmed, D.; Nelson, B. J., Magnetic cilia carpets with programmable metachronal waves. *Nature Communications* **2020**, *11* (1), 10.
133. Bayaniahangar, R.; Ahangar, S. B.; Zhang, Z. T.; Lee, B. P.; Pearce, J. M., 3-D printed soft magnetic helical coil actuators of iron oxide embedded polydimethylsiloxane. *Sensors and Actuators B-Chemical* **2021**, *326*, 10.
134. Goudu, S. R.; Yasa, I. C.; Hu, X. H.; Ceylan, H.; Hu, W. Q.; Sitti, M., Biodegradable Untethered Magnetic Hydrogel Milli-Grippers. *Advanced Functional Materials* **2020**, *30* (50), 9.
135. Breger, J. C.; Yoon, C.; Xiao, R.; Kwag, H. R.; Wang, M. O.; Fisher, J. P.; Nguyen, T. D.; Gracias, D. H., Self-Folding Thermo-Magnetically Responsive Soft Microgrippers. *Acs Applied Materials & Interfaces* **2015**, *7* (5), 3398-3405.
136. Hwang, G.; Paula, A. J.; Hunter, E. E.; Liu, Y.; Babeer, A.; Karabucak, B.; Stebe, K.; Kumar, V.; Steager, E.; Koo, H., Catalytic antimicrobial robots for biofilm eradication. *Science Robotics* **2019**, *4* (29), 13.
137. Brisbois, C. A.; Tasinkevych, M.; Vazquez-Montejo, P.; de la Cruz, M. O., Actuation of magnetoelastic membranes in precessing magnetic fields. *Proceedings of the National Academy of Sciences of the United States of America* **2019**, *116* (7), 2500-2505.
138. Chin, S. Y.; Poh, Y. C.; Kohler, A. C.; Sia, S. K., An Additive Manufacturing Technique for the Facile and Rapid Fabrication of Hydrogel-based Micromachines with Magnetically Responsive Components. *Jove-Journal of Visualized Experiments* **2018**, (137), 12.
139. Ugelstad, J.; Berge, A.; Ellingsen, T.; Schmid, R.; Nilsen, T. N.; Mork, P. C.; Stenstad, P.; Hornes, E.; Olsvik, O., PREPARATION AND APPLICATION OF NEW MONOSIZED POLYMER PARTICLES. *Progress in Polymer Science* **1992**, *17* (1), 87-161.
140. Fonnum, G.; Johansson, C.; Molteberg, A.; Morup, S.; Aksnes, E., Characterisation of Dynabeads (R) by magnetization measurements and Mossbauer spectroscopy. *Journal of Magnetism and Magnetic Materials* **2005**, *293* (1), 41-47.
141. Treleaven, J. G.; Gibson, F. M.; Ugelstad, J.; Rembaum, A.; Philip, T.; Caine, G. D.; Kemshead, J. T., REMOVAL OF NEURO-BLASTOMA CELLS FROM BONE-

- MARROW WITH MONOCLONAL-ANTIBODIES CONJUGATED TO MAGNETIC MICROSPHERES. *Lancet* **1984**, *1* (8368), 70-73.
142. Kemshead, J. T.; Heath, L.; Gibson, F. M.; Katz, F.; Richmond, F.; Treleaven, J.; Ugelstad, J., MAGNETIC MICROSPHERES AND MONOCLONAL-ANTIBODIES FOR THE DEPLETION OF NEUROBLASTOMA-CELLS FROM BONE-MARROW - EXPERIENCES, IMPROVEMENTS AND OBSERVATIONS. *British Journal of Cancer* **1986**, *54* (5), 771-778.
  143. Uhlen, M.; Hultman, T.; Wahlberg, J.; Lundeberg, J.; Bergh, S.; Pettersson, B.; Holmberg, A.; Stahl, S.; Moks, T., SEMIAUTOMATED SOLID-PHASE DNA SEQUENCING. *Trends in Biotechnology* **1992**, *10* (1-2), 52-55.
  144. Rimstad, E.; Hornes, E.; Olsvik, O.; Hyllseth, B., IDENTIFICATION OF A DOUBLE-STRANDED-RNA VIRUS BY USING POLYMERASE CHAIN-REACTION AND MAGNETIC SEPARATION OF THE SYNTHESIZED DNA SEGMENTS. *Journal of Clinical Microbiology* **1990**, *28* (10), 2275-2278.
  145. Wright, D. J.; Chapman, P. A.; Siddons, C. A., IMMUNOMAGNETIC SEPARATION AS A SENSITIVE METHOD FOR ISOLATING ESCHERICHIA-COLI O157 FROM FOOD SAMPLES. *Epidemiology and Infection* **1994**, *113* (1), 31-39.
  146. Woywodt, A.; Schroeder, M.; Gwinner, W.; Mengel, M.; Jaeger, M.; Schwarz, A.; Haller, H.; Haubitz, M., Elevated numbers of circulating endothelial cells in renal transplant recipients. *Transplantation* **2003**, *76* (1), 1-4.
  147. Backman, A.; Lantz, P. G.; Radstrom, P.; Olcen, P., Evaluation of an extended diagnostic PCR assay for detection and verification of the common causes of bacterial meningitis in CSF and other biological samples. *Molecular and Cellular Probes* **1999**, *13* (1), 49-60.
  148. Satterly, N. G.; Voorhees, M. A.; Ames, A. D.; Schoepp, R. J., Comparison of MagPix Assays and Enzyme-Linked Immunosorbent Assay for Detection of Hemorrhagic Fever Viruses. *Journal of Clinical Microbiology* **2017**, *55* (1), 68-78.
  149. Baker, H. N.; Murphy, R.; Lopez, E.; Garcia, C., Conversion of a Capture ELISA to a Luminex xMAP Assay using a Multiplex Antibody Screening Method. *Jove-Journal of Visualized Experiments* **2012**, (65).
  150. Kyaw, S. P.; Hanthamrongwit, J.; Jangpatarapongsa, K.; Khaenam, P.; Leepiyasakulchai, C., Sensitive detection of the IS6110 sequence of Mycobacterium tuberculosis complex based on PCR-magnetic bead ELISA. *Rsc Advances* **2018**, *8* (59), 33674-33680.
  151. Su, R. Q.; Tang, X. M.; Feng, L.; Yao, G. L.; Chen, J., Development of quantitative magnetic beads-based flow cytometry fluorescence immunoassay for aflatoxin B-1. *Microchemical Journal* **2020**, 155.

152. Yang, S. Y.; Lien, K. Y.; Huang, K. J.; Lei, H. Y.; Lee, G. B., Micro flow cytometry utilizing a magnetic bead-based immunoassay for rapid virus detection. *Biosensors & Bioelectronics* **2008**, *24* (4), 855-862.
153. Furuya, H.; Pagano, I.; Chee, K.; Kobayashi, T.; Wong, R. S.; Lee, R.; Rosser, C. J., Comparison of Commercial ELISA Kits, a Prototype Multiplex Electrochemoluminescent Assay, and a Multiplex Bead-Based Immunoassay for Detecting a Urine-Based Bladder-Cancer-Associated Diagnostic Signature. *Diagnostics* **2019**, *9* (4).
154. Srisa-Art, M.; Boehle, K. E.; Geiss, B. J.; Henry, C. S., Highly Sensitive Detection of Salmonella typhimurium Using a Colorimetric Paper-Based Analytical Device Coupled with Immunomagnetic Separation. *Analytical Chemistry* **2018**, *90* (1), 1035-1043.
155. Perraut, R.; Richard, V.; Varela, M. L.; Trape, J. F.; Guillotte, M.; Tall, A.; Toure, A.; Sokhna, C.; Vigan-Womas, I.; Mercereau-Puijalon, O., Comparative analysis of IgG responses to Plasmodium falciparum MSP1p19 and PF13-DBL1 alpha 1 using ELISA and a magnetic bead-based duplex assay (MAGPIX (R)-Luminex) in a Senegalese meso-endemic community. *Malaria Journal* **2014**, *13*.
156. Koffi, D.; Toure, A. O.; Varela, M. L.; Vigan-Womas, I.; Beourou, S.; Brou, S.; Ehouman, M. F.; Gnamien, L.; Richard, V.; Djaman, J. A.; Perraut, R., Analysis of antibody profiles in symptomatic malaria in three sentinel sites of Ivory Coast by using multiplex, fluorescent, magnetic, bead-based serological assay (MAGPIX (TM)). *Malaria Journal* **2015**, *14*.
157. Varela, M. L.; Mbengue, B.; Basse, A.; Loucoubar, C.; Vigan-Womas, I.; Dieye, A.; Toure, A.; Perraut, R., Optimization of a magnetic bead-based assay (MAGPIX (R)-Luminex) for immune surveillance of exposure to malaria using multiple Plasmodium antigens and sera from different endemic settings. *Malaria Journal* **2018**, *17*.
158. Hung, L. Y.; Chang, J. C.; Tsai, Y. C.; Huang, C. C.; Chang, C. P.; Yeh, C. S.; Lee, G. B., Magnetic nanoparticle-based immunoassay for rapid detection of influenza infections by using an integrated microfluidic system. *Nanomedicine-Nanotechnology Biology and Medicine* **2014**, *10* (4), 819-829.
159. Srinivasan, S. Y.; Paknikar, K. M.; Bodas, D.; Gajbhiye, V., Applications of cobalt ferrite nanoparticles in biomedical nanotechnology. *Nanomedicine* **2018**, *13* (10), 1221-1238.
160. Kohama, N.; Suwabe, C.; Ishii, H.; Hayashi, K.; Nagao, D., Characterization on magnetophoretic velocity of the cluster of submicron-sized composite particles applicable to magnetic separation and purification. *Colloids and Surfaces a-Physicochemical and Engineering Aspects* **2019**, *568*, 141-146.



161. Fan, A. P.; Lau, C. W.; Lu, J. Z., Magnetic bead-based chemiluminescent metal immunoassay with a colloidal gold label. *Analytical Chemistry* **2005**, *77* (10), 3238-3242.
162. Wang, X.; Niessner, R.; Knopp, D., Magnetic Bead-Based Colorimetric Immunoassay for Aflatoxin B1 Using Gold Nanoparticles. *Sensors* **2014**, *14* (11), 21535-21548.
163. Xiong, L. H.; He, X. W.; Xia, J. J.; Ma, H. W.; Yang, F.; Zhang, Q.; Huang, D. N.; Chen, L.; Wu, C. L.; Zhang, X. M.; Zhao, Z.; Wan, C. S.; Zhang, R. L.; Cheng, J. Q., Highly Sensitive Naked-Eye Assay for Enterovirus 71 Detection Based on Catalytic Nanoparticle Aggregation and Immunomagnetic Amplification. *Acs Applied Materials & Interfaces* **2017**, *9* (17), 14691-14699.
164. Wilson, R.; Spiller, D. G.; Prior, I. A.; Veltkamp, K. J.; Hutchinson, A., A simple method for preparing spectrally encoded magnetic beads for multiplexed detection. *Acs Nano* **2007**, *1* (5), 487-493.
165. Kim, C.; Hoffmann, G.; Searson, P. C., Integrated Magnetic Bead Quantum Dot Immunoassay for Malaria Detection. *Acs Sensors* **2017**, *2* (6), 766-772.

## Chapter 2

### Two-Dimensional Gadolinium Oxide Nanoplates as T<sub>1</sub> Magnetic Resonance Imaging Contrast Agents<sup>†</sup>

† Reprinted (adapted) with permission from Villanova J\*.; Taheri N.\*; Stinnett G.\*;  
Bohloul A.; Guo X.; Esposito E. P.; Xiao Z.; Stueber D.; Avendano C.; Decuzzi P.; Pautler R.  
G.; Colvin V. L., 2D Gadolinium Oxide Nanoplates as T1 Magnetic Resonance Imaging  
Contrast Agents, *Advanced Healthcare Materials* **2021**, 10(11), 2001780. © 2021 Wiley-  
VCH GmbH

\*These authors contributed equally to this work.

## Chapter 2 Two-Dimensional Gadolinium Oxide Nanoplates as T<sub>1</sub> Magnetic Resonance Imaging Contrast Agents

### 2.1. Abstract

Millions of people a year receive MRI contrast agents for the diagnosis of conditions as diverse as fatty liver disease and cancer. Gadolinium chelates, which provide preferred  $T_1$  contrast, are the current standard but face an uncertain future due to increasing concerns about their nephrogenic toxicity as well as poor performance in high field MRI scanners. Gadolinium-containing nanocrystals are interesting alternatives as they bypass the kidneys and can offer the possibility of both intracellular accumulation and active targeting. Nanocrystal contrast performance has been notably limited, however, as their organic coatings block water from close interactions with surface Gadoliniums. Here these steric barriers to water exchange are minimized through shape engineering of plate-like nanocrystals that possess accessible Gadoliniums at their edges. Sulfonated surface polymers promote second-sphere relaxation processes that contribute remarkable contrast even at the highest fields ( $r_1 = 32.6 \text{ mM-Gd}^{-1}\text{s}^{-1}$  at 9.4 T). These non-cytotoxic materials release no detectable free Gadolinium even under mild acidic conditions. They preferentially accumulate in the liver of mice with a circulation half-life fifty percent longer than commercial agents. These features allow these  $T_1$  MRI contrast agents to be applied for the first time to the ex-vivo detection of non-alcoholic fatty liver disease (NAFLD) in mice.

### 2.2. Introduction

Roughly sixty million people per year undergo MRI imaging. Half of these procedures require Gadolinium-containing contrast agents (CA) to visualize soft tissue, organs, and

possible abnormalities associated with disease.<sup>1-3</sup> These clinical contrast agents operate exclusively by reducing the longitudinal spin magnetization relaxation times ( $T_1$ ) of protons found mostly in water throughout the body.<sup>4,5</sup> Other types of MRI contrast, such as that resulting from the reduction of transverse spin relaxation times ( $T_2$ ), can be generated from iron oxide nanoparticles.<sup>6</sup> While these materials were approved for use by 2009 by the US FDA, their dark contrast is difficult to interpret as well as concerns about hepatic toxicity from iron overload has led to their commercial failure.<sup>2, 3, 7-10</sup> As a result molecular  $T_1$  contrast agents remain the gold standard for CA-enhanced MRI. The best agents possess large absolute  $T_1$  relaxivities ( $r_1$ ) under clinically relevant ( $B_0 > 1.4$  T) field strengths. Additionally maximum  $T_1$  signal is typically enhanced when there is a match between the longitudinal and transverse relaxation times ( $r_2/r_1 \sim 1$ ).<sup>3, 11, 12</sup> When CA meet these conditions the bright features in  $T_1$ -weighted MRI images can lead to definitive diagnoses and treatment monitoring.<sup>1, 4, 5, 10, 11</sup>

Eight FDA-approved Gadolinium chelates (GCCA) are available for clinical use and ongoing research seeks to improve and expand these molecular platforms.<sup>10, 13</sup> Gadolinium is an essential component of these materials. With 7 unpaired electrons ( $S = 7/2$ ), a large magnetic moment ( $7.94 \mu_B$ ), and long electron spin relaxation times ( $10^{-9} - 10^{-8}$  s), this atom is ideally suited for promoting the efficient relaxation of water protons.<sup>2, 5</sup> However, as the field strength of MRI scanners has increased the performance of these conventional contrast agents has fallen as their dominant inner-sphere relaxation processes are strongly depressed at higher magnetic fields.<sup>11, 14-16</sup> One solution is to increase the physical dimensions of the chelates so as to slow their tumbling rates and

improve  $T_1$  contrast at higher Larmor frequencies.<sup>1, 5, 10, 17, 18</sup> Larger GCCA also provide an avenue for biomolecular conjugation and possible targeting, thereby opening the door to more functional imaging.<sup>1, 5, 10</sup> Despite these advances, there is growing concern about the nephrogenic toxicity of even these macromolecular contrast agents due to release of  $Gd^{3+}$  from their chelators. Several of the commercial GCCA are contraindicated in patients with renal insufficiency due to prolonged circulation times and the European Medicines agency has in 2017 restricted the use of some of the GCCA because of these concerns.<sup>3, 10, 13, 19-22</sup>

Gadolinium-containing nanocrystals offer a promising alternative to molecular Gadolinium complexes for  $T_1$ -enhanced MRI.<sup>23-25</sup> Studies at clinically relevant field strengths report that these materials can possess ionic  $r_1$  (e. g. per  $[Gd^{3+}]$ ) comparable to commercial agents ( $r_1 = 3 - 7 \text{ mM-Gd}^{-1}\text{s}^{-1}$ ) and in some cases even larger  $r_1$  ( $\sim 60 \text{ mM-Gd}^{-1}\text{s}$  at 1.5 T).<sup>10, 15, 20, 26-39</sup> Johnson *et al.* formed high-contrast ultrasmall ( $\sim 10 \text{ nm}$ )  $\text{NaGdF}_4$  nanoparticles ( $r_1 = 78.2 \text{ mM}^{-1}\text{s}^{-1}$ ,  $r_2/r_1 = 1.5$ , 1.41 T) small enough to undergo clearance through the kidneys. Previous reports demonstrate that the  $r_1$  of pure Gadolinium-containing nanocrystals (e.g.,  $\text{Gd}_2\text{O}_3$  or  $\text{NaGdF}_4$ ) is optimized at smaller nanoparticle dimensions presumably because there are proportionally more surface  $Gd^{3+}$  per particle.<sup>20, 26, 38, 40-44</sup> A more relevant metric for nanoparticle CA may be their overall or per-particle contrast. Using this metric,  $\text{Gd}_2\text{O}_3$  nanoparticles – by virtue of the many Gadolinium ions they contain – possess relaxivities thousands of times larger than GCCA. Such high contrast Gadolinium-containing nanocrystals could reduce the effective dosage for CA-enhanced MRI thereby limiting possible toxicity; alternatively, such materials may

also enable molecular imaging using MRI to detect small amounts of targeted Gadolinium-containing nanocrystals.<sup>35, 39</sup>

Fully realizing the opportunities of these nanocrystal  $T_1$  agents requires a material design that overcomes the apparent contradiction between surface  $Gd^{3+}$  accessibility and the need for particle stability in biological media. Gadolinium must come within 2 – 3 Å of water in order to affect the most efficient inner-sphere spin relaxation processes.<sup>10, 11, 14</sup> Such accessibility is not easily achieved as nanocrystal surfaces are necessarily coated with surfactants or polymers that prevent particle aggregation and non-specific protein adsorption.<sup>41, 45-47</sup> One approach is to give up on inner-sphere relaxation processes and amplify the less efficient second-sphere relaxation processes that occur when water associates with ligands bound to the Gadolinium.<sup>16, 33, 34, 38, 48-55</sup> As an example, Zheng *et al.* showed that charged polymer coatings exhibited strong hydrogen bonding with water and resulted in nanoparticles with larger  $T_1$  relaxivities.<sup>38</sup> Two-dimensional nanoparticles could offer a resolution to the problem of surface access: their edges could remain unblocked by coatings thus providing an avenue for the close approach of water while their large faces provide a platform for polymer functionalization. Xiao *et al.* has explored this strategy with Gd-doped iron oxide nanoplates, but the approach has not been pursued in pure Gadolinium-containing nanomaterials.<sup>35</sup>

Here  $Gd_2O_3$  nanoplates (GONP) by virtue of their unusual shape and highly charged coatings are shown to possess excellent  $T_1$  MRI contrast even at high applied fields.<sup>20, 56,</sup>

<sup>57</sup> Inspired by the importance of CA-enhanced MRI in detecting and assessing liver disease, this efforts exploits the role of the liver in nanoparticle clearance and

demonstrates how  $T_1$  CA-enhanced MRI from nanoscale materials be used to detect non-alcoholic fatty liver disease (NAFLD).<sup>8, 46, 58-65</sup> Symptoms of this disease can be aggravated by iron overload, and an iron-free, high  $r_1$ , and liver-specific CA such as the one described here could offer many advantages over the current approaches.<sup>66, 67</sup> At clinically relevant field strengths the ionic relaxivities (per  $[\text{Gd}^{3+}]$ ) of these nanoplates are almost twenty times larger than the commercial agent, Magnevist (63.0 vs. 3.5 mM-Gd<sup>-1</sup>s<sup>-1</sup>) with a much lower  $r_2/r_1$  (1.17 vs. 1.5); per contrast agent the relaxivity (*e.g.* per particle) is over fifty thousand times larger than commercial contrast agents. The magnetic field (at 1.4, 3, and 9.4 T) and weak size-dependence of their relaxivities suggest that both inner-sphere and second-sphere relaxation mechanisms contribute to their extraordinary performance. These nanoparticles show no appreciable acute *in-vitro* cytotoxicity despite being readily taken into cells where they remain active as  $T_1$  CA. These contrast agents clear the blood and the body approximately twice as fast as molecular agents and distribute through tissues three times slower. They also accumulate more readily in extracellular and intravascular spaces and like many nanoparticles are cleared predominantly hepatically likely *via* the Kupffer cells of the reticuloendothelial system (RES). The natural biodistribution of these materials suggest opportunities for applying these  $T_1$  CA to liver imaging, and this potential is demonstrated by using nanoscale  $T_1$  CA-enhanced *ex vivo* MRI to detect early-stage liver disease in an ex-vivo mouse model.

## 2.3. Results and Discussion

### 2.3.1. Synthesis of Gadolinium Oxide Nanoplates

In 2004 Cao was the first to report an approach for forming uniform  $\text{Gd}_2\text{O}_3$  nanoplates in organic solutions; this route has been fully explored and expanded upon to produce a wide range of rare earth nanoparticles.<sup>68-75</sup> Specifically, soluble Gadolinium oleate forms at 110 °C from Gadolinium salts, oleyl amine (OLAM), oleic acid (OA), and 1-octadecene.<sup>76</sup> At temperatures greater than 290 °C this precursor decomposes and initiates nucleation and subsequent nanocrystal growth. The dimensions of these materials increase with the ratio of OLAM to OA, as well as time, trends are observed by others who have used a similar chemistry to form other rare-earth and transition metal oxides.<sup>68-75, 77</sup> A consistent observation with rare-earth oxide materials, however, is the frequent appearance of plate-like nanocrystals with edge thicknesses on the order of 1 to 2 nm. Some ascribe the asymmetric shape to the crystallographic structure of these oxides, while others invoke the influence of soft templating around lamellar micelles formed from aggregated OLAM and OA.<sup>20, 72, 74</sup> Whatever the mechanism of formation, multiple studies have revealed that these plate-like nanocrystals possess surface coatings bound preferentially to their larger faces.<sup>68, 71, 74</sup>

Achieving dimensional control over these  $\text{Gd}_2\text{O}_3$  nanoparticles is important for potential MRI applications as nanocrystalline size is known to affect the relative amount of surface Gadolinium as well as nanoparticle biodistribution, pharmacokinetics, and cellular uptake.<sup>23-25</sup> For the proposed synthesis the overall size of these nanoparticles increases with the ratio of OLAM to OA or with reaction time. This approach yielded a library of



Gd<sub>2</sub>O<sub>3</sub> nanoparticles with face edges ranging from 2 nm to 15 nm (**Figure S2.1**). When reaction time was held constant at 18 hours, increasing the amount of OA relative to the OLAM resulted in smaller nanoparticles (**Figure S2.1a**). Oleic acid increases the amount of

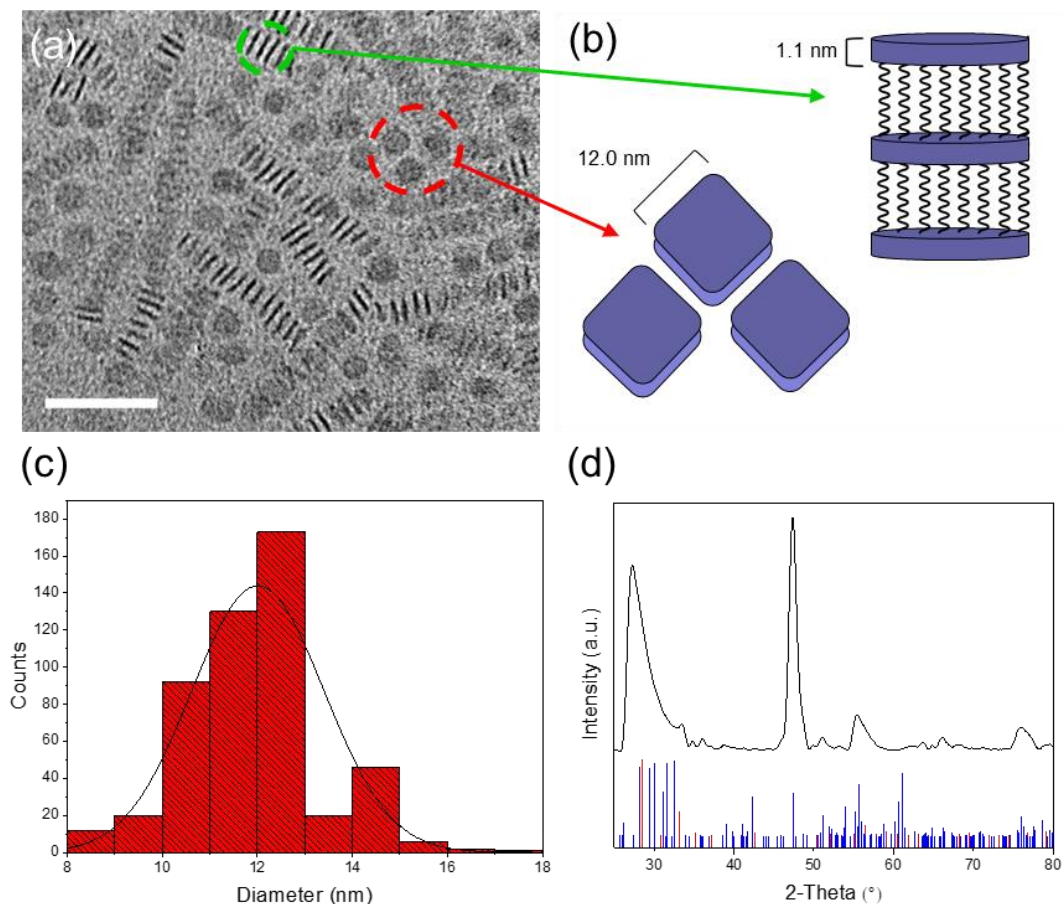


**Figure 2.1 GONP core characterization.** (a) TEM image of as-synthesized GONP sample (scale bar = 50 nm). (b) Diagram depicting edge-to-edge (red) and face-to-face (orange) alignment of GONP on the TEM grid. (c) Size distributions for the diameter of GONP ( $n = 502$ ). Using a 95 % CI and accounting for the resolution limit in the TEM used (0.23 nm), the average diameter of the monodisperse sample is  $12.0 \pm 0.36$  nm. (d) XRD patterns for GONP. The sample diffraction pattern is well matched with the standard JCPDS card for cubic Gd<sub>2</sub>O<sub>3</sub> (red) and slightly matched with the standard JCPDS card for monoclinic cubic Gd<sub>2</sub>O<sub>3</sub> (blue).

soluble precursor and, therefore, speeds nucleation at the expense of growth. Alternatively, increasing the amount of OLAM apparently promotes nanocrystal growth (**Figure S2.1b**). Since an amino group is a stronger binding ligand for the Gadolinium precursor, its presence results in less rapid decomposition, fewer nucleation events, and consequently larger particles.<sup>71</sup> Reaction time also increases the dimensions of the nanocrystals but has the unwanted effect of increasing their size distributions (**Figure S2.1c**). Ostwald ripening can occur at longer reaction times after the precursor Gadolinium is depleted. Because growth can only occur from the dissolution of smaller nanocrystals, the size distributions under these conditions also broaden with time.<sup>78</sup> Because of this, dimensional control in this study was achieved solely through manipulation of the surfactant (OLAM/OA) ratios.

The dimensions and morphology of Gd<sub>2</sub>O<sub>3</sub> nanoplates (GONP) sample were characterized using transmission electron microscopy (TEM) (**Figure 2.1a**). These nanoplates have 12.0 nm faces with thin edges (~ 1.1 nm) and relatively uniform dimensional distribution (**Figure 2.1c**). Further TEM images show that while face length is varied from 6 – 15 nm (**Figure S2.2a-d**) the GONP edge width remains fixed at approximately 1.1 nm, or roughly the length of one unit cell of cubic Gd<sub>2</sub>O<sub>3</sub>.<sup>69, 79</sup> The two-dimensional morphology of these samples is evidenced by edge-to-edge and face-to-face organization on the TEM grid (**Figure 2.1a-b**, inset of **Figure S2.2b**). X-ray diffraction (XRD) data suggest the presence of cubic ( $Ia\bar{3}$ ) and monoclinic (C2/m) phase bulk Gd<sub>2</sub>O<sub>3</sub> (Figure 1d). However, the contributions of monoclinic Gd<sub>2</sub>O<sub>3</sub> to the XRD pattern is minor, thus confirming the predominance of cubic phase Gd<sub>2</sub>O<sub>3</sub> (bixbyite) in these GONP. Peak broadening is

consistent with the small dimensions of the 12.0 nm Gd<sub>2</sub>O<sub>3</sub> nanoplates and the peak width

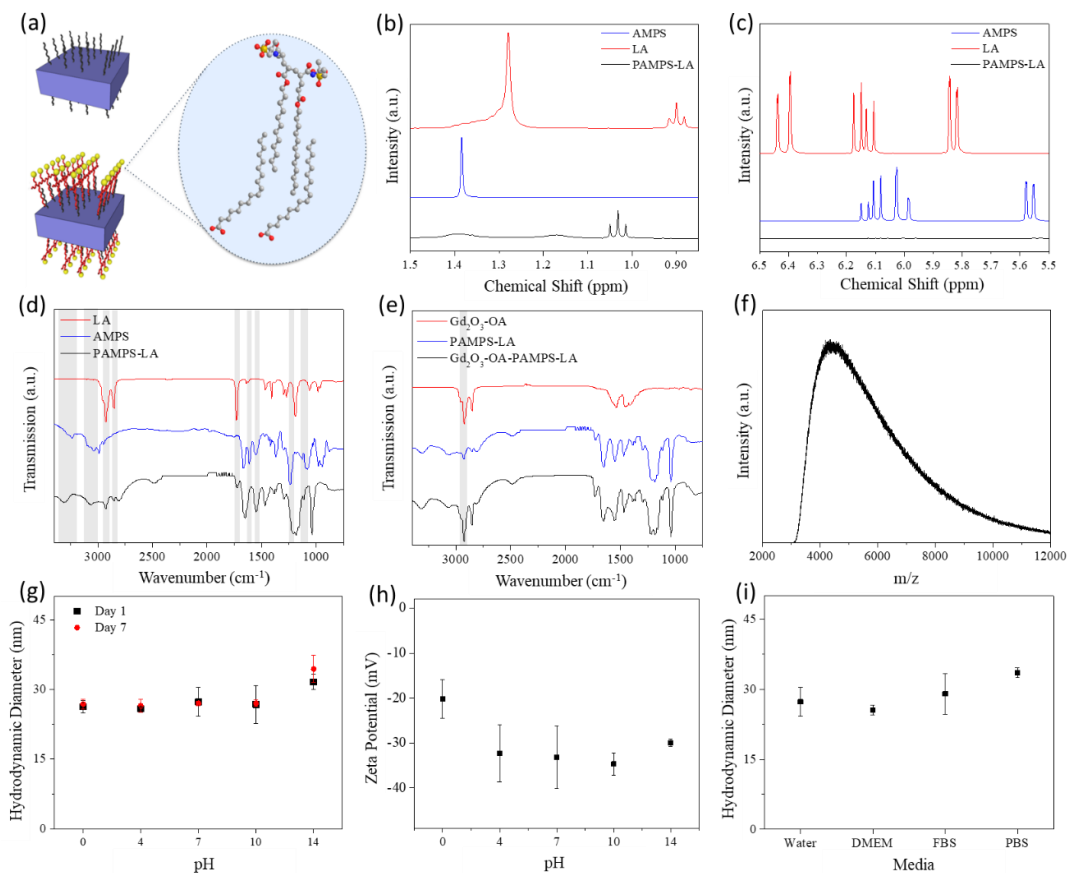


**Figure 2.2 GONP surface characterization.** (a) Schematic illustration of encapsulation process of GONP using PAMPS-LA amphiphilic copolymer. In this structural model red, gray, blue, and yellow spheres represent oxygen, carbon, nitrogen, and sulfur atoms, respectively. (b – c) NMR spectra at different regions for PAMPS-LA and its monomers. (d) FT-IR spectra of PAMPS-LA and its monomers and (e) GONP before and after PAMPS-LA encapsulation. (d-e) Significant peaks highlighted in gray. (f) MALDI-TOF mass spectrum of PAMPS-LA polymer with average molecular weight of 4300 Da. DLS data indicating that the (g) hydrodynamic diameter and (h) zeta potential of GONP-5 remains unchanged over a broad pH range (0-14). (i) These nanoplates also demonstrate similar hydrodynamic stability in a variety of biologically relevant dispersion media (water, DMEM, FBS, and PBS). (g-i) Reported hydrodynamic diameters and zeta-potentials are the average of three independent measurements with the standard deviation represented by error bars.

for the (440) plane is markedly larger than other reflections which is consistent with the observed two-dimensional morphology of these nanocrystals. The large face of the nanoplate has been reported to vary from squares and rounded squares to quasi-circular polygons, an observation consistent with our own results.<sup>68, 70, 72, 73, 77</sup>

### 2.3.2. Surface Modification of Gadolinium Oxide Nanoplates

To form non-aggregating nanoparticles in aqueous biological media their as-prepared hydrophobic surfaces are typically modified by polymers or surfactants.<sup>47, 80, 81</sup> These coatings can block water protons from coming within 2 – 3 Å of surface Gadolinium effectively limiting the most efficient inner-sphere spin relaxation processes.<sup>10, 11, 14</sup> The two-dimensional geometry of these materials provides a solution to these two opposing materials requirements as illustrated in the scheme (**Figure 2.2a**) depicting plate-like nanocrystals and the surface-associated polymers. The nanoplates were initially coated with oleic acid (OA); which anchors the hydrophobic end of an amphiphilic copolymer.<sup>80</sup> Due to the formation mechanism of plate-like rare earth oxides, the edges have little or no OA surface coating.<sup>20, 68, 72, 74</sup> It is on these narrow edges that surface Gadolinium are located, and are accessible for close, inner-sphere interactions with water protons.<sup>20, 56,</sup>

57

Previously several other surface coatings were explored to optimize both colloidal stability and MRI contrast for these nanoplates.<sup>20</sup> Here a sulfonated copolymer, poly (2-acrylamido-2-methylpropane sulfonic acid-lauryl acrylate), or PAMPS-LA, confers excellent colloidal stability while maintaining optimal contrast performance (**Figure S2.3**). Originally developed for use in the harsh environments of oil and gas reservoirs, this class

of polymer has not previously been used in nanomedicine.<sup>82, 83</sup> Its sulfonic acid functional group ensures excellent colloidal stability over a wide range of conditions and we note that other sulfonated polymers are biocompatible at clinically relevant concentrations.<sup>82-85</sup> Also, more negatively charged surface coatings enhance the relaxivity of Gadolinium-containing nanocrystals.<sup>20, 38, 86</sup> Here we expect that the sulfonic acid groups will structure water around the nanoplates and accelerate second-sphere relaxation processes.<sup>11, 14-16, 33, 34, 38, 48-55</sup> Additionally, inner-sphere  $Gd^{3+}$ -water interactions are facilitated as amphiphilic encapsulation leaves the Gadolinium at the edges uncoated (**Figure 2.2a**).

Nuclear magnetic resonance (NMR) and Fourier-transform infrared spectroscopy (FT-IR) were used to characterize PAMPS-LA and encapsulated nanoplates (**Figure 2.2b-e**). NMR data confirm the polymerization of AMPS and LA into PAMPS-LA. Vinylic  $^1H$  peaks (5.5 – 6.5 ppm) in monomers are absent in PAMPS-LA. Also, the methyl group triplet of LA (0.85 – 1.1 ppm) and singlet of AMPS (1.35 – 1.45 ppm) are present in PAMPS-LA. The downfield shift in the methyl triplet from LA to PAMPS-LA is attributed to sulfonate-associated cation deshielding. Broadening of the AMPS methyl singlet in PAMPS-LA is likely due to tumbling rate deceleration. FT-IR data indicate that PAMPS-LA exhibits vibrational modes characteristic of its monomers, but without their C=C stretching mode ( $1612\text{ cm}^{-1}$ ), further confirming AMPS-LA polymerization. For instance, asymmetric and symmetric S=O stretching (AMPS) at  $1238$  and  $1079\text{ cm}^{-1}$ , AMPS N-H (stretch) and amide (II) at  $3236/3038$  and  $1551\text{ cm}^{-1}$ , and C=O and C-H stretches (LA) at  $1729$  and  $2825/2855\text{ cm}^{-1}$  are all present in PAMPS-LA. Figure 2e shows the IR spectra of as-synthesized nanoplates, PAMPS-LA, and PAMPS-LA coated nanoplates. Spectra of PAMPS-LA-GONP and PAMPS-LA are mostly

identical with a stronger presence of CH<sub>2</sub> peaks (2924 cm<sup>-1</sup>) because of the encapsulation of OA. Matrix-assisted laser desorption ionization-time of flight mass spectrometry (MALDI-TOF MS) data indicated a weight average molecular weight of 4300 Da for PAMPS-LA, corresponding to approximately 20 monomers (**Figure 2.2f**). We found the PAMPS-LA molecular weight to be an important variable to control as larger polymers could cause aggregation and or block edge Gd<sup>3+</sup>-water interactions.

The colloidal stability of encapsulated Gd<sub>2</sub>O<sub>3</sub> nanoplates (GONP) in various media was confirmed with dynamic light scattering (DLS) (**Figure 2.2g-i**). While hydrodynamic diameter ( $D_H$ ) is only a semi-quantitative measure of dimension, significant increase in  $D_H$  can indicate early stages of aggregation and colloidal instability.<sup>87</sup> The  $D_H$  for 5 nm GONP (GONP-5) is between 25 and 31 nm, encompassing the Gd<sub>2</sub>O<sub>3</sub> core, OA surface layer, PAMPS-LA, and associated electric double layer (**Figure 2.2i** and **S2.4**). Due to the acidic nature of the AMPS sulfonate,  $D_H$  depends only weakly on pH and remains approximately constant over a broad pH range (**Figure 2.2g**). However, at conditions below the  $pK_a$  of AMPS (1.9), PAMPS-LA becomes slightly more positive (**Figure 2.2h**).<sup>84</sup> Nanoplate average dimensions were also measured in biologically relevant media including Dulbecco's Modified Eagle's Medium (DMEM), fetal bovine serum (FBS), and phosphate buffer saline (PBS) (**Figure 2.2i** and **Figure S2.4**). GONP-5 dimensions remained approximately constant in all these environments.

### 2.3.3. Relaxivity Measurements

Water proton relaxation time measurements, both longitudinal ( $T_1$ ) and transverse ( $T_2$ ), as well as the corresponding relaxivities ( $r_1$  and  $r_2$ ) and their ratio ( $r_2/r_1$ ) are an important

metric of MRI contrast. Large relaxivities, or fast water proton relaxation rate per  $\text{Gd}^{3+}$  ion ( $\text{mM-Gd}^{-1}\text{s}^{-1}$ ), generally correspond to greater contrast, more resolved MRI data, and lower effective CA dosages. For  $T_1$  CA specifically, the relaxivity ratio ( $r_2/r_1$ ) should be close to 1 to mitigate confounding effects of  $M_{xy}$  on image analysis and consequent reduction in image contrast.<sup>12, 88</sup> Commercial, clinically available  $T_1$  contrast agents are molecular  $\text{Gd}^{3+}$  chelates stable in biological media. For field strengths of 1.5 T, these contrast agents have ionic  $r_1$  between 3 – 7  $\text{mM}^{-1}\text{s}^{-1}$  and relaxivity ratios between one and two.<sup>10, 14</sup>

PAMPS-LA encapsulated  $\text{Gd}_2\text{O}_3$  nanoplates (GONP) have ionic  $r_1$  10 – 20 times larger than these commercial contrast agents (60.9 – 63.0  $\text{mM-Gd}^{-1}\text{s}^{-1}$ ) and  $r_2/r_1$  close to 1 (1.17 – 1.29). Ionic relaxivities are weighted necessarily by the amount of Gadolinium that leads to a signal, not the amount of contrast agent; such ionic relaxivities, which report the signal contrast as a function of the molar concentration of  $\text{Gd}^{3+}$ , are standard metrics for comparing contrast agent design. **Figure 2.3** (a and b) show the relaxation rates ( $1/T_n$ ,  $n = 1$  or 2) of GONP of varying face length (2, 5, and 12 nm) as a function of  $\text{Gd}^{3+}$  concentration. As a benchmark, these data were compared to the response of the commercial contrast agent, Magnevist. These data can be used to determine relaxivity ( $r_1$  or  $r_2$ ) by finding the slope of the linear regression (**Table 2.1**). The  $r_1$  for the smallest (2 nm, GONP-2) and largest (12 nm, GONP-12) GONP are  $61.0 \pm 2.7$  and  $63.0 \pm 4.4$   $\text{mM-Gd}^{-1}\text{s}^{-1}$ , respectively. These are nearly 20 times larger than the  $r_1$  of Magnevist ( $3.4 \pm 0.1$   $\text{mM}$

**Table 2.1** Relaxivity values for PAMPS-LA-GONP and Magnevist in DI water at 1.4 T.

Contrast Agent	Core [nm]	$r_1/[\text{Gd}^{3+}]$ [ $\text{mM}^{-1}\text{s}^{-1}$ ]	$r_1/M$ [(mg/mL) $^{-1}\text{s}^{-1}$ ]	$r_1/\text{NP}$ [ $\text{mM}^{-1}\text{s}^{-1}$ ]	$r_2/[\text{Gd}^{3+}]$ [ $\text{mM}^{-1}\text{s}^{-1}$ ]	$r_2/M$ [(mg/mL) $^{-1}\text{s}^{-1}$ ]	$r_2/\text{NP}$ [ $\text{mM}^{-1}\text{s}^{-1}$ ]	$r_2/r_1$
Magnevist	-	$3.5 \pm 0.1$	-	-	$5.1 \pm 0.2$	-	-	1.5
Gd <sub>2</sub> O <sub>3</sub> -PAMPS-LA (GONP-2)	2	$61.0 \pm 2.7$	338	4950	$75.9 \pm 2.1$	419	6160	1.24
Gd <sub>2</sub> O <sub>3</sub> -PAMPS-LA (GONP-5)	5	$60.9 \pm 0.7$	336	30900	$78.6 \pm 3.6$	434	39800	1.29
Gd <sub>2</sub> O <sub>3</sub> -PAMPS-LA (GONP-12)	12	$63.0 \pm 4.4$	348	184000	$73.5 \pm 2.4$	406	215000	1.17

$^{-1}\text{s}^{-1}$ ). However, on a per CA basis – which may be the most accurate relaxometric measure of nanoscale CA performance – these nanoplates exhibit  $T_1$  relaxivities more than fifty thousand times that of the clinical agent, Magnevist. Also important is the relative ratio of  $r_2$  to  $r_1$  and the  $r_2/r_1$  for these GONP are nearly 1 over a broad range of sizes and magnetic field strengths. Without complex and unconventional pulse sequences, highly active  $T_2$  relaxation can diminish the effect of a  $T_1$  CA as the signal decays due to processes other than those ascribed to  $T_1$  contrast.<sup>12</sup>

The relaxivities ( $r_1$  and  $r_2$ ) of any contrast agent depend on a combination of inner-, second-, and outer-sphere relaxation mechanisms.<sup>4, 5, 10</sup> In all cases, protons must come within some distance of magnetically active ion(s) contained in the contrast agent in order to be affected; the underlying mechanism of spin transfer leads to different distance sensitivities.<sup>4, 5, 10</sup> Though inner-sphere relaxation mechanisms are usually dominant for molecular contrast agents, the significance of second-sphere processes is also recognized – especially in slower tumbling nanoscale contrast agents.<sup>16, 33, 34, 38, 48-55</sup> One characteristic indication of inner-sphere relaxation processes is the strong dependence of



$r_1$  on external magnetic field strength ( $B_0$ ).<sup>7, 20, 26, 33, 34, 38, 40, 51, 81</sup> Caravan *et al.* showed for molecular complexes that large magnetic fields can quench inner-sphere  $r_1$  yet have little impact on other relaxation processes.<sup>11</sup> They derived a quantitative relationship for the dependence of  $r_1$  on static  $B_0$  due to inner-sphere relaxation processes.<sup>11, 14</sup> According to the model, the maximum in  $r_1$  is achieved once the tumbling rate ( $1/\tau_r$ ) reaches the proton Larmor frequency ( $\omega_H$ ); as the Larmor frequency increases at higher field strengths the relaxivity is expected to fall.<sup>14</sup> For nanoscale and macromolecular CA with slower tumbling rates, the maximum  $r_1$  usually falls between approximately 60 and 100 MHz ( $\sim 1.4 - 2.3$  T for  $^1\text{H}$ ).<sup>4, 7, 33, 48</sup>

To explore this field dependence over a clinically relevant range, the performance of these materials was measured in different MRI scanners operating at three field strengths, 1.4, 3 and 9.4 T. **Figure 2.3c** shows that  $r_1$  decreases as  $B_0$  increases which is consistent with an inner-sphere relaxation mechanism as described by Caravan *et al.* However, what is notable is that these 2D nanocrystals possess substantial relaxivity at the highest field strengths (32.6 mM-Gd<sup>-1</sup>s<sup>-1</sup> at 9.4 T). Commercial molecular contrast agents have  $T_1$  relaxivities of at most approximately 5 – 6 mM-Gd<sup>-1</sup>s<sup>-1</sup> at field strengths above 3 T (**Figure S2.6**).<sup>10, 15, 33, 34</sup> These data illustrate that the nanocrystals studied here also possess substantial second-sphere contributions to their spin relaxation processes which are less sensitive to the applied field.

To further examine the role of second-sphere processes, the performance of the nanocrystals was measured with different surface coatings. Two charged polymer surface coatings (PAMPS-LA and PAA-LA, similar molecular weights) and a neutral polymer

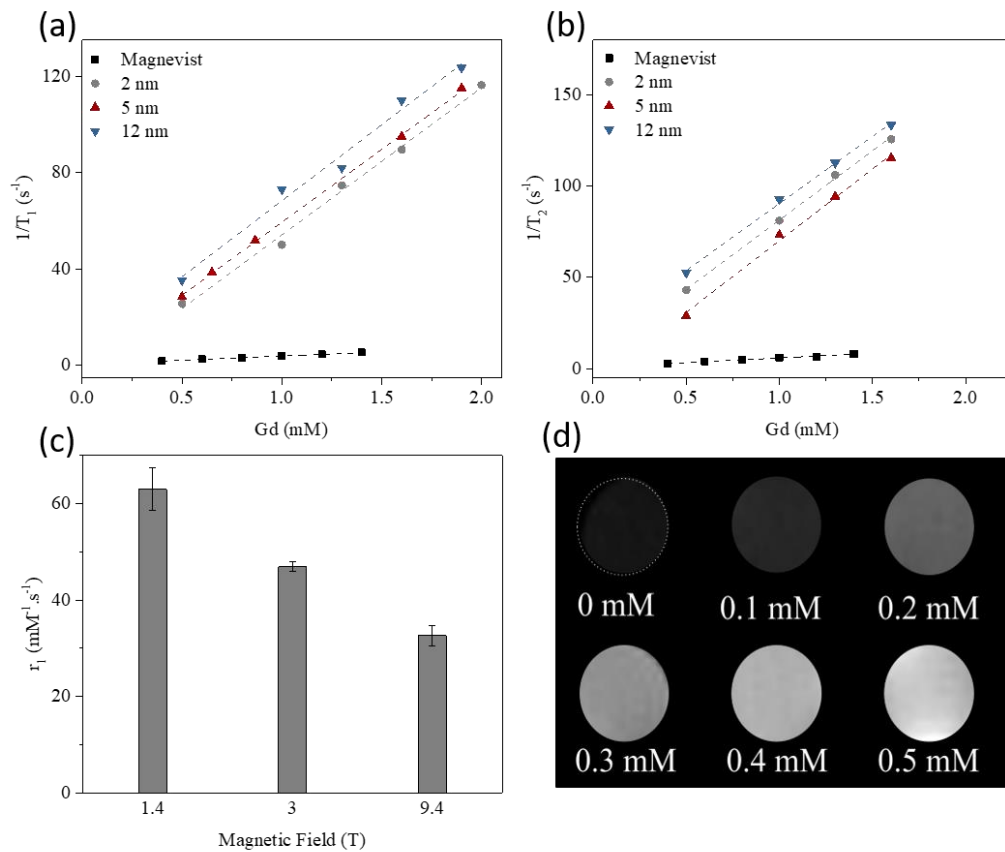


**Figure 2.3 Relaxometric characterization of GONP.** (a) Longitudinal and (b) transverse relaxation rates as a function of Gadolinium concentration for PAMPS-LA-GONP (2, 5, and 12 nm) compared to Magnevist at 1.4 T. (c)  $R_1$  for GONP-12 at 1.4, 3, and 9.4 T are 63.0, 46.9, and 32.6 mM<sup>-1</sup>s<sup>-1</sup>, respectively, thus illustrating its inverse relationship with field strength. (d)  $T_1$ -weighted images of GONP (12 nm) at different concentrations of Gadolinium at 9.4 T. (a-c) All reported  $T_1$  and  $r_1$  are the average of three independent measurements with the standard deviation represented by error bars.

coating (PEG) were applied to the same type of Gadolinium-containing nanocrystals (**Figure S2.6** and **Table S2.1**). These data demonstrate that relaxometric performance is severely diminished with a neutral hydrophilic surface coating (PEG) as opposed to highly charged hydrophilic surface coatings with H-bonding capabilities (PAMPS-LA and PAA-LA). Neutral hydrophilic surface coatings are not able to structure water very efficiently,

thereby reducing the second-sphere contributions to nanoparticle  $r_1$ .<sup>15, 16, 49, 53, 55</sup> These results agree with relaxation theory that indicates second-sphere interactions increase with the number of water molecules in that coordination sphere ( $q'$ ).<sup>15, 16</sup> Potential methods for maximizing second-sphere contributions to  $r_1$  would be to increase the grafting density of – or number of charged groups on – the charged, hydrophilic monomer in the encapsulation copolymer.

Notably, while the  $r_1$  of GONP-12 may decrease at higher  $B_0$ , this does not necessarily influence detectability when used for MRI imaging because signal-to-noise (SNR) is known to increase with field strength.<sup>14, 89</sup> However, phantom images in **Figure 2.3d** show that the optimized nanocrystal contrast agents exhibit significant contrast even at 9.4 T. In conjunction with the direct relationship between field strength and SNR, it can be inferred that these materials would perform exceptionally well at high field strengths.

Another striking feature of these nanoplates is that their large dimension has little impact on their  $r_1$  (**Table 2.1**). The most significant factors affecting the inner-sphere relaxation of a  $T_1$  CA are its tumbling rate, electron spin angular momentum of its magnetically active ion(s) ( $S$ ), hydration number ( $q$ ), and the distance between the magnetically active ion(s) and water protons ( $r_H$ ).<sup>4, 5, 10, 11, 14</sup> Gadolinium (III), with its seven unpaired d-electrons, has the largest possible electron spin angular momentum of any metal ion ( $S = 7/2$ ), which makes it the atom of choice for  $T_1$  CA.<sup>2, 5</sup> Since  $r_1$  is indirectly proportional to the tumbling rate and scales linearly with increasing  $q$ , it would be expected that Gadolinium-containing nanocrystals would generally have larger  $r_1$  than molecular contrast agents because of their larger size and low coordination number surface Gadolinium ions.<sup>11, 14, 15,</sup>

<sup>31, 45, 47, 48, 81</sup> Additionally, Gadolinium-containing nanocrystals should allow for cooperative water proton relaxation, an advantage that traditional chelates cannot provide.<sup>31, 74</sup> The relatively weak size dependence observed here suggests that vacant edges play a significant role in the relaxation process. Briefly, as nanoplate size increases, the number of surface Gadolinium ions facilitating water proton relaxation per contrast agent volume decreases, a trend that opposes the expected increase in  $r_1$  due to lower tumbling rates.<sup>31, 81</sup> The overall magnitude of nanoplate  $r_1$  also indicate the presence of vacant edges because for inner-sphere  $T_1$  relaxation mechanisms,  $1/T_1$  decreases with increasing Gd<sup>3+</sup>-water distance to the power of 6 ( $1/T_1 \propto 1/r_H^6$ ).<sup>4, 5, 10, 11, 14</sup> This, along with second-sphere contributions, might explain why, despite being similar in size and composition to other reported Gadolinium-containing nanoparticles, these materials have much larger  $r_1$  at clinically relevant  $B_0$ .

#### 2.3.4. Pharmacokinetics and Biodistribution

The pharmacokinetics and biodistribution of MRI contrast agents creates both opportunities and constraints for the imaging of specific organs and diseases. A biodistribution study of GONP-12 24 h after administration confirms the hepatobiliary system as the primary clearance pathway (**Figure 2.4a**). This is the expected clearance pathway for negatively charged nanomaterials with hydrodynamic diameters of about 25 nm.<sup>3, 23-25, 90</sup> In general, the specific hydrodynamic diameter of particles with dimensions

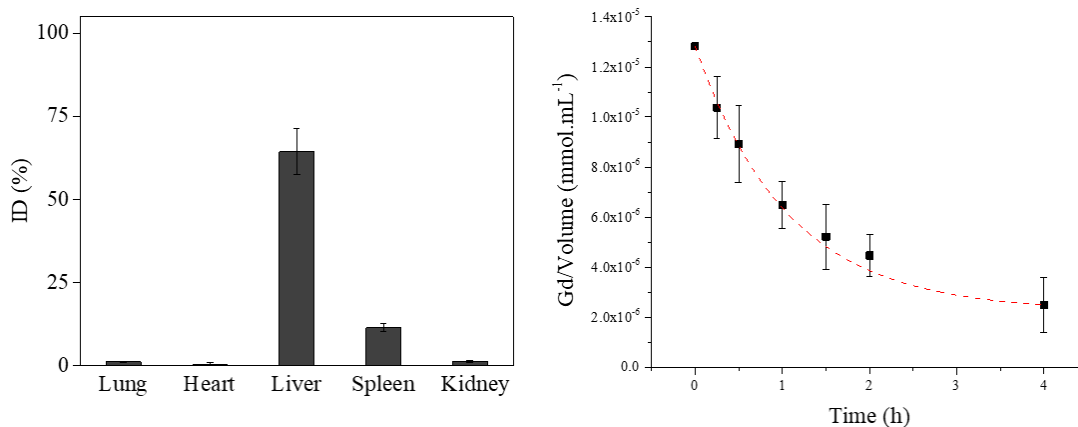


**Figure 2.4 Biodistribution and pharmacokinetics of GONP in mice.** (a) Biodistribution profile of GONP-12 measured by percent injection dosage of Gd<sup>3+</sup> for various organs 24 h after administration. (b) Pharmacokinetic profile of GONP-12 measured by Gadolinium per volume blood of mice as a function of time (up to 4 h) after injection in hours. All reported values are the average measurement of six samples (mice) with the standard deviation represented by error bars.

between 20 nm and 100 nm does not significantly impact biodistribution or biological activity. In this size range the surface coating has more influence over clearance times from the blood, and the route of elimination is often observed to be through the reticuloendothelial system (RES).<sup>3, 23-25, 46, 90</sup>

High accumulation of Gadolinium ions in the liver and spleen provides strong evidence of RES clearance of GONP-12. Phagocytic Kupffer macrophage cells of the liver serve as highly effective hosts for uptake of the negatively surface charged nanocrystals.<sup>91</sup> This observation was the motivation for the application of GONP-12 to the diagnosis of liver disorders related to macrophage activity such as NAFLD as described later.

After Gadolinium-chelate contrast agents (GCCA) are administered intravenously, they distribute in the blood, the extracellular and intravascular spaces, and are later eliminated

**Table 2.2** Plasma kinetics of Magnevist and Gadolinium oxide nanocrystals

Contrast Agent	$Cl_{tot}$ [mL.min <sup>-1</sup> .kg <sup>-1</sup> ]	$\alpha_{1/2}$ [h]	$\beta_{1/2}$ [h]	$V_d$ [L.kg <sup>-1</sup> ]
Magnevist	1.94	0.2	1.6	0.26
GONP-12	1.03	0.6	0.8	0.07

from the body through excretory organs.<sup>92</sup> It is well documented that elimination half-life plays an important role in determining the safety of GCCA. In fact, the combination of extended elimination half-life and kinetic stability of GCCA seem to be closely linked to the presence of nephrogenic systemic fibrosis in patients suffering from renal failure and the deposition of Gadolinium in various tissue (brain, bone, skin, etc.) in healthy patients with multiple administrations.<sup>3, 10, 13, 20-22</sup> Though the majority of GCCA are extracellular fluid agents, there are also blood-pool agents (Ablavar) and liver-specific agents (MultiHance and Primovist/Eovist).<sup>1, 13, 21, 28, 92</sup> Extracellular fluid agents, like Magnevist, distribute in the blood quickly, and in a patient with normal renal function they clear from the blood with an approximate elimination half-life of 1.5 hours.<sup>10, 24</sup>

It is important to determine how long it takes for GONP-12 to distribute in the body as well as the speed at which they clear from the blood. **Figure 2.4b** shows the concentration of Gadolinium in the blood of six healthy mice 4 h post injection. It is evident from the plasma kinetics that, after an hour, the blood was cleared of half of the initial injection doses of GONP-12. This is compared to the experimental circulation half-life of 1.5 h for commercial Gadolinium-chelates.<sup>10</sup> Moreover, the secondary pharmacokinetic parameters were determined more accurately based on the fit of a two-component biexponential function to the clearance data (**Equation 1-4, Table 2.2**).<sup>92</sup> While more time

points would help improve this model, the data collected do allow an estimate of the total clearance rate of the CA based on the blood ( $Cl_{tot}$ ), the distribution half-life ( $\alpha_{1/2}$ ), the elimination half-life ( $\beta_{1/2}$ ), and the volume of distribution ( $V_d$ ).

$$C_P = Ae^{-at} + Be^{-bt} \quad (1)$$

$$\alpha_{1/2} = \frac{\ln(2)}{a} \quad (2)$$

$$\beta_{1/2} = \frac{\ln(2)}{b} \quad (3)$$

$$Cl_{tot} = V_d \cdot b \quad (4)$$

The distribution half-life for GONP-12 is 0.6 h, which is longer than Magnevist (0.2 h). However, GONP-12 have a shorter elimination half-life (0.8 h) than Magnevist (1.6 h). This means that GONP-12 have a slower distribution rate constant ( $a$  in Equations 1-2), and a faster elimination rate constant ( $b$  in Equations 1, 3, and 4). The 0.07 L.kg<sup>-1</sup> volume of distribution for GONP reflects the plasma volume, which suggests their presence in the intravascular space. This stands in contrast to the volume of distribution of Magnevist (0.26 L.kg<sup>-1</sup>), which indicates its presence in the extracellular space.<sup>92</sup> A faster elimination and smaller volume of distribution results in an overall slower total clearance rate of blood for GONP-12 (1.03 mL.min<sup>-1</sup>.kg<sup>-1</sup>) than for Magnevist (1.94 mL.min<sup>-1</sup>.kg<sup>-1</sup>). It is well established that as much as 90 % of similarly sized, non-degradable nanocrystals are removed from vital organs and excreted over longer periods of time (> 7 days), and there is little reason to expect these materials would have significantly different rates of accumulation.<sup>46, 93, 94</sup> Specifically in the case of several types of Gadolinium-containing

nanoparticles at most a few percent of the injected dose remains in the organism after several weeks.<sup>95-97</sup>

### 2.3.5. Cellular Uptake, Cytotoxicity, and Gadolinium Dissolution

The negatively charged surfaces of these nanoplates suggests that they will be readily taken up by phagocytic cells such as macrophages.<sup>91</sup> **Figure 2.5a** confirms this expectation and shows the amount of Gadolinium taken up by macrophage (Raw 264.7) cells after 24 hours of incubation time. The cells exhibit maximal uptake at 50  $\mu\text{M}$  of  $\text{Gd}^{3+}$ . These results are in striking contrast to Magnevist which, after 2 h, only exhibit marginal cellular uptake compared to GONP-12 (**Figure S2.7**). Given their presence inside of cells, there is an opportunity for MRI-based cellular imaging.

Here we investigated whether the high  $r_1$  of  $\text{Gd}_2\text{O}_3$  nanoplates (GONP) was maintained intracellularly. Figure 5b shows that relaxation times of cells labeled with GONP dramatically decreased as compared to the unlabeled control cells. *In vitro*  $T_1$ - and  $T_2$ -weighted images of corresponding cell pellets further confirms the contrast enhancement of labeled cells (**Figure S2.8**). Despite the complex intracellular matrix and the competition that water protons may have with intracellular biomolecules for interaction with the edge Gadolinium, these findings are extremely promising for MR cellular imaging applications such as the visualization of stem cell-based therapies.<sup>98</sup>



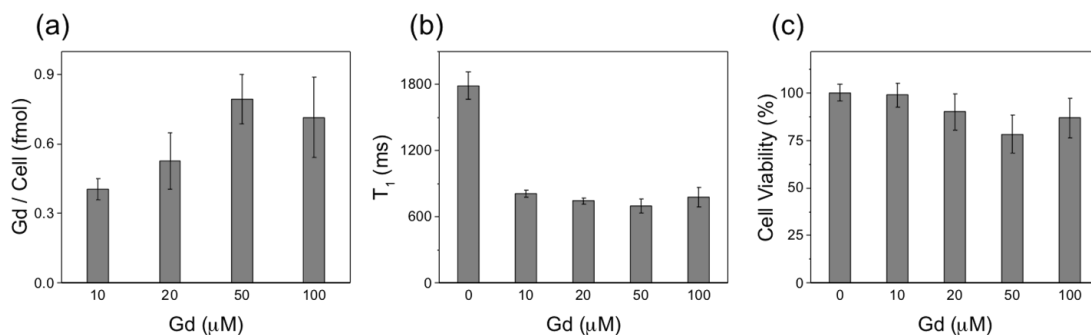


**Figure 2.5 Cell uptake and viability of GONP.** (a) Average Gadolinium per cell, and (b) average  $T_1$  relaxation times of cells (seeding density:  $6 \times 10^6$ /well) incubated with GONP-12 (0 – 100  $\mu\text{M}$   $\text{Gd}^{3+}$ ) for 24 h. (c) Average viable fraction of cells (seeding density:  $2 \times 10^4$ /well) incubated with GONP-12 (0 – 100  $\mu\text{M}$   $\text{Gd}^{3+}$ ) evaluated by MTS assay after 24 h. All reported values are the average of triplicate measurements with standard deviation represented by error bars.

Cytotoxicity assays based on 3-(4,5-dimethylthiazol-2-yl)-5-(3-carboxymethoxyphenyl)-2-(4-sulfophenyl)-2H-tetrazolium (MTS) are a convenient, sensitive, and colorimetric method for evaluating cell viability.<sup>98</sup> Using this MTS assay, Raw 264.7 macrophage viability was not significantly affected by incubation with GONP-12 over a wide range of physiologically relevant Gadolinium concentrations (**Figure 2.5c** and **Figure S2.9**). GONP retain a viability of nearly 100 % at the maximum concentration of 300  $\mu\text{M}$  (Figure S9d). These results were confirmed using a live-dead assay which is a common cytotoxicity test used to differentiate viable from nonviable cells based on plasma membrane integrity.<sup>99-101</sup> Fluorescent microscopy of HDF and Raw 264.7 stained cells revealed no cell death even at the highest dose of Gadolinium oxide nanoplates (**Figure S2.9a**). In addition to cell viability, the micrographs show that the spindle shape of HDF cells and the round shape of Raw 264.7 cells were not affected by the addition of different concentrations of surface-coated nanoplates.

A more sensitive cellular assay was applied to measure the effects of nanoparticle exposure on fibroblast function. Commonly referred to as a scratch or wound-healing assay, this test is a straightforward, inexpensive, and well-developed *in vitro* method for investigating cell migration.<sup>102</sup> After scratching a monolayer cell culture, the migration of cells to fill the gap over time (wound healing) is observed via an optical microscope.<sup>103</sup> This study can be particularly useful for indirectly investigating the toxic effects of Gd-containing compounds on fibroblasts – a cell type integrally involved in fibrosis and tissue healing in Gd-associated NSF. Optical micrographs of cells incubated with and without nanocrystals were captured at various time intervals as fibroblasts moved to fill in empty space (**Figure S2.9b**). Fibroblasts were remarkably insensitive to GONP and even at the highest nanocrystal concentration (200  $\mu\text{M}$ ) the artificial wound was healed by more than 60% (**Figure S2.9c**). The results of this experiment may not be representative of an *in vivo* response, but they do provide a means to screen novel contrast materials based on their more subtle effects on important cellular processes.<sup>102</sup>

Clinical doses of 0.1  $\text{mmol}\cdot\text{kg}^{-1}$  are typically given for Magnevist, a value approximately equal to the maximum Gadolinium concentration of 300  $\mu\text{M}$  used here.<sup>28, 92</sup> Given the high  $r_1$  of these nanoplates, and their different possible imaging applications, lower effective dosages would be likely. Further studies of both the acute and chronic toxicity of these materials *in vivo* is required, but the *in vitro* cytotoxicity results for nanoplates as compared to Magnevist is promising.<sup>20, 31</sup>

To further characterize the safety profile of these nanoparticles, we evaluated their propensity to dissolve (**Figure S2.10**) in a variety of aqueous media. There was no

measurable release of Gadolinium from the GONP except under the most acidic (pH = 2) conditions. Samples were placed in dialysis membranes which allowed the passage of free Gadolinium into the dialysate but retained intact nanocrystals.<sup>104, 105</sup> After three days of equilibration at a 1:1000 volume ratio, Gadolinium concentrations in both the dialysate and sample were determined by ICP-MS (Figure S10). No Gadolinium was detected in the dialysate of nanoplate samples except for the most acidic case (pH = 2) and we can conclude that at least 97% of the Gadolinium remained in a nanoparticle form. A longer time study, over several weeks, confirmed that the materials have no measurable ion release even in mildly acidic (pH = 4.3) conditions (**Figure S2.11**). This chemical stability could arise from the particle's organic coatings, or it could reflect the insolubility of bulk Gadolinium oxide in water. Given that a bulk Gadolinium oxide powder did show some, albeit small, release of free Gadolinium in these experiments, we conclude that the surface coatings play some role in protecting these GONP against dissolution.

### 2.3.6. Differentiation of Non-Alcoholic Fatty Liver Disease

A spectrum liver disorder, non-alcoholic fatty liver disease ranges from relatively benign hepatic steatosis to the necro-inflammatory stage of non-alcoholic steatohepatitis, to fibrosis, cirrhosis, and hepatocellular carcinoma.<sup>106</sup> Non-alcoholic fatty liver disease (NAFLD) has emerged as the most common liver disease, and has been identified as a major public health problem affecting approximately 10 – 40 % of the population – depending on sex, geographic location, and diagnostic metric used – in the developed world.<sup>107-109</sup> Disease development and progression is traditionally described as a two-stage process. The first stage is characterized by non-inflammatory and non-fibrotic

hepatic steatosis – the accumulation of fat in the liver. The second stage, often called non-alcoholic steatohepatitis (NASH), is less well defined but can be characterized by inflammation-induced necrosis, fibrosis, cirrhosis, elevated reactive oxygen species (ROS), hepatocellular carcinoma, liver failure, and increased rate of mortality.<sup>106-109</sup> Studies show that approximately 20 % of baseline borderline-NASH NAFLD patients develop NASH and 60 % of first stage NAFLD patients develop borderline-NASH or NASH.<sup>109</sup> The cause of this progression to more advanced stages of NAFLD (*e.g.* NASH) is still under debate, and improved imaging is needed to better understand the disease and its progression.

The traditional method of NAFLD diagnosis and assessment of disease severity is the liver biopsy. However, this method is limited by sampling error and variability, grading inconsistency, and invasiveness.<sup>64, 110</sup> As a result, there has been ongoing research into the use of non-invasive imaging to assess the state of the liver using ultrasonography (US), computed tomography (CT), magnetic resonance spectroscopy, and GCCA and ION contrast-based MRI.<sup>8, 58-65</sup> Small GCCA such as Magnevist™ have limited value for liver imaging as they clear through the kidneys; hepatobiliary GCCA, such as Primavist™ (gadoxetic acid), can be effective for liver imaging, but their use has been associated with various levels of hepatotoxicity.<sup>29, 59, 61-63</sup> While the mechanism has not been unequivocally proven, the presence of Gadolinium deposits suggests that the GCCA release toxic, free Gadolinium most likely from acidic lysosomal compartments within the Kupffer cells.<sup>111-113</sup> While nanocrystals are also taken up by Kupffer cells in the liver, the remarkable chemical stability of these materials, even under mildly acidic conditions,

should limit the release of free Gadolinium and reduce the likelihood of this particular toxicity mechanism (**Figure S2.9, S2.10**).

Nanoparticle-based T<sub>2</sub> CA-enhanced assessment has been used with success in both animal models and humans to assess liver uptake and provide a functional evaluation for NAFLD.<sup>8, 58, 60, 65</sup> As previously mentioned, it is widely accepted that the second stage in NAFLD is characterized by inflammation and the overproduction of reactive oxygen species (ROS).<sup>114</sup> A confounding factor in ROS production is iron overload, which further increases ROS and other advanced NAFLD symptoms.<sup>66, 67</sup> Therefore, an iron-free, high *r*<sub>1</sub>, and liver-specific CA-based approach to the detection of NAFLD would pose multiple advantages over the current approaches.

To assess liver accumulation of GONP, *ex vivo* MR imaging was performed four hours after injection of GONP-12 into live mice (**Figure 2.6a-d**). For the purposes of this study, *ex vivo* MR imaging offers some advantages over *in vivo* imaging. *Ex vivo* MR imaging eliminates the need for shorter imaging times and reduces movement artifacts, resulting in better imaging resolution and sensitivity – hence its use elsewhere and in similar applications.<sup>115, 116</sup> Both of these advantages are important in an application dependent on quantitatively measuring the differences in the change in contrast enhancement at the same time point post administration. Liver *T*<sub>1</sub> were compared between normal and high-fat diet age-matched mice with and without injected GONP-12 (**Figure 2.6e**). The effect of nanoplate administration on liver *T*<sub>1</sub> is assessed using a two-way analysis of variance (ANOVA). The effect of GONP-12 is significantly reduced in the NAFLD, high fat diet, mouse model. Specifically, the decrease in liver *T*<sub>1</sub> due to GONP-12 administration is significantly smaller

in the NAFLD, high fat diet, mouse model than in the age-matched mice fed normal chow. Similar experiments have chosen to use signal intensity or signal-to-noise ratios (SNR) as a metric for probing uptake.<sup>58, 65</sup> However, by averaging curve-fit liver  $T_1$  values from a

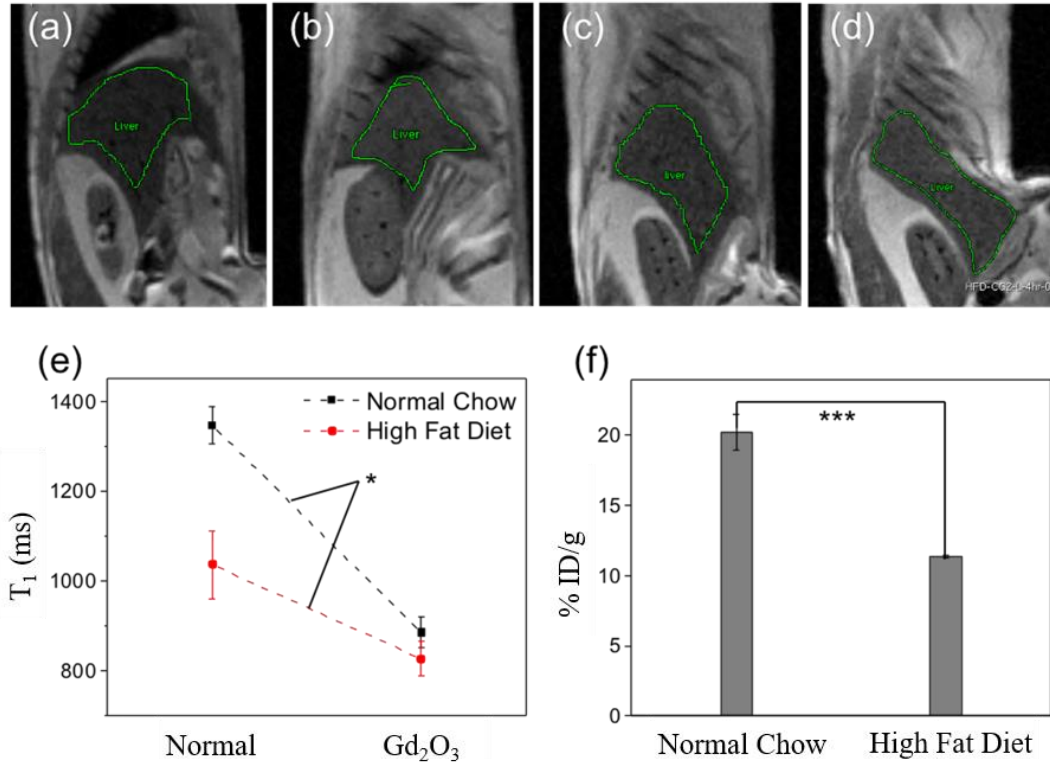


**Figure 2.6 Ex vivo  $T_1$ -weighted MRI of mice using GONP.**  $T_1$ -weighted images (RAREVTR protocol) of normal chow mice (a) without and (b) with GONP-12 administration (liver outlined in green).  $T_1$ -weighted images of high fat diet mice (c) without and (d) with GONP-12 administration (liver outlined in green). All mice with GONP-12 were sacrificed for imaging 4 h after administration. (e) Liver  $T_1$  with and without (control) GONP-12. The average liver  $T_1$  of normal chow mice decreased 34.3 % compared to a 20.2 % decrease for the high fat diet mice. Statistics: Two-way ANOVA. (f) Percentage of injected doses of Gadolinium per gram of tissue in normal and fatty liver. The high fat diet mice livers had significantly lower % ID/g than those of mice fed with normal chow. Statistics: One-way ANOVA. (e-f) Reported  $T_1$  and %ID/g are the average of two samples (mice) with the standard deviation represented by error bars. \*  $p < 0.05$ , \*\*  $p < 0.01$ , and \*\*\*  $p < 0.001$ .

series of images across multiple rodents, the error included (error bars) reflects both animal-to-animal variation and the signal-to-noise in the system (**Figure 2.6e-f**). The animal-to-animal variation is orders of magnitude larger than that contributed by signal fluctuations and SNR and thus completely defines the reported error. Also, it is thought that calculating relaxation times ( $T_1$ ) is relatively unaffected by changes in signal and SNR over time, and therefore provides a better quantitative metric than either.<sup>89</sup> In previous studies, reduced nanoparticle uptake in liver affected by non-alcoholic fatty liver disease is attributed to reduced uptake by hepatic macrophages, or Kupffer cells.<sup>58</sup> The leading theory to explain reduced uptake involves activation of Kupffer cells by, and increased sensitivity to, lipopolysaccharide endotoxin from gut bacteria due to the accumulation of fatty acids and cholesterol.<sup>117-123</sup> When in this activated state, macrophages demonstrate reduced phagocytosis.<sup>117-123</sup> The average normal chow liver  $T_1$  decrease was 34.3 %, compared to a 20.2 % average  $T_1$  decrease in the high fat diet mice. After imaging, the liver was dissected and analyzed for Gadolinium content by ICP-MS. The livers of the high fat diet mice had a significantly lower percent injected dose of Gadolinium per gram (% ID/g) than the normal chow mice (**Figure 2.6f**).

In rodent models of non-alcoholic fatty liver disease (NAFLD) using the methionine choline-deficient diet, nanoparticle uptake has been demonstrated to decrease throughout the disease progression, with Kupffer cell populations remaining the same or even increasing.<sup>60</sup> The measurable decrease in GONP-12 uptake in a mild NAFLD model presented here, as well as the previously reported decrease in phagocytosis throughout

disease progression, demonstrate the opportunity to fully characterize NAFLD mouse models' disease state through a non-invasive  $T_1$  nanoparticle-based MRI.

#### 2.4. Conclusion

In this study,  $Gd_2O_3$  nanoplates (GONP) were stabilized by an amphiphilic, sulfonated copolymer (PAMPS-LA); these materials demonstrated contrast in  $T_1$  MRI, measured by the relaxivity or  $r_1$ , an order of magnitude larger than commercial  $T_1$  agents. This increase in contrast performance can be attributed in part due to their plate-like morphology and negatively charged surface coatings which together promote spin relaxation processes. *In vitro* studies show that, unlike commercial contrast agents, nanoplates are readily taken up by cells where they retain their contrast in MRI. Further development of GONP for clinical applications will require longer term biodistribution studies to quantify clearance from the liver given the growing awareness of the risks of even small accumulations of Gadolinium in the body.<sup>13, 21, 22, 124</sup> Additionally, while the remarkable chemical stability of the  $Gd_2O_3$  nanoplates and their favorable in-vitro cytotoxicity profiles suggest a positive biosafety profile, their in-vivo toxicity remains to be fully characterized. The performance advantages of these high  $T_1$  contrast materials were exploited in the application of GONP to the detection of non-alcoholic fatty liver disease (NAFLD). These imaging results demonstrate the potential of GONP to differentiate and assess NAFLD of different severity in mice. These highly stable Gadolinium-containing nanocrystals have great promise as  $T_1$  contrast agents for the characterization of non-alcoholic fatty liver disease / non-alcoholic steatohepatitis characterization as well as other applications that require targeted  $T_1$  contrast imaging.



## 2.5. Experimental Section

**Materials:** Syntheses requiring inert atmosphere conditions were carried out using high purity Argon gas (>99%) purchased from TechAir. Ethanol (100%) from Koptec USP and acetone (Certified ACS), hexanes (Certified ACS), DMF (Certified ACS), DEE (Certified ACS), methanol (Certified ACS), methanol (HPLC grade), nitric acid (Certified ACS), and water (HPLC grade) from Fisher Chemical were used as received. The following reagents were received from Sigma-Aldrich: 1-octadecene (ODE, 90%), oleylamine (OAm, 70%), oleic acid (OAc, 90%), Gadolinium(III) nitrate hexahydrate ( $\text{Gd}(\text{NO}_3)_3 \cdot 6\text{H}_2\text{O}$ , 99.99%), 2,2'-azobis(2-methylpropionitrile) (AIBN, 98%), lauryl acrylate (LA, 90%), 2-acrylamido-2-methyl-1-propanesulfonic acid (AMPS, 99%), acrylic acid (AA, anhydrous), poly(ethylene glycol) (PEG, 6 kDa),  $\alpha$ -cyano-4-hydroxycinnamic acid (MALDI-TOF MS), Gadolinium standard for ICP (TraceCERT). The following reagents were received from Cambridge Isotope Laboratories, Inc.: chloroform-d ( $\text{CDCl}_3$ , 99.8%) and deuterium oxide ( $\text{D}_2\text{O}$ , 99.9%). Raw 264.7 cells, DMEM, FBS, PBS, and MTS reagents were obtained from ATCC in Manassas, Virginia. For Gadolinium leaching experiments, bovine calf serum (BCS) was obtained from SAFC (USA sourced) and the DMEM (10x), DPBS (10x), and Gadolinium(III) oxide ( $\geq 99.9\%$ ) were all obtained from Sigma. Unless specified otherwise, all DI water used was purified using a Millipore Milli-Q Water Purification System.

For syntheses requiring photoinitiation, AIBN was further purified as follows: unpurified AIBN dissolved in methanol at 50 °C, solution filtered into ice bath cooled beaker until recrystallization, and AIBN precipitate vacuum filter dried. All other reagents were used without further purification.

**Synthesis and Characterization of Gadolinium Oxide Nanocrystals:** In a three-neck flask (50 mL),  $\text{Gd}(\text{NO}_3)_3 \cdot 6\text{H}_2\text{O}$  (1.8 g, 4 mmol) was dissolved in oleic acid (1.25 – 3.75 mL, 4-12 mmol) and 1-octadecene (12.7 mL, 80 mmol). The reaction mixture was heated to 100 – 110 °C under inert argon atmosphere conditions and medium stir for 5 h to remove low boiling point impurities and generate the clear yellow to light brown Gadolinium oleate precursor. After this period, oleylamine (0 – 4 mL, 0 – 12 mmol) was added, followed by raising the temperature to 290 °C for 3 – 18 h. At this temperature, the Gadolinium oleate complexes decompose, initiating nucleation and nanocrystal growth, generating an opaque brown solution. While still stirring and under argon, solution allowed to cool gradually to room temperature. After cooling, the following purification procedure was done three times: product dissolved in hexanes (5 – 10 mL), transferred into a centrifuge tube (50 mL) and filled with a solution of ethanol and acetone (1:5 vol %), and centrifuged for 10 min at 10,000 rpm. The final precipitate was resuspended in hexanes (10 mL).

Size, morphology, and composition of nanocrystals were characterized with a JEOL 2100 field emission gun TEM operated at 200 kV with a single tilt holder and a Bruker D8 Discovery 2D X-ray diffractometer operating at 40 kV and 40 mA with a Cu tube (1.5413 Å). Diffraction pattern smoothed using Origin Pro 2016. For TEM, samples were diluted in hexanes until almost colorless and then drop-cast onto Formvar/Carbon coated 400 mesh, copper grids (approximate grid hole size: 42µm, Ted Pella). For XRD, samples were highly concentrated, drop-cast onto glass slides, and heat-dried.

**Synthesis and Characterization of Amphiphilic Polymer (PAMPS-LA):** To make PAMPS-LA (Figure S3), AMPS (0.5175 g, 10 mmol) was dissolved in LA (0.135 mL, 2 mmol) and

DMF (3 mL, 155 mmol) in a glass scintillation vial (20 mL). Once completely dissolved, AIBN (3.75 mg, 0.091 mmol) was added as the photoinitiator. The resulting solution was polymerized inside a UV reactor (Luzchem, 253 nm) for 4 h.

Polymer synthesis was confirmed using a Thermo Nicolet NEXUS 670 FT-IR with a Mercury Cadmium Telluride (MCT) detector cooled with liquid nitrogen and a Bruker high field NMR spectrometer (400 MHz) with z-BBFO probe. For NMR, PAMPS-LA (10 – 20 mg) was mixed with D<sub>2</sub>O (700 µL) and pipetted into an NMR tube for analysis. Monomers (10 – 20 mg), AMPS and LA, were mixed with D<sub>2</sub>O (700 µL) and CDCl<sub>3</sub> (700 µL) and pipetted into NMR tube for analysis, respectively. NMR spectra were analyzed using TopSpin software.

PAMPS-LA number averaged molecular weight was measured using MALDI-TOF MS. For MS analysis, a 1:1 by volume mixture was made with a solution of PAMPS-LA in ethanol (30 – 50 mg mL<sup>-1</sup>) and a saturated solution of  $\alpha$ -cyano-4-hydroxycinnamic acid (MALDI matrix) in ethanol.

**Surface Modification of Gadolinium Oxide Nanocrystals:** To achieve dispersion of the nanocrystals in an aqueous phase, PAMPS-LA was used as an encapsulating agent. A 1:1 by volume mixture of a GONP solution in DEE (25 mg mL<sup>-1</sup>) and a solution of PAMPS-LA in DMF (80 – 120 mg mL<sup>-1</sup>) were added to a glass scintillation vial (20 ml). Both solutions were probe sonicated (Hielscher, UP100H) for 5 min prior to preparing the 1:1 mixture. The mixture was stirred vigorously for 12 h (cap on) to allow encapsulation to occur. After that time, DI water (10 mL) was added to the mixture and stirred vigorously for another 12 h (cap off) to evaporate DMF and DEE and allow the PAMPS-LA encapsulated GONP to transfer into water. After centrifuging the sample for 30 min at 6000 rpm and discarding

the precipitate to remove uncoated GONP, the following purification procedure was done three times: separated sample equally between eight ultracentrifuge bottles (26 mL, polycarbonate, Beckman Coulter), filled each bottle with DI water, centrifuged for 1 h at 45,000 rpm using an ultracentrifuge (Beckman Coulter, Optima L-90K), gently extracted supernatant liquid, and resuspended precipitate in DI water. Finally, purified GONP were probe sonicated for 5 minutes and filtered using 0.2  $\mu\text{m}$  polyethersulfone (PES) membrane filters (Watman, Pauradisk 25 mm syringe filter PES, non-sterile).

Nanocrystal encapsulation was assessed using a Thermo Nicolet NEXUS 670 FT-IR with a Mercury Cadmium Telluride (MCT) detector cooled with liquid nitrogen. Nanocrystal colloidal stability was assessed using hydrodynamic diameter (based on intensity-weighted measurements; Z-average) and zeta potential data obtain using a Malvern Zen6300 Zetasizer NanoS equipped with a 633 nm laser.

**Relaxivity Measurement and Calculations:** The concentration of  $\text{Gd}^{3+}$  was measured using a Perkin Elmer Nexion 300 inductively coupled optical mass spectrometer (ICP-MS) equipped with an autosampler. The sample preparation started with digesting nanocrystals (100  $\mu\text{L}$ ) in nitric acid (70 %, 500  $\mu\text{L}$ , trace metal basis) on a hotplate at  $\sim 90$   $^{\circ}\text{C}$  for 2 h. Acidified solutions were filtered and diluted to 10 mL with deionized water using a 0.2  $\mu\text{m}$  PES syringe filter. Calibration curve samples were prepared using dilutions of Gadolinium standard solution (0.5, 1.0, 2.5, 5.0, and 10.0  $\text{mg mL}^{-1}$ ) for ICP (1002 ppm in 2% nitric acid) using nitric acid solution (2%). GONP sample solutions (0.5 to 2 mM  $\text{Gd}^{3+}$ ) were prepared for relaxometric analysis.

$T_1$  and  $T_2$  measurements were carried out on a MR relaxometer (NMR analyzer mq60, Bruker, Billerica, MA) at 1.4 T, and on 3.0 T and 9.4 T Bruker Biospec MRI scanners (Bruker BioSpin, Billerica, MA) with varying TR and TE values. The inverse of relaxation time ( $1/T_1$  or  $1/T_2$ ,  $s^{-1}$ ) was plotted as a function of GONP sample  $Gd^{3+}$  concentration (mM). A linear regression was made using the GONP sample concentration data points and the ionic relaxivities per  $Gd^{3+}$  (mM- $Gd^{-1}s^{-1}$ ) were extracted from its slope. Mass (M) relaxivities (mL  $mg^{-1} s^{-1}$ ) were calculated from the ionic relaxivities ( $r_n$ ,  $n = 1$  or 2):

$$r_n/M \left( \frac{mL}{mg \text{ Gd}2O3 * s} \right) = r_n \left( \frac{L}{mmol \text{ Gd} * s} \right) \times \frac{2 \text{ mmol Gd}}{1 \text{ mmol Gd}2O3} \times \frac{1 \text{ mmol Gd}2O3}{362.49 \text{ mg Gd}2O3} \times \frac{1000 \text{ mL}}{1 \text{ L}}$$

Assuming a circular GONP of dimensions 12.0 x 1.1 nm, the per CA relaxivity (mM- $CA^{-1}s^{-1}$ ) was calculated as follows:

$$M_{GONP} = \left( \pi \times \left( \frac{1.2 \times 10^{-6} \text{ cm}}{2} \right)^2 \times 1.1 \times 10^{-7} \text{ cm} \right) \times \frac{7070 \text{ mg Gd}2O3}{1 \text{ mL}} \times \frac{1 \text{ g}}{1000 \text{ mg}} = \frac{8.80 \times 10^{-19} \text{ g Gd}2O3}{1 \text{ GONP}}$$

$$r_1/NP \left( \frac{L}{mmol \text{ GONP} * s} \right) = r_1 \left( \frac{L}{mmol \text{ Gd} * s} \right) \times \frac{2 \text{ mmol Gd}}{1 \text{ mmol Gd}2O3} \times \frac{1 \text{ mmol Gd}2O3}{362.49 \text{ mg Gd}2O3} \times \frac{1000 \text{ mg Gd}2O3}{1 \text{ g Gd}2O3} \times \times$$

$$\frac{6.022 \times 10^{23} \text{ GONP}}{1 \text{ mol GONP}} \times \frac{1 \text{ mol GONP}}{1000 \text{ mmol GONP}}$$

**Biodistribution and Pharmacokinetics:** All animal work for this study was performed in Association for Assessment and Accreditation of Laboratory Animal Care (AAALAC) accredited facilities, and the Institutional Animal Care and Use Committee approved all procedures. To accomplish biodistribution studies, six C57BL/6-J immune-competent mice (6 months old) were injected with Gadolinium oxide nanocrystals (100  $\mu$ L of 2.5 mM) in PBS *via* tail vein. Mice were sacrificed by cervical dislocation and tissue was obtained and weighed for measurement by ICP-MS (Perkin Elmer Nexion 300) at 24 h post injection.

Organ weights are as follows: lungs (0.5285 g), heart (0.598 g), liver (1.5360 g), spleen (0.2151 g), and kidneys (0.3578 g). For pharmacokinetic studies, blood (20  $\mu$ L) was drawn at time intervals up to 4 hours post injection and stored in glass vials for ICP-MS analysis.

**Cell Labeling:** Cell labeling was conducted in preparation for internalization, MRI, and cell viability studies. First, macrophage (Raw 264.7) cells were cultured over a certain amount of time in DMEM with penicillin (1 %) and FBS (10 %). For the purposes of MR imaging, cell pellets of 6 million cells or larger are required; therefore, cells were separated into aliquots of at least  $6 \times 10^6$  cells and seeded into 6-well cell culture plates. Cell labeling was carried out by adding Gadolinium oxide nanocrystals or Magnevist (0 – 100  $\mu$ M) for 24 or 2 h at 37 °C and CO<sub>2</sub> (5 %). After Trypsinization, cells were washed 2 times in PBS and then pelleted a third time in PCR tubes for imaging or ICP-MS experiments.

**Cell Viability Assay:** An MTS toxicity assay was performed in a 96-well plate for Raw 264.7 macrophages, and each dataset was measured in triplicate. When preparing the assay after detachment from the original culture flask, cells were plated in the first three rows of a 96-well plate (seeding density:  $2 \times 10^4$ /well, 100  $\mu$ L). The fourth 96 row was filled with 100  $\mu$ L media without cells to act as the blank. In rows 1 to 3, 20  $\mu$ L of nanocrystals with various concentrations was added from column 3 to 11 (this step was repeated in exactly the same manner for the 2nd and 3rd rows). Instead of nanocrystals, the 1st column was filled with 20  $\mu$ L of media and the 2nd column was filled with 20  $\mu$ L of PBS (negative control). The last column (12th) was filled with 20  $\mu$ L of ethanol (positive control) to produce dead cells. Rows 5-9 were filled in the same way, but with different concentrations of nanocrystals.

The prepared 96-well plates were placed in the incubator for 24 h. After the incubation period, the solutions were removed from all wells using glass pipettes attached to the aspiration tube and fresh pre-warmed media (100  $\mu$ L), and MTS reagent (20  $\mu$ L) was subsequently added to all wells. After another 1h incubation period, absorbance of each well at 490 nm was measured using a microplate reader (TECAN Infinite M1000).

To calculate cell viability, first the average absorbance of blank wells was subtracted from the negative control wells, nanocrystal-containing wells, and positive control wells to remove the absorbance of media or nanocrystals. Then the average absorbance of all wells (except the blank wells) was divided by the average absorbance of the negative control. In this study, all negative control cells were considered viable cells where cell viability is the percentage of the resulting value.

**Live-Dead Assay:** For the live-dead cytotoxicity assay, cell media were aspirated after HDF and Raw 264.7 cells were incubated with nanocrystals for the desired period of time. Cells were then washed three times with PBS to remove any media residue. The working solution of dyes was prepared fresh by diluting the assay dyes in PBS with the final concentration of 2  $\mu$ M of calcein-AM dye and 4  $\mu$ M of ethidium homodimer-1 (EthD-1). To achieve these concentrations, a 20  $\mu$ L of 2 mM EthD-1 stock solution was first added to 10 mL of PBS and vortexed to ensure complete mixing (with a final concentration of 4  $\mu$ M). Second, 5  $\mu$ L of 4 mM calcein-AM was added to the mixture to achieve the final concentration of 2  $\mu$ M of calcein-AM. These working solutions were then added directly to the cells (1 mL in each well on the 6-well plate). Cells were incubated for 30-45 minutes

at room temperature before observing them under the fluorescence microscope (EVOS fluorescence microscope).

**Wound-Healing Assay:** For the wound-healing assay, HDF cells were seeded and cultured in the marked 6-well plate until they became nearly confluent (80-90%). Media was aspirated, and then the surface of the cells was scratched using a 100  $\mu$ L pipette tip moving perpendicular to the line marked at the back of the plate (Figure 2.15). Next, the cells were washed gently with PBS to remove the dead scratched cells, and pre-warmed media containing different concentrations of nanocrystals were added. After certain time intervals (0, 2, 6, 15, 24, and 48h), wounds were inspected microscopically (4X and 10X magnifications) with an orientation at the cross point of the wound and the marked line.

**Mouse Model for Non-Alcoholic Fatty Liver Disease Application:** A mouse model was used to study the application of the nanocrystals in MR imaging to assess for non-alcoholic fatty liver disease. Wild-type immune-competent mice on background C57B6/J were fed a 60 % kcal fat diet for seven months (D12492, Research Diets, New Brunswick, NJ, USA). This mouse model is beginning to exhibit elevated alanine aminotransferase and aspartate aminotransferase levels, which is often used as an indicator of onset NAFLD.

For this experiment, mice were injected with Gadolinium oxide nanocrystals (11 nmol g<sup>-1</sup>, GONP-12) *via* tail vein from a stock solution containing Gd<sup>3+</sup> in DI water (7.6 mM). Controls were left un-injected. Four hours after administration, mice were sacrificed by cervical dislocation and immediately imaged in the MRI. Mice were maintained at 37 °C by rectal temperature probe and heated air circulation.



**Ex vivo MR Imaging:** *Ex vivo* MR imaging was performed on the mice after they were sacrificed. Images were acquired on a 9.4 T Bruker AvanceBiospec Spectrometer, 21-cm bore horizontal scanner with a 72 mm volume resonator (Bruker BioSpin, Billerica, MA) with Paravision 5.1 software (Bruker BioSpin, Billerica, MA). Mice were imaged using a Rapid Acquisition with Refocused Echoes protocol with Variable Acquisition repetition time (RAREVTR) TR = 30.984 – 15000 ms (5 images), TE = 6.57 ms, RF = 4, FOV = 3 × 3 cm, matrix size = 128 × 128, 11 m, 48 s and 399 ms. Beforehand, acquisition on a FLASH tripilot was run for placement. Liver T<sub>1</sub> was measured in the sagittal plane, and slices were aligned with the right kidney to ensure consistent measurement. Liver was masked out and analyzed for T1 time in Paravision 5.1. T1 calculations were done using the built-in tools in Paravision 5.1.

**Gadolinium Leaching:** Dialysis experiments coupled with ICP-AES were used to determine the amount of Gd<sup>3+</sup> leaching from Gd-containing samples (GONP, bulk Gd<sub>2</sub>O<sub>3</sub>, or Gd(NO<sub>3</sub>)<sub>3</sub>) dispersed in a variety of biologically relevant media (water, pH 4 – 4.5, pH 2, PBS, DPBS, or BCS) over time (3, 7, 14, and 20 days). Stock sample Gd<sup>3+</sup> concentrations were approximately 3 – 4 mM for GONP, 50 mM for bulk Gd<sub>2</sub>O<sub>3</sub>, and 5 mM for Gd(NO<sub>3</sub>)<sub>3</sub>. Spectra/Por 6 dialysis membranes (pre-wetted RC tubing, 1 kDa MWCO) were used in all dialysis experiments. A Thermo Scientific iCAP 7400 DUO inductively coupled plasma atomic emission spectrometer was used to measure Gd<sup>3+</sup> concentrations of samples, tubing, and dialysate. Samples were digested with tubing in a Milestone Ultrawave SRC microwave digestion system in preparation for ICP analysis. Calibration curve standards were prepared using 0.044, 0.082, 0.248, 0.490, 0.992, 2.493, 5.012, 9.267, and 49.408

ppm dilutions of a Gadolinium standard solution for ICP (1002 ppm  $Gd^{3+}$  in 2% nitric acid) using 2% nitric acid solution. The following experiments always had total mass recoveries of more than 85 %, except in the case of Nano  $Gd_2O_3$  in BCS.

For 3-day dialysis experiments, approximately 1 mL of sample (GONP, bulk  $Gd_2O_3$ , or  $Gd(NO_3)_2$ ) was pipetted into a 3 – 4-inch section of dialysis tubing, sealed with clips, and placed in a beaker of medium (water, pH 4 – 4.5, pH 2, PBS, DMEM, or BCS) on continuous stir for three days. Samples were often diluted (99/100 or 9/10) to achieve the same media concentration as the dialysate without reducing the  $Gd^{3+}$  concentration too much. Also, in the case of the bulk powder homogeneous solution could not be prepared, and micrograms of material weighed on an analytical balance were introduced in the media with vortexing. The concentration of these bulk powders was as a result ten times larger than that of the nanoparticles and Gadolinium salt. Experiments using BCS required a 1/10 dilution of samples to maintain a BCS concentration as close to 100 % as possible (90 %). For water, pH 4 – 4.5, pH 2, and PBS, the volume ratio of sample to dialysate was 1:1000. For BCS experiments the volume ratio of sample to dialysate was 1:100. After three days, dialysate and samples (with tubing) were collected, digested, and prepared for ICP analysis. Experiments performed in triplicate unless noted otherwise.

For time-dependent dialysis experiments, approximately 0.9 mL of sample (GONP, bulk  $Gd_2O_3$ , and  $Gd(NO_3)_3$ ) was pipetted into a 3 – 4-inch section of dialysis tubing, sealed with clips, and placed in a beaker of medium (water, pH 4 – 4.5, pH 2, or PBS) for 20 days. Beakers were stirred twice daily, and 10 mL of dialysate was collected at 3, 7, 14, and 20 days for ICP analysis. Some samples were diluted (99/100 or 9/10) to achieve the same

media concentration as the dialysate without reducing the  $\text{Gd}^{3+}$  concentration too much. After 20 days, samples (with tubing) were collected, digested, and prepared for ICP analysis.

**Statistical Analysis:** Electron microscopy was used for dimensional measurement (Figures 1, S1, and S2). TEM images of nanoplate samples were saved as TIF and Gatan DigitalMicrograph Image Document 3 files. For each sample, the dimensions (face length and width) of a minimum of 200 particles (Figures S1 and S2) or 500 particles (Figure 1) were manually measured using the image processing software ImageJ. The average (reported throughout and in Figures 1, S1, and S2 and Table 1), standard deviation (reported throughout and as error bars in Figures S1 and S2), and the margin of error based on a 95 % CI and resolution limit of 0.23 nm (Figure 1) of the nanoplate dimensions are reported.

Relaxivity was found as described previously in experimental section. The inverse of longitudinal and transverse relaxation times ( $1/T_1$  or  $1/T_2$ ,  $\text{s}^{-1}$ ) were plotted as a function of GONP sample  $\text{Gd}^{3+}$  concentration (mM). A linear regression of each data set was made and ionic relaxivities per  $\text{Gd}^{3+}$  ( $\text{mM-Gd}^{-1}\text{s}^{-1}$ ) were extracted from its slope. The reported average relaxivity (or individual  $T_1$ ) and standard deviation (reported with mean throughout and as error bars) were calculated from the results of three independent experiments (Figures 3, 5, 6, S5, S6, S7 and Tables 1 and S1). Quantification of  $\text{Gd}^{3+}$  content in solutions, organs and nanoparticles using ICP-MS were done using calibration curves as discussed previously in the experimental section. All measurements were performed in triplicate except for the biodistribution, pharmacokinetic, and *ex-vivo*  $T_1$ -

weighted imaging experiments. The sample sizes for the biodistribution and pharmacokinetic experiments were six (Figure 4). The sample sizes for the *ex-vivo*  $T_1$ -weighted images were two (Figure 6). Gadolinium concentrations and % ID are reported as the average with the standard deviation as error bars (Figures 4, 5, and S7).

DLS measurements were performed in triplicate. Hydrodynamic size (based on intensity-weighted measurements; Z-average) and zeta-potential are reported as the average with the standard deviation as error bars (Figure 2).

Student's t-test was used to analyze the significance of differences in liver  $T_1$  and  $Gd^{3+}$  content for mice with fatty and normal diets (Figure 6). The significance of difference becomes greater with decreasing p-value (significant difference,  $p < 0.05$ ; very significant difference,  $p < 0.01$ ; extremely significant difference  $p < 0.001$ ).

All statistical analyses performed in Microsoft Office Excel and or OriginPro.

## 2.6. Supporting Information

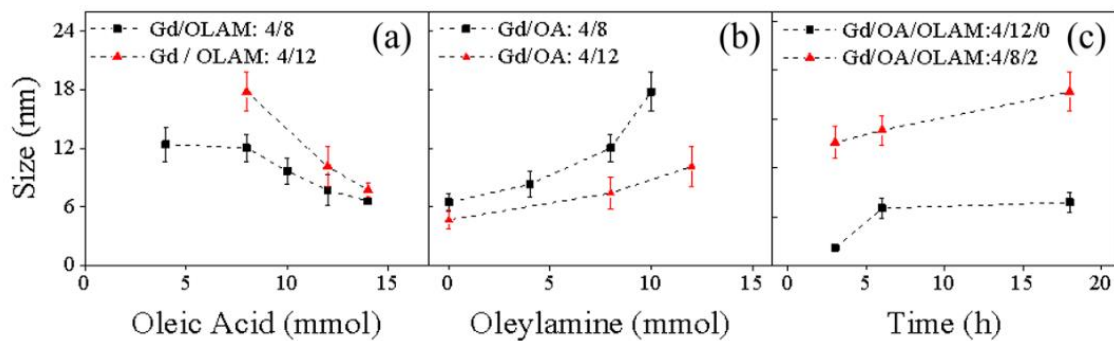


**Figure S2.1 Reaction condition size dependence.** Size control of GON by varying amount of (a) oleic acid, (b) oleylamine, and (c) time at different mol ratios of Gadolinium (III) to oleylamine (Gd/OLAM: 4/8 and 4/12), Gadolinium (III) to oleic acid (Gd/OA: 4/8 and 4/12), and Gadolinium (III) to oleic acid to oleylamine (Gd/OA/OLAM: 4/12/0 and 4/8/0), respectively. Reported plate face sizes are the average of three independent measurements with the standard deviation represented by error bars.

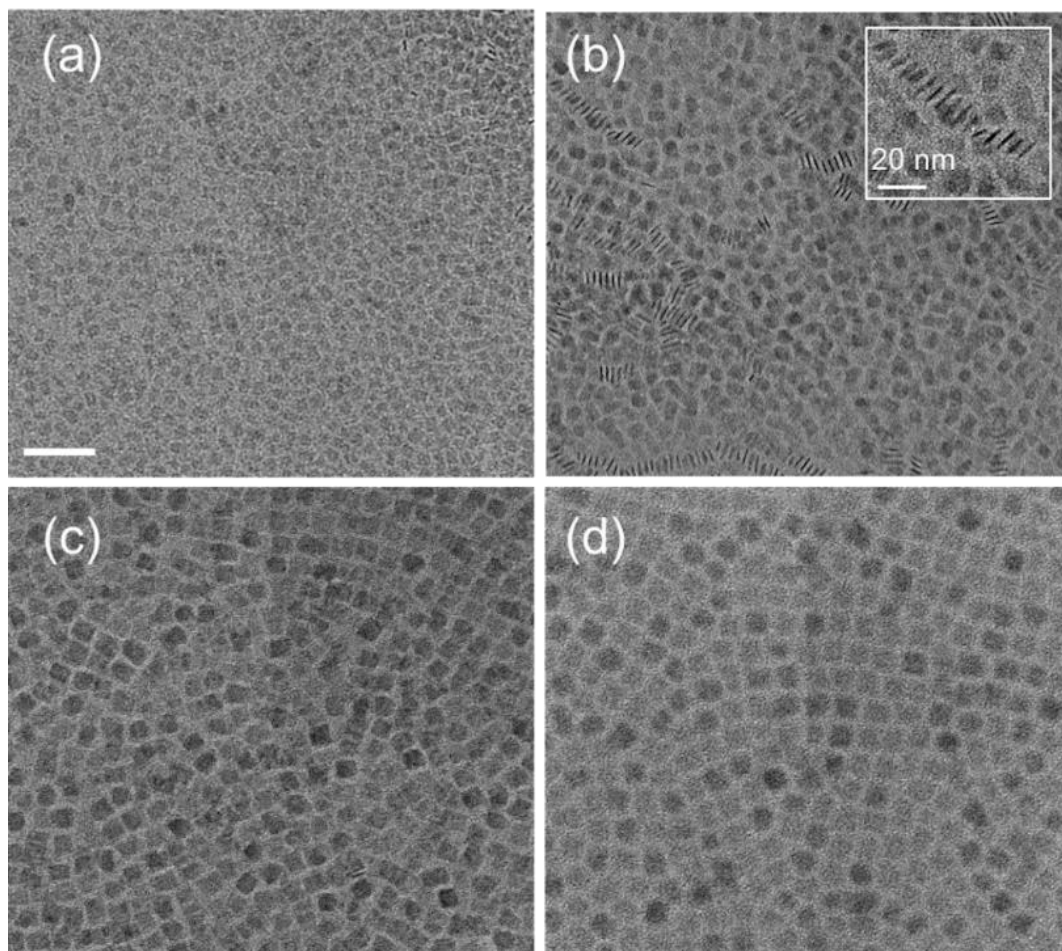


**Figure S2.2 TEM images of GONP.** TEM images of monodisperse GONP with dimensions of (a)  $6.6 \pm 0.3$ , (b)  $9.7 \pm 1.3$ , (c)  $12.0 \pm 1.3$ , (d)  $15.6 \pm 1.9$  nm formed after thermal decomposition (290 oC) of Gadolinium oleate in a solution of oleic acid and oleylamine in 1-octadecene solvent. The inset figure further illustrates the stacking phenomenon that occurs because of face-to-face interactions of GONP.

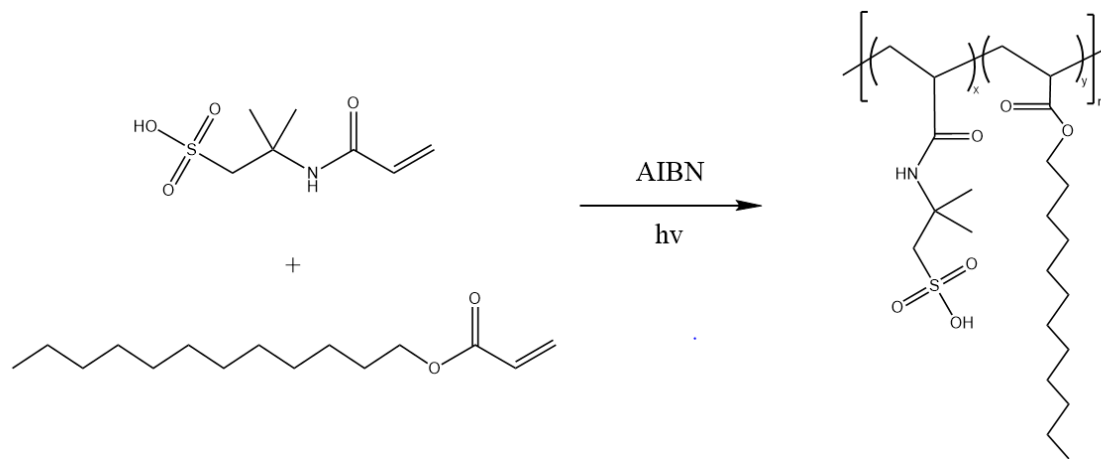


**Figure S2.3 Chemical structure of PAMPS-LA.** Schematic representation of PAMPS-LA, its monomers, and synthesis.

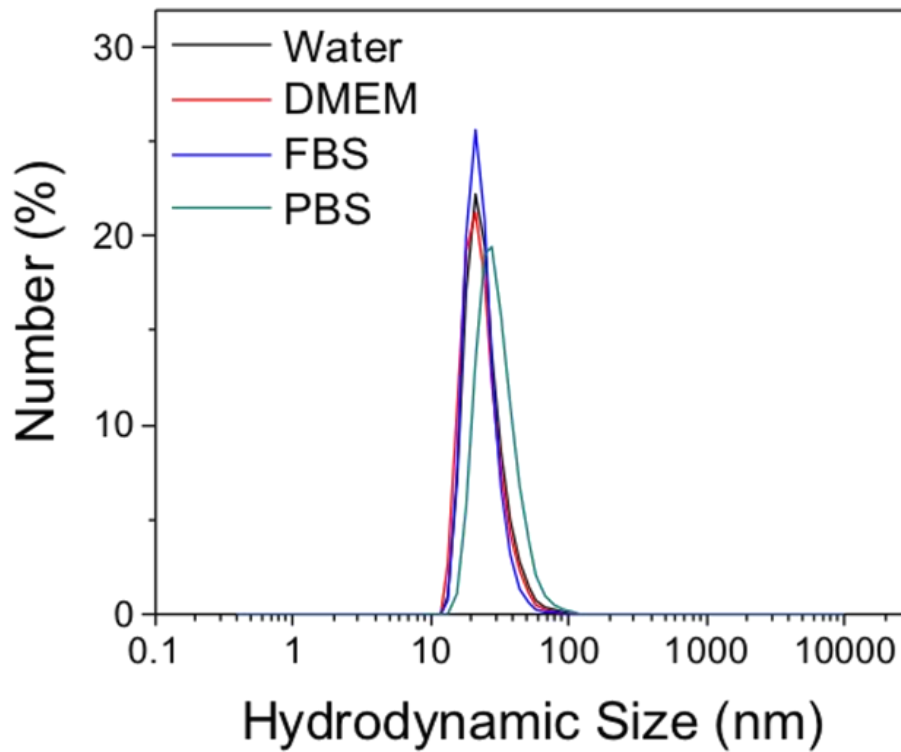


**Figure S2.4 GONP sample uniformity.** DLS data providing hydrodynamic size distributions of GONP-12 in a variety of biologically relevant dispersion media (water, DMEM, FBS, and PBS).



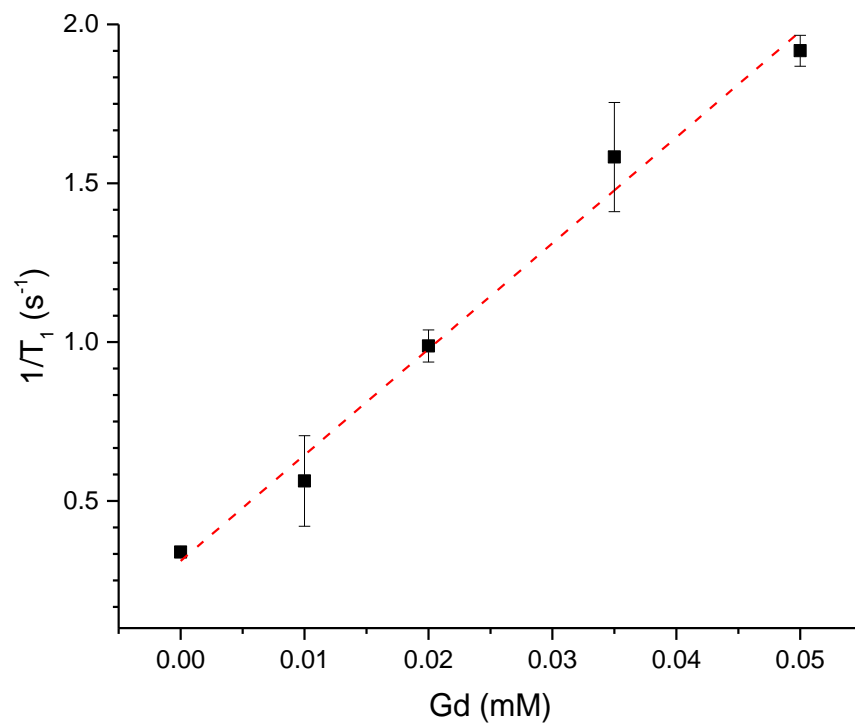


**Figure S2.5 High field strength T1 relaxation plot of GONP.** Longitudinal relaxation rates as a function of Gadolinium concentration for PAMPS-LA-GONP compared to Magnevist at 9.4 T. Reported T1 are the average of three independent measurements with the standard deviation represented by error bars.

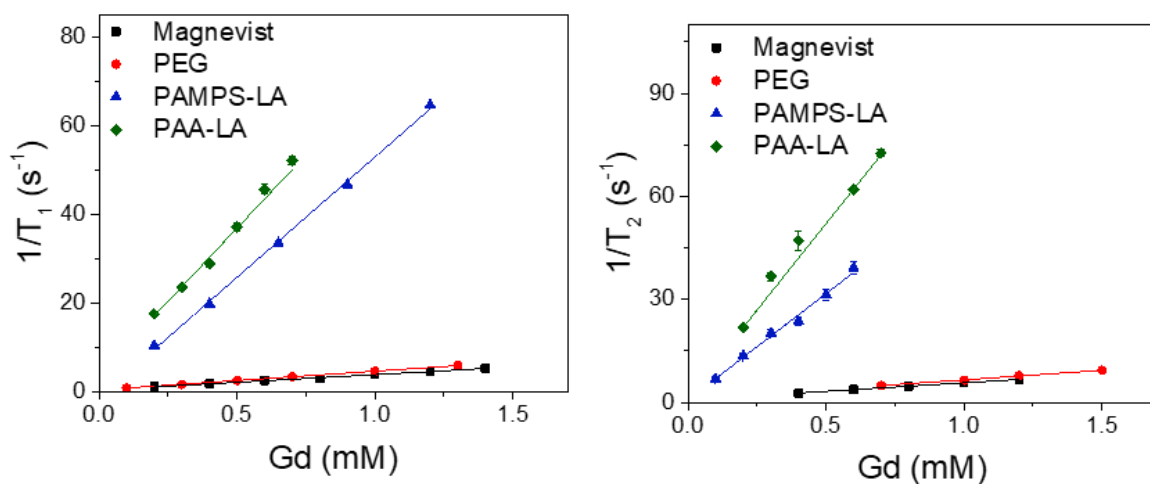


**Figure S2.6 T1 relaxivity of Magnevist and GONP with different surface coatings.** (a) Longitudinal and (b) transverse relaxation rates as a function of Gd<sup>3+</sup> concentration at 1.4 T. All samples are of similar hydrodynamic size (~ 25 – 45 nm). Reported T1 are the average of three independent measurements with the standard deviation represented by error bars.

**Table S2.1** Properties of Magnevist and GONP with various surface coatings at 1.4 T.

Contrast Agent	Surface Coating	$r_1/[\text{Gd}^{3+}]$ [ $\text{mM}^{-1}\text{s}^{-1}$ ]	$r_2/[\text{Gd}^{3+}]$ [ $\text{mM}^{-1}\text{s}^{-1}$ ]	$r_2/r_1$
<b>Magnevist</b>	-	$3.4 \pm 0.1$	$4.9 \pm 0.2$	1.4
<b>GONP</b>	PEG	$4.2 \pm 0.03$	$45.5 \pm 0.1$	1.3
<b>GONP</b>	PAMPS-LA	$54.1 \pm 1.1$	$61.7 \pm 2.5$	1.1
<b>GONP</b>	PAA-LA	$65.8 \pm 2.94$	$100.5 \pm 1.5$	1.5

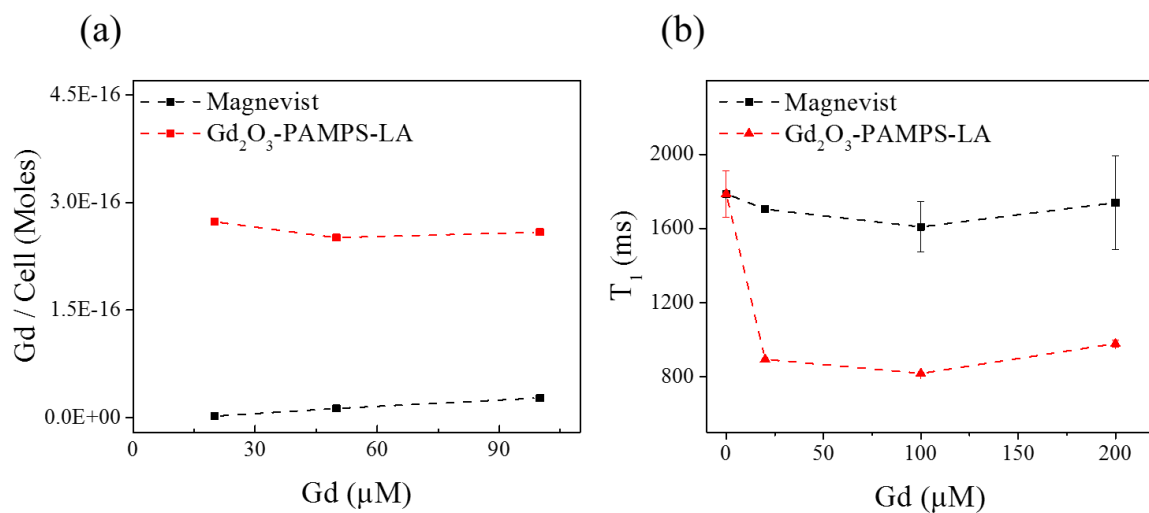


**Figure S2.7 Cell uptake capacity of GONP.** Cellular uptake capacity of PAMPS-LA-GONP and Magnevist measured by (a) Gd<sup>3+</sup> per cell and (b) T<sub>1</sub> relaxation times of cells ((seeding density: 6x10<sup>6</sup>/well)) incubated with GONP-12 or Magnevist at Gd<sup>3+</sup> concentrations between 20 and 100 μM for 2 h. All reported values are the average of triplicate measurements with standard deviation represented by error bars.

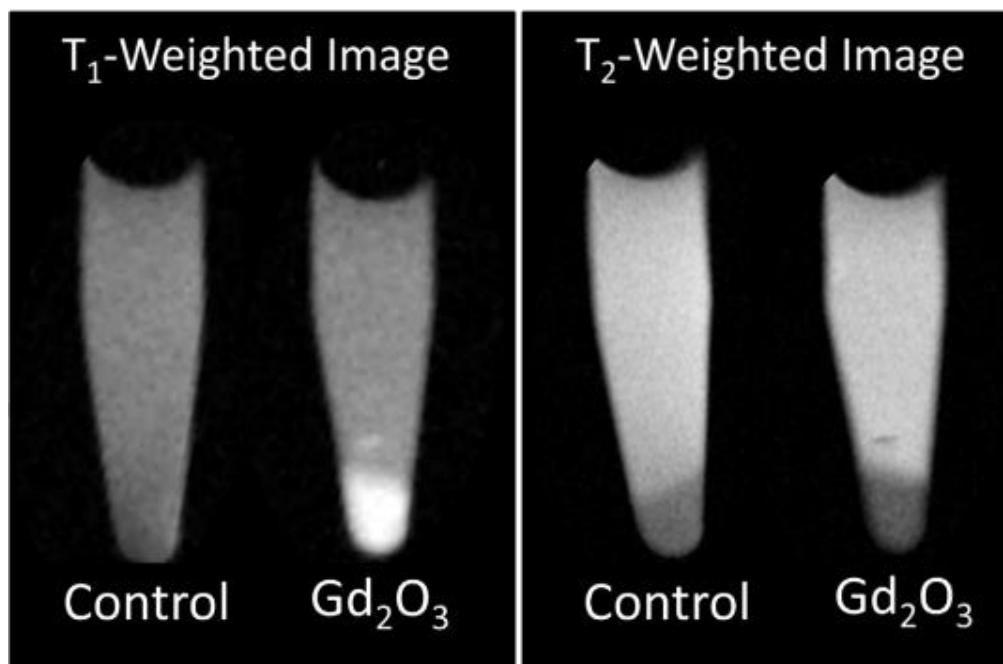


**Figure S2.8 T1- and T2-weighted MR phantom images.** T1- and T2-weighted MR images of macrophage cells labeled with GONP-12 compared to control samples without GONP.

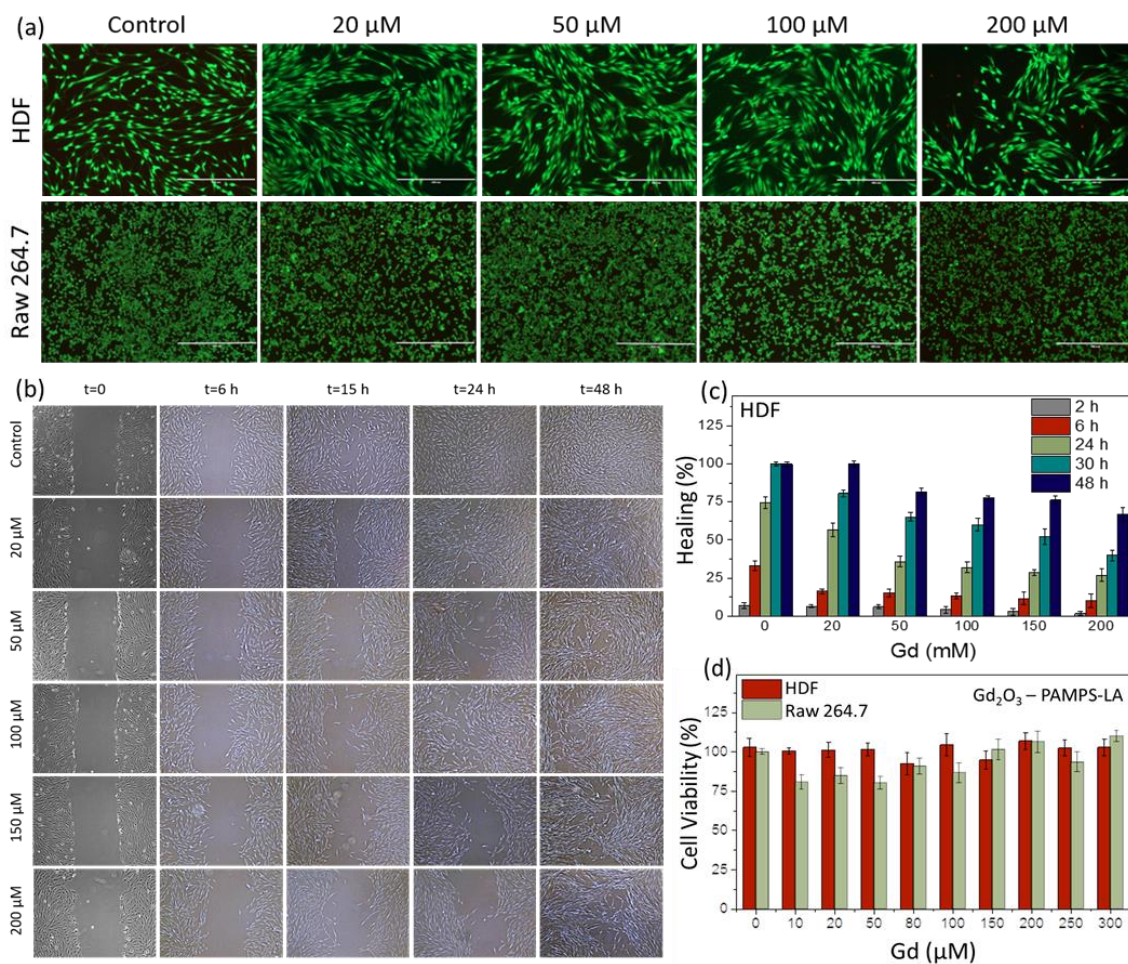


**Figure S2.9 In vitro cytotoxicity studies.** (A) Live-dead assay fluorescent images from HDF and Raw 264.7 cells incubated with different concentrations of PAMPS-LA coated nanoplates (scale bars = 400 nm). (b) Wound-healing assay optical microscopy images of scratched HDF cell culture with different concentrations of PAMPS-LA coated nanoplates up to 48 hr. (c) Percent reduction of the distance between HDF cells on the leading edge of the scratch in the wound-healing assay. (d) Viable percentage of HDF and macrophage (Raw 264.7) cells after incubation with PAMPS-LA coated nanoplates evaluated by an MTS assay.

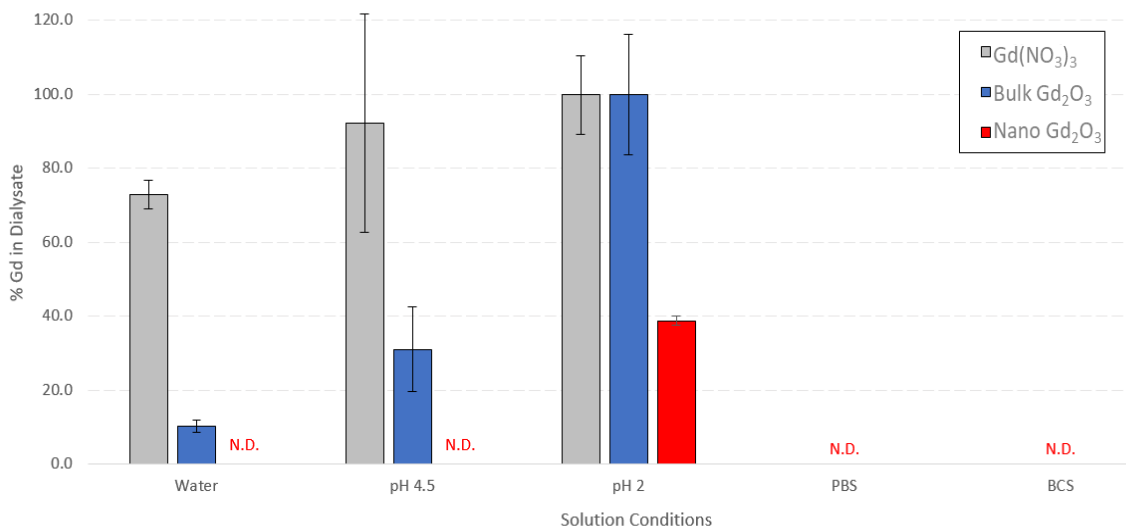


**Figure S2.10 Three-day Gadolinium release experiment.** For these experiments, 1 mL of sample (Nano Gd<sub>2</sub>O<sub>3</sub>, bulk Gd<sub>2</sub>O<sub>3</sub>, and Gd(NO<sub>3</sub>)<sub>3</sub>) was placed in a 3 – 4-inch section of dialysis tubing (1 kDa MWCO), sealed with clips, and set in 1 L of the indicated solution (water, pH 4.5, pH 2, phosphate buffered saline (PBS) or bovine calf serum (BCS)) for 3 days under continuous stirring. Samples were measured in triplicate and error bars are the replicate standard deviation. “N.D.” refers to “not detectable” defined by the ICP-AES instrument as below the limit of detection found from multiplying the ratio of the standard deviation of each measurement to the slope (sensitivity) of the calibration curve.<sup>125</sup> Given that roughly 600 micrograms of Gadolinium were in the sample, we can conclude that at least 97% of the GONP remained in nanoparticle form for those experiments labelled “N.D.”.

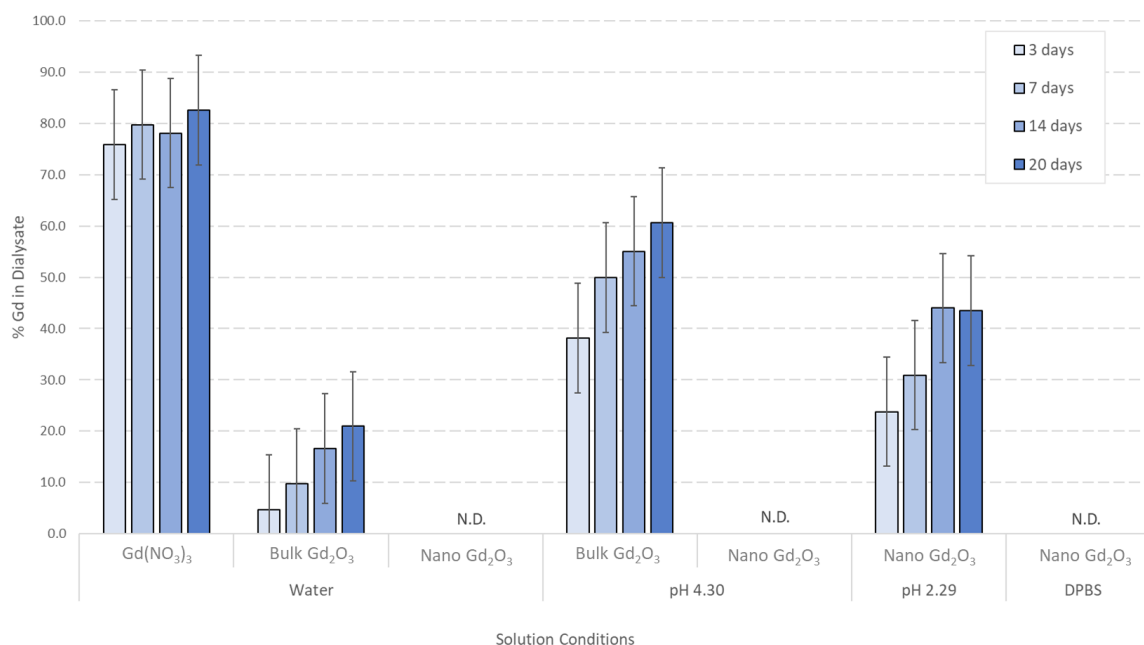


**Figure S2.11 Twenty-day Gadolinium release experiments.** For these experiments, 0.9 mL of sample (Nano Gd<sub>2</sub>O<sub>3</sub>, bulk Gd<sub>2</sub>O<sub>3</sub>, and Gd(NO<sub>3</sub>)<sub>3</sub>) was pipetted into a 3 – 4-inch section of dialysis tubing (1 kDa MWCO), sealed with clips, and placed in 900 mL of the indicated solution (water, pH 4.5, pH 2, or DPBS) for 20 days. Dialysates were stirred twice daily, and 10 mL of dialysate was collected at 3, 7, 14, and 20 days for ICP analysis. The reported error bars reflect the average replicate error from the three-day experiments (Figure S10). “N.D.” indicates that the Gadolinium measured by ICP-MS was below the instrumentally defined detection limit of 12.7 ppb which was determined from a separate calibration of known Gadolinium standards. Given that roughly 600 micrograms of Gadolinium were in the sample, we can conclude that at least 97% of the GONP remained in nanoparticle form.



## 2.7. References

1. Cao, Y.; Xu, L. J.; Kuang, Y.; Xiong, D. S.; Pei, R. J., Gadolinium-based nanoscale MRI contrast agents for tumor imaging. *J. Mater. Chem. B* **2017**, *5* (19), 3431-3461.
2. Faucher, L.; Tremblay, M.; Lagueux, J.; Gossuin, Y.; Fortin, M. A., Rapid Synthesis of PEGylated Ultrasmall Gadolinium Oxide Nanoparticles for Cell Labeling and Tracking with MRI. *ACS Appl. Mater. Interfaces* **2012**, *4* (9), 4506-4515.
3. Wei, H.; Bruns, O. T.; Kaul, M. G.; Hansen, E. C.; Barch, M.; Wisniowska, A.; Chen, O.; Chen, Y.; Li, N.; Okada, S.; Cordero, J. M.; Heine, M.; Farrar, C. T.; Montana, D. M.; Adam, G.; Ittrich, H.; Jasanoff, A.; Nielsen, P.; Bawendi, M. G., Exceedingly small iron oxide nanoparticles as positive MRI contrast agents. *Proc. Natl. Acad. Sci. U. S. A.* **2017**, *114* (9), 2325-2330.
4. Lauffer, R. B., PARAMAGNETIC METAL-COMPLEXES AS WATER PROTON RELAXATION AGENTS FOR NMR IMAGING - THEORY AND DESIGN. *Chem. Rev.* **1987**, *87* (5), 901-927.
5. Ni, D. L.; Bu, W. B.; Ehlerding, E. B.; Cai, W. B.; Shi, J. L., Engineering of inorganic nanoparticles as magnetic resonance imaging contrast agents. *Chem. Soc. Rev.* **2017**, *46* (23), 7438-7468.
6. Li, Y.; Xu, D.; Chan, H.-N.; Poon, C.-Y.; Ho, S.-L.; Li, H.-W.; Wong, M. S., Dual-Modal NIR-Fluorophore Conjugated Magnetic Nanoparticle for Imaging Amyloid- $\beta$  Species In Vivo. *Small* **2018**, *14* (28), 1800901.
7. Faucher, L.; Guay-Begin, A. A.; Lagueux, J.; Cote, M. F.; Petitclerc, E.; Fortin, M. A., Ultra-small gadolinium oxide nanoparticles to image brain cancer cells in vivo with MRI. *Contrast Media Mol. Imaging* **2011**, *6* (4), 209-218.
8. Wang, Y. X. J.; Idee, J. M., A comprehensive literatures update of clinical researches of superparamagnetic resonance iron oxide nanoparticles for magnetic resonance imaging. *Quant. Imaging. Med. Surg.* **2017**, *7* (1), 88-122.
9. Jeon, M.; Halbert, M. V.; Stephen, Z. R.; Zhang, M., Iron Oxide Nanoparticles as T1 Contrast Agents for Magnetic Resonance Imaging: Fundamentals, Challenges, Applications, and Prospectives. *Adv. Mater.* **2020**, 1-18.
10. Wahsner, J.; Gale, E. M.; Rodriguez-Rodriguez, A.; Caravan, P., Chemistry of MRI Contrast Agents: Current Challenges and New Frontiers. *Chem. Rev.* **2019**, *119* (2), 957-1057.
11. Caravan, P.; Ellison, J. J.; McMurry, T. J.; Lauffer, R. B., Gadolinium(III) chelates as MRI contrast agents: Structure, dynamics, and applications. *Chem. Rev.* **1999**, *99* (9), 2293-2352.
12. Hagberg, G. E.; Scheffler, K., Effect of  $r(1)$  and  $r(2)$  relaxivity of gadolinium-based contrast agents on the T-1-weighted MR signal at increasing magnetic field strengths. *Contrast Media Mol. Imaging* **2013**, *8* (6), 456-465.

13. Fraum, T. J.; Ludwig, D. R.; Bashir, M. R.; Fowler, K. J., Gadolinium-based contrast agents: A comprehensive risk assessment. *J. Magn. Reson. Imaging* **2017**, *46* (2), 338-353.
14. Caravan, P., Strategies for increasing the sensitivity of gadolinium based MRI contrast agents. *Chem. Soc. Rev.* **2006**, *35* (6), 512-523.
15. Caravan, P.; Farrar, C. T.; Frullano, L.; Uppal, R., Influence of molecular parameters and increasing magnetic field strength on relaxivity of gadolinium- and manganese-based T(1) contrast agents. *Contrast Media Mol. Imaging* **2009**, *4* (2), 89-100.
16. Jacques, V.; Dumas, S.; Sun, W. C.; Troughton, J. S.; Greenfield, M. T.; Caravan, P., High-relaxivity magnetic resonance imaging contrast agents. Part 2. Optimization of inner- and second-sphere relaxivity. *Invest. Radiol.* **2010**, *45* (10), 613-24.
17. Wei, Z.; Jiang, Z.; Pan, C.; Xia, J.; Xu, K.; Xue, T.; Yuan, B.; Akakuru, O. U.; Zhu, C.; Zhang, G.; Mao, Z.; Qiu, X.; Wu, A.; Shen, Z., Ten-Gram-Scale Facile Synthesis of Organogadolinium Complex Nanoparticles for Tumor Diagnosis. *Small* **2020**, *16* (11), 1906870.
18. Zhang, H.; Wu, Y.; Wang, J.; Tang, Z.; Ren, Y.; Ni, D.; Gao, H.; Song, R.; Jin, T.; Li, Q.; Bu, W.; Yao, Z., In Vivo MR Imaging of Glioma Recruitment of Adoptive T-Cells Labeled with NaGdF<sub>4</sub>-TAT Nanoprobables. *Small* **2018**, *14* (3), 1702951.
19. EMA issues final opinion on linear gadolinium agents. *Reactions Weekly* **2017**, *1663* (1), 2-2.
20. Cho, M. J.; Sethi, R.; Narayanan, J. S. A.; Lee, S. S.; Benoit, D. N.; Taheri, N.; Decuzzi, P.; Colvin, V. L., Gadolinium oxide nanoplates with high longitudinal relaxivity for magnetic resonance imaging. *Nanoscale* **2014**, *6* (22), 13637-13645.
21. Choi, J. W.; Moon, W. J., Gadolinium Deposition in the Brain: Current Updates. *Korean J. Radiol.* **2019**, *20* (1), 134-147.
22. Le Fur, M.; Caravan, P., The biological fate of gadolinium-based MRI contrast agents: a call to action for bioinorganic chemists. *Metallomics* **2019**, *11* (2), 240-254.
23. Decuzzi, P.; Godin, B.; Tanaka, T.; Lee, S. Y.; Chiappini, C.; Liu, X.; Ferrari, M., Size and shape effects in the biodistribution of intravascularly injected particles. *J. Controlled Release* **2010**, *141* (3), 320-327.
24. Alexis, F.; Pridgen, E.; Molnar, L. K.; Farokhzad, O. C., Factors affecting the clearance and biodistribution of polymeric nanoparticles. *Mol. Pharm.* **2008**, *5* (4), 505-515.
25. He, C. B.; Hu, Y. P.; Yin, L. C.; Tang, C.; Yin, C. H., Effects of particle size and surface charge on cellular uptake and biodistribution of polymeric nanoparticles. *Biomaterials* **2010**, *31* (13), 3657-3666.

26. Johnson, N. J. J.; He, S.; Hun, V. A. N.; Almutairi, A., Compact Micellization: A Strategy for Ultrahigh T-1 Magnetic Resonance Contrast with Gadolinium-Based Nanocrystals. *ACS Nano* **2016**, *10* (9), 8299-8307.
27. Kuang, Y.; Cao, Y.; Liu, M.; Zu, G. Y.; Zhang, Y. J.; Zhang, Y.; Pei, R. J., Geometrical Confinement of Gadolinium Oxide Nanoparticles in Poly(ethylene glycol)/Arginylglycylaspartic Acid-Modified Mesoporous Carbon Nanospheres as an Enhanced T-1 Magnetic Resonance Imaging Contrast Agent. *ACS Appl. Mater. Interfaces* **2018**, *10* (31), 26099-26107.
28. Lohrke, J.; Frenzel, T.; Endrikat, J.; Alves, F. C.; Grist, T. M.; Law, M.; Lee, J. M.; Leiner, T.; Li, K. C.; Nikolaou, K.; Prince, M. R.; Schild, H. H.; Weinreb, J. C.; Yoshikawa, K.; Pietsch, H., 25 Years of Contrast-Enhanced MRI: Developments, Current Challenges and Future Perspectives. *Adv. Ther.* **2016**, *33* (1), 1-28.
29. Meenambal, R.; Poojar, P.; Geethanath, S.; Kannan, S., Substitutional limit of gadolinium in beta-tricalcium phosphate and its magnetic resonance imaging characteristics. *J. Biomed. Mater. Res. B Appl. Biomater.* **2017**, *105* (8), 2545-2552.
30. Ni, D. L.; Zhang, J. W.; Wang, J.; Hu, P.; Jin, Y. Y.; Tang, Z. M.; Yao, Z. W.; Bu, W. B.; Shi, J. L., Oxygen Vacancy Enables Markedly Enhanced Magnetic Resonance Imaging-Guided Photothermal Therapy of a Gd<sup>3+</sup>-Doped Contrast Agent. *ACS Nano* **2017**, *11* (4), 4256-4264.
31. Park, J. Y.; Baek, M. J.; Choi, E. S.; Woo, S.; Kim, J. H.; Kim, T. J.; Jung, J. C.; Chae, K. S.; Chang, Y.; Lee, G. H., Paramagnetic Ultrasmall Gadolinium Oxide Nanoparticles as Advanced T-1 MR1 Contrast Agent: Account for Large Longitudinal Relaxivity, Optimal Particle Diameter, and In Vivo T-1 MR Images. *ACS Nano* **2009**, *3* (11), 3663-3669.
32. Sanchez, P.; Valero, E.; Galvez, N.; Dominguez-Vera, J. M.; Marinone, M.; Poletti, G.; Corti, M.; Lascialfari, A., MRI relaxation properties of water-soluble apoferritin-encapsulated gadolinium oxide-hydroxide nanoparticles. *Dalton Trans.* **2009**, (5), 800-804.
33. Shen, Z. Y.; Fan, W. P.; Yang, Z.; Liu, Y. J.; Bregadze, V. I.; Mandal, S. K.; Yung, B. C.; Lin, L. S.; Liu, T.; Tang, W.; Shan, L. L.; Liu, Y.; Zhu, S. J.; Wang, S.; Yang, W. J.; Bryant, L. H.; Nguyen, D. T.; Wu, A. G.; Chen, X. Y., Exceedingly Small Gadolinium Oxide Nanoparticles with Remarkable Relaxivities for Magnetic Resonance Imaging of Tumors. *Small* **2019**, *15* (41), 9.
34. Shen, Z. Y.; Liu, T.; Yang, Z.; Zhou, Z. J.; Tang, W.; Fan, W. P.; Liu, Y. J.; Mu, J.; Li, L.; Bregadze, V. I.; Mandal, S. K.; Druzina, A. A.; Wei, Z. N.; Qiu, X. Z.; Wu, A. G.; Chen, X. Y., Small-sized gadolinium oxide based nanoparticles for high-efficiency theranostics of orthotopic glioblastoma. *Biomaterials* **2020**, *235*, 12.
35. Xiao, N.; Gu, W.; Wang, H.; Deng, Y. L.; Shi, X.; Ye, L., T-1-T-2 dual-modal MRI of brain gliomas using PEGylated Gd-doped iron oxide nanoparticles. *J. Colloid Interface Sci.* **2014**, *417*, 159-165.

36. Zeng, L. Y.; Wu, D.; Zou, R. F.; Chen, T. X.; Zhang, J. C.; Wu, A. G., Paramagnetic and Superparamagnetic Inorganic Nanoparticles for T-1-Weighted Magnetic Resonance Imaging. *Curr. Med. Chem.* **2018**, *25* (25), 2970-2986.
37. Zeng, Y.; Wang, L. Q.; Zhou, Z. J.; Wang, X. Y.; Zhang, Y.; Wang, J. Q.; Mi, P.; Liu, G.; Zhou, L. M., Gadolinium hybrid iron oxide nanocomposites for dual T-1- and T-2-weighted MR imaging of cell labeling. *Biomater. Sci.* **2017**, *5* (1), 50-56.
38. Zheng, X. Y. Z., K.; Tang, J.; Wang, X. Y.; Li, L. D.; Chen, N. X.; Wang, Y. J.; Shi, S.; Zhang, X.; Malaisamy, S.; Sun, L. D.; Wang, X.; Chen, C.; yan, C. H., Gd-Dots with Strong Ligand-Water Interaction for Ultrasensitive Magnetic Resonance Renography. *ACS Nano* **2017**, *11*, 3640-3650.
39. Zhou, Z. J.; Huang, D. T.; Bao, J. F.; Chen, Q. L.; Liu, G.; Chen, Z.; Chen, X. Y.; Gao, J. H., A Synergistically Enhanced T-1-T-2 Dual-Modal Contrast Agent. *Adv. Mater.* **2012**, *24* (46), 6223-6228.
40. He, S.; Johnson, N. J. J.; Huu, V. A. N.; Cory, E.; Huang, Y. R.; Sah, R. L.; Jokerst, J. V.; Almutairi, A., Simultaneous Enhancement of Photoluminescence, MRI Relaxivity, and CT Contrast by Tuning the Interfacial Layer of Lanthanide Heteroepitaxial Nanoparticles. *Nano Lett.* **2017**, *17* (8), 4873-4880.
41. Johnson, N. J. J.; Oakden, W.; Stanisz, G. J.; Prosser, R. S.; van Veggel, F., Size-Tunable, Ultrasmall NaGdF<sub>4</sub> Nanoparticles: Insights into Their T-1 MRI Contrast Enhancement. *Chem. Mater.* **2011**, *23* (16), 3714-3722.
42. Li, F. Y.; Liang, Z. Y.; Liu, J. N.; Sun, J. H.; Hu, X.; Zhao, M.; Liu, J. X.; Bai, R. L.; Kim, D.; Sun, X. L.; Hyeon, T.; Ling, D. S., Dynamically Reversible Iron Oxide Nanoparticle Assemblies for Targeted Amplification of T1-Weighted Magnetic Resonance Imaging of Tumors. *Nano Lett.* **2019**, *19* (7), 4213-4220.
43. Lin, H. Y.; Liu, K.; Gao, J. H., Surface Engineering to Boost the Performance of Nanoparticle-Based T-1 Contrast Agents. *Eur. J. Inorg. Chem.* **2019**, *2019* (34), 3801-3809.
44. Zhou, Z. J.; Yang, L. J.; Gao, J. H.; Chen, X. Y., Structure-Relaxivity Relationships of Magnetic Nanoparticles for Magnetic Resonance Imaging. *Adv. Mater.* **2019**, *31* (8), 32.
45. Fortin, M. A.; Petoral, R. M.; Soderlind, F.; Klasson, A.; Engstrom, M.; Veres, T.; Kall, P. O.; Uvdal, K., Polyethylene glycol-covered ultra-small Gd<sub>2</sub>O<sub>3</sub> nanoparticles for positive contrast at 1.5 T magnetic resonance clinical scanning. *Nanotechnology* **2007**, *18* (39).
46. Yang, G.; Phua, S. Z. F.; Bindra, A. K.; Zhao, Y., Degradability and Clearance of Inorganic Nanoparticles for Biomedical Applications. *Adv. Mater.* **2019**, *31* (10), 1805730.
47. Ahrén, M.; Selegård, L.; Klasson, A.; Söderlind, F.; Abrikosova, N.; Skoglund, C.; Bengtsson, T.; Engström, M.; Käll, P.-O.; Uvdal, K., Synthesis and Characterization

of PEGylated Gd<sub>2</sub>O<sub>3</sub> Nanoparticles for MRI Contrast Enhancement. *Langmuir* **2010**, *26* (8), 5753-5762.

48. Ananta, J. S.; Godin, B.; Sethi, R.; Moriggi, L.; Liu, X.; Serda, R. E.; Krishnamurthy, R.; Muthupillai, R.; Bolskar, R. D.; Helm, L.; Ferrari, M.; Wilson, L. J.; Decuzzi, P., Geometrical confinement of gadolinium-based contrast agents in nanoporous particles enhances T1 contrast. *Nat. Nanotechnol.* **2010**, *5* (11), 815-21.
49. Courant, T.; Roullin, V. G.; Cadiou, C.; Callewaert, M.; Andry, M. C.; Portefaix, C.; Hoeffel, C.; de Goltstein, M. C.; Port, M.; Laurent, S.; Elst, L. V.; Muller, R.; Molinari, M.; Chuburu, F., Hydrogels incorporating GdDOTA: towards highly efficient dual T1/T2 MRI contrast agents. *Angew. Chem. Int. Ed.* **2012**, *51* (36), 9119-22.
50. Dash, A.; Blasiak, B.; Tomanek, B.; van Veggel, F., Validation of Inner, Second, and Outer Sphere Contributions to T-1 and T-2 Relaxation in Gd<sup>3+</sup>-Based Nanoparticles Using Eu<sup>3+</sup> Lifetime Decay as a Probe. *J. Phys. Chem. C* **2018**, *122* (21), 11557-11569.
51. Ni, K.; Zhao, Z.; Zhang, Z.; Zhou, Z.; Yang, L.; Wang, L.; Ai, H.; Gao, J., Geometrically confined ultrasmall gadolinium oxide nanoparticles boost the T(1) contrast ability. *Nanoscale* **2016**, *8* (6), 3768-74.
52. Pothayee, N.; Balasubramaniam, S.; Pothayee, N.; Jain, N.; Hu, N.; Lin, Y.; Davis, R. M.; Sriranganathan, N.; Koretsky, A. P.; Riffle, J. S., Magnetic nanoclusters with hydrophilic spacing for dual drug delivery and sensitive magnetic resonance imaging. *J. Mater. Chem. B* **2013**, *1* (8), 1142-1149.
53. Rotz, M. W.; Culver, K. S.; Parigi, G.; MacRenaris, K. W.; Luchinat, C.; Odom, T. W.; Meade, T. J., High relaxivity Gd(III)-DNA gold nanostars: investigation of shape effects on proton relaxation. *ACS Nano* **2015**, *9* (3), 3385-96.
54. Rowe, M.; Thamm, D.; Kraft, S.; Boyes, S., Polymer-Modified Gadolinium Metal-Organic Framework Nanoparticles Used as Multifunctional Nanomedicines for the Targeted Imaging and Treatment of Cancer. *Biomacromolecules* **2009**, *10*, 983-93.
55. Wartenberg, N.; Fries, P.; Raccurt, O.; Guillermo, A.; Imbert, D.; Mazzanti, M., A Gadolinium Complex Confined in Silica Nanoparticles as a Highly Efficient T1/T2 MRI Contrast Agent. *Chem. - Eur. J.* **2013**, *19* (22), 6980-6983.
56. Zhou, Z.; Wu, C.; Liu, H.; Zhu, X.; Zhao, Z.; Wang, L.; Xu, Y.; Ai, H.; Gao, J., Surface and interfacial engineering of iron oxide nanoplates for highly efficient magnetic resonance angiography. *ACS Nano* **2015**, *9* (3), 3012-22.
57. Zhou, Z.; Zhu, X.; Wu, D.; Chen, Q.; Huang, D.; Sun, C.; Xin, J.; Ni, K.; Gao, J., Anisotropic Shaped Iron Oxide Nanostructures: Controlled Synthesis and Proton Relaxation Shortening Effects. *Chem. Mater.* **2015**, *27* (9), 3505-3515.
58. Asanuma, T.; Ono, M.; Kubota, K.; Hirose, A.; Hayashi, Y.; Saibara, T.; Inanami, O.; Ogawa, Y.; Enzan, H.; Onishi, S.; Kuwabara, M.; Oben, J. A., Super

- paramagnetic iron oxide MRI shows defective Kupffer cell uptake function in non-alcoholic fatty liver disease. *Gut* **2010**, *59* (2), 258-266.
59. Ba-Ssalamah, A.; Bastati, N.; Wibmer, A.; Fagner, R.; Hodge, J. C.; Trauner, M.; Herold, C. J.; Bashir, M. R.; Van Beers, B. E., Hepatic Gadoteric Acid Uptake as a Measure of Diffuse Liver Disease: Where Are We? *J. Magn. Reson. Imaging* **2017**, *45* (3), 646-659.
  60. Cheong, H.; Lee, S. S.; Lee, J. S.; Kim, J.; Kim, S. W.; Lee, W. J., Phagocytic Function of Kupffer Cells in Mouse Nonalcoholic Fatty Liver Disease Models: Evaluation With Superparamagnetic Iron Oxide MRI. *J. Magn. Reson. Imaging* **2015**, *41* (5), 1218-1227.
  61. Costa, A. F.; St-Germain, A. T.; Abdoell, M.; Smoot, R. L.; Cleary, S.; Jhaveri, K. S., How Do Different Indices of Hepatic Enhancement With Gadoteric Acid Compare in Predicting Liver Failure and Other Major Complications After Hepatectomy? *J. Comput. Assist. Tomogr.* **2018**, *42* (3), 380-386.
  62. Ding, Y.; Rao, S. X.; Meng, T.; Chen, C. Z.; Li, R. C.; Zeng, M. S., Usefulness of T1 mapping on Gd-EOB-DTPA-enhanced MR imaging in assessment of non-alcoholic fatty liver disease. *Eur. Radiol.* **2014**, *24* (4), 959-966.
  63. Kubota, K.; Tamura, T.; Aoyama, N.; Nogami, M.; Hamada, N.; Nishioka, A.; Ogawa, Y., Correlation of liver parenchymal gadolinium-ethoxybenzyl diethylenetriaminepentaacetic acid enhancement and liver function in humans with hepatocellular carcinoma. *Oncol. Lett.* **2012**, *3* (5), 990-994.
  64. Lee, S. S.; Park, S. H., Radiologic evaluation of nonalcoholic fatty liver disease. *World J. Gastroenterol.* **2014**, *20* (23), 7392-7402.
  65. Tonan, T.; Fujimoto, K.; Qayyum, A.; Morita, Y.; Nakashima, O.; Ono, N.; Kawahara, A.; Kage, M.; Hayabuchi, N.; Ueno, T., CD14 expression and Kupffer cell dysfunction in non-alcoholic steatohepatitis: Superparamagnetic iron oxide-magnetic resonance image and pathologic correlation. *J. Gastroenterol. Hepatol.* **2012**, *27* (4), 789-796.
  66. Chitturi, S.; Farrell, G. C., Etiopathogenesis of nonalcoholic steatohepatitis. *Semin. Liver Dis.* **2001**, *21* (1), 27-41.
  67. Seitz, H. K.; Stickel, F., Risk factors and mechanisms of hepatocarcinogenesis with special emphasis on alcohol and oxidative stress. *Biol. Chem.* **2006**, *387* (4), 349-360.
  68. Cao, Y. C., Synthesis of square gadolinium-oxide nanoplates. *J. Am. Chem. Soc.* **2004**, *126* (24), 7456-7457.
  69. Jung, E.; Yu, T.; Kim, W. S., Synthesis of rare earth oxide nanoplates with single unit cell thickness using a thermal decomposition method. *Korean J. Chem. Eng.* **2016**, *33* (2), 683-687.

70. Seo, S.; Yang, H.; Holloway, P. H., Controlled shape growth of Eu- or Tb-doped luminescent Gd<sub>2</sub>O<sub>3</sub> colloidal nanocrystals. *J. Colloid Interface Sci.* **2009**, *331* (1), 236-242.
71. Si, R.; Zhang, Y. W.; Zhou, H. P.; Sun, L. D.; Yan, C. H., Controlled-synthesis, self-assembly behavior, and surface-dependent optical properties of high-quality rare-earth oxide nanocrystals. *Chem. Mater.* **2007**, *19* (1), 18-27.
72. Singh, G.; McDonagh, B. H.; Hak, S.; Peddis, D.; Bandopadhyay, S.; Sandvig, I.; Sandvig, A.; Glomm, W. R., Synthesis of gadolinium oxide nanodisks and gadolinium doped iron oxide nanoparticles for MR contrast agents. *J. Mater. Chem. B* **2017**, *5* (3), 418-422.
73. Yuan, J. Q.; Peng, E. W.; Xuea, J. M., Controlled loading of paramagnetic gadolinium oxide nanoplates in PMAO-g-PEG as effective T-1-weighted MRI contrast agents. *J. Mater. Res.* **2014**, *29* (15), 1626-1634.
74. Zhou, Z. J.; Hu, R.; Wang, L. R.; Sun, C. J.; Fu, G.; Gao, J. H., Water bridge coordination on the metal-rich facets of Gd<sub>2</sub>O<sub>3</sub> nanoplates confers high T-1 relaxivity. *Nanoscale* **2016**, *8* (41), 17887-17894.
75. Paik, T.; Gordon, T. R.; Prantner, A. M.; Yun, H.; Murray, C. B., Designing Tripodal and Triangular Gadolinium Oxide Nanoplates and Self-Assembled Nanofibrils as Potential Multimodal Bioimaging Probes. *ACS Nano* **2013**, *7* (3), 2850-2859.
76. Liu, G. Z.; Conn, C. E.; Drummond, C. J., Lanthanide Oleates: Chelation, Self-assembly, and Exemplification of Ordered Nanostructured Colloidal Contrast Agents for Medical Imaging. *J. Phys. Chem. B* **2009**, *113* (49), 15949-15959.
77. Si, R.; Zhang, Y. W.; You, L. P.; Yan, C. H., Rare-earth oxide nanopolyhedra, nanoplates, and nanodisks. *Angew. Chem. Int. Ed.* **2005**, *44* (21), 3256-3260.
78. Peng, X. G.; Wickham, J.; Alivisatos, A. P., Kinetics of II-VI and III-V colloidal semiconductor nanocrystal growth: "Focusing" of size distributions. *J. Am. Chem. Soc.* **1998**, *120* (21), 5343-5344.
79. Machado, I. P.; Teixeira, V. C.; Pedroso, C. C. S.; Brito, H. F.; Rodrigues, L. C. V., X-ray scintillator Gd<sub>2</sub>O<sub>2</sub>S:Tb<sup>3+</sup> materials obtained by a rapid and cost-effective microwave-assisted solid-state synthesis. *J. Alloys Compd.* **2019**, *777*, 638-645.
80. Yu, W. W.; Chang, E.; Falkner, J. C.; Zhang, J. Y.; Al-Somali, A. M.; Sayes, C. M.; Johns, J.; Drezek, R.; Colvin, V. L., Forming biocompatible and nonaggregated nanocrystals in water using amphiphilic polymers. *J. Am. Chem. Soc.* **2007**, *129* (10), 2871-2879.
81. Bridot, J.-L.; Faure, A.-C.; Laurent, S.; Rivière, C.; Billotey, C.; Hiba, B.; Janier, M.; Josserand, V.; Coll, J.-L.; Vander Elst, L.; Muller, R.; Roux, S.; Perriat, P.; Tillement, O., Hybrid Gadolinium Oxide Nanoparticles: Multimodal Contrast Agents for in Vivo Imaging. *J. Am. Chem. Soc.* **2007**, *129* (16), 5076-5084.

82. El-Mahdy, G. A.; Atta, A. M.; Al-Lohedan, H. A., Synthesis and Evaluation of Poly(Sodium 2-Acrylamido-2-Methylpropane Sulfonate-co-Styrene)/Magnetite Nanoparticle Composites as Corrosion Inhibitors for Steel. *Molecules* **2014**, *19* (2), 1713-1731.
83. Gad, Y. H., Preparation and characterization of poly(2-acrylamido-2-methylpropane-sulfonic acid)/Chitosan hydrogel using gamma irradiation and its application in wastewater treatment. *Radiat. Phys. Chem.* **2008**, *77* (9), 1101-1107.
84. Cavus, S., Poly(methacrylamide-co-2-acrylamido-2-methyl-1-propanesulfonic acid) Hydrogels: Investigation of pH- and Temperature-Dependent Swelling Characteristics and Their Characterization. *J. Polym. Sci., Part B: Polym. Phys.* **2010**, *48* (23), 2497-2508.
85. Zhang, X.; Zhang, Q.; Ma, T.; Liu, Q.; Wu, S.; Hua, K.; Zhang, C.; Chen, M.; Cui, Y., Enhanced Stability of Gold Magnetic Nanoparticles with Poly(4-styrenesulfonic acid-co-maleic acid): Tailored Optical Properties for Protein Detection. *Nanoscale Res. Lett.* **2017**, *12* (1).
86. Ma, X. H.; Gong, A.; Xiang, L. C.; Chen, T. X.; Gao, Y. X.; Liang, X. J.; Shen, Z. Y.; Wu, A. G., Biocompatible composite nanoparticles with large longitudinal relaxivity for targeted imaging and early diagnosis of cancer. *J. Mater. Chem. B* **2013**, *1* (27), 3419-3428.
87. Pencer, J.; Hallett, F. R., Effects of vesicle size and shape on static and dynamic light scattering measurements. *Langmuir* **2003**, *19* (18), 7488-7497.
88. Sattler, K. D., *Handbook of Nanophysics: Nanomedicine and Nanorobotics*. CRC Press: 2010.
89. Tang, T.; Louie, A. Y.; Gale, E. M.; Caravan, P.; Farrar, C. T.; Keil, B., Chapter 7 Standard Biological and in vivo Methods. In *Contrast Agents for MRI: Experimental Methods*, The Royal Society of Chemistry: 2018; pp 499-584.
90. Hoshyar, N.; Gray, S.; Han, H. B.; Bao, G., The effect of nanoparticle size on in vivo pharmacokinetics and cellular interaction. *Nanomedicine* **2016**, *11* (6), 673-692.
91. Frohlich, E., The role of surface charge in cellular uptake and cytotoxicity of medical nanoparticles. *Int. J. Nanomed.* **2012**, *7*, 5577-5591.
92. Aime, S.; Caravan, P., Biodistribution of Gadolinium-Based Contrast Agents, Including Gadolinium Deposition. *J. Magn. Reson. Imaging* **2009**, *30* (6), 1259-1267.
93. Bourquin, J.; Milosevic, A.; Hauser, D.; Lehner, R.; Blank, F.; Petri-Fink, A.; Rothen-Rutishauser, B., Biodistribution, Clearance, and Long-Term Fate of Clinically Relevant Nanomaterials. *Adv. Mater.* **2018**, *30* (19), e1704307.



94. Malfatti, M. A.; Palko, H. A.; Kuhn, E. A.; Turteltaub, K. W., Determining the pharmacokinetics and long-term biodistribution of SiO<sub>2</sub> nanoparticles in vivo using accelerator mass spectrometry. *Nano Lett.* **2012**, *12* (11), 5532-8.
95. Dai, Y.; Wu, C.; Wang, S.; Li, Q.; Zhang, M.; Li, J.; Xu, K., Comparative study on in vivo behavior of PEGylated gadolinium oxide nanoparticles and Magnevist as MRI contrast agent. *Nanomedicine* **2018**, *14* (2), 547-555.
96. Tian, X.; Yang, F.; Yang, C.; Peng, Y.; Chen, D.; Zhu, J.; He, F.; Li, L.; Chen, X., Toxicity evaluation of Gd<sub>2</sub>O<sub>3</sub>@SiO<sub>2</sub> nanoparticles prepared by laser ablation in liquid as MRI contrast agents in vivo. *Int. J. Nanomed.* **2014**, *9*, 4043-4053.
97. Zhang, B. B.; Yang, W. T.; Yu, J. N.; Guo, W. S.; Wang, J.; Liu, S. Y.; Xiao, Y.; Shi, D. L., Green Synthesis of Sub-10 nm Gadolinium-Based Nanoparticles for Sparkling Kidneys, Tumor, and Angiogenesis of Tumor-Bearing Mice in Magnetic Resonance Imaging. *Adv. Healthcare Mater.* **2017**, *6* (4), 11.
98. Ngen, E. J.; Artemov, D., Advances in Monitoring Cell-Based Therapies with Magnetic Resonance Imaging: Future Perspectives. *Int. J. Mol. Sci.* **2017**, *18* (1), 26.
99. Hirsch, L. R.; Stafford, R. J.; Bankson, J. A.; Sershen, S. R.; Rivera, B.; Price, R. E.; Hazle, J. D.; Halas, N. J.; West, J. L., Nanoshell-mediated near-infrared thermal therapy of tumors under magnetic resonance guidance. *Proceedings of the National Academy of Sciences* **2003**, *100* (23), 13549-13554.
100. Loo, C.; Lin, A.; Hirsch, L.; Lee, M. H.; Barton, J.; Halas, N.; West, J.; Drezek, R., Nanoshell-enabled photonics-based imaging and therapy of cancer. *Technol. Cancer Res. Treat.* **2004**, *3* (1), 33-40.
101. Sayes, C. M.; Fortner, J. D.; Guo, W.; Lyon, D.; Boyd, A. M.; Ausman, K. D.; Tao, Y. J.; Sitharaman, B.; Wilson, L. J.; Hughes, J. B.; West, J. L.; Colvin, V. L., The Differential Cytotoxicity of Water-Soluble Fullerenes. *Nano Lett.* **2004**, *4* (10), 1881-1887.
102. Todaro, G. J.; Lazar, G. K.; Green, H., The initiation of cell division in a contact-inhibited mammalian cell line. *J. Cell. Physiol.* **1965**, *66* (3), 325-33.
103. Liang, C.-C.; Park, A. Y.; Guan, J.-L., In vitro scratch assay: a convenient and inexpensive method for analysis of cell migration in vitro. *Nat. Protoc.* **2007**, *2* (2), 329-333.
104. Perera, V. S.; Chen, G.; Cai, Q.; Huang, S. D., Nanoparticles of gadolinium-incorporated Prussian blue with PEG coating as an effective oral MRI contrast agent for gastrointestinal tract imaging. *The Analyst* **2016**, *141* (6), 2016-2022.
105. Yokel, R. A.; Hancock, M. L.; Grulke, E. A.; Unrine, J. M.; Dozier, A. K.; Graham, U. M., Carboxylic acids accelerate acidic environment-mediated nanoceria dissolution. *Nanotoxicology* **2019**, *13* (4), 455-475.

106. Angulo, P., Medical progress - Nonalcoholic fatty liver disease. *N. Engl. J. Med.* **2002**, *346* (16), 1221-1231.
107. Bugianesi, E.; Leone, N.; Vanni, E.; Marchesini, G.; Brunello, F.; Carucci, P.; Musso, A.; De Paolis, P.; Capussotti, L.; Salizzoni, M.; Rizzetto, M., Expanding the natural history from cryptogenic cirrhosis to of nonalcoholic steatohepatitis: Hepatocellular carcinoma. *Gastroenterology* **2002**, *123* (1), 134-140.
108. James, O.; Day, C., Non-alcoholic steatohepatitis: another disease of affluence. *Lancet* **1999**, *353* (9165), 1634-1636.
109. Vernon, G.; Baranova, A.; Younossi, Z. M., Systematic review: the epidemiology and natural history of non-alcoholic fatty liver disease and non-alcoholic steatohepatitis in adults. *Aliment. Pharmacol. Ther.* **2011**, *34* (3), 274-285.
110. Chalasani, N.; Younossi, Z.; Lavine, J. E.; Diehl, A. M.; Brunt, E. M.; Cusi, K.; Charlton, M.; Sanyal, A. J., The Diagnosis and Management of Non-alcoholic Fatty Liver Disease: Practice Guideline by the American Association for the Study of Liver Diseases, American College of Gastroenterology, and the American Gastroenterological Association (vol 107, pg 811, 2012). *Am. J. Gastroenterol.* **2012**, *107* (10), 1598-1598.
111. Fretellier, N.; Salhi, M.; Schroeder, J.; Siegmund, H.; Chevalier, T.; Bruneval, P.; Jestin-Mayer, G.; Delaloge, F.; Factor, C.; Mayer, J. F.; Fabicki, J. M.; Robic, C.; Bonnemain, B.; Idée, J. M.; Corot, C., Distribution profile of gadolinium in gadolinium chelate-treated renally-impaired rats: role of pharmaceutical formulation. *Eur. J. Pharm. Sci.* **2015**, *72*, 46-56.
112. Garcia, J.; Liu, S. Z.; Louie, A. Y., Biological effects of MRI contrast agents: gadolinium retention, potential mechanisms and a role for phosphorus. *Philos Trans A Math Phys Eng Sci* **2017**, *375* (2107).
113. Mercantepe, T.; Tümkaya, L.; Çeliker, F. B.; Topal Suzan, Z.; Çinar, S.; Akyildiz, K.; Mercantepe, F.; Yilmaz, A., Effects of gadolinium-based MRI contrast agents on liver tissue. *J. Magn. Reson. Imaging* **2018**, *48* (5), 1367-1374.
114. Marchesini, G.; Brizi, M.; Bianchi, G.; Tomassetti, S.; Bugianesi, E.; Lenzi, M.; McCullough, A. J.; Natale, S.; Forlani, G.; Melchionda, N., Nonalcoholic fatty liver disease - A feature of the metabolic syndrome. *Diabetes* **2001**, *50* (8), 1844-1850.
115. Lerch, J. P.; Gazdzinski, L.; Germann, J.; Sled, J. G.; Henkelman, R. M.; Nieman, B. J., Wanted dead or alive? The tradeoff between in-vivo versus ex-vivo MR brain imaging in the mouse. *Front. Neuroinform.* **2012**, *6*, 6.
116. Tempel-Brami, C.; Schiffenbauer, Y. S.; Nyska, A.; Ezov, N.; Spector, I.; Abramovitch, R.; Maronpot, R. R., Practical Applications of in Vivo and ex Vivo MRI in Toxicologic Pathology Using a Novel High-performance Compact MRI System. *Toxicol. Pathol.* **2015**, *43* (5), 633-50.

117. Dixon, L. J.; Barnes, M.; Tang, H.; Pritchard, M. T.; Nagy, L. E., Kupffer Cells in the Liver. *Compr. Physiol.* **2013**, *3* (2), 785-797.
118. Feng, X. Y.; Deng, T. T.; Zhang, Y.; Su, S. B.; Wei, C. J.; Han, D. S., Lipopolysaccharide inhibits macrophage phagocytosis of apoptotic neutrophils by regulating the production of tumour necrosis factor alpha and growth arrest-specific gene 6. *Immunology* **2011**, *132* (2), 287-295.
119. Frausto-Del-Rio, D.; Soto-Cruz, I.; Garay-Canales, C.; Ambriz, X.; Soldevila, G.; Carretero-Ortega, J.; Vazquez-Prado, J.; Ortega, E., Interferon gamma induces actin polymerization, Rac1 activation and down regulates phagocytosis in human monocytic cells. *Cytokine* **2012**, *57* (1), 158-168.
120. Kazankov, K.; Jorgensen, S. M. D.; Thomsen, K. L.; Moller, H. J.; Vilstrup, H.; George, J.; Schuppan, D.; Gronbaek, H., The role of macrophages in nonalcoholic fatty liver disease and nonalcoholic steatohepatitis. *Nat. Rev. Gastroenterol. Hepatol.* **2019**, *16* (3), 145-159.
121. Kerr, T. A.; Davidson, N. O., Cholesterol and nonalcoholic fatty liver disease: renewed focus on an old villain. *Hepatology* **2012**, *56* (5), 1995-8.
122. Thuy, S.; Ladurner, R.; Volynets, V.; Wagner, S.; Strahl, S.; Konigsrainer, A.; Maier, K. P.; Bischoff, S. C.; Bergheim, I., Nonalcoholic fatty liver disease in humans is associated with increased plasma endotoxin and plasminogen activator inhibitor 1 concentrations and with fructose intake. *J. Nutr.* **2008**, *138* (8), 1452-1455.
123. Varin, A.; Mukhopadhyay, S.; Herbein, G.; Gordon, S., Alternative activation of macrophages by IL-4 impairs phagocytosis of pathogens but potentiates microbial-induced signalling and cytokine secretion. *Blood* **2010**, *115* (2), 353-362.
124. Pasquini, L.; Napolitano, A.; Visconti, E.; Longo, D.; Romano, A.; Toma, P.; Espagnet, M. C. R., Gadolinium-Based Contrast Agent-Related Toxicities. *CNS Drugs* **2018**, *32* (3), 229-240.
125. Christian, G. D., *Analytical Chemistry*. 6th ed.; John Wiley and Sons Inc.: Hoboken, 2003; p 111-113.

## Chapter 3

### The Role of Surface Coating in Designing Highly Sensitive T<sub>2</sub> MRI Contrast Agents<sup>†</sup>

† Reprinted (adapted) with permission from Villanova J.\*; Cho M.\*; Lee S. S.; Ines D.; Xiao Z.; Guo X.; Dunn J. A.; Stueber D. D.; Decuzzi P.; Colvin V. L., The Role of Surface Coating in Designing Highly Sensitive T<sub>2</sub> MRI Contrast Agents, *in submission to Journal of Physical Chemistry C*.

\*These authors contributed equally to this work.

## Chapter 3 The Role of Surface Coating in Designing Highly Sensitive T<sub>2</sub> MRI Contrast Agents

### 3.1. Abstract

Iron oxide nanocrystals (IONCs) are an FDA approved and gadolinium free alternative to standard magnetic resonance imaging (MRI) contrast agents. While their magnetic cores are responsible for T<sub>2</sub> contrast, the non-magnetic polymers at IONC interfaces can affect the diffusion of bulk water close to particles. This can potentially impact the spin relaxation dynamics governing proton relaxivity and consequently lead to notable changes in imaging performance. Here we illustrate these effects by evaluating the diameter-dependent contrast performance of iron oxide nanocrystals with different types of surface coatings. As a group, these biocompatible and colloidally stable materials have excellent imaging properties; the largest core diameter (33 nm) coated with an oleic acid bilayer has to our knowledge the largest T<sub>2</sub> relaxivity ever reported (510 mM<sup>-1</sup> s<sup>-1</sup>) for an isolated, spherical iron oxide nanocrystal. A comparison of the different functional surfaces reveals that retention of bulk water by IONC coatings will shift the diameter-dependent relaxivity allowing smaller diameter cores to reach the static dephasing regime and maximum T<sub>2</sub> relaxivity. Both the grafting density and thickness of polymer coatings can slow water diffusion which can be accounted for in an effective diffusion constant ( $D_{eff}$ ); with this conceptual framework we can explain the structure-performance trends found here and in the existing literature. Localized water diffusion at IONC interfaces can be an important variable to control in the rational design of highly sensitive T<sub>2</sub> MRI contrast agents.

### 3.2. Introduction

Iron oxide nanocrystals (IONCs) have garnered considerable interest as gadolinium free MRI contrast agents.<sup>1-3</sup> In a strong external magnetic field, IONCs generate localized inhomogeneous fields that accelerate transverse water  $^1\text{H}$  relaxation ( $T_2$ ) near their surface thus producing negative (dark) contrast. Due to their biocompatibility, hepatobiliary biodistribution and clearance, and contrast performance (relaxivity), IONCs are the only gadolinium free nanoscale contrast agents that have previously received US Food and Drug Administration (FDA) approval as MRI contrast agents.<sup>1</sup> Commercial IONCs like ferumoxytol (Feraheme) have been used for a variety of clinical applications from tumor imaging (e.g., liver, spleen, lymph nodes, brain) and stem cell tracking to angiography and perfusion imaging.<sup>4</sup> These clinical applications would be greatly enhanced by a new generation of contrast agents with stimuli responsive performance; such “smart” contrast agents could identify in a MRI image key biomarkers of interest or signal important physiochemical conditions. Existing strategies take advantage of nanocrystal clustering to modulate the relaxivity around the materials, but aggregation can be difficult to control precisely and leads to drastic changes in pharmacokinetic, biodistribution, and toxicity profiles all of which has frustrated the clinical translation of molecular MRI agents based on nanoparticle platforms.<sup>5-19</sup> Thus, there is a need for alternative strategies to modulate CA performance in response to local chemical or biological cues, an advance that will require a complete description of how contrast agents operate at a molecular level such that researchers can rationally design IONC capable of responding to their local environment.<sup>2-4, 20, 21</sup>

Current models that describe the water proton relaxation processes around  $T_2$  contrast agents (CA) recognize that contrast derives from the perturbation of water proton spin dynamics by the varying magnetic fields present near a nanocrystal surface; the resulting spread in Larmor frequencies that result,  $\Delta\omega$ , and the amount of time water spends in this spin perturbing region,  $\tau_D$ , together define how big of an impact a given contrast agent will have on water proton  $T_2$  relaxation.<sup>22-24</sup> The best performance results when water spends the entirety of the MRI measurement time diffusing through the inhomogeneous magnetic fields near nanocrystals, no more and no less.<sup>3, 24, 25</sup> Achieving this optimal timescale is most often achieved through careful manipulation of the core dimension.<sup>22, 23, 26-28</sup> However, other inorganic nanocrystal characteristics such as crystallinity, composition, shape, and aggregation state may also contribute as these factors affect the extent of the inhomogeneous magnetic field experienced by freely diffusing water.<sup>29-39</sup> These approaches focus on the inorganic core and increasing its magnetization such that diffusing water molecules experience a greater spread in their Larmor frequencies,  $\Delta\omega$ , and as a result differential relaxivity.

Relatively less attention has centered on how the contrast agent coatings, typically polymers, affect the relaxation processes central for  $T_2$  contrast agent performance. The surface coatings of magnetic nanocrystal contrast agents are usually designed with an eye towards ensuring optimal colloidal stability, pharmacokinetics, biodistribution, and biocompatibility.<sup>2, 3</sup> However, water proton  $T_2$  processes should also be affected by both the thickness and nature of the surface coating as this interface mediates the diffusion of water through the core's inhomogeneous magnetic field. Studies of colloidally stable and

non-aggregating T<sub>2</sub> nanocrystal contrast agents have reported coating thickness and chemical composition can both impact spin relaxation processes.<sup>40-54</sup> For instance, water impermeable coatings can affect these relaxation processes by excluding water from the core's field, causing as much as a 70 – 90 % decrease in r<sub>2</sub> with increasing thickness.<sup>48, 49</sup> However, it has been shown that this 'exclusionary model' cannot fully account for more complex trends found with water permeable surface coatings.<sup>51-53</sup> For instance, Bao et al. and Nandwana et al. used similar PEG coated nanocrystals and showed that r<sub>2</sub> increases (15 – 120 %) then decreases (60 – 90 %) with increasing coating thickness and molecular weight.<sup>51-53</sup> These results have inspired the hypothesis that the exclusionary model is balanced by a 'slow compartment' model in which water permeable surface coatings interact with and slow the diffusion of water inside the core's field, thus facilitating relaxation increasing r<sub>2</sub> with coating thickness.<sup>50-53</sup> However, the exclusionary model may not be needed for water permeable coatings where these apparently conflicting trends could reflect the different dynamical regimes of T<sub>2</sub> contrast agents existing within a slow compartment model: whether surface coating induced water deceleration increases or decreases contrast agent performance will depend on whether the time water spends in the coating is well matched to its relaxation time. If changes in surface coating properties can affect notable changes in relaxivity and that relationship were properly understood, *intraparticle* effects could supplant *interparticle* clustering strategies as a new and more reliable approach to the development of smart T<sub>2</sub> contrast agents.

Here, iron oxide nanocrystals with different polymeric surface coatings are used to provide a comprehensive understanding of how the surface coating of an IONC may



change its relaxivity. Size controlled, hydrophobic nanocrystals (4 – 33 nm) are monodisperse and amenable to several surface coating strategies for good biocompatibility, and excellent colloidal and relaxometric stability over a range of physiologically relevant conditions. IONCs have size and surface dependent  $T_2$  relaxivity profiles that together can be rationalized by recognizing that water diffusion within surface coatings can be slower than that found in bulk water ( $D_{\text{coating}}$ ). For  $T_2$  contrast agents small enough to be in the motional averaging regime (MAR), slowing water protons in their near surface region leads to an increase in relaxivity as compared to impermeable surface coatings that exclude water and decrease  $r_2$ .<sup>48, 49</sup> Such a model can explain coating dependent  $r_2$  trends found in this work and elsewhere.<sup>51-53, 55</sup> Optimization of  $r_2$  involves consideration of both hydrodynamic diameter as well as surface coating structure, with our highest performing samples greater than commercial IONCs ( $< 200 \text{ mM}^{-1} \text{ s}^{-1}$ ) and isolated IONCs found in the literature ( $< 385 \text{ mM}^{-1} \text{ s}^{-1}$ ).<sup>4, 28-37, 56-58</sup> In particular, large (33 nm) oleic acid bilayer coated samples achieve the largest recorded  $r_2$  for single core, spherical IONCs ( $510 \text{ mM}^{-1} \text{ s}^{-1}$ ). The accompanying description of these trends showcases the essential role that surface coatings play in CA performance and suggest responsive surface coatings offer another strategy for molecular imaging in contrast enabled MRI.

### 3.3. Results and Discussion

#### 3.3.1. Synthesis of Surface Coated Iron Oxide Nanocrystals

Iron oxide nanocrystals (IONCs) are prepared via thermal decomposition of iron precursors in the presence of oleic acid at high temperature (320 °C). Transmission

electron microscopy (TEM) images indicate as synthesized IONCs are monodisperse and quasi spherical with diameters of approximately 4, 10, 16, and 33 nm (**Figure 3.1a-d**). Diameter control is achieved by either changing the reaction time or the molar ratio of iron precursor to oleic acid. Because of Ostwald ripening, the latter is generally a preferred approach as nanocrystal uniformity diminishes after several hours. As has been reported before, IONCs are crystalline and non-aggregated with a structure consistent with the magnetite ( $\text{Fe}_3\text{O}_4$ ) phase of iron oxide (**Figure 3.1e**).<sup>59, 60</sup>

The hydrophobic nanocrystals are formed with oleic acid bound to their surfaces, but their hydrophobicity can be modified by transferring them into aqueous solution via either encapsulation or ligand exchange methods.<sup>61, 62</sup> Encapsulation results in bilayer stabilized IONCs and utilizes a phase transfer process facilitated by the addition of oleic acid or amphiphilic polymers like octylamine-modified poly (acrylic acid) (PAA-OA),

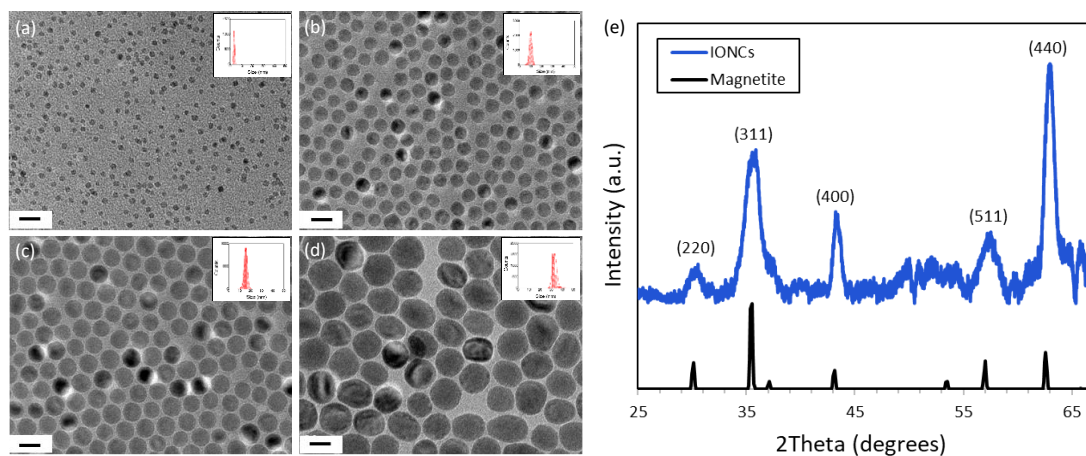


**Figure 3.1 IONC core characterization.** Transmission electron microscopy (TEM) images with inset size distribution histograms of as-synthesized, monodisperse iron oxide nanocrystals of varying core diameter (a-d). Core diameters are (a)  $4.0 \pm 0.6$ , (b)  $10.2 \pm 0.7$ , (c)  $16.0 \pm 1.4$ , and (d)  $33.1 \pm 2.5$  nm. Scale bars are 20 nm. (e) XRD pattern for a representative sample of iron oxide nanocrystals. The sample diffraction pattern (blue) is consistent with a standard pattern for magnetite ( $\text{Fe}_3\text{O}_4$ ; black).

poly(2-acrylamido-2-methylpropane sulfonic acid)-lauryl acrylate (PAMPS-LA), and poly(maleic anhydride-alt-1-octadecene)-poly(ethylene glycol) (PMAO-PEG) (**Figure 3.2a and S3.1**). Alternatively, as synthesized IONCs can also have their original oleic acid removed and replaced by poly (ethylene glycol) (PEG; 0.2, 1, and 10 kDa), poly (vinyl pyrrolidone) (PVP; 1 kDa), and poly (acrylic acid) (PAA; 15 kDa). These phase transfer processes are efficient with typical yields of 70%. Either method provides IONCs in a colloidal stable, clear, and brownish black colloidal suspension. Dynamic light scattering (DLS) reveals that the hydrodynamic diameter (HD) of the nanocrystals increases with

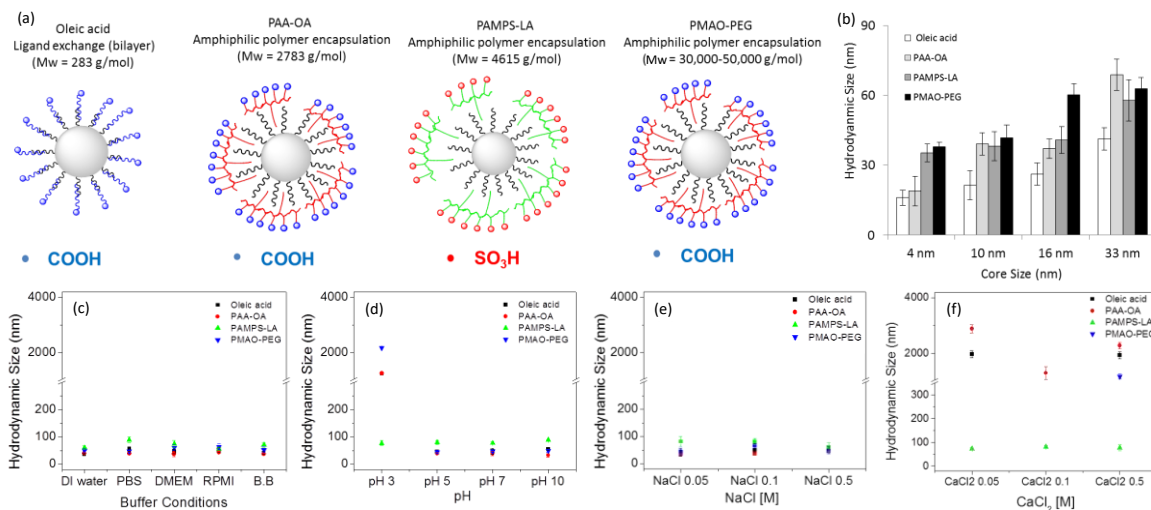


**Figure 3.2 IONC surface coating characterization.** (a) Schematic depiction of iron oxide nanocrystals with various encapsulation phase transfer agents (oleic acid bilayer, PAA-OA, PAMPS-LA, and PMAO-PEG). (b) The hydrodynamic diameter (HD) and of 4, 10, 16, and 33 nm iron oxide nanocrystals with different surface coatings (oleic acid bilayer, PAA-OA, PAMPS-LA, and PMAO-PEG). Hydrodynamic sizes of iron oxide nanocrystals dispersed in different (c) buffer solutions (distilled ionized water (DI water), phosphate buffer saline (PBS), Dulbecco's Modified Eagle's Medium (DMEM) and Roswell Park Memorial Institute medium (RPMI), and borate buffer (B.B)), (d) pH 3 – 10, (e) NaCl 0.05 – 0.5 M, and (f) CaCl<sub>2</sub> 0.05 – 0.5 M.

core size and the molecular weight of the coating; for these samples HD is always well

under 100 nm (**Figure 3.2b, Table 3.1 and S3.1**). A consideration of the core dimensions, as well as estimates for the surface coating thickness, yields dimensions in good agreement with DLS data indicating the IONCs are well dispersed and non-aggregated (**Figure 3.2b, Table 3.1 and S3.1**). After transfer into water, or other physiologically relevant media, there are no visible precipitates over days.

### 3.3.2. Colloidal Stability

The average core size and morphology of the iron oxide nanocrystals (IONCs) coated and in aqueous solutions are identical to those observed for as synthesized IONCs (**Figure 3.1a-d and S3.1**). Moreover, dynamic light scattering (DLS) and TEM image analysis reveal that water soluble IONCs are well dispersed with a range of surface coating thicknesses (**Figure 3.2b, Table 3.1 and S3.1**). As nanocrystal core size increases from 4 to 33 nm, the hydrodynamic diameter of phase transferred IONCs coated with oleic acid bilayer increases from 16 nm to 41 nm with a uniform average coating thickness of approximately  $5.2 \pm 0.7$  nm (**Figure 3.2b and Table 3.1**) – the approximate length of two oleic acid

**Table 3.1** T2 relaxivity ( $r_2$ ) and hydrodynamic diameter (HD) of iron oxide nanocrystals with different sizes and phase transfer coatings.

Core Size/Coating	Oleic acid bilayer		PAA-OA		PAMPS-LA		PMAO-PEG	
	HD (nm)	$r_2$ ( $\text{mM}^{-1}\text{s}^{-1}$ )	HD (nm)	$r_2$ ( $\text{mM}^{-1}\text{s}^{-1}$ )	HD (nm)	$r_2$ ( $\text{mM}^{-1}\text{s}^{-1}$ )	HD (nm)	$r_2$ ( $\text{mM}^{-1}\text{s}^{-1}$ )
<b>4 nm</b>	16.0 $\pm 3.1$	11.1 $\pm 3.1$	18.9 $\pm 6.4$	81.9 $\pm 6.4$	35.3 $\pm 3.9$	108.7 $\pm 3.9$	37.8 $\pm 2.1$	126.6 $\pm 3.1$
<b>10 nm</b>	21.3 $\pm 6.2$	50.5 $\pm 2.8$	39.1 $\pm 4.9$	158.9 $\pm 5.9$	38.2 $\pm 6.2$	152.4 $\pm 7.2$	41.7 $\pm 5.6$	201.1 $\pm 5.7$
<b>16 nm</b>	26.2 $\pm 4.7$	159.8 $\pm 10.7$	37.1 $\pm 4.2$	327.7 $\pm 12.5$	40.8 $\pm 5.7$	385.2 $\pm 10.1$	60.2 $\pm 4.7$	260.4 $\pm 12.9$
<b>33 nm</b>	41.3 $\pm 4.8$	510.3 $\pm 18.8$	68.8 $\pm 6.8$	301.2 $\pm 10.4$	57.8 $\pm 8.8$	355.1 $\pm 6.7$	62.9 $\pm 4.8$	339.9 $\pm 8.3$

molecules (~4.8 nm). With larger molecular weight polymer surface coatings. The IONCs have much larger HD sizes (~19 – 69 nm) with less uniform coating thicknesses from approximately 7.5 to 22 nm (**Figure 3.2b and Table 3.1**). The average zeta potentials for oleic acid bilayer, PAA-LA, PAMPS-LA, and PMAO-PEG coated IONCs are  $-48.3 \pm 8.7$ ,  $-55.8 \pm 8.6$ ,  $-51.7 \pm 8.5$ , and  $-45.0 \pm 7.0$  mV, respectively.

Encapsulated IONCs, coated with oleic acid, PAA-OA, PMAO-PEG, and PAMPS-LA, are colloidally stable in a range of physiologically relevant media like deionized water (DI water), phosphate buffer saline (PBS), Dulbecco's Modified Eagle Medium (DMEM), Roswell Park Memorial Institute medium (RPMI), and borate buffer (B.B) (**Figure 3.2c**). Similarly, these materials maintain their colloidal stability under a wide range of pH conditions (5 – 10) and at high monovalent salt concentrations (0.05 – 0.5 M NaCl) (**Figure 3.2d, e**). When polymer surface coatings contained carboxylate functionality, however, the materials lost colloidal stability under highly acidic conditions (pH 3) and in the presence of high divalent salt concentrations (0.05 – 0.5 M CaCl<sub>2</sub>) (**Figure 3.2d+f**). The relatively high pKa of most organic acids suggests these functional groups may protonate at lower pH removing any electrostatic stabilization of the IONCs; additionally, divalent metal cations like Ca<sup>2+</sup> can interact with these groups and bridge between nanocrystals causing aggregation.<sup>63, 64</sup> PMAO-PEG encapsulated nanocrystals behave similarly as anhydride functional groups are hydrolyzed to carboxyl groups especially at low pH and in the presence divalent metal cations. Phase transferred nanocrystals with sulfonate containing polymer coatings (PAMPS-LA) provide for the most stable suspensions under all conditions – even low pH and high CaCl<sub>2</sub> (0.05 – 0.5 M) conditions. This is to be

expected for sulfonated polymers because of their low pKa (< 2), hydrogen bond donor and acceptor properties, and lack of interaction with divalent cations.<sup>63-68</sup> As such, relatively novel sulfonated polymeric surface coatings like PAMPS-LA demonstrate significant promise in biomedical applications of nanomaterials.<sup>65-67, 69</sup>

### 3.3.3. T2 Relaxation Dynamics

#### 3.3.3.1. Theory for Magnetic Nanocrystals

In the presence of an external magnetic field, iron oxide nanocrystals (IONCs) induce inhomogeneous local magnetic fields that shorten the T<sub>2</sub> of water protons. The concentration dependent capacity of IONCs to accelerate the transverse relaxation rate (1/T<sub>2</sub>) of water protons is called T<sub>2</sub> relaxivity, or r<sub>2</sub> (mM<sup>-1</sup> s<sup>-1</sup>), and it is a widely accepted metric of IONC contrast agent performance. The interaction between magnetic nanocrystals and local water protons is dominated by outer sphere relaxation mechanisms, so r<sub>2</sub> can be approximated by an outer sphere model termed the motional averaging regime (MAR).<sup>3</sup> This results in the following relationship for how relaxivity depends on key contrast agent features:

$$r_2 = \frac{4 v_{mat} (\gamma_H \mu_0 M_v d)^2}{405 D_{bulk}} \quad (2)$$

where  $\gamma_H$  is the water <sup>1</sup>H nuclei gyromagnetic ratio (2.68 x 10<sup>8</sup> rad T<sup>-1</sup> s<sup>-1</sup>),  $\mu_0$  is the permeability of vacuum (4 $\pi$  x 10<sup>-7</sup> T m A<sup>-1</sup>), D is the translational diffusion constant of water (D<sub>bulk</sub> = 3.1 x 10<sup>-9</sup> m<sup>2</sup> s<sup>-1</sup> at 37 °C),  $v_{mat}$  is the molar volume of magnetic ions, d is the nanocrystal diameter (m), and M<sub>v</sub> is the saturation magnetization (A m<sup>-1</sup>).<sup>22-24</sup> Equation 2 is a valid approximation of r<sub>2</sub> only when a nanocrystal's localized magnetic

field ( $\Delta\omega = \gamma_H \mu_0 M_v / 3$ ) and the time it takes water to diffuse through the characteristic dimensions of that field ( $\tau_D = d^2/4D_{\text{bulk}}$ ) are sufficiently small.<sup>3, 22-25, 70</sup> This criterion is referred to as the Redfield condition ( $\Delta\omega\tau_D \ll 1$ ). This condition is easily met for smaller contrast agents, and with increasing IONC dimension the length of the perturbed magnetic field grows larger and has a larger impact on the proton relaxation in freely diffusing water. As long as the Redfield condition is met, magnetic nanocrystal core size ( $d$ ) and magnetization ( $M_v$ ) will both increase IONC relaxivity,  $r_2$ , and are the only relevant material parameters for optimizing contrast agent performance.<sup>22-24, 70</sup> The dynamics described by equation [2] are no longer applicable once the time that diffusing water spends in a perturbing magnetic field equals or exceeds the measurement timescale. This regime, termed the static dephasing regime (SDR), is easily identified in systematic studies as a high plateau in contrast agent performance with IONC core diameter.<sup>23, 24, 71, 72</sup> It reflects the conditions where the near core regions of inhomogeneous field strength are large enough that freely diffusing water experiences these relaxation inducing fields for the entire duration of the MRI measurement ( $\Delta\omega\tau_D > 1$ ). At even larger dimensions of contrast agent, ( $\Delta\omega\tau_D > 20$ ), the water interaction with the inhomogeneous magnetic field around IONCs becomes so long that it exceeds the interval between the echoes of the  $T_2$  weighted spin echo MR sequence. In this echo limited regime (ELR)  $r_2$  decreases with increasing IONC dimension and is a condition best avoided in the design of contrast agents.<sup>3, 22, 23, 25, 70</sup>

Contrast agents that are just large enough to be described well by the static dephasing regime (SDR) have the largest relaxivity. Generally IONC magnetization, a property which

can be enhanced through CA composition and nanocrystal clustering, and core diameter, are used to increase  $\Delta\omega$  to meet the Redfield condition.<sup>22, 23, 26-39</sup> For a magnetite ( $\text{Fe}_3\text{O}_4$ ) contrast agent ( $M_{V(\text{bulk})} = 4.76 \times 10^5 \text{ A m}^{-1}$ ), the SDR model would predict theoretical maximum  $r_2$  of approximately  $960 \text{ mM}^{-1}\text{s}^{-1}$ .<sup>70, 73</sup> As saturation magnetization in a nanocrystal is reduced by at least 10 % from the bulk value due to surface disorder, a more reasonable estimate for optimum IONC contrast agents performance would be an  $r_2$  of  $860 \text{ mM}^{-1}\text{s}^{-1}$ .<sup>74</sup> The smallest core diameter for which the SDR plateau is reached, which we define as the critical core diameter,  $d_{\text{sdr}}$ , can be estimated from the product of  $\Delta\omega$  and  $\tau_D$ ; for  $\Delta\omega\tau_D = 5$  and a magnetite IONC the  $d_{\text{sdr}}$  is approximately 36 nm. This is in good agreement with other studies showing surface coated magnetic nanomaterials clearly in SDR after approximately 50 nm.<sup>24, 72</sup>

These conventional models do not account for the effects of polymeric coatings around contrast agents. Bao et al. develops a model that describes the impact of an impermeable surface coating on the dynamics describes by the motional averaging regime. Such a coating excludes water access to the most substantial inhomogeneous field gradients, and thus leads to a modification in the MAR model (Equation 2) to account for the 'exclusion radius' formed by the coating thickness.<sup>51, 53</sup> Water impermeable coatings always lead to a decrease in  $r_2$  with increasing thickness.<sup>48, 49</sup> Many IONC surface coatings, however, are permeable to water and rather than completely blocking access of water to the near core area could simply slow down any water that came into contact.<sup>51-53 55, 75</sup> The 'slow compartments' for water diffusion created by surface coatings, a concept introduced by Bao et al., would have an impact reflective of the hydrophilicity, thickness,



as well as density of the permeable materials.<sup>50-53</sup> We envision water effectively decelerating as it comes into contact with the surface coating for at least a portion of the measurement time and modify equation [2] with a new effective water diffusion constant in the motional averaging regime MAR:

$$r_2 = C \frac{(M_v d)^2}{D_{coating}} \quad (3)$$

$D_{coating}$  is the effective diffusion constant taking into that bulk water will spend some time during the measurement interacting with the coating, and C is a coefficient that captures relevant constants in equation [2] for magnetite ( $C = 0.0166 \text{ m}^5 \text{ mol}^{-1} \text{ s}^{-2} \text{ A}^{-2}$ ). This modified MAR model (Equation 3), provides another means to optimize the relaxivity of a  $T_2$  contrast agent in the motional averaging regime. If water can slowly diffuse through the surface coating, and therefore increase the time it spends interacting with the inhomogeneous field around the nanocrystal, then relaxivity in this regime can be increased.

An important consequence of introducing the diffusion of water through the coating in these systems is that the Redfield condition is also modified as the time water spends in the nanocrystal's localized field depends on its diffusion constant ( $\tau_D = d^2/4D_{coating}$ ). Slowing water down with surface coating interactions will increase their time spent in the nanocrystal's localized field and make it possible to achieve the static dephasing regime ( $5 < \Delta\omega\tau_D < 20$ ) achievable at smaller core diameters. For example, assuming the diffusion constant of water is reduced by 10% because of a water permeable surface coating then

the critical IONC/magnetite diameter to reach the static dephasing plateau,  $d_{SDR}$ , is 26 nm as compared to 36 nm for a non-interacting coating.

### 3.3.3.2. Surface-Coating Dependence

The libraries of surface coated IONCs synthesized allow us to test the impact of water permeable coatings over the different spin dynamics regimes relevant for creating  $T_2$  contrast. We first confirmed the diameter dependent trends expected for the motional averaging regime are observed over a range of iron oxide nanocrystal dimensions (**Figure S3.2**). The relaxivity ( $r_2$ ) of different diameter IONCs (4 – 33 nm) with four types of surface coatings (oleic acid, PAA-OA, PAMPS-LA, and PMAO-PEG) was found from the slope of iron concentration versus  $1/T_2$  plots measured at 1.41 T (**Figure S3.3, Table 3.1**). Consistent with the motional averaging regime we find that for all surface coatings,  $r_2$  increases with core diameter ( $d$ ), magnetization ( $M_v$ ), and hydrodynamic size at smaller sizes (**Figure 3.3a-c and S3.4**).<sup>24, 76</sup> This trend is most evident for the oleic acid bilayer coated nanocrystals whose  $r_2$  values increase from 11 to 510  $\text{mM}^{-1} \text{s}^{-1}$  as their core size increases from 4 to 33 nm (**Table 3.1**). The exceptional performance of the 33 nm oleic acid IONCs results from their large core size and thin, impermeable bilayer coating ( $5.2 \pm$

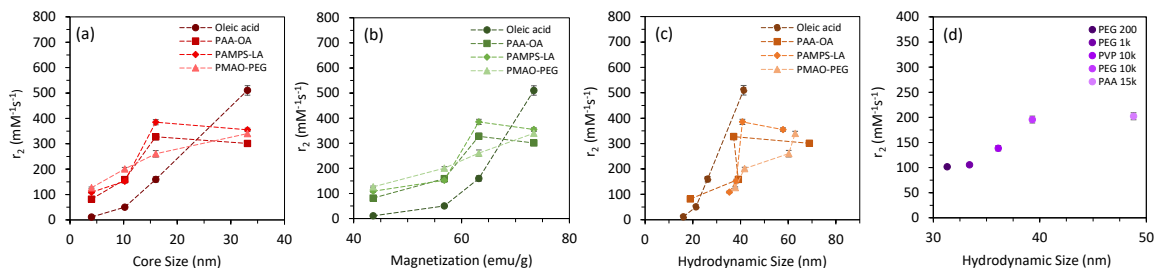


**Figure 3.3 T2 relaxivity dependence of IONCs.** Plots of  $r_2$  values of iron oxide nanocrystals depending on their core diameters (a) and hydrodynamic size (b). The  $r_2$  values of 10 nm core iron oxide nanocrystals with different molecular weight of polymers and hydrodynamic size.

0.7 nm), approximating well our calculation of  $d_{\text{SDR}}$  for a bare magnetite nanocrystal (36 nm). Under these conditions, coating dependent increases in the time water spends diffusing in the nanocrystal's localized field ( $\tau_D$ ) are minimized, keeping the Redfield parameter ( $\Delta\omega\tau_D$ ) low and allowing  $r_2$  to continue increasing with core size (MAR).

Like oleic bilayer coatings, polyacrylate (PAA) and polysulfonated (PAMPS-LA) coated IONCs of smaller dimension also show an increase in relaxivity,  $r_2$ , with core dimension, indicative of motional averaging, but the largest 33 nm core materials do not continue the trend indicating a transition to the static dephasing regime in these materials (**Figure 3.3a+c**). The experimental data brackets the  $d_{\text{SDR}}$  to between 16 and 33 nm diameter for these systems. Thick water permeable polymeric coatings will interact with water, increasing the time water spends in the nanocrystal's localized field ( $\tau_D$ ), thus shifting  $d_{\text{SDR}}$  to smaller core size. As a result, the peak  $r_2$  for PAA-OA and PAMPS-LA coated IONCs

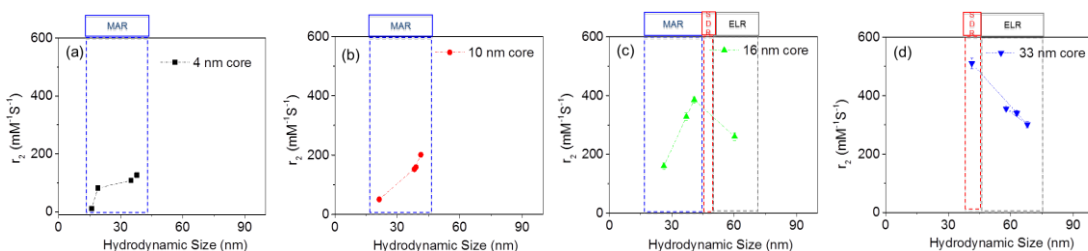


**Figure 3.4 T2 relaxivity hydrodynamic diameter dependence of IONCs.** The plots of  $r_2$  of iron oxide nanocrystals with different cores (4, 10, 16, and 33 nm) (a-d). The points indicate the surface coatings oleic acid bilayer, PAA-OA, PAMPS-LA, and PMAO-PEG, respectively (left to right). The samples have an increase in hydrodynamic diameter, as measured by dynamic light scattering, because the different polymer coatings vary in their molecular weight. Above the graphs the relevant dynamical regime is noted; MAR (motional averaging regime), SDR (static dephasing regime), ELR (echo limited regime).

(327.7 and 385.2 mM<sup>-1</sup>s<sup>-1</sup>, respectively) occurs at a much smaller core dimension (16 nm) than observed for the thinner oleic bilayer coatings (33 nm) (**Table 3.1**).

An examination of how the coating thickness influences the observed contrast agent performance provides additional evidence for the importance of water interactions with the IONC surface coatings (**Figure 3.4**). Here the relaxivity is expressed for the different cores, as a function of the hydrodynamic diameter of the different coatings, with oleic acid being the thinnest at 5.2 ± 0.7 nm and PMAO-PEG being the thickest at 17.5 ± 2.8 nm. For smaller core sizes (4 and 10 nm), the motional averaging regime dominates as water is not spending a significant amount of time diffusing through the nanocrystal's localized field (MAR;  $\Delta\omega\tau_D \ll 1$ ); in this limit increasing coating thickness will increase that time ( $\tau_D$ ) and increase  $r_2$ . For larger core diameters (16 nm), water is already spending a significant portion of its relaxation time diffusing through the nanocrystal's localized field, so  $r_2$  will increase with coating thickness until the static dephasing regime is reached. Similar behaviour is seen for 10 nm IONCs coated with increasing molecular weight coatings (PEG 200 – 10k, and PVP 10k) (**Figure 3.3d, Table S3.1**). For the largest core sizes (33 nm), water is already spending its entire relaxation time in the nanocrystal's field (SDR;  $5 < \Delta\omega\tau_D < 20$ ), so further increases in that time with thicker coatings push the system into the unfavorable regime where relaxation effects are limited by the MRI echo sequence, decreasing  $r_2$  (ELR; > 50 nm). Increasing surface coating thickness for water permeable coatings can be an effective strategy for increasing contrast agent performance (**Figure 3.4a-c**) if the core diameters are small enough that the IONC is well described by the motional averaging regime (MAR). For larger core diameters, however,

which are closer to the static dephasing limit (SDR) similar changes in coating thickness can lead to substantially reduced  $T_2$  relaxivities (**Figure 3.4c+d**).

Given the significant impact of the water permeability on  $T_2$  contrast agent performance, methods to tailor a coating's permeability are of great value. Because larger molecular weight polymers are not packed together as tightly on the nanocrystal surface (lower grafting density), water should more readily diffuse into the coating and with fewer interactions.<sup>75, 77</sup> The grafting density of nanocrystal surface coatings can be determined by total organic carbon (TOC) analysis, and in the grafting-to methods used to prepare these materials it is a strong function of the polymer molecular weight: as the coating increases in length there are fewer and fewer chains bound to nanocrystals due to steric hindrance.<sup>77, 78</sup> The molecular weight of oleic acid, PAA-OA, PAMPS-LA, and PMAO-PEG phase transfer agents are 283, 2783, 4615, and 30,000 – 50,000 Da, respectively (**Figure S3.5, Table S3.2**) and, as expected, grafting decreases with increasing molecular weight (**Figure S3.6 and Table S3.2**).

The large molecular weight of PMAO-PEG is thus significant in that it contributes to a thick coating but also leads to a sparse coverage of the IONCs. In this case we might expect water would have fewer interactions with this coating and exhibit diffusion constants more comparable to bulk water. The  $r_2$  of low grafting density PMAO-PEG coated IONCs continue to increase with core size consistent with motional averaging (MAR) while the  $r_2$  of higher grafting density PAMPS-LA and PAA-OA coated IONCs show a decrease at the largest dimensions (ELR) (**Figure 3.3c**). Moreover, approximately controlling for coating thickness, the three, polymer coated 33 nm nanocrystals exhibit similarly large

hydrodynamic sizes ( $\sim 63$  nm), yet  $r_2$  continues to increase with dimension for PMAO-PEG coatings (MAR). A consideration of the grafting density of surface coatings thus could help rationalize similarly complex surface dependent trends in  $r_2$  found elsewhere.<sup>51-53</sup>

**Table 3.2** summarizes the performance ( $r_2$ ) of the IONC contrast agents examined here compared to commercial  $T_2$  contrast agents and previously published reports of single core, spherical IONC of similar structure. The IONC contrast agents studied here, when

**Table 3.2** Summary of relevant physiochemical, magnetic, and relaxometric parameters for IONCs reported here and the highest performing, single core, spherical iron oxide nanocrystal  $T_2$  MRI contrast agents found in the literature.

Reference	Surface Coating	Core Size (nm)	HD (nm)	$M_v$ ( $10^5 \text{ A m}^{-1}$ ) <sup>o</sup>	$r_2$ ( $\text{mM}^{-1}\text{s}^{-1}$ )	$\Delta\omega\tau_D$
Jun et al.	DMSA	12	-	5.23 <sup>h</sup>	218 <sup>a,h</sup>	0.94 <sup>m</sup>
Huang et al.	PVP	65.3	118.3	-	249 <sup>l</sup>	-
Jang et al.	DMSA	15	$\sim 17.5$	5.91 <sup>b</sup>	276 <sup>a,k</sup>	1.56 <sup>n</sup>
Vuong et al.	PAA (5k)	17.8	-	3.27 <sup>f</sup>	292.6 <sup>c,d</sup>	0.97
Mohapatra et al.	BPEI	16	48	4.30 <sup>b,j</sup>	297 <sup>i</sup>	1.30 <sup>n</sup>
Lartigue et al.	Rhamnose	18.5	23.6	3.37 <sup>b</sup>	$\sim 300$ <sup>a,h</sup>	1.31 <sup>n</sup>
Nandwana et al.	NDOPA-PEG	8.1	34	2.64 <sup>b,e</sup>	355 <sup>i</sup>	0.20 <sup>n</sup>
LaConte et al.	DSPE-PEG750	13.6	10.35	-	360 <sup>a,d</sup>	-
Tong et al.	DSPE-mPEG1000	14	28.6	-	385 <sup>c,d</sup>	-
This work		4.0	16.0 – 37.8	2.26 <sup>b,f</sup>	11.1 – 126.6 <sup>a,g</sup>	0.04 <sup>n</sup>
	Oleic acid, PAA-OA, PAMPS-LA, PMAO-PEG	10.2	21.3 – 41.7	2.94 <sup>b,f</sup>	50.5 – 201.1 <sup>a,g</sup>	0.36 <sup>n</sup>
		16.0	26.2 – 60.2	3.27 <sup>b,f</sup>	159.8 – 385.2 <sup>a,g</sup>	0.99 <sup>n</sup>
		33.1	41.3 – 68.8	3.80 <sup>b,f</sup>	301.2 – 510.3 <sup>a,g</sup>	4.92 <sup>n</sup>

<sup>a</sup> Room temperature (15-25 C), <sup>b</sup> 27 C, <sup>c</sup> 40 C, <sup>d</sup> 0.47 T, <sup>e</sup> 0.5 T, <sup>f</sup> 1 T, <sup>g</sup> 1.41 T, <sup>h</sup> 1.5 T, <sup>i</sup> 3 T, <sup>j</sup> 4 T, <sup>k</sup> 4.7 T, <sup>l</sup> 7 T, <sup>m</sup>  $D_{25C} = 2.25 \times 10^{-9} \text{ m}^2 \text{ s}^{-1}$ , <sup>n</sup>  $D_{27C} = 2.37 \times 10^{-9} \text{ m}^2 \text{ s}^{-1}$ , <sup>o</sup>  $\rho_{\text{magnetite}} = 5.18 \times 10^6 \text{ g m}^{-3}$  assumed for conversions from  $M_s$  ( $\text{emu g}^{-1}$ ) to  $M_v$  ( $\text{A m}^{-1}$ ). 2,3-dimercaptosuccinic acid (DMSA), polyvinylpyrrolidone (PVP), branched polyethyleneimine (BPEI), polyacrylic acid (PAA), polyethylene glycol (PEG), methoxy-PEG (mPEG), nitrodopamine (NDOPA), 1, 2-Distearoyl-sn-glycero-3-phosphoethanolamine (DSPE), octylamine (OA), poly(2-acrylamido-2-methylpropane sulfonic acid) (PAMPS), lauryl acrylate (LA), Poly(maleic anhydride-alt-1-octadecene) (PMAO), external magnetic field ( $B_0$ ),  $T_2$  relaxivity ( $r_2$ ), mass saturation magnetization ( $M_s$ ), and volumic saturation magnetization ( $M_v$ ).

optimized for the static dephasing regime, are much better than commercial IONC materials ( $< 200 \text{ mM}^{-1}\text{s}^{-1}$ ). They also, as a group, compare well to those characterized by the research community and one, the largest core bilayer coated sample, has to our knowledge the largest recorded  $r_2$  ( $510.3 \text{ mM}^{-1}\text{s}^{-1}$ ) for single core iron oxide nanocrystals.<sup>4, 28-37, 56-58</sup> Where possible we also examined whether the core diameter-dependent and surface coating trends observed in this existing literature could be rationalized in light of the relevant dynamical regime (MAR vs. SDR vs. ELR). By accounting

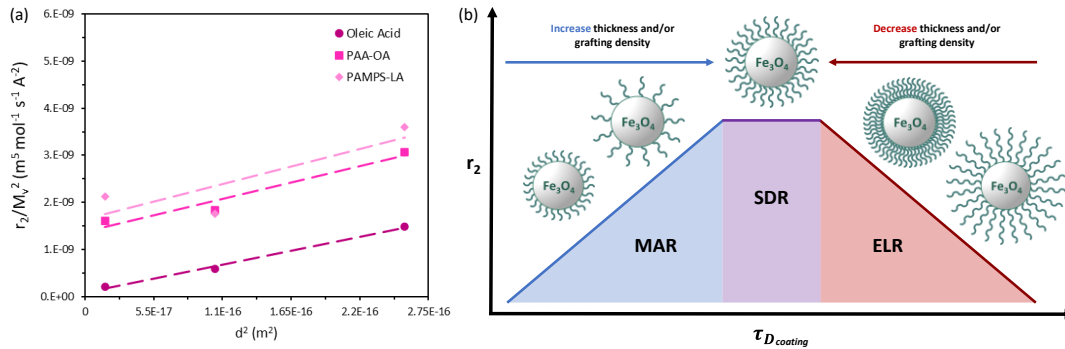


**Figure 3.5 Surface coating dependent diffusion constants.** (a) Using Equation 3,  $C/D_{\text{coating}}$  and therefore  $D_{\text{coating}}$  can be approximated from the slope of the line generated from a plot of  $r_2/M_v^2$  as a function of  $d^2$  for each coating using samples in MAR (according to Figure 3.4). The  $D_{\text{coating}}$  for oleic acid bilayer, PAA-OA, and PAMPS-LA is  $3.08 \times 10^{-9}$ ,  $2.63 \times 10^{-9}$ , and  $2.44 \times 10^{-9} \text{ m}^2 \text{ s}^{-1}$ , respectively. Since the oleic acid bilayer coating is thin and likely impermeable to water, its  $D_{\text{coating}}$  can be used as an approximation of  $D_{\text{bulk}}$  for the conditions of our nanocrystal solutions. Therefore, the  $D_{\text{coating}}$  for larger polymer coatings like PAA-OA and PAMPS-LA are approximately 79.2 – 85.4 % of  $D_{\text{bulk}}$ . (b) Schematic approximating the relationship between  $r_2$  and  $\tau D_{\text{coating}}$  when iron oxide nanocrystal core size and magnetization, and therefore  $\Delta\omega$ , are held constant. Under these conditions, hydrophilic surface coating thickness and grafting density can be used to optimize the diffusion of water near its surface ( $D_{\text{coating}}$  and  $\tau D_{\text{coating}}$ ) and therefore maximize  $r_2$ .

for both core size and magnetization with the Redfield parameter ( $\Delta\omega\tau_D$ ), we find that most high  $r_2$  IONCs are just large enough to be in the static dephasing regime assuming a bulk water diffusion constant ( $\Delta\omega\tau_D \geq \sim 1$ ). Those reports of increasing relaxivity with increasing core dimension generally had lower performance consistent with early MAR ( $\Delta\omega\tau_D \ll 1$ ).<sup>24</sup> As such, compared to  $\tau_D$  and  $\Delta\omega\tau_D$ ,  $\tau_{D_{coating}}$  and  $\Delta\omega\tau_{D_{coating}}$  would be expected to be larger by a factor of  $D_{coating}/D_{bulk}$  according to equation [4]. For our surface coated IONCs most obviously in MAR,  $D_{coating}$  is approximately 20 % lower than  $D_{bulk}$  (**Figure 3.5a**) which increases  $\tau_D$  and  $\Delta\omega\tau_D$  by roughly 20%. Depending on the physiochemical parameters of the surface coating, the retardation of water diffusion in the coating could be even more significant.<sup>50, 55, 75</sup> This could explain why the NDOPA-PEG IONCs reported by Nandwana et al. have high  $r_2$  despite having low  $\Delta\omega\tau_D - \Delta\omega\tau_{D_{coating}}$  is probably significantly higher.<sup>52</sup> This sets a precedent for developing high performing IONCs: when core diameter and magnetization ( $\Delta\omega$ ) are held constant,  $r_2$  can be maximized by optimizing surface coating thickness and/or grafting density (**Figure 3.5b**).

#### 3.3.3.3. Solution Condition Dependence

While the relaxivity characterization presented in Figures X and Y was completed in pure water, *in vivo* the solution environment for IONCs will be very different. The presence of salts and proteins can lead to aggregation of IONCs, for example (Figure 2c-f), with consequences for their contrast agent performance. We find that the iron oxide nanocrystal (IONCs)  $T_2$  relaxivity changes in different solutions tracks well with their colloidal stability under these same solutions (**Figure 3.2c-f and 3.6a-d**). Uncontrolled IONC aggregation drastically increases their physical dimension leading to a decrease in



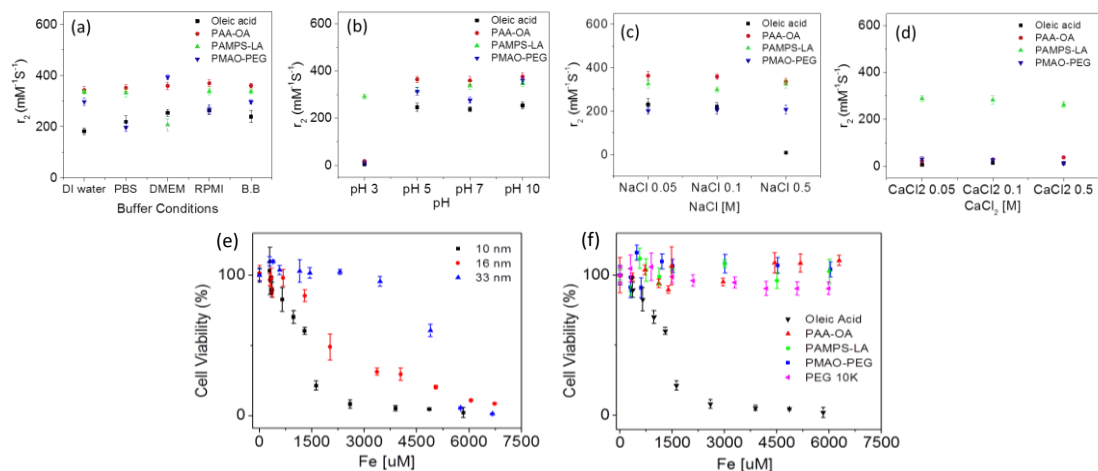


**Figure 3.6 Surface coating-dependent relaxometric stability and cell viability of IONC.** The  $r_2$  of iron oxide nanocrystals dispersed in different (a) buffer solutions (distilled ionized water (DI water), phosphate buffer saline (PBS), Dulbecco's Modified Eagle's Medium (DMEM) and Roswell Park Memorial Institute medium (RPMI), and borate buffer (B.B)), (b) pH 3 – 10, (c) NaCl 0.05 – 0.5 M, and (d)  $\text{CaCl}_2$  0.05 – 0.5 M. In vitro cell viability assays (MTS) of oleic acid coated iron oxide nanocrystals with (e) different core sizes (10, 16, 33 nm) and (f) 10 nm iron oxide nanocrystals with various surface coatings (oleic acid bilayer, PAA-OA, PAMPS-LA, PMAO-PEG, and 10k PEG).

$r_2$  as the  $T_2$  dynamics is better described by the ELR. Across various buffer solutions and under a range of pH (5 – 10) and monovalent salt concentrations (0.05 – 0.5 M NaCl), colloidally stable IONCs mostly maintain their high  $T_2$  relaxivity ( $r_2 \geq \sim 200 \text{ mM}^{-1} \text{ s}^{-1}$ ) (**Figure 3.2c-e and 3.6a-c**). Notably, IONCs with carboxylate containing encapsulation agents (oleic acid bilayer, PAA-LA, and PMAO-PEG) have a significantly reduced  $r_2$  under highly acidic conditions (pH 3) and in the presence of high divalent salt concentrations (0.05 – 0.5 M  $\text{CaCl}_2$ ) (**Figure 3.2d+f and 3.6b+d**). As discussed above, carboxylate containing surface coating agents become less stable at low pH and in the presence of divalent metal cations like  $\text{Ca}^{2+}$ , leading to aggregation and a reduction in  $r_2$ .<sup>63, 64</sup> However, because of

more stable sulfonated polymers, PAMPS-LA-coated IONCs maintain high  $T_2$  relaxometric performance under all conditions – even at low pH and high  $\text{CaCl}_2$  (0.05 – 0.5 M).<sup>63-68</sup>

#### 3.3.4. Size- and Surface Coating-Dependent Cytotoxicity

One of the greatest advantages of iron oxide nanocrystals (IONCs) as MRI contrast agents is their biocompatibility.<sup>79</sup> However, there are still concerns about the possibility that the materials could release free iron ion disrupting iron homeostasis; additionally nanocrystals can promote pro-inflammatory responses and increase reactive oxygen species under some circumstances.<sup>6,80-85</sup> We conducted a preliminary *in vitro* experiment to identify any core diameter or surface coating cytotoxicity trends using our expansive library of IONCs. A simple and standard assay was used to assess the viability of human dermal fibroblast cells after 24 hours in the presence of increasing concentrations IONCs with varied dimensions (10 – 33 nm) and surface coatings (oleic acid bilayer, PAA-OA, PAMPS-LA, PMAO-PEG, and 10k PEG) (**Figure 3.6e+f**).

There is no significant cytotoxic effect up to atomic iron concentrations of 1200  $\mu\text{M}$  (67 ppm) for all materials and up to the 6000  $\mu\text{M}$  (335 ppm), the highest concentration we could prepare, for all materials except the oleic acid IONCs. The null result in cytotoxicity seen for most of these materials limits our analysis of diameter and surface coating dependent trends to the bilayer coated materials. We speculate that the hydrophobic bilayer could increase cell-nanocrystal surface interactions contributing to the observed cytotoxicity at higher concentration; this surface coating is may also be more prone to biotransformation and upon removal could lead to more cytotoxicity.<sup>6, 80-85</sup> The cell viability decreases with decreasing core dimension as well, a trend observed for many

other *in vitro* cytotoxicity studies of metal oxide nanocrystals (**Figure 3.6e**). The size dependent difference in cytotoxicity could be due to differences in cellular uptake and/or increased presence of dissolved iron at smaller core sizes.<sup>6, 80-85</sup>

### 3.4. Conclusion

This study probes the size and surface coating dependent relaxation dynamics of iron oxide nanocrystals (IONCs) to optimize their performance as  $T_2$  MRI contrast agents. Synthesized IONCs are monodispersed, size tunable (4 – 33 nm), and are easily transferred into aqueous solution using a variety of hydrophilic surface coating agents (oleic acid bilayer, PAA-OA, PAMPS-LA, PMAO-PEG, PEG 200 – 10 k, PVP 10k, and PAA 15k). Phase transferred nanocrystals display good colloidal stability under a range of physiologically relevant conditions. Relaxation dynamics data demonstrate that maximal  $r_2$  can be achieved by tuning surface coating dependent water diffusion constants ( $D_{\text{coating}}$ ) with coating thickness and grafting density. IONCs with a large core size (33 nm) and thin surface coating (oleic acid bilayer) have the highest reported  $T_2$  relaxivity for this class of materials ( $r_2 = 510 \text{ mM}^{-1} \text{ s}^{-1}$ ). Their  $r_2$  are stable under a variety of solution conditions and demonstrate no significant cytotoxicity in human dermal fibroblasts at iron concentrations as high as 1200  $\mu\text{M}$ . Thicker, lower grafting density surface coatings (PAA-OA, PAMPS-LA, and PMAO-PEG) exhibit no significant cytotoxicity at iron concentrations as high as 6,000  $\mu\text{M}$  and retain high and stable  $r_2$  ( $> 300 \text{ mM}^{-1} \text{ s}^{-1}$ ) over a range of similar solution conditions. In particular, PAMPS-LA coated nanocrystals can maintain colloidal stability and high  $r_2$  even under the harshest conditions tested (pH 3 and 0.05 – 0.1 M  $\text{CaCl}_2$ ).

These data provide great insight into the rational design of  $T_2$  contrast agents for advanced MRI applications. For molecular imaging, the ideal nanocrystal size is between 5 and 50 nm, where they can escape phagocytosis better than larger nanoparticles and therefore have longer blood circulation times.<sup>86</sup> Fortunately, this size range can coincide with late MAR or SDR for these IONCs, meaning their  $r_2$  can be optimized and still be useful for molecular imaging. Commercial IONCs used as MRI contrast agents are generally within this size range but exhibit much lower  $r_2$  values ( $< 200 \text{ mM}^{-1} \text{ s}^{-1}$ ) – likely because of smaller core sizes, poor sample uniformity, and unoptimized surface coatings.<sup>4, 24</sup> In general, for high  $r_2$  IONCs, the largest core size and smallest coating thickness possible – while still maintaining SDR, colloidal stability, and low toxicity – are ideal. However, if a larger hydrodynamic diameter is needed for other reasons (e.g., biocompatibility, colloidal stability, functionalization), reducing grafting density may help to maintain a high  $r_2$ . Finally, “smart”  $T_2$  contrast agents could use in situ stimuli responsive changes in surface coating – an *intraparticle* effect – rather than clustering – an *interparticle* effect – for enhanced contrast in molecular imaging without the same risk of uncontrolled aggregation.<sup>5-19</sup> Under this new *intraparticle* paradigm, IONCs could be designed to “turn on” (ELR to SDR; increasing  $r_2$ ) or “turn off” (SDR to MAR; decreasing  $r_2$ ) by reducing their coating thickness or grafting density (i.e., via degradation or shedding), and therefore water diffusion time, in response to molecular stimuli (**Figure 3.5b**).

### 3.5. Experimental Section

**Materials:** Iron(III) oxide (FeO(OH), hydrated, catalyst grade, 30-50 mesh), 1-octadecene (1-ODE, technical grade 90 %), oleic acid (OA, technical grade 90 %), octylamine (99 %), 2-

acrylamido-2-methylpropane sulfonic acid copolymer (PAMPS), poly(acrylic acid) (PAA,  $M_w = 1800$  Da), lauryl acrylate (LA, technical grade 90 %), poly(maleic anhydride-alt-1-octadecene) (PMAO,  $M_w = 30,000 - 50,000$ ), calcium sulfate ( $\geq 97.0$  %), 1 % penicillin-streptomycin (PS), Dulbecco's Modified Eagle's Medium (DMEM, ATTC, Manassas, VA), fetal bovine serum (FBS), and trypsin-EDTA were obtained from Sigma-Aldrich. Acetone (99.5 %), nitric acid ( $\text{HNO}_3$ , 70 %), diethyl ether (DEE, certified ACS), ethanol (99.8 %), methanol (certified ACS), dimethylformamide (DMF, 99.8 %), hexanes (98.5 %), 1-ethyl-3-[3-dimethylaminopropyl] carbodiimide hydrochloride (EDC), sodium bicarbonate (99.7 %), and hydrogen peroxide ( $\text{H}_2\text{O}_2$ , 30 %) were obtained from Fisher Scientific. Methyl ether poly(ethylene glycol) amine (mPEG-NH<sub>2</sub>) ( $M_w = 2,000$  Da) was obtained from Laysan Bio. Human dermal fibroblasts (HDF) were obtained from Cambrex. CellTiter 96® Aqueous One solution Cell Proliferation Assay (MTS assay) was obtained from Promega.

**Synthesis of size-controlled iron oxide nanocrystals:** Hydrophobic iron oxide nanocrystals (IONCs) were synthesized by a modified procedure reported previously by our group.<sup>92</sup> Iron(III) oxide ( $\text{FeO}(\text{OH})$ , 0.178 g), oleic acid (OA, 2.26 g), and 1-octadecene (1-ODE, 5 g) are mixed in a 100 ml three neck flask and heated to 120 °C for 2 h to remove residual water. The solution is then heated to 240 °C for 30 min to generate iron oleate which is a precursor to nanocrystal formation. After further heating to 320 °C for 2 h under inert conditions ( $\text{N}_2$ ), the precursor decomposes yielding IONCs. To purify the resulting black colloidal nanocrystal sample, 20 mL of methanol and 20 mL acetone are added to 5 mL of sample and centrifuged at 4150 rpm for 30 min. Treatment with hexanes allows this precipitate to be dissolved, and the process of centrifugation and resuspension is

repeated six times. The final solution containing 10 nm IONCs is stored in hexanes. For 16 nm IONCs, the molar ratio between FeO(OH) and oleic acid is changed from 1:4 to 1:5 with all other conditions remaining the same. For 4 nm IONCs, the above prepared iron oleate (0.15 mmol, 0.09 g) and oleic acid (0.3 mmol, 0.08 g) are mixed with 5 g 1-ODE at 320 °C for 0.5 h under inert conditions (N<sub>2</sub>). For 33 nm IONCs, a mixture of FeO(OH) (50 mmol, 4.5 g), oleic acid (200 mmol, 56 g), and 1-ODE (40 mmol, 10 g) are heated to 240 °C for 2 h and then 320 °C for 12 h.

**Oleic acid bilayer coating:** An oleic acid bilayer serves as a suitable coating for these materials and is generated following a previously published procedure.<sup>97</sup> Briefly, oleic acid (0.95 – 9.5 μM) is mixed with 1 mL of nanocrystal solution dispersed in ethyl ether (1,500 – 4,000 mg Fe L<sup>-1</sup>). After stirring the mixture for 24 h, ultrapure water (Millipore, 18.2 MΩ) or 0.1 M sodium bicarbonate (pH 9) solution is added and stirred for an additional 2 h. To facilitate dispersion in water, the sample is probe sonicated (UP 50H, Hielscher Ultrasonics) at a 60 % amplitude for 10 min. While stirring, the sample is uncovered for 24 h resulting in the complete evaporation of residual organic solvent. Sample purification is carried out using ultracentrifugation (Optima L-90K ultracentrifuge, Beckman coulter) at 35,000 rpm for 3 h twice, followed by syringe filtration (pore size of 0.45 μM, Whatman NYL). Inductively coupled plasma–optical emission spectroscopy (Agilent, ICP-OES) is used to determine the phase transfer yield by the iron concentration of samples before and after phase transfer.

**Octylamine (OA)-modified poly(acrylic acid) (PAA-OA) coating:** Octylamine-modified poly(acrylic acid) (PAA-OA) polymer and PAA-OA coated nanocrystals were prepared by a

previously published procedure.<sup>98</sup> To generate PAA-OA, PAA (0.6 g, 0.33 mmol) is dissolved in DMF (10 g) and stirred for 10 min. Then, EDC (0.58 g, 3 mmol) is added to PAA/DMF solution, followed by octylamine (0.5 mL, 3 mmol). After stirring overnight, a rotary evaporator (Buchi Rotavapor R-200) is used to remove DMF as the PAA-OA solution is subjected to vacuum. The final PAA-OA solution (15 mg mL<sup>-1</sup>) is dispersed in chloroform (40 mL).

PAA-OA polymer solutions (1 – 7 mL) are mixed with 1mL nanocrystal solution (typically 1,500 – 4,000 mg Fe L<sup>-1</sup> in chloroform) and stirred for 24 h. Chloroform is allowed to evaporate using air or vacuum. Sodium bicarbonate (0.1 M) is added for every 10 mL of solution and the resulting suspension is probe sonicated at 60 % amplitude for 10 min. Purification relies on ultracentrifugation (40,000 rpm for 3 hours, twice) and syringe filtration (0.45 μM, Whatman NYL) providing a black product that is easily dispersed in ultrapure water (Millipore, 18.2 MΩ).<sup>61</sup> Inductively coupled plasma–optical emission spectroscopy (ICP-OES) is used to determine the phase transfer yield through the measurement of the iron concentration of samples before and after phase transfer.

#### **Poly(2-acrylamido-2-methylpropane sulfonic acid) (PAMPS)-lauryl acrylate (LA)**

**(PAMPS-LA) coating:** Poly(2-acrylamido-2-methylpropane sulfonic acid)-lauryl acrylate (PAMPS-LA) is synthesized via copolymerization of 30 g of AMPS (207.23 Da, 0.1447 mol) and 22.5 mL of LA (240.38 Da, 0.0827 mol) in 300 mL of DMF solution. This photoinitiated reaction occurs when exposed to ultraviolet light of 352 nm wavelength. As synthesized PAMPS-LA was used without further purification. The varied ratios of PAMPS-LA polymer per nanocrystal are prepared by adding 1 – 7 mL (15 mg ml<sup>-1</sup> in DMF) to 1 mL nanocrystal

solution (typically 1,500 – 4,000 mg Fe L<sup>-1</sup> in diethyl ether (DEE)). If the mixture is cloudy, more DMF may be added to further solubilize the polymer. After stirring for 24 h, 10 mL of ultrapure Milli-Q water is added, and the solution is stirred uncovered for 24 h and the diethyl ether is evaporated. Samples are purified of excess free polymer in solution using ultracentrifugation (40,000 rpm for 3 hours, twice) and syringe filtration (0.45 μM, Whatman NYL) and redispersed in ultrapure water. Inductively coupled plasma–optical emission spectroscopy (Agilent, ICP-OES) is used to determine the phase transfer yield from the iron concentration of samples before and after phase transfer.

**Poly(maleic anhydride-alt-1-octadecene) (PMAO)- poly(ethylene glycol) (PEG) methyl ethers (mPEG-NH<sub>2</sub>) (PMAO-PEG) coating:** The method for coating poly(maleic anhydride-alt-1-octadecene-poly(ethylene glycol) (PMAO-PEG) onto nanocrystals is adapted from a previously reported protocol.<sup>62</sup> PMAO (M<sub>w</sub> = 30 – 50 kDa) is mixed with mPEG-NH<sub>2</sub> (M<sub>w</sub> = 2 kDa) in chloroform and stirred overnight to make the PMAO-PEG amphiphilic copolymer (molar ratio of PMAO/PEG, 1:5 to 1:30). The varied ratios of PMAO-PEG to nanocrystal are prepared by adding 1 – 7 mL (20 mg L<sup>-1</sup>) of polymer solutions to 1 mL nanocrystal solutions (typically 1,500 – 4,000 mg Fe L<sup>-1</sup> in chloroform) followed by 24 hours of stirring. During this time chloroform is allowed to evaporate using air or vacuum. After adding 0.1 M sodium bicarbonate (10 mL), the mixture is probe sonicated at 60 % amplitude for 10 min. Purification proceeds using ultracentrifugation (40,000 rpm for 3 hours, twice) and syringe filtration (0.45 μM, Whatman NYL), followed by redispersion of purified product into ultrapure water. Inductively coupled plasma–optical emission spectroscopy (ICP-



OES) is used to determine the phase transfer yield by the iron concentration of samples before and after phase transfer.

**Transmission electron microscopy (TEM):** The nanocrystal sample diameter and size variation are determined using a field emission JEOL 2100 transmission electron microscope (TEM) operating at 200 kV with a single tilt holder. Samples are prepared for TEM by evaporating one drop of nanocrystal solution on an ultrathin 400 mesh copper grid (Ted Pella Inc.). Average nanocrystal size is determined using Image-Pro Plus 5.0 (Media Cybernetics, Inc., Silver Spring, MD) image analysis software to detect edges, smooth holes, and determine the diameter for at least 500 nanocrystals per sample.

**X-Ray Diffraction (XRD):** The nanocrystal sample crystallinity is determined using a Bruker D8 Discovery 2D x-ray diffractometer operating at 40 mA and 40 kV with a Cu tube (1.5413 Å). A highly concentrated representative nanocrystal sample is drop cast onto a glass slide and allowed to dry. The diffraction pattern is smoothed using Microsoft Excel.

**Dynamic light scattering (DLS):** The hydrodynamic diameter (nm) and zeta potential (mV) of all synthesized and surface functionalized materials is measured using a ZEN-3600 Zetasizer Nano (Malvern, UK) equipped with a HeNe 633 nm laser. The recorded number averaged hydrodynamic diameter (nm) is the average of five measurements for each sample.

**Inductively coupled plasma-optical emission spectroscopy (ICP-OES):** To measure the concentration of iron, a Perkin Elmer ICP-OES equipped with an auto sampler is used.

Samples are prepared for ICP-OES analysis by acid digestion using nitric acid (HNO<sub>3</sub>, 70 %) followed by hydrogen peroxide (H<sub>2</sub>O<sub>2</sub>, 30 %).

**Matrix assisted laser desorption ionization time-of-flight mass spectroscopy (MALDI-TOF-MS):** To measure the molecular weight of polymers a matrix assisted laser desorption ionization time-of-flight (MALDI-TOF) mass spectrometer (Bruker Autoflex II MALDI-ToF) equipped with a nitrogen laser operated at 337 nm is used. To prepare samples for analysis, 1  $\mu$ L of polymer is dissolved in a 4:1 solution of acetonitrile and water with 0.1 % (v/v) trifluoroacetic acid. Then, trace  $\alpha$ -cyano-4-hydroxycinnamic acid matrix is dissolved in a 4:1 solution of acetonitrile and water with 0.1% (v/v) trifluoroacetic acid. After evaporating 1  $\mu$ L of the sample solution on the plate, another 1  $\mu$ L of matrix solution is overlaid on sample spot and allowed to dry.

**Vibrating Sample Magnetometry (VSM):** Sample saturation magnetization was measured using a Lake Shore 7400 Series vibrating sample magnetometer. Prior to analysis, solid samples obtained from dried nanocrystal solutions were mixed with a non-magnetic matrix. Solid samples were prepared by mixing 100  $\mu$ L of nanocrystal solution (1000 ppm Fe) with 10 mg calcium sulfate and drying at 60 °C. The hysteresis loop was measured at room temperature between 10,000 and -10,000 Oe. Representative 5, 8, 13, 19, and 31 nm IONCs were synthesized as previously reported and used for these experiments. The mass saturation magnetization ( $M_s$ , emu g<sup>-1</sup>) of these samples at 10,000 Oe were plotted against their diameters (nm). These data were fit logarithmically and used as a standard curve to find the saturation magnetization for the 4, 10, 16, and 33 nm IONCs used in all previous experiments. For comparisons of literature magnetization values in Table 2,  $M_s$

is converted to volumic saturation magnetization ( $M_v$ ,  $10^5 \text{ A m}^{-1}$ ) using  $\rho_{\text{magnetite}} = 5.18 \times 10^6 \text{ g m}^{-3}$  and the conversion factor from emu to  $\text{A m}^2$  ( $1 \text{ emu} = 10^3 \text{ A m}^2$ ).

**Relaxivity measurements:** Various concentrations of nanocrystals are prepared by dilution from stock aqueous solutions of nanocrystals with different coatings for MR relaxivity measurement. The concentration of nanocrystals in the stock is determined as described below. An MR relaxometer (NMR analyzer, mq60, Bruker, 1.41 T) is used to determine the  $1/T_2$  of each sample over a range of concentrations. The  $r_2$  of each sample is determined from the slope of  $1/T_2$  plotted as a function of Fe concentration. Using Equation 3,  $C/D_{\text{coating}}$  and therefore  $D_{\text{coating}}$  can be approximated from the slope of the line generated from a plot of  $r^2/M_v^2$  as a function of  $d^2$  for each coating using samples in MAR (according to Figure 3.4).  $v_{\text{mat}}$  is the molar volume of magnetic ions in the material defined as the ratio of the volume fraction of nanocrystals in solution ( $f$ ) to the atomic concentration of magnetic ions  $[M]$  ( $v_{\text{mat}} = f/[M]$ ;  $v_{\text{magnetite}} = 0.2314 \text{ kg mol}^{-1} / 3(5180 \text{ kg m}^{-3}) = 1.49 \times 10^{-5} \text{ m}^3 \text{ mol}^{-1}$ ),

**In vitro MRI phantoms:** *In vitro*  $T_2$  weighted MR phantom studies were performed in a clinical 3 T scanner (Philips Ingenia®) using a turbo spin echo (TSE) sequence with TR = 2500 ms, TE = 100 ms and a slice thickness of 400 mm. Images are collected from IONC samples with different concentrations, core sizes, and coating.

**Cell Culture and MTS Assay:** Human dermal fibroblasts (HDF, Cambrex) are cultured in Dulbecco's Modified Eagle's Medium (DMEM, ATCC, Manassas, VA) with 10 % fetal bovine serum (FBS) and 1 % penicillin-streptomycin (PS). HDF cells are floated by trypsin-EDTA and resuspended in media (DMEM with 10 % FBS and 1 % PS) solution for the passaging.

A standard colorimetric MTS assay (CellTiter 96, Promega) is used to determine the nanocrystal cytotoxicity. HDF cells are grown in 96 well culture plates with over 80 % confluency. Each set is prepared with different concentrations of nanocrystal solutions. One set is treated as a blank (no nanocrystals) and the last set is used for the untreated control (ethanol). Cells are incubated with select aqueous nanocrystal solution for 24 h. This solution is then suctioned out and replaced with 100  $\mu$ L of fresh media (DMEM with FBS 10 % and 1 % PS) solution and 20  $\mu$ L MTS agent in each well. After incubation for 1 h at 37 °C and 5 % CO<sub>2</sub>, the solution absorbance at 490 nm is measured via plate reader (Spectra Max, M2, Molecular devices). All experiments are done in triplicate. The LD<sub>50</sub> for each sample, which gives the dose required for 50 % cell death, is calculated by the percentage of cell viability.

**Total organic carbon (TOC) analysis:** A Shimadzu TOC-L is used to measure the carbon concentration for surface functionalized nanocrystals in water. Samples are prepared by diluting 1 ml of the stock nanocrystal solution to 8.5 mL with Milli-Q water. Each sample is run on a total non-purgeable organic carbon (NPOC) assay with triplicate 50  $\mu$ L injections. A standard calibration curve is made based on a range of carbon concentrations (0.5 – 60 ppm) prepared using a TOC standard solution (Sigma-Adrich) (R<sup>2</sup> = 0.998).

**Grafting Density Calculation:** Grafting density ( $\sigma$ ) is calculated from TOC data using the equation below:<sup>99</sup>

$$\sigma = \frac{[C]*M_n}{M_p*C_n*[NP]*(4\pi r_{core}^2)} \quad (1)$$

The non-purgeable organic carbon concentration ( $[C]$ ) from the TOC analysis is converted from  $\text{mg L}^{-1}$  (ppm) to  $\text{mol L}^{-1}$  (M) by using molar mass of carbon ( $12,010 \text{ mg mol}^{-1}$ ). To determine the number of polymer molecules grafted on the nanocrystal surface ( $\sigma$ ), the carbon concentration is multiplied by the molecular weight of the monomer ( $M_n$ ) and divided by the polymer molecular weight ( $M_p$ ), number of carbons per monomer ( $C_n$ ), molar concentration of nanocrystals ( $[NP]$ ), and surface area of the nanocrystal ( $4\pi r_{core}^2$ ).

### 3.6. Supporting Information

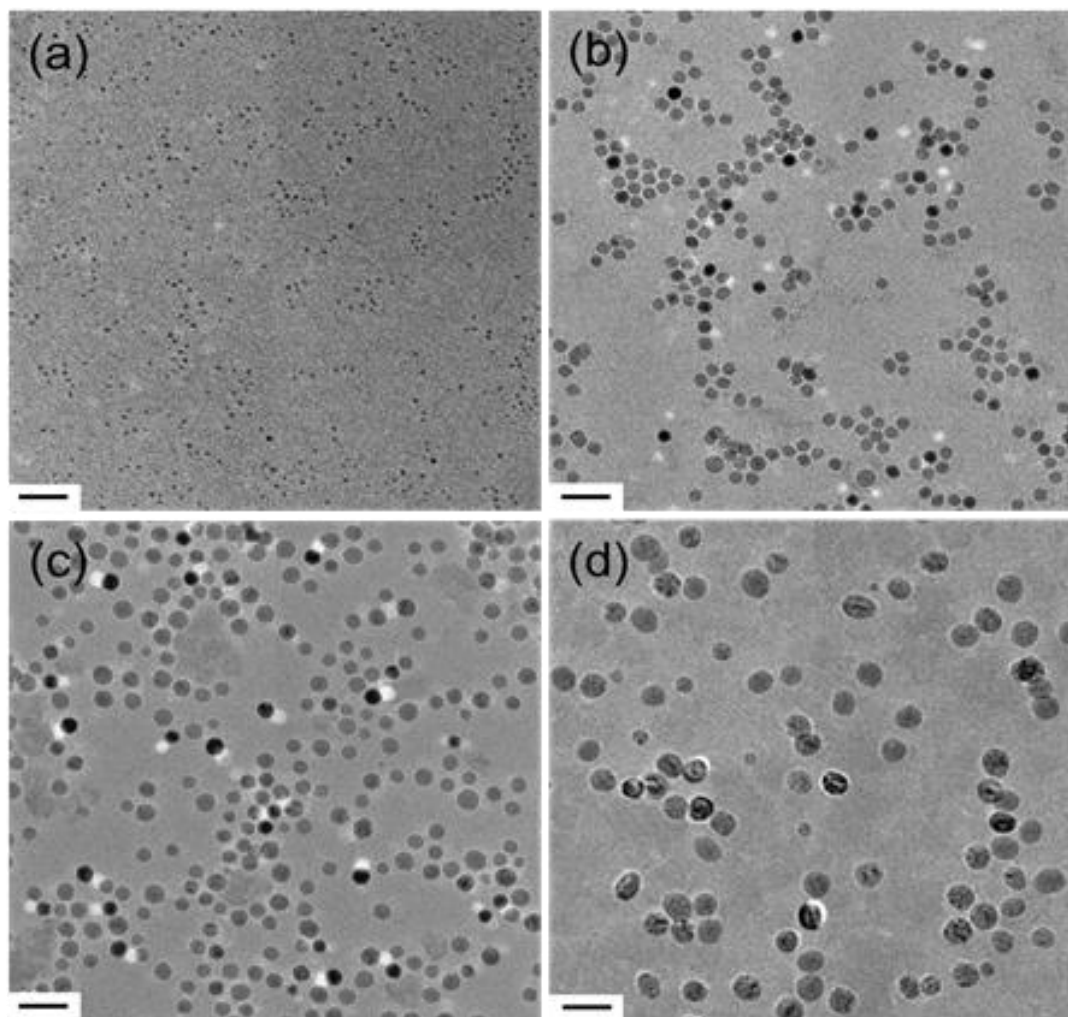


**Figure S3.1 TEM images of IONC.** TEM images of iron oxide nanocrystals phase transferred using (a) oleic acid bilayer, (b) PAA-OA, (c) PAMPS-LA, and (d) PMAO-PEG polymers with core sizes  $4.1 \pm 0.8$ ,  $10.4 \pm 1.2$ ,  $16.6 \pm 0.8$ , and  $33.4 \pm 2.3$  nm, respectively (scale bars = 20 nm). Size and morphology maintained before and after phase transfer.

**Table S3.1** Hydrodynamic size of iron oxide nanocrystals with single layer surface coatings.

Sample (10 nm iron oxide)	PEG 200	PEG 1K	PVP 10K	PEG 10K	PAA 15K
Hydrodynamic size (nm)	31.3 ± 8.7	33.4 ± 6.8	36.1 ± 5.3	39.3 ± 6.1	48.8 ± 4.5
$r_2$ (mM <sup>-1</sup> s <sup>-1</sup> ) at 1.41T	101.5 ± 1.3	105.7 ± 3.0	138.6 ± 5.3	195.7 ± 6.7	202.3 ± 6.9

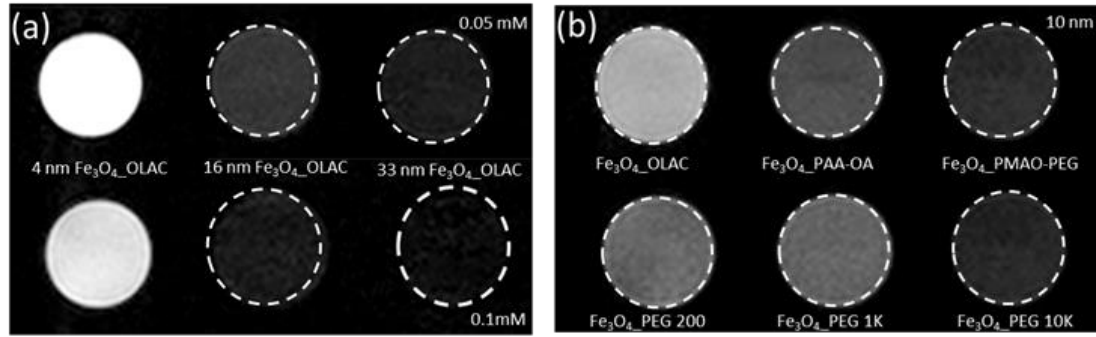


**Figure S3.2 T2-weighted MR phantom images of IONCs.** (a) Iron oxide nanocrystals depending on their sizes (4, 16, 33 nm) at different concentration of Fe ions (0.05 mM, 0.1 mM), and (b) iron oxide nanocrystals (10 nm core, 0.05 mM) with different surface coatings (oleic acid (OLAC) bilayer, PAA-OA, PMAO-PEG, PEG 200, PEG 1K, and PEG 10K). Darker contrast corresponds to a shorter T2 and therefore larger nanocrystal  $r_2$ .



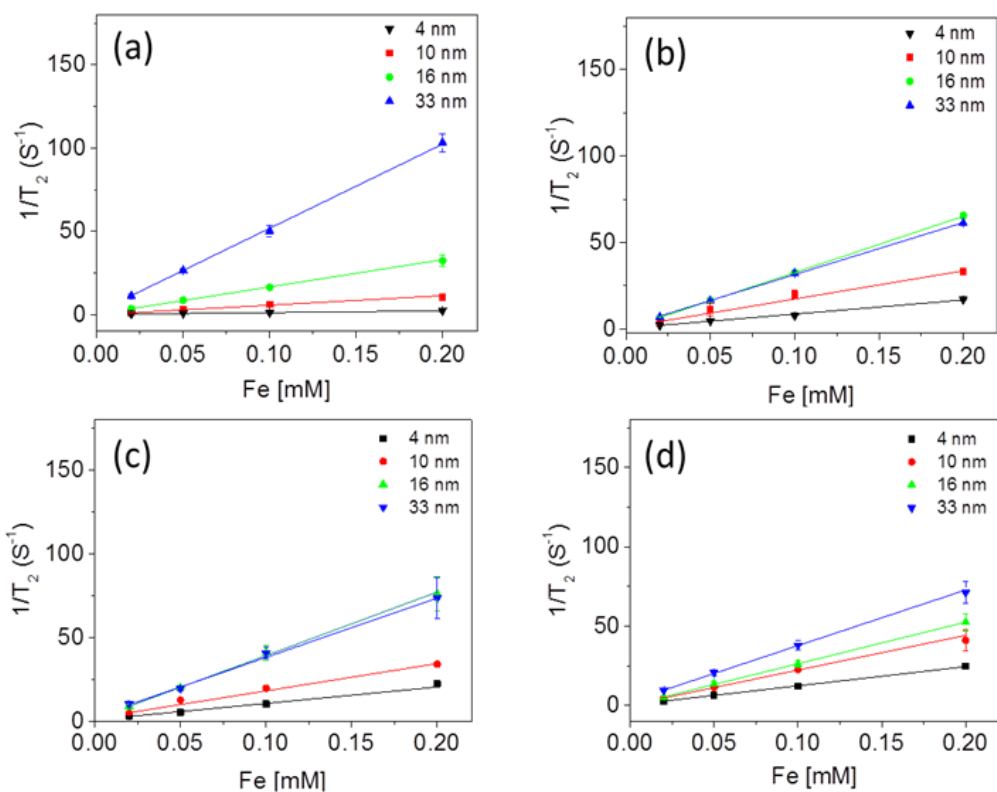


**Figure S3.3 Plots of  $1/T_2$  values of iron oxide nanocrystals.** Plots of  $r_2$  values of iron oxide nanocrystals depending on their core diameters (4 to 33 nm) and surface coatings (oleic acid, PAA-OA, PAMPS-LA, and PAMO-PEG) (a-d).

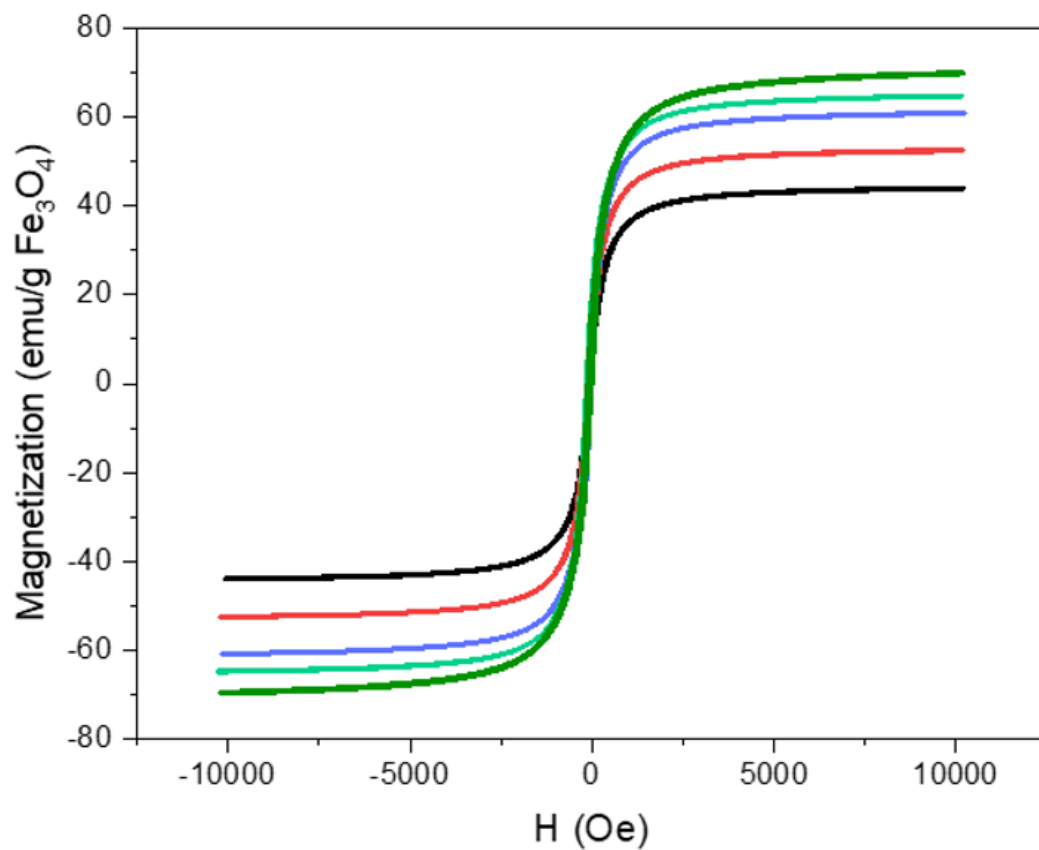


**Figure S3.4 IONC magnetization.** Magnetization curves for 5, 8, 13, 19, and 31 nm iron oxide nanocrystals (black, red, blue, light green, and dark green). Magnetization values for 4.0, 10.2, 16.0, and 33.1 nm iron oxide nanocrystals used experimentally obtained from standard curve using these data.

**Table S3.2** Molecular weight and grafting densities of iron oxide nanocrystals with different surface coatings.

33 nm iron oxide	Oleic acid	PAA-OA	PAMPS-LA	PMAO-PEG
Molecular Weight (g mol <sup>-1</sup> )	283	2783	4615	30,000 - 50,000
Grafting Density (molecules nm <sup>-2</sup> )	12.13	4.11	3.67	0.00362

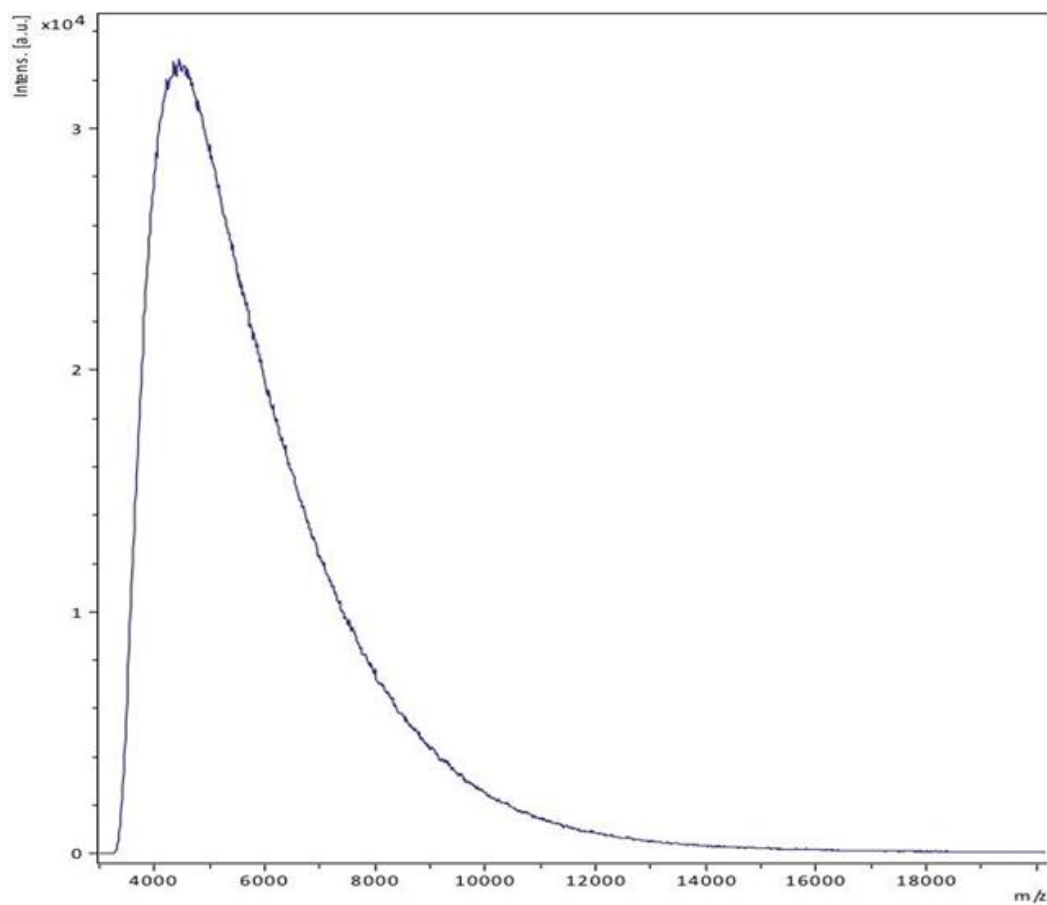
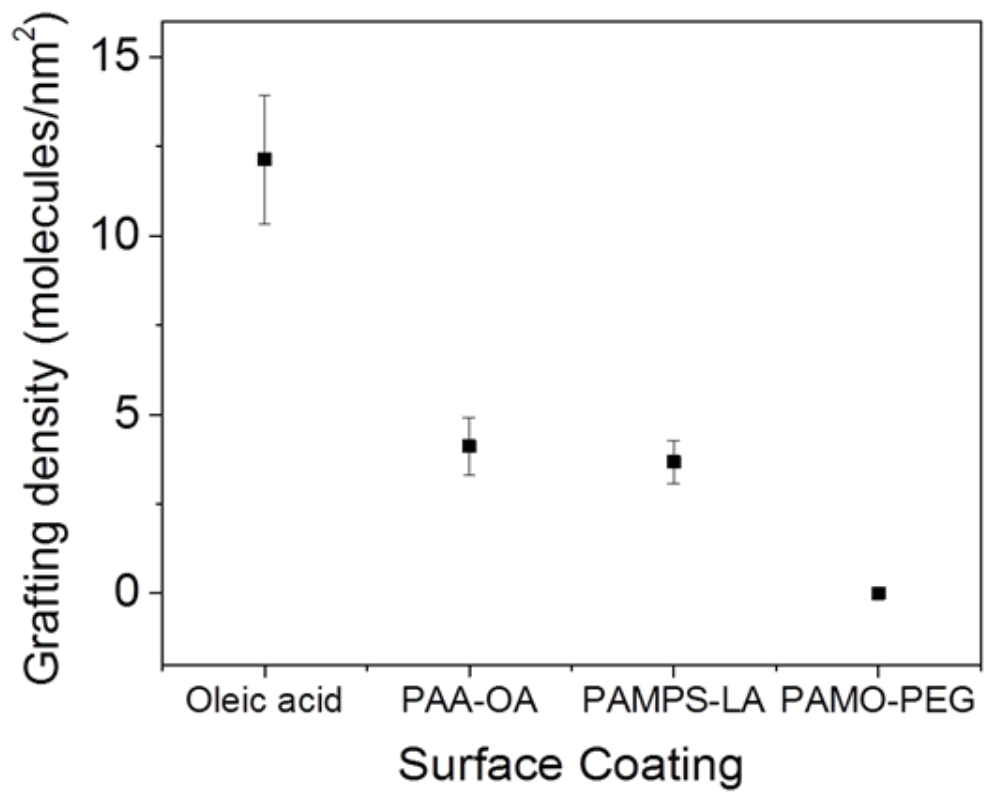


Figure S3.5 MALDI-TOF of PAMPS-LA. The average m/z of PAMPS-LA is 4615 Da.



**Figure S3.6 IONC surface coating grafting density.** Grafting densities of iron oxide nanocrystal with oleic acid bilayer, PAA-OA, PAMPS-LA, and PMAO-PEG surface coatings.

### 3.7. References

1. Wahsner, J.; Gale, E. M.; Rodriguez-Rodriguez, A.; Caravan, P., Chemistry of MRI Contrast Agents: Current Challenges and New Frontiers. *Chem. Rev.* **2019**, *119* (2), 957-1057.
2. Ni, D. L.; Bu, W. B.; Ehlerding, E. B.; Cai, W. B.; Shi, J. L., Engineering of inorganic nanoparticles as magnetic resonance imaging contrast agents. *Chem. Soc. Rev.* **2017**, *46* (23), 7438-7468.
3. Zhou, Z. J.; Yang, L. J.; Gao, J. H.; Chen, X. Y., Structure-Relaxivity Relationships of Magnetic Nanoparticles for Magnetic Resonance Imaging. *Adv. Mater.* **2019**, *31* (8), 32.
4. Stueber, D. D.; Villanova, J.; Aponte, I.; Xiao, Z.; Colvin, V. L., Magnetic Nanoparticles in Biology and Medicine: Past, Present, and Future Trends. *Pharmaceutics* **2021**, *13* (7), 943.
5. Arami, H.; Khandhar, A.; Liggitt, D.; Krishnan, K. M., In vivo delivery, pharmacokinetics, biodistribution and toxicity of iron oxide nanoparticles. *Chemical Society reviews* **2015**, *44* (23), 8576-8607.
6. Malhotra, N.; Lee, J.-S.; Liman, R. A. D.; Ruallo, J. M. S.; Villaflores, O. B.; Ger, T.-R.; Hsiao, C.-D., Potential Toxicity of Iron Oxide Magnetic Nanoparticles: A Review. *Molecules* **2020**, *25* (14), 3159.
7. Yeap, S. P.; Lim, J.; Ooi, B. S.; Ahmad, A. L., Agglomeration, colloidal stability, and magnetic separation of magnetic nanoparticles: collective influences on environmental engineering applications. *Journal of Nanoparticle Research* **2017**, *19* (11), 368.
8. Gao, G. H.; Im, G. H.; Kim, M. S.; Lee, J. W.; Yang, J.; Jeon, H.; Lee, J. H.; Lee, D. S., Magnetite-Nanoparticle-Encapsulated pH-Responsive Polymeric Micelle as an MRI Probe for Detecting Acidic Pathologic Areas. *Small* **2010**, *6* (11), 1201-1204.
9. Gallo, J.; Kamaly, N.; Lavdas, I.; Stevens, E.; Nguyen, Q. D.; Wylezinska-Arridge, M.; Aboagye, E. O.; Long, N. J., CXCR4-targeted and MMP-responsive iron oxide nanoparticles for enhanced magnetic resonance imaging. *Angew Chem Int Ed Engl* **2014**, *53* (36), 9550-4.
10. Hsieh, V.; Okada, S.; Wei, H.; Garcia-Alvarez, I.; Barandov, A.; Alvarado, S. R.; Ohlendorf, R.; Fan, J. X.; Ortega, A.; Jasanoff, A., Neurotransmitter-Responsive Nanosensors for T2-Weighted Magnetic Resonance Imaging. *Journal of the American Chemical Society* **2019**, *141* (40), 15751-15754.
11. Li, F. Y.; Liang, Z. Y.; Liu, J. N.; Sun, J. H.; Hu, X.; Zhao, M.; Liu, J. X.; Bai, R. L.; Kim, D.; Sun, X. L.; Hyeon, T.; Ling, D. S., Dynamically Reversible Iron Oxide Nanoparticle Assemblies for Targeted Amplification of T1-Weighted Magnetic Resonance Imaging of Tumors. *Nano Lett.* **2019**, *19* (7), 4213-4220.

12. Liu, W.; Yin, S. Y.; Hu, Y. C.; Deng, T.; Li, J. S., Microemulsion-Confined Biomineralization of PEGylated Ultrasmall Fe<sub>3</sub>O<sub>4</sub> Nanocrystals for T<sub>2</sub>-T<sub>1</sub> Switchable MRI of Tumors. *Analytical Chemistry* **2021**, *93* (42), 14223-14230.
13. Lu, J. X.; Sun, J. H.; Li, F. Y.; Wang, J.; Liu, J. N.; Kim, D.; Fan, C. H.; Hyeon, T.; Ling, D. S., Highly Sensitive Diagnosis of Small Hepatocellular Carcinoma Using pH-Responsive Iron Oxide Nanocluster Assemblies. *Journal of the American Chemical Society* **2018**, *140* (32), 10071-10074.
14. Osborne, E. A.; Jarrett, B. R.; Tu, C. Q.; Louie, A. Y., Modulation of T<sub>2</sub> Relaxation Time by Light-Induced, Reversible Aggregation of Magnetic Nanoparticles. *Journal of the American Chemical Society* **2010**, *132* (17), 5934-+.
15. Perez, J. M.; Josephson, L.; O'Loughlin, T.; Högemann, D.; Weissleder, R., Magnetic relaxation switches capable of sensing molecular interactions. *Nature Biotechnology* **2002**, *20* (8), 816-820.
16. Wu, B.; Deng, K.; Lu, S. T.; Zhang, C. J.; Ao, Y. W.; Wang, H.; Mei, H.; Wang, C. X.; Xu, H. B.; Hu, B.; Huang, S. W., Reduction-active Fe<sub>3</sub>O<sub>4</sub>-loaded micelles with aggregation-enhanced MRI contrast for differential diagnosis of Neuroglioma. *Biomaterials* **2021**, 268.
17. Yigit, M. V.; Mazumdar, D.; Kim, H. K.; Lee, J. H.; Odintsov, B.; Lu, Y., Smart "turn-on" magnetic resonance contrast agents based on aptamer-functionalized superparamagnetic iron oxide nanoparticles. *ChemBioChem* **2007**, *8* (14), 1675-8.
18. Yigit, M. V.; Mazumdar, D.; Lu, Y., MRI Detection of Thrombin with Aptamer Functionalized Superparamagnetic Iron Oxide Nanoparticles. *Bioconjugate Chemistry* **2008**, *19* (2), 412-417.
19. Yuan, Y.; Ding, Z.; Qian, J.; Zhang, J.; Xu, J.; Dong, X.; Han, T.; Ge, S.; Luo, Y.; Wang, Y.; Zhong, K.; Liang, G., Casp3/7-Instructed Intracellular Aggregation of Fe<sub>3</sub>O<sub>4</sub> Nanoparticles Enhances T<sub>2</sub> MR Imaging of Tumor Apoptosis. *Nano Letters* **2016**, *16* (4), 2686-2691.
20. Danhier, F., To exploit the tumor microenvironment: Since the EPR effect fails in the clinic, what is the future of nanomedicine? *J. Control. Release* **2016**, *244*, 108-121.
21. Hingorani, D. V.; Bernstein, A. S.; Pagel, M. D., A review of responsive MRI contrast agents: 2005-2014. *Contrast Media & Molecular Imaging* **2015**, *10* (4), 245-265.
22. Brooks, R. A.; Moyny, F.; Gillis, P., On T<sub>2</sub>-shortening by weakly magnetized particles: The chemical exchange model†. *Magnetic Resonance in Medicine* **2001**, *45* (6), 1014-1020.
23. Gillis, P.; Moyny, F.; Brooks, R. A., On T<sub>2</sub>-shortening by strongly magnetized spheres: a partial refocusing model. *Magn Reson Med* **2002**, *47* (2), 257-63.

24. Vuong, Q. L.; Berret, J.-F.; Fresnais, J.; Gossuin, Y.; Sandre, O., A Universal Scaling Law to Predict the Efficiency of Magnetic Nanoparticles as MRI T2-Contrast Agents. *Advanced Healthcare Materials* **2012**, *1* (4), 502-512.
25. Xiao, Y.; Du, J., Superparamagnetic nanoparticles for biomedical applications. *J Mater Chem B* **2020**, *8* (3), 354-367.
26. Kim, B. H.; Lee, N.; Kim, H.; An, K.; Park, Y. I.; Choi, Y.; Shin, K.; Lee, Y.; Kwon, S. G.; Na, H. B.; Park, J. G.; Ahn, T. Y.; Kim, Y. W.; Moon, W. K.; Choi, S. H.; Hyeon, T., Large-scale synthesis of uniform and extremely small-sized iron oxide nanoparticles for high-resolution T1 magnetic resonance imaging contrast agents. *J Am Chem Soc* **2011**, *133* (32), 12624-31.
27. Huang, J.; Bu, L.; Xie, J.; Chen, K.; Cheng, Z.; Li, X.; Chen, X., Effects of Nanoparticle Size on Cellular Uptake and Liver MRI with Polyvinylpyrrolidone-Coated Iron Oxide Nanoparticles. *ACS Nano* **2010**, *4* (12), 7151-7160.
28. Jun, Y.-w.; Huh, Y.-M.; Choi, J.-s.; Lee, J.-H.; Song, H.-T.; Kim, S.; Yoon, S.; Kim, K.-S.; Shin, J.-S.; Suh, J.-S.; Cheon, J., Nanoscale Size Effect of Magnetic Nanocrystals and Their Utilization for Cancer Diagnosis via Magnetic Resonance Imaging. *Journal of the American Chemical Society* **2005**, *127* (16), 5732-5733.
29. Choo, E. S. G.; Peng, E.; Rajendran, R.; Chandrasekharan, P.; Yang, C.-T.; Ding, J.; Chuang, K.-H.; Xue, J., Superparamagnetic Nanostructures for Off-Resonance Magnetic Resonance Spectroscopic Imaging. *Advanced Functional Materials* **2013**, *23* (4), 496-505.
30. de Moura, C. L.; Gallo, J.; Garcia-Hevia, L.; Pessoa, O. D. L.; Ricardo, N.; Banobre-Lopez, M., Magnetic Hybrid Wax Nanocomposites as Externally Controlled Theranostic Vehicles: High MRI Enhancement and Synergistic Magnetically Assisted Thermo/Chemo Therapy. *Chemistry-a European Journal* **2020**, *26* (20), 4531-4538.
31. He, J. P.; Liu, X. H.; Niu, D. C.; Chen, J. Z.; Qin, X.; Li, Y. S., Supramolecular-based PEGylated magnetic hybrid vesicles with ultra-high transverse relaxivity. *Applied Materials Today* **2018**, *11*, 238-245.
32. Jang, J. T.; Nah, H.; Lee, J. H.; Moon, S. H.; Kim, M. G.; Cheon, J., Critical Enhancements of MRI Contrast and Hyperthermic Effects by Dopant-Controlled Magnetic Nanoparticles. *Angewandte Chemie-International Edition* **2009**, *48* (7), 1234-1238.
33. Kostevsek, N.; Cheung, C. C. L.; Sersa, I.; Kreft, M. E.; Monaco, I.; Franchini, M. C.; Vidmar, J.; Al-Jamal, W. T., Magneto-Liposomes as MRI Contrast Agents: A Systematic Study of Different Liposomal Formulations. *Nanomaterials* **2020**, *10* (5).
34. Lee, N.; Choi, Y.; Lee, Y.; Park, M.; Moon, W. K.; Choi, S. H.; Hyeon, T., Water-Dispersible Ferrimagnetic Iron Oxide Nanocubes with Extremely High r2 Relaxivity for Highly Sensitive in Vivo MRI of Tumors. *Nano Letters* **2012**, *12* (6), 3127-3131.



35. Tromsdorf, U. I.; Bigall, N. C.; Kaul, M. G.; Bruns, O. T.; Nikolic, M. S.; Mollwitz, B.; Sperling, R. A.; Reimer, R.; Hohenberg, H.; Parak, W. J.; Forster, S.; Beisiegel, U.; Adam, G.; Weller, H., Size and surface effects on the MRI relaxivity of manganese ferrite nanoparticle contrast agents. *Nano Letters* **2007**, *7* (8), 2422-2427.
36. Yang, L.; Ma, L.; Xin, J.; Li, A.; Sun, C.; Wei, R.; Ren, B. W.; Chen, Z.; Lin, H.; Gao, J., Composition Tunable Manganese Ferrite Nanoparticles for Optimized T2 Contrast Ability. *Chemistry of Materials* **2017**, *29* (7), 3038-3047.
37. Zhao, Z.; Zhou, Z.; Bao, J.; Wang, Z.; Hu, J.; Chi, X.; Ni, K.; Wang, R.; Chen, X.; Chen, Z.; Gao, J., Octapod iron oxide nanoparticles as high-performance T<sub>2</sub> contrast agents for magnetic resonance imaging. *Nat Commun* **2013**, *4*, 2266.
38. Mohapatra, J.; Mitra, A.; Tyagi, H.; Bahadur, D.; Aslam, M., Iron oxide nanorods as high-performance magnetic resonance imaging contrast agents. *Nanoscale* **2015**, *7* (20), 9174-9184.
39. Xiao, Z.; Zhang, Q.; Guo, X.; Villanova, J.; Hu, Y.; Külaots, I.; Garcia-Rojas, D.; Guo, W.; Colvin, V. L., Libraries of Uniform Magnetic Multicore Nanoparticles with Tunable Dimensions for Biomedical and Photonic Applications. *ACS Applied Materials & Interfaces* **2020**, *12* (37), 41932-41941.
40. Cowger, T. A.; Tang, W.; Zhen, Z.; Hu, K.; Rink, D. E.; Todd, T. J.; Wang, G. D.; Zhang, W.; Chen, H.; Xie, J., Casein-Coated Fe<sub>5</sub>C<sub>2</sub> Nanoparticles with Superior r<sub>2</sub> Relaxivity for Liver-Specific Magnetic Resonance Imaging. *Theranostics* **2015**, *5* (11), 1225-32.
41. Ahmadpoor, F.; Masood, A.; Feliu, N.; Parak, W. J.; Shojaosadati, S. A., The Effect of Surface Coating of Iron Oxide Nanoparticles on Magnetic Resonance Imaging Relaxivity. *Frontiers in Nanotechnology* **2021**, *3*.
42. Jedlovsky-Hajdú, A.; Tombácz, E.; Bányai, I.; Babos, M.; Palkó, A., Carboxylated magnetic nanoparticles as MRI contrast agents: Relaxation measurements at different field strengths. *Journal of Magnetism and Magnetic Materials* **2012**, *324* (19), 3173-3180.
43. Neto, D. M. A.; Freire, R. M.; Gallo, J.; Freire, T. M.; Queiroz, D. C.; Ricardo, N. M. P. S.; Vasconcelos, I. F.; Mele, G.; Carbone, L.; Mazzetto, S. E.; Bañobre-López, M.; Fachine, P. B. A., Rapid Sonochemical Approach Produces Functionalized Fe<sub>3</sub>O<sub>4</sub> Nanoparticles with Excellent Magnetic, Colloidal, and Relaxivity Properties for MRI Application. *The Journal of Physical Chemistry C* **2017**, *121* (43), 24206-24222.
44. Park, J. C.; Lee, G. T.; Kim, H.-K.; Sung, B.; Lee, Y.; Kim, M.; Chang, Y.; Seo, J. H., Surface Design of Eu-Doped Iron Oxide Nanoparticles for Tuning the Magnetic Relaxivity. *ACS Applied Materials & Interfaces* **2018**, *10* (30), 25080-25089.
45. Liu, X. L.; Wang, Y. T.; Ng, C. T.; Wang, R.; Jing, G. Y.; Yi, J. B.; Yang, J.; Bay, B. H.; Yung, L.-Y. L.; Fan, D. D.; Ding, J.; Fan, H. M., Coating Engineering of MnFe<sub>2</sub>O<sub>4</sub>

- Nanoparticles with Superhigh T2 Relaxivity and Efficient Cellular Uptake for Highly Sensitive Magnetic Resonance Imaging. *Advanced Materials Interfaces* **2014**, *1* (2), 1300069.
46. Duan, H.; Kuang, M.; Wang, X.; Wang, Y. A.; Mao, H.; Nie, S., Reexamining the Effects of Particle Size and Surface Chemistry on the Magnetic Properties of Iron Oxide Nanocrystals: New Insights into Spin Disorder and Proton Relaxivity. *The Journal of Physical Chemistry C* **2008**, *112* (22), 8127-8131.
  47. Hu, F.; MacRenaris, K. W.; Waters, E. A.; Liang, T.; Schultz-Sikma, E. A.; Eckermann, A. L.; Meade, T. J., Ultrasmall, Water-Soluble Magnetite Nanoparticles with High Relaxivity for Magnetic Resonance Imaging. *The Journal of Physical Chemistry C* **2009**, *113* (49), 20855-20860.
  48. Joshi, H.; De, M.; Richter, F.; He, J.; Prasad, P.; Dravid, V., Effect of silica shell thickness of Fe<sub>3</sub>O<sub>4</sub> SiO<sub>x</sub> core-shell nanostructures on MRI contrast. *Journal of Nanoparticle Research* **2013**, *15*, 1-8.
  49. Arsalani, S.; Guidelli, E. J.; Silveira, M. A.; Salmon, C. E. G.; Araujo, J. F. D. F.; Bruno, A. C.; Baffa, O., Magnetic Fe<sub>3</sub>O<sub>4</sub> nanoparticles coated by natural rubber latex as MRI contrast agent. *Journal of Magnetism and Magnetic Materials* **2019**, *475*, 458-464.
  50. Paquet, C.; de Haan, H. W.; Leek, D. M.; Lin, H.-Y.; Xiang, B.; Tian, G.; Kell, A.; Simard, B., Clusters of Superparamagnetic Iron Oxide Nanoparticles Encapsulated in a Hydrogel: A Particle Architecture Generating a Synergistic Enhancement of the T2 Relaxation. *ACS Nano* **2011**, *5* (4), 3104-3112.
  51. LaConte, L. E.; Nitin, N.; Zurkiya, O.; Caruntu, D.; O'Connor, C. J.; Hu, X.; Bao, G., Coating thickness of magnetic iron oxide nanoparticles affects R2 relaxivity. *J Magn Reson Imaging* **2007**, *26* (6), 1634-41.
  52. Nandwana, V.; Ryoo, S.-R.; Kanthala, S.; De, M.; Chou, S. S.; Prasad, P. V.; Dravid, V. P., Engineered Theranostic Magnetic Nanostructures: Role of Composition and Surface Coating on Magnetic Resonance Imaging Contrast and Thermal Activation. *ACS Applied Materials & Interfaces* **2016**, *8* (11), 6953-6961.
  53. Tong, S.; Hou, S.; Zheng, Z.; Zhou, J.; Bao, G., Coating Optimization of Superparamagnetic Iron Oxide Nanoparticles for High T2 Relaxivity. *Nano Letters* **2010**, *10* (11), 4607-4613.
  54. Zeng, J.; Jing, L.; Hou, Y.; Jiao, M.; Qiao, R.; Jia, Q.; Liu, C.; Fang, F.; Lei, H.; Gao, M., Anchoring Group Effects of Surface Ligands on Magnetic Properties of Fe<sub>3</sub>O<sub>4</sub> Nanoparticles: Towards High Performance MRI Contrast Agents. *Advanced Materials* **2014**, *26* (17), 2694-2698.
  55. de Haan, H. W.; Paquet, C., Enhancement and Degradation of the R-2\* Relaxation Rate Resulting From the Encapsulation of Magnetic Particles with Hydrophilic Coatings. *Magnetic Resonance in Medicine* **2011**, *66* (6), 1759-1766.

56. Mohapatra, J.; Zeng, F. H.; Elkins, K.; Xing, M. Y.; Ghimire, M.; Yoon, S.; Mishra, S. R.; Liu, J. P., Size-dependent magnetic and inductive heating properties of Fe<sub>3</sub>O<sub>4</sub> nanoparticles: scaling laws across the superparamagnetic size. *Physical Chemistry Chemical Physics* **2018**, *20* (18), 12879-12887.
57. Norek, M.; Kampert, E.; Zeitler, U.; Peters, J. A., Tuning of the size of DY2O3 nanoparticles for optimal performance as an MRI contrast agent. *Journal of the American Chemical Society* **2008**, *130* (15), 5335-5340.
58. Pothayee, N.; Balasubramaniam, S.; Pothayee, N.; Jain, N.; Hu, N.; Lin, Y.; Davis, R. M.; Sriranganathan, N.; Koretsky, A. P.; Riffle, J. S., Magnetic nanoclusters with hydrophilic spacing for dual drug delivery and sensitive magnetic resonance imaging. *J. Mater. Chem. B* **2013**, *1* (8), 1142-1149.
59. Yu, W. W.; Falkner, J. C.; Yavuz, C. T.; Colvin, V. L., Synthesis of monodisperse iron oxide nanocrystals by thermal decomposition of iron carboxylate salts. *Chemical Communications* **2004**, (20), 2306-2307.
60. Bosi, F.; Halenius, U.; Skogby, H., Crystal chemistry of the magnetite-ulvospinel series. *American Mineralogist* **2009**, *94* (1), 181-189.
61. Lee, S. S.; Zhu, H.; Contreras, E. Q.; Prakash, A.; Puppala, H. L.; Colvin, V. L., High Temperature Decomposition of Cerium Precursors To Form Ceria Nanocrystal Libraries for Biological Applications. *Chemistry of Materials* **2012**, *24* (3), 424-432.
62. Prakash, A.; Zhu, H.; Jones, C. J.; Benoit, D. N.; Ellsworth, A. Z.; Bryant, E. L.; Colvin, V. L., Bilayers as Phase Transfer Agents for Nanocrystals Prepared in Nonpolar Solvents. *ACS Nano* **2009**, *3* (8), 2139-2146.
63. Akaighe, N.; Depner, S. W.; Banerjee, S.; Sharma, V. K.; Sohn, M., The effects of monovalent and divalent cations on the stability of silver nanoparticles formed from direct reduction of silver ions by Suwannee River humic acid/natural organic matter. *Science of The Total Environment* **2012**, *441*, 277-289.
64. Ji, L.; Chen, W.; Zheng, S.; Xu, Z.; Zhu, D., Adsorption of Sulfonamide Antibiotics to Multiwalled Carbon Nanotubes. *Langmuir* **2009**, *25* (19), 11608-11613.
65. Cavus, S., Poly(methacrylamide-co-2-acrylamido-2-methyl-1-propanesulfonic acid) Hydrogels: Investigation of pH- and Temperature-Dependent Swelling Characteristics and Their Characterization. *J. Polym. Sci., Part B: Polym. Phys.* **2010**, *48* (23), 2497-2508.
66. El-Mahdy, G. A.; Atta, A. M.; Al-Lohedan, H. A., Synthesis and Evaluation of Poly(Sodium 2-Acrylamido-2-Methylpropane Sulfonate-co-Styrene)/Magnetite Nanoparticle Composites as Corrosion Inhibitors for Steel. *Molecules* **2014**, *19* (2), 1713-1731.
67. Gad, Y. H., Preparation and characterization of poly(2-acrylamido-2-methylpropane-sulfonic acid)/Chitosan hydrogel using gamma irradiation and its

- application in wastewater treatment. *Radiat. Phys. Chem.* **2008**, *77* (9), 1101-1107.
68. Zhang, X.; Zhang, Q.; Ma, T.; Liu, Q.; Wu, S.; Hua, K.; Zhang, C.; Chen, M.; Cui, Y., Enhanced Stability of Gold Magnetic Nanoparticles with Poly(4-styrenesulfonic acid-co-maleic acid): Tailored Optical Properties for Protein Detection. *Nanoscale Res. Lett.* **2017**, *12* (1).
  69. Stinnett, G.; Taheri, N.; Villanova, J.; Bohloul, A.; Guo, X.; Esposito, E. P.; Xiao, Z.; Stueber, D.; Avendano, C.; Decuzzi, P.; Pautler, R. G.; Colvin, V. L., 2D Gadolinium Oxide Nanoplates as T1 Magnetic Resonance Imaging Contrast Agents. *Advanced Healthcare Materials* **2021**, *10* (11), 2001780.
  70. Lartigue, L.; Coupeau, M.; Lesault, M., Luminophore and Magnetic Multicore Nanoassemblies for Dual-Mode MRI and Fluorescence Imaging. *Nanomaterials (Basel)* **2019**, *10* (1).
  71. Pösel, E.; Kloust, H.; Tromsdorf, U.; Janschel, M.; Hahn, C.; Maßlo, C.; Weller, H., Relaxivity Optimization of a PEGylated Iron-Oxide-Based Negative Magnetic Resonance Contrast Agent for T2-Weighted Spin-Echo Imaging. *ACS Nano* **2012**, *6* (2), 1619-1624.
  72. Xie, X.; Zhang, C., Controllable Assembly of Hydrophobic Superparamagnetic Iron Oxide Nanoparticle with mPEG-PLA Copolymer and Its Effect on MR Transverse Relaxation Rate. *Journal of Nanomaterials* **2011**, *2011*, 152524.
  73. Cullity, B. D.; Frahm, C. D., Ferrimagnetism. In *Introduction to Magnetic Materials*, 2008; pp 175-195.
  74. Demortière, A.; Panissod, P.; Pichon, B. P.; Pourroy, G.; Guillon, D.; Donnio, B.; Bégin-Colin, S., Size-dependent properties of magnetic iron oxide nanocrystals. *Nanoscale* **2011**, *3* (1), 225-232.
  75. Vergara, A.; Paduano, L.; Vitagliano, V.; Sartorio, R., Mutual diffusion in aqueous solution of poly(ethyleneglycol) samples. Some comments on the effect of chain length and polydispersity. *Physical Chemistry Chemical Physics* **1999**, *1* (23), 5377-5383.
  76. Mues, B.; Buhl, E. M.; Schmitz-Rode, T.; Slabu, I., Towards optimized MRI contrast agents for implant engineering: Clustering and immobilization effects of magnetic nanoparticles. *Journal of Magnetism and Magnetic Materials* **2019**, *471*, 432-438.
  77. Benoit, D. N.; Zhu, H.; Lillierose, M. H.; Verm, R. A.; Ali, N.; Morrison, A. N.; Fortner, J. D.; Avendano, C.; Colvin, V. L., Measuring the Grafting Density of Nanoparticles in Solution by Analytical Ultracentrifugation and Total Organic Carbon Analysis. *Analytical Chemistry* **2012**, *84* (21), 9238-9245.
  78. Cho, M.; Sethi, R.; Ananta narayanan, J. S.; Lee, S. S.; Benoit, D. N.; Taheri, N.; Decuzzi, P.; Colvin, V. L., Gadolinium oxide nanoplates with high longitudinal relaxivity for magnetic resonance imaging. *Nanoscale* **2014**, *6* (22), 13637-13645.

79. Bawa, R., *Handbook of Clinical Nanomedicine*. Pan Stanford Publishing: 2016.
80. Patil, U. S.; Adireddy, S.; Jaiswal, A.; Mandava, S.; Lee, B. R.; Chrisey, D. B., In Vitro/In Vivo Toxicity Evaluation and Quantification of Iron Oxide Nanoparticles. *Int J Mol Sci* **2015**, *16* (10), 24417-50.
81. Kornberg, T. G.; Stueckle, T. A.; Coyle, J.; Derk, R.; Demokritou, P.; Rojanasakul, Y.; Rojanasakul, L. W., Iron Oxide Nanoparticle-Induced Neoplastic-Like Cell Transformation in Vitro Is Reduced with a Protective Amorphous Silica Coating. *Chem Res Toxicol* **2019**, *32* (12), 2382-2397.
82. Avramescu, M. L.; Rasmussen, P. E.; Chénier, M.; Gardner, H. D., Influence of pH, particle size and crystal form on dissolution behaviour of engineered nanomaterials. *Environmental Science and Pollution Research* **2017**, *24* (2), 1553-1564.
83. Foroozandeh, P.; Aziz, A. A., Insight into Cellular Uptake and Intracellular Trafficking of Nanoparticles. *Nanoscale Research Letters* **2018**, *13* (1), 339.
84. Abakumov, M. A.; Semkina, A. S.; Skorikov, A. S.; Vishnevskiy, D. A.; Ivanova, A. V.; Mironova, E.; Davydova, G. A.; Majouga, A. G.; Chekhonin, V. P., Toxicity of iron oxide nanoparticles: Size and coating effects. *J Biochem Mol Toxicol* **2018**, *32* (12), e22225.
85. Feng, Q.; Liu, Y.; Huang, J.; Chen, K.; Huang, J.; Xiao, K., Uptake, distribution, clearance, and toxicity of iron oxide nanoparticles with different sizes and coatings. *Sci Rep* **2018**, *8* (1), 2082.
86. Tanimoto, A.; Kuribayashi, S., Application of superparamagnetic iron oxide to imaging of hepatocellular carcinoma. *Eur J Radiol* **2006**, *58* (2), 200-16.

## Chapter 4

### The T<sub>1</sub> Relaxivity of Gadolinium Nanoparticles in Biologically Relevant Media: The Role of Ionic Strength and Protein Association<sup>†</sup>

<sup>†</sup> Reprinted (adapted) with permission from Villanova J.\*; Taheri N.\*; Bohloul A.; Bi Y.; Ines D.; Guo X.; Xiao Z.; Dunn J. A.; Avendano C.; Decuzzi P.; Pautler R. G.; Colvin V. L., The T<sub>1</sub> Relaxivity of Gadolinium Nanoparticles in Biologically Relevant Media: The Role of Ionic Strength and Protein Association, *in preparation*.

\*These authors contributed equally to this work.

## Chapter 4 The $T_1$ Relaxivity of Gadolinium Nanoparticles in Biologically Relevant Media: The Role of Ionic Strength and Protein Association

### 4.1. Abstract

Protein association with nanoparticles has a significant impact on their biodistribution and pharmacokinetics, but the impact of these interactions on the performance of nanocrystal MRI contrast agents has received limited attention. As larger biomolecules bind through weak or strong interactions with nanoparticles, particularly  $T_1$  contrast agents, we would anticipate changes to the rotational tumbling rate and water access to the particle, both of which will significantly impact the MRI contrast agent performance. Here, we examine the effects of serum, as well as some of its constituent components (serum albumin and salt), on the  $T_1$  relaxivity of gadolinium oxide nanoplates. As might be expected, the surface coating of these materials confers different relaxometric responses in complex media. A carboxylate coating (PAA-LA) yields excellent colloidal stability and lower protein affinity as revealed by size-exclusion chromatography (SEC) has MRI contrast that is relatively unaffected by solution conditions; in contrast a polymer coating rich in sulfonate (PAMPS-LA) is prone to aggregation in higher ionic strength and more strongly associates with a model protein, human serum albumin (HSA). This system has MRI contrast performance that varies markedly in different media. Design and optimization of highly sensitive  $T_1$  nanocrystal contrast agents require consideration of these factors in order to ensure optimal performance in-vivo.

## 4.2. Introduction

Over the past several decades, nanocrystals have garnered considerable interest for their potential use in medicine.<sup>1-3</sup> Applications in diagnostics, bioimaging, biosensing, therapy, and movement and separation have all been demonstrated at the lab scale, but translating these demonstrations into widespread use has been more limited.<sup>4-6</sup> One major challenge to the clinical translation of these materials is the difficulty with predicting their interactions with the complex environments of biological media.<sup>7</sup> Biological components can passively coat nanoparticles, or actively work to transform them chemically, both of which can lead to concerns about nanoscale-specific toxicity and difficulty with predicting biological behavior.<sup>8,9</sup>

Arguably the most significant obstacle to the effective intravenous use of nanocrystals in biomedicine is the difficulty with predicting and controlling their interactions with serum – particularly proteins.<sup>9-13</sup> Much work has gone into understanding the adsorption of protein layers, often termed a ‘corona’, on nanocrystals in physiological media. This phenomenon can be leveraged for some benefit in a few examples.<sup>10, 11, 14-19</sup> However, often the formation of ill-defined protein coronas around nanoparticles complicates the design and application of these materials. In the case of nanocrystal magnetic resonance imaging (MRI) contrast agents, protein coronas could change the rotational tumbling rate of a nanocrystal and access of water to its surface, which could dramatically affect its contrast performance.<sup>20-24</sup>

Forming high performance T<sub>1</sub> contrast agents is of great importance broadly in medicine. Tens of millions of people per year undergo MRI procedures, approximately half of which



require contrast agents to enhance their images and help visualize and differentiate between soft tissue, organs, and possible abnormalities associated with disease.<sup>25-27</sup>

Contrast agents enhance images by reducing the relaxation time of water protons, thus increasing signal production. T<sub>1</sub> contrast agent, often preferred over T<sub>2</sub> contrast agents by radiologists, enhance contrast positively showing up bright white in an image.<sup>5</sup>

Nanoparticle T<sub>1</sub> contrast agents generally rely on gadolinium-containing nanoparticles and offer the possibility of reduced nephrotoxicity and improved performance as compared to the clinical gadolinium chelate standards. Contrast performance is generally captured by an agent's relaxivity,  $r_1$ , which measured the contrast agent's acceleration of the water proton relaxation. This metric is affected by both inner and second sphere relaxation mechanisms.<sup>28</sup> The inner and second spheres of a contrast agent are the region where water is coordinated to the magnetically active ion of the contrast agent and the region just beyond that, respectively. The contribution of second sphere relaxation mechanisms is primarily impacted by the number of water molecules in the second sphere.<sup>23, 24, 29</sup> For nanocrystal contrast agents, this is affected by the hydrophilic surface coating and if more water molecules are bound in the second sphere, the better the performance. The contribution of inner sphere relaxation mechanisms is most affected by the number of water molecules in the inner sphere, the exchange rate between the inner sphere and the bulk, and the overall rotational tumbling rate of the contrast agent in solution.<sup>23, 24, 29</sup> Generally, higher performance results from increasing inner sphere water molecules and exchange rates but decreasing tumbling rate.

Upon introduction to biological media, particularly intravenous administration to blood serum, the formation of protein coronas around nanocrystal contrast agents could affect both inner and outer sphere relaxation processes. Depending on the extent of protein interactions, relaxivity could be drastically altered by decreases in tumbling and access of water to the inner and second spheres. In the case of tumbling, moderate decreases in tumbling increase relaxivity, while excessive decreases in tumbling could drastically decrease it.<sup>20, 22, 24, 29</sup> To what extent this plays a role in imaging performance is not known.

Here, we examine the effects of serum, as well as some of its constituent components (protein and salt), on the  $T_1$  relaxivity of high-performance gadolinium oxide nanoplates with different coatings (PAMPS-LA and PAA-LA). The differences in functional groups between the two encapsulation agents, PAMPS-LA (sulfonate) and PAA-LA (carboxylate), confer different relaxometric responses to protein and salt concentrations. Our results support the hypothesis that coatings with low protein affinity, but good colloidal stability, may be ideal for retaining high relaxivity under physiologically relevant conditions where there is always a very high concentration of protein relative to nanocrystal.

#### 4.3. Results and Discussion

The synthesis of gadolinium oxide nanoplates (GONP) was reported by Cao et al. and modified slightly in this work to offer broader size control and improved uniformity.<sup>28, 30-</sup>

<sup>40</sup> Briefly, gadolinium oleate precursor in a high boiling point solvent (1-octadecene) is decomposed in the presence of surfactant (oleyl amine and/or oleic acid) at high temperature (290 – 380 C) to initiate nucleation and the formation of gadolinium oxide nanocrystals. Either because of the unique crystallography of rare earth oxides and/or

solution-phase soft templating of surfactants during their formation, these hydrophobic nanocrystals have a plate-like morphology with uncoated edges.<sup>28, 38-42</sup> The face shape can range from roughly square to quasi-spherical and even completely anisotropic.<sup>28, 30, 33, 38</sup> Though nanoplate edge width remains relatively constant, face dimension can be reliably controlled by reaction time and the molar ratio of reagents.<sup>28, 37-39</sup> Dimensional control is important for any prospective nanomedicine, including nanoscale MRI contrast agents, because the physical size of a nanomaterial can affect its performance, toxicity, biodistribution, cellular uptake and retention, and pharmacokinetics.<sup>43-47</sup>

Transmission electron microscopy (TEM) is used to characterize GONP size and shape (**Figure 4.1a-d and S4.1a-d**). The plate-like morphology of these samples is evidenced by particles lying flat and edgewise on the TEM grids. GONPs are monodispersed and exhibit face sizes from about 6 to 17 nm with a constant edge width of about 1.1 nm – the approximate unit cell length of cubic gadolinium oxide (1.0824 Å).<sup>48</sup> X-ray diffraction (XRD) and Raman spectroscopy indicate that the crystal phase of GONPs is cubic Gd<sub>2</sub>O<sub>3</sub> (Ia $\bar{3}$ , bixbyite) (**Figure S4.2 and S4.3**). In particular, strong peaks in the GONP XRD pattern are consistent with the miller indices of cubic Gd<sub>2</sub>O<sub>3</sub>: (222), (400), (440), (622), and (662).<sup>49</sup> Relative broadening in the (222) peak compared to others provides additional support for the anisotropic morphology of GONPs. Similarly, a range of bands in the GONP raman spectrum are consistent with those of cubic Gd<sub>2</sub>O<sub>3</sub>: 95 (strong), 108 (very weak), 235 (weak), 316 (medium), 361 (very strong), 447 (medium), and 568 (medium) cm<sup>-1</sup>.<sup>50</sup>

To provide colloidal stability in physiologically relevant media, robust and biocompatible surface coatings are needed for nanoscale contrast agents.<sup>51-54</sup> However, because the

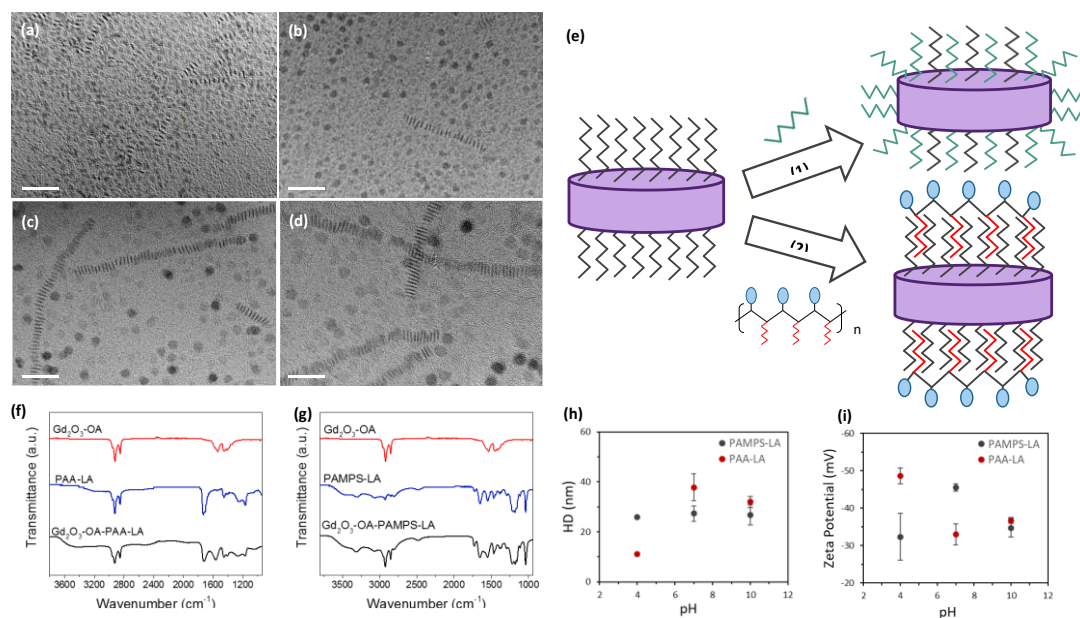


**Figure 4.1 Characterization of Gd<sub>2</sub>O<sub>3</sub> nanoplates cores and surface coating.** TEM images of monodisperse Gd<sub>2</sub>O<sub>3</sub> nanoplates with dimensions of (a)  $6.5 \pm 1.1$ , (b)  $10.0 \pm 1.6$ , (c)  $11.5 \pm 1.3$ , and (d)  $17.0 \pm 1.6$  nm. The scale bar (white) for all images is 50 nm. (e) Schematic representation of the phase transfer of Gd<sub>2</sub>O<sub>3</sub> nanoplates using (1) ligand replacement and (2) encapsulation. FTIR spectra of oleic acid coated (OA) Gd<sub>2</sub>O<sub>3</sub> nanoplates before and after phase transfer with (f) PAA-LA or (g) PAMPS-LA. (h) Hydrodynamic diameter and (i) zeta potential of PAA-LA and PAMPS-LA coated Gd<sub>2</sub>O<sub>3</sub> as a function of pH (4 – 10).

contrast performance of T<sub>1</sub> contrast agents is dependent on close (2.7 – 3.3 Å) inner-sphere interactions between water and gadolinium, surface coatings must also maintain adequate surface accessibility.<sup>39, 55-59</sup> These two requirements – colloidal stability and surface accessibility – are often in tension, but the anisotropic morphology and asymmetric hydrophobic coating (oleyl amine and/or oleic acid) of GONP provide an opportunity to secure both post-phase transfer.<sup>28, 38-42</sup> To examine a range of possible

surface chemistry, in this work three polymeric surface coatings were applied to the GONPs as a means to ensure good colloidal stability and high contrast performance.

Two different methods were used to form the surface coatings in these systems. In a ligand replacement phase transfer, some or all of the original hydrophobic surface coating (oleyl amine and/or oleic acid) is replaced with a water-soluble ligand with a higher affinity for the GONP surface. The new water-soluble ligand coats the entire GONP surface, including its edges – limiting water accessibility (**Figure 4.1e**). Polyethylene glycol (PEG) – a neutral, hydrophilic, biocompatible polymer commonly used to enhance the colloidal stability and pharmacokinetic behavior of nanomedicines – is typically used to phase transfer nanocrystals via ligand replacement.<sup>41, 60-62</sup> Such ligand replacement phase transfer procedures result in water-soluble GONPs but offer sub-optimal contrast performance.<sup>32, 36-38, 40</sup> Alternatively an encapsulation phase transfer procedure results in water-soluble GONPs with exceptional contrast performance.<sup>28, 39</sup> In an encapsulation phase transfer an amphiphile is used to overcoat existing hydrophobic ligands. For the nanoplate geometry the amphiphilic encapsulation agent confers colloidal stability while also maintaining vacant edges for water accessibility (**Figure 4.1e**). Here, lauryl acrylate (LA) modified poly(acrylic acid) (PAA) and poly (2-acrylamido-2-methyl propane sulfonic acid) (PAMPS) amphiphilic copolymers (PAA-LA and PAMPS-LA, respectively) are used to phase transfer GONPs via encapsulation. Hydrophobic LA monomers function as anchors to the hydrocarbon tails of oleyl amine and/or oleic acid ligands on the as-synthesized GONP surface. PAA and PAMPS are both highly charged, biocompatible polymers used to confer colloidal stability even under a range of harsh conditions.<sup>28, 63-69</sup> Notably,

differences in charge density, hydrogen bonding, and acid character between sulfonate ( $pK_a = 1.9$ ) and carboxylate ( $pK_a = 4.5$ ) functional groups on PAMPS and PAA could affect GONP contrast performance, colloidal stability, and toxicity.<sup>70, 71</sup>

To facilitate efficient phase transfer, as-synthesized GONP are purified by multiple rounds of washing and centrifugation to remove excess solvent, unreacted reagents, and unintended reaction products. Thermogravimetric analysis (TGA) data suggest that only oleyl amine and/or oleic acid (boiling point  $\approx 360$  C) are present on the surface of GONPs post-purification (**Figure S4.4**). Polymeric phase transfer agents are characterized using matrix-assisted laser desorption ionization-time of flight mass spectrometry (MALDI-TOF MS) and Fourier transform infrared spectroscopy (FTIR). From MALDI-TOF MS, PAMPS-LA and PAA-LA are found to have similar average molecular weights of about 4300 and 4200 Da, respectively. Smaller ( $< 10,000$  kDa) and similar polymer sizes like these could help limit obstructions to water accessibility, reduce aggregation, and mitigate differences in grafting density.<sup>28</sup> From FTIR, all polymer samples have vibrational modes consistent with their characteristic functional groups, absent that of C=C ( $1612\text{ cm}^{-1}$ ) – confirming they are polymerized (**Figure S4.5**). The FTIR spectrum for PAMPS-LA has peaks corresponding to an amide II band ( $1570 - 1470\text{ cm}^{-1}$ ) and S=O ( $1372 - 1335\text{ cm}^{-1}$ ), N-H ( $3500 - 3100\text{ cm}^{-1}$ ), C=O ( $\sim 1680\text{ cm}^{-1}$ ), and C-H ( $3000 - 2840\text{ cm}^{-1}$ ) stretching vibrational modes. The FTIR spectrum for PAA-LA has peaks corresponding to O-H bending ( $1440 - 1395\text{ cm}^{-1}$ ) and C=O ( $1720 - 1706\text{ cm}^{-1}$ ), O-H (broad,  $3300 - 2500\text{ cm}^{-1}$ ), and C-H ( $3000 - 2840\text{ cm}^{-1}$ ) stretching vibrational modes. As confirmation of phase transfer, GONPs are also characterized before and after the addition of polymeric surface coatings using FTIR

(**Figure 4.1f+g**). Most notably, as-synthesized hydrophobic GONPs exhibit prominent C-H ( $3000 - 2840 \text{ cm}^{-1}$ ) and  $\text{COO}^-$  ( $1600 - 1400 \text{ cm}^{-1}$ ) stretching peaks characteristic of oleic acid coordinated to a nanoparticle surface.<sup>72, 73</sup> FTIR spectra for PAMPS-LA and PAA-LA coated GONP all have the characteristic peaks of their respective polymer coatings as well as those of oleic acid – indicating successful encapsulation. Dynamic light scattering (DLS) is used post-phase transfer on GONP to characterize their initial colloidal stability in water (pH 7) and acidic and basic conditions (pH 4 and 10). The hydrodynamic diameter and zeta potential remain consistent across the pH range, indicative of no significant change in colloidal stability (**Figure 4.1h+i and Table S4.1**). Slight changes in hydrodynamic diameter and zeta potential for PAA-LA coated GONPS is reflective of the fact that the carboxylate functional group of PAA-LA has a pKa around 4.5 while the sulfonate on PAMPS-LA has a pKa of 1.9.<sup>71, 74, 75</sup> Phase transferred, polymer coated GONPs have no visible precipitates or signs of aggregation over a period of several weeks.

While not the central focus of this work, we would note that the gadolinium-based nanoplates studies here have among the highest contrast performance of any reported gadolinium-containing material.<sup>28, 39, 76-91</sup> The ability of a contrast agent to produce contrast in MR images is a function of the relaxation rates of water protons in the presence of the contrast agent.<sup>92</sup> Higher relaxation rates for both longitudinal ( $T_1$ ) and transverse ( $T_2$ ) processes lead to more contrast between normal and abnormal tissues. Materials that possess high relaxivity,  $r_1$ , can be administered at low doses minimizing toxicity without sacrificing resolution. To examine this potential for enhanced relaxivity to increase the contrast of these agents in MR imaging, we evaluated the performance of

surface functionalized gadolinium oxide nanoplates in comparison with the commercial contrast agent Magnevist. **Table 4.1** summarizes the relaxivity values for the molecular contrast agent, Magnevist, and all three polymer-coated gadolinium oxide nanoplates. Magnevist has an  $r_1$  of  $3.4 \pm 0.1 \text{ mM}^{-1}\text{s}^{-1}$ , which is comparable to what can be found in the literature.<sup>24</sup> For PAMPS-LA-coated GONPs,  $r_1$  has a value of  $54.1 \pm 1.1 \text{ mM}^{-1}\text{s}^{-1}$ , and for PAA-LA-coated nanocrystals,  $r_1$  is even higher with a value of  $65.8 \pm 2.9 \text{ mM}^{-1}\text{s}^{-1}$ .

The most reasonable explanation for these notable findings is that they are the result of the inner- and second-sphere relaxation process.<sup>20, 28</sup> The tumbling rate of our GONP compared to the molecular-sized Magnevist is much slower, and this led to a significant boost in  $T_1$  relaxivity because it allows water to have more effective interactions with surface gadolinium. If water can get close enough to gadolinium, nearly 2.7-3.3 Å, the inner-sphere relaxation process will play a major role compared to the other mechanisms that are accountable for relaxivity.<sup>20, 28, 93, 94</sup> Getting water close to the nanocrystal core, however, is always a challenge in these systems since the core is protected by a surface

**Table 4.1**  $T_1$  relaxivities of Magnevist and polymer-coated  $\text{Gd}_2\text{O}_3$  nanoplates in various media.

Contrast Agent	Surface Coating	$r_1$ (Water)	$r_1$ (10 mg/mL HSA)	$r_1$ (100 mM NaCl)
Magnevist	-	$3.4 \pm 0.1$	$3.8 \pm 0.05$	$3.5 \pm 0.03$
$\text{Gd}_2\text{O}_3$ Nanoplates	PAMPS-LA	$59.9 \pm 1.9$	$83.9 \pm 5.1$	$38.9 \pm 2.1$
$\text{Gd}_2\text{O}_3$ Nanoplates	PAA-LA	$65.8 \pm 1.1$	$65.3 \pm 4.2$	$65.5 \pm 1.5$



coating. The special geometry of nanoplates offers an alternative in that the edges of these nanoplates are available for close interactions while the large plate faces are covered in polymers suitable for engineering biodistribution or enhancing even further performance.<sup>28</sup> This finding is indeed promising for the potential of these nanocrystals as effective contrast agents. Also, the second-sphere mechanisms likely play an important role here.<sup>84, 85, 90, 95-103</sup> Highly charged polymers with significant H-bonding potential like PAMPS-LA and PAA-LA could attract water into the second sphere thus significantly increasing  $T_1$  relaxivity.<sup>28</sup>

Solution conditions of serum, mainly salt and protein, can significantly affect the relaxivity of MRI contrast agents by changing their interactions with water (**Figure 4.2, Table 4.1, Figure S4.6**). The relaxivities of Magnevist and PAMPS-LA- and PAA-LA-coated GONPs

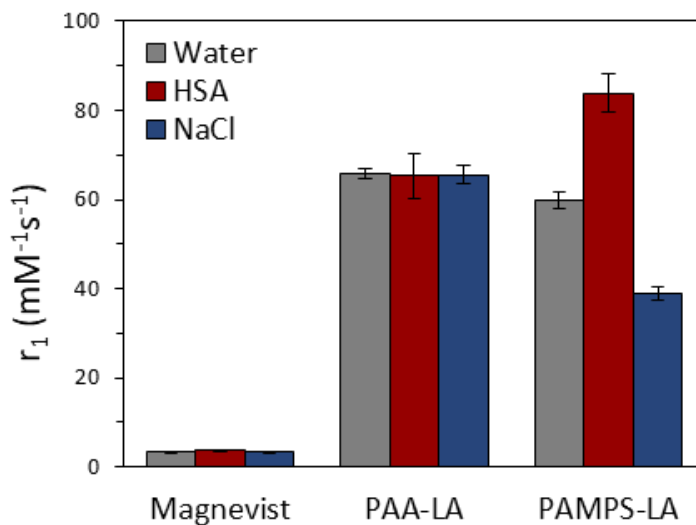


**Figure 4.2 Characterization of Gd<sub>2</sub>O<sub>3</sub> nanoplates cores and surface coating.**  $T_1$  relaxivities of Magnevist, and PAA-LA and PAMPS-LA coated Gd<sub>2</sub>O<sub>3</sub> nanoplates in water, 10 mg/mL HSA, and 100 mM NaCl at 1.4 T.

were measured in 100 mM and 10 mg/mL solutions of NaCl and human serum albumin, HSA, respectively, and compared with their values in water (**Figure 4.2, Table 4.1, Figure S4.6**). We selected HSA as a model protein given its abundance in serum.<sup>104</sup> In all three media, the  $T_1$  relaxivity of Magnevist remains approximately the same. This makes sense because Magnevist is not known to significantly interact with proteins or monovalent ions.<sup>24</sup> In contrast the GONPS can be quite sensitive to the aqueous media conditions depending on whether their surface chemistry. For coated GONPS, despite being similarly charged, they have very different responses to media conditions. Like the commercial agent Magnevist, the relaxivity of PAA-LA coated GONPs is apparently unaffected by the different solution conditions. On the other hand, the relaxivity of PAMPS-LA coated GONPs is significantly affected by the different solution conditions.

These basic observations were also seen in studies of the concentration-dependent impact of salts and proteins on relaxivity. Even across these concentration ranges, the trend remains – PAMPS-LA coated GONPs significantly respond to protein and ionic strength while PAA-LA coated GONPs do not. We further explored these apparently conflicting media-dependent trends in  $T_1$  relaxivity with a range of NaCl and HSA concentrations (**Figure 4.3, Figure S4.7**). For the protein solutions, the  $T_1$  relaxivity of PAMPS-LA coated GONPs increases by about 60 % with the addition of a small amount of protein (2 mg/mL) and then remains there at concentrations up to 30 mg/mL (**Figure 4.3a+b**, gray). This is in contrast to the PAA-LA-coated GONPs which exhibit no significant change in  $T_1$  relaxivity over the entire HSA concentration range (**Figure 4.3a+b**, red). These data may be explained by differential interactions between HSA and the two surface

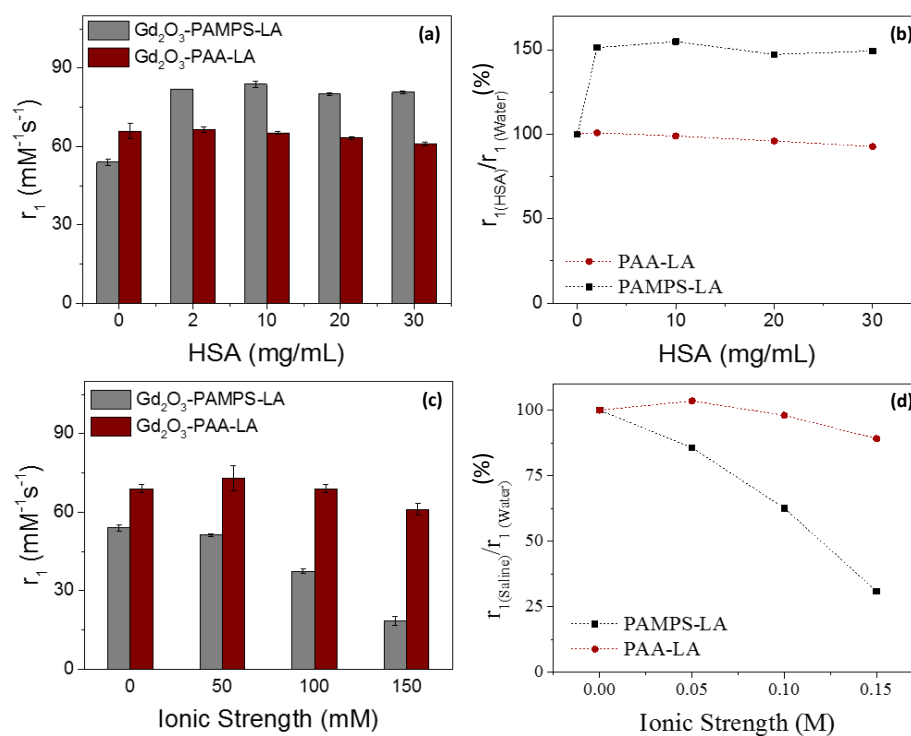


**Figure 4.3** T<sub>1</sub> relaxivity of PAMPS-LA and PAA-LA coated Gd<sub>2</sub>O<sub>3</sub> nanoplates in various concentrations of HSA and salt. Effect of (a-b) protein concentration (0 – 30 mg/mL HSA) and (c-d) ionic strength (0 – 150 mM NaCl) on the T<sub>1</sub> relaxivity ( $r_1$ ) of PAMPS-LA and PAA-LA coated Gd<sub>2</sub>O<sub>3</sub> nanoplates at 1.4 T.

coatings. PAMPS-LA may have stronger interactions with HSA than PAA-LA, causing a hydrodynamic diameter-dependent decrease in tumbling rate and therefore an increase in  $r_1$ .<sup>20, 21, 23, 24, 29</sup> In fact, the sulfonate functional groups on PAMPS-LA do offer greater potential for H-bonding than the carboxylate groups on PAA-LA. Electrostatic and H-bonding interactions were found to be the most significant factors affecting protein absorption to sulfonated/carboxylated microspheres.<sup>74</sup> In general, this seems to match the literature which suggests that sulfonate bearing polymers, surfactants, and dyes bind well to proteins and albumin and have a greater affinity for, and stronger binding to, albumin (and other proteins) than carboxylate bearing polymers and surfactants.<sup>105-115</sup>

For the NaCl solutions, the  $T_1$  relaxivity of PAA-LA coated GONPs only slightly decreases with increasing ionic strength (**Figure 4.3c+d**, red). This is contrasted with PAMPS-LA-coated GONPs which decrease in  $T_1$  relaxivity by about 70 % with increasing ionic strength (**Figure 4.3a+b**, gray). These results may be explained by differences in zeta potential and H-bonding potential. With a more negative zeta potential in water, sodium ions may be more apt to replace water molecules in PAMPS-LA than PAA-LA, thus reducing the number of water molecules in the inner and second spheres, and thus  $r_1$  much more significantly. PAMPS-LA may also be retaining more water to be removed in the first place because of greater H-bonding potential. Also, this greater degree of dehydration decreases the hydrodynamic diameter of PAMPS-LA coated GONPs more, thus increasing its tumbling rate and decreasing  $r_1$  (**Figure S4.8**).

Equipped with a better understanding of how salt and protein solutions affect the  $T_1$  relaxivity of surface coated GONPs, we now turn to their relaxometric behavior in fetal bovine serum (FBS) which is a combination of both. The  $T_1$  relaxivity of PAMPS-LA and PAA-LA coated GONPs in FBS are compared to their relaxivities in water (**Figure 4.4**). PAA-LA coated GONPs exhibit little to no change in  $T_1$  relaxivity in response to the new media, while PAMPS-LA coated GONPs increases by about 20 % in FBS. We examine the  $T_1$  relaxivity of PAMPS-LA coated GONPs in water, 100 mM NaCl, 10 mg/mL HSA, and a mixture of both (HSA + NaCl) and compare them to the contrast performance in FBS (**Figure S4.9**, **Figure S4.10**). First, the mixture has a lower  $r_1$  than HSA alone because of the addition of NaCl. This could be because of reasons explained in previously (dehydration) or that NaCl is disrupting protein NP interactions, preventing tumbling-

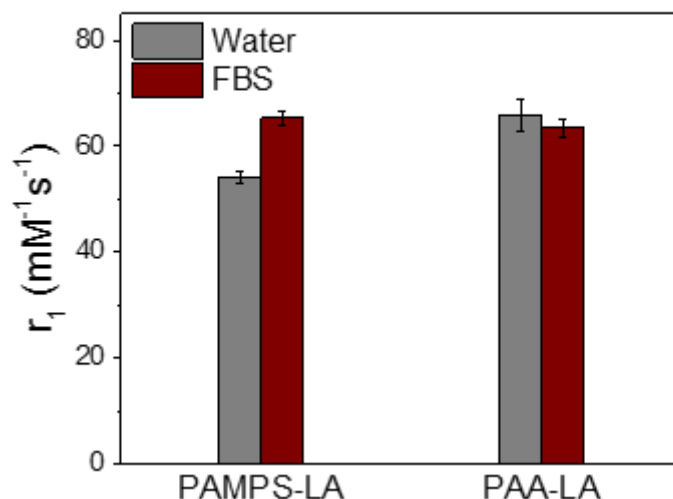
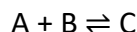


**Figure 4.4**  $T_1$  relaxivity of PAMPS-LA and PAA-LA coated  $Gd_2O_3$  nanoplates in FBS and water.  $T_1$  relaxivity ( $r_1$ ) of PAMPS-LA and PAA-LA coated  $Gd_2O_3$  nanoplates in water and 10% FBS solution (3.7 mg/mL total protein; 12.5 – 14.3 mM  $Na^+$ ; 9.8 – 10.8 mM  $Cl^-$ ) at 1.4T.

dependent increases in  $r_1$ . In fact, it has been shown that increasing NaCl concentration can decrease protein adsorption onto sulfonated polymers.<sup>116, 117</sup> Second, PAMPS-LA coated GONPs in FBS has a lower  $r_1$  than the mixture solution. This is because 10 % FBS has a different profile of proteins, salts, and solutes and at different concentrations – for 10 % FBS, NaCl and protein concentrations are lower, but there are other proteins, salts, and solutes present.<sup>118, 119</sup> As such, it makes sense that nanocrystal interactions with proteins in FBS could be weaker, leading to a lower  $r_1$  than HSA alone or the mixture. Finally, the  $r_1$  of the mixture is closer to HSA alone than NaCl alone, which tells us the effects of proteins on  $r_1$  are likely more significant here. However, all this analysis is predicated on there being a significant difference in protein interactions between PAMPS-LA and PAA-LA coated GONPs, thus meriting further examination.

To confirm our expectations that the sulfonated polymers were more likely to strongly associate with proteins than the carboxylate coatings we turned to size-exclusion high performance liquid chromatography (SE-HPLC). Chromatograms are recorded for PAMPS-LA and PAA-LA coated GONPs before and after incubation in HSA and FBS solutions and are compared with the profiles for the protein solutions alone (**Figure 4.5**). Because of their differences in size and therefore elution times, free nanocrystals and free protein have distinct peaks (blue vs red). In size exclusion chromatography for nanocrystal-protein interactions, there is an exchange between free nanocrystals and proteins (slow moving) and nanocrystal-protein complexes (fast moving) dictated by the following kinetic equations:



$$\frac{dc}{dt} = abk_{formation} - ck_{dissociation}$$

where the association rate constant ( $k_{formation}$ ) and dissociation rate constant ( $k_{dissociation}$ ) dictate the exchange rate and a, b, and c are the concentrations of nanocrystal, protein, and nanocrystal-protein complexes, respectively.<sup>120, 121</sup> If the exchange is slow, free nanocrystals and proteins move together (one peak, monophasic) because they all spend equal time being sped up by complexation – this would indicate the formation of a high affinity, ‘hard’ protein corona around the nanocrystal.<sup>17, 120, 121</sup> If the exchange is fast, some nanocrystals and proteins never complex, causing nanocrystal-protein complexes to move faster and separately (multiple peaks, multiphasic) complexation – this would

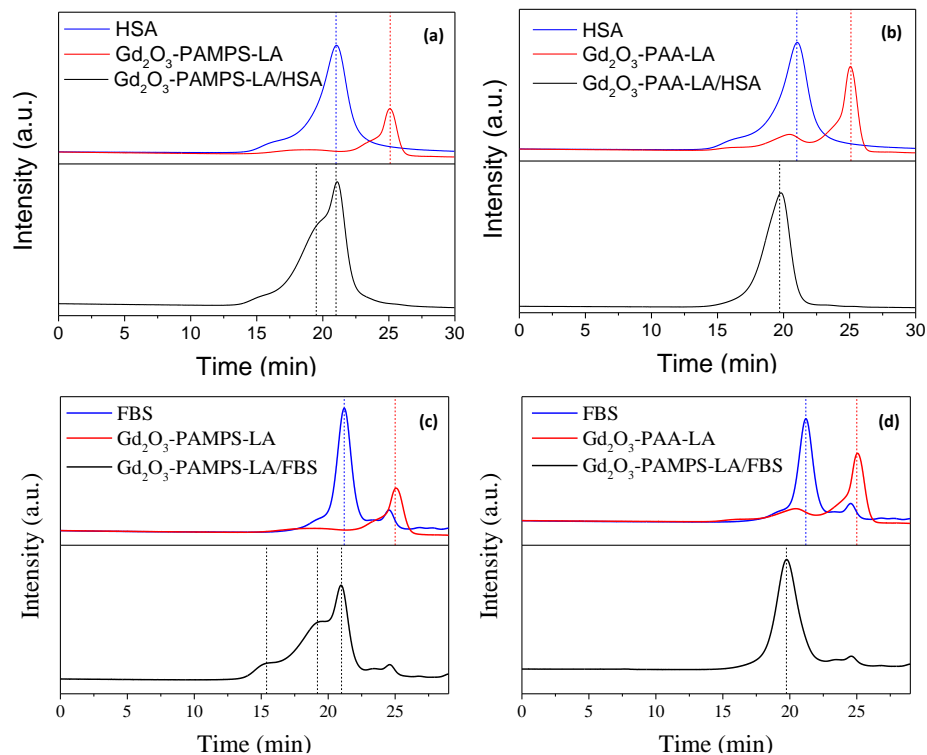


**Figure 4.5** Size exclusion chromatography profiles for PAMPS-LA and PAA-LA coated  $Gd_2O_3$  nanoplates in HSA and FBS solution. SE-HPLC profile of (a+c) PAMPS-LA and (b+d) PAA-LA coated  $Gd_2O_3$  nanoplates with and without (a+b) 10 mg/mL HSA or (c+d) 10 % FBS.

indicate the formation of a low affinity, ‘soft’ protein corona around the nanocrystal.<sup>17,</sup>

120, 121

The SE-HPLC profiles of PAMPS-LA and PAA-LA coated GONPs indicate that they form hard and soft protein coronas, respectively. PAMPS-LA coated GONPs in HSA and FBS have multiphasic profiles that are stable over a wide range of protein solution incubation times (0 – 24 hr) and therefore exhibit slow exchange (hard corona) (**Figure 4.5a+c, Figure S4.11a+b**). Dissociation rate differences between monophasic and multiphasic profiles can be estimated to be about 1 – 2 orders of magnitude.<sup>120</sup> The profile for PAMPS-LA

coated GONPs in FBS has three significant peaks compared to the two for HSA. This is because, for the HSA solution, the only complex that can form is an HSA-nanocrystal complex, resulting in an earlier complex peak and free HSA peak. For the FBS solution, there are many other proteins than just albumin, so while the first earlier peak may represent the formation of a nanocrystal-protein complex with a smaller protein like albumin, the second even earlier peak could represent a complex formed between nanocrystals and other larger/abundant proteins in FBS like phosphodiesterase subunits, plasminogen, lactoperoxidase, ubiquinones, prothrombin, microglobulins, trypsin inhibitor chains, and integrins.<sup>119, 122</sup> PAA-LA coated GONPs in HSA and FBS have monophasic profiles that are stable over a wide range of protein solution incubation times (0 – 24 hr) and therefore exhibit slow exchange (soft corona) (**Figure 4.5b+d, Figure S4.11c+d**). Because PAA-LA coated GONPs have such rapid exchange, this allows them to briefly interact with all proteins in solution, hence the single peak at an earlier elution time – even in a solution like FBS where there are many different types of proteins. However, this ability to interact with all the proteins in solution can be overwhelmed by increasing the concentration of protein (**Figure S4.12**).

These SE-HPLC data support our hypothesis that the different relaxometric behavior between the two different surface coatings, PAMPS-LA and PAA-LA, in protein solutions can be attributed to their differential interactions with proteins. Since proteins do not spend a lot of time interacting with PAA-LA coated GONPs (soft corona), it may be the case that this is not sufficient to slow the tumbling of nanoparticles in solution and affect  $r_1$ . However, proteins do spend a long enough time associated with PAMPS coated



nanocrystals (hard corona) to slow their tumbling rate and increase  $r_1$  – even in the presence of salt and other solutes present in FBS.

However, as the protein-nanocrystal concentration ratio increases there is a critical point at which  $r_1$  decreases (**Figure 4.6** and **Figure S4.13**). This decrease in  $r_1$  is likely the result of too much protein built-up on the nanocrystal surface, causing excessive increases in hydrodynamic diameter and aggregation, which can happen at high protein concentrations (**Figure S4.14**).<sup>123-125</sup> There are two ways such a scenario could negatively impact  $T_1$  relaxivity. First, excessive size-dependent decreases in tumbling can eventually and drastically reduce  $r_1$ .<sup>24</sup> Second, with increased aggregation or protein build-up on each nanocrystal, a semi-hydrophobic layer could start to form around the nanocrystal as a result of phase separation, thus disrupting the accessibility of water to the inner or second spheres and decreasing  $r_1$ .<sup>126</sup> For PAMPS-LA coated GONPs (hard corona), as FBS goes from 10 to 75 %, more nanocrystals are required to keep this critical point from happening until eventually there is so much protein present (75 % FBS) that no amount of nanocrystals (in the 0.1 – 1.8 mM Gd range) can overcome those forces. For PAA-LA coated GONPs, which has a weaker interaction with proteins (soft corona), it is more difficult to get an excessive amount of protein build-up on the nanocrystals and reach that critical point. Therefore, it isn't until the protein-nanocrystal ratio is very large (75 % FBS, 0.1 – 0.5 mM Gd) that the critical point can occur, decreasing  $r_1$ .

A simple model for how the protein-nanocrystal could impact relaxivity suggests that under physiologically relevant conditions (high protein-nanocrystal concentration ratio), PAA-LA coated GONPs could outperform PAMPS-LA coated GONPs by over 350 % (**Figure**

4.6). By making a few assumptions, the protein-nanocrystal concentration ratio at which this critical point occurs can be calculated for each surface coating. This critical point should be constant for each surface coating no matter the FBS concentration. To calculate the concentration of nanocrystals (mM) from the concentration of gadolinium, we assume a circular nanoplate with a diameter of 12 nm and width of 1.1 nm and a density for cubic  $\text{Gd}_2\text{O}_3$  of 7610 mg/mL.<sup>127</sup> To calculate the concentration of proteins in 10, 30, and 75 % FBS solution, we estimated the average MW of proteins in 100 % FBS solution using a weighted average of the 19 most abundant proteins primarily found in FBS (~59.2 kDa) and the average mass of a total protein found in three commonly used types of 100 % FBS stock solutions (37.2 g/L).<sup>119</sup> Using these assumptions, we find the critical protein-nanocrystal concentration ratio (moles protein per moles of nanocrystal) to be about

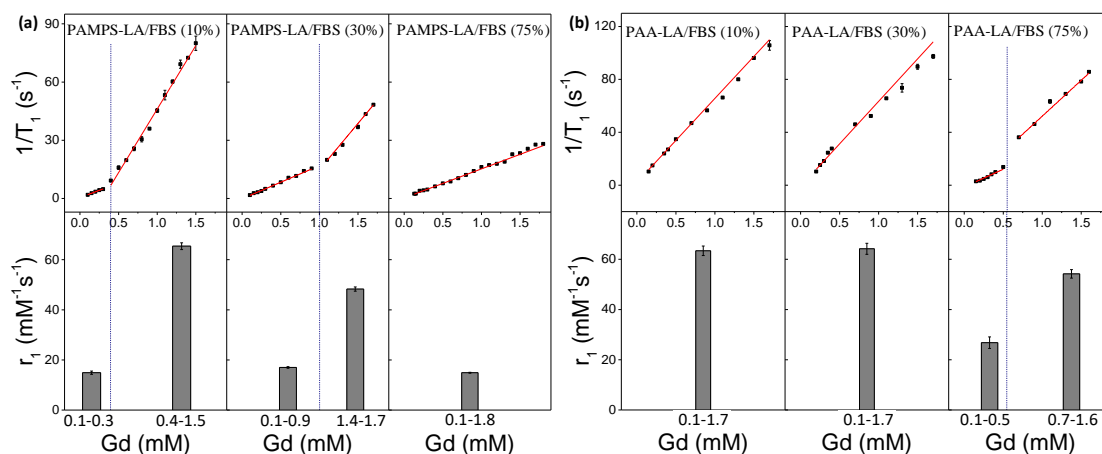


**Figure 4.6**  $T_1$  relaxation rates of PAMPS-LA and PAA-LA coated  $\text{Gd}_2\text{O}_3$  nanoplates at different FBS:nanocrystal concentration ratios. Longitudinal relaxation rate ( $1/T_1$ , top) and  $T_1$  relaxivity ( $r_1$ , bottom) of (a) PAMPS-LA and (b) PAA-LA coated  $\text{Gd}_2\text{O}_3$  nanoplates in 10, 30, and 75 % FBS over a range of  $\text{Gd}^{+3}$  concentrations at 1.4 T.

2100 and 500 for PAA-LA and PAMPS-LA coated nanocrystals, respectively. This makes PAA-LA about 4.2 times more resistant to excessive protein-induced reductions in  $T_1$  relaxivity. In the body, where the protein-nanocrystal concentration ratio will always be very high, this may suggest that low affinity coatings (soft coronas) like PAA-LA may be able to maintain high performance whereas high affinity coatings (hard coronas) like PAMPS-LA would not. This would be counterintuitive from the water-based  $T_1$  relaxivity values alone, where PAMPS-LA coated GONPs outperform the PAA-LA coated GONPs by about 30 % (**Figure 4.2**).

Given our interest in clinical translation of these agents, we also screened these materials for indications of cytotoxicity and gadolinium release (**Figure 4.7** and **Figure S4.15**). Using an MTS assay, surface chemistry dependent human dermal fibroblast (HDF) viability data indicated none of the materials are significantly cytotoxic up to the highest concentrations we could reasonably prepare (**Figure 4.7**). In the range of about 50 – 200  $\mu\text{M}$  both PAMPS-LA and PAA-LA exhibit as much as about a 20 % decrease in viability before recovering to about 100 % at higher Gd concentrations. We also explored whether the materials released free gadolinium under a range of different conditions. An important mode of toxicity for metal oxide particle is the release of free metals into the biological environment.<sup>128</sup> We examined this process using a dialysis method to distinguish free and nanoplate gadolinium in solution (**Figure S4.15**). Over a period of 21 days in water, PAMPS-LA and PAA-LA coated GONPs do not exhibit significant dissolution (< 7 %) while uncoated  $\text{Gd}_2\text{O}_3$  powder does (> 30 %). Over the same period in acetate buffer (pH 4.5) – conditions similar to what can be found inside cellular lysosomes (pH 4.5

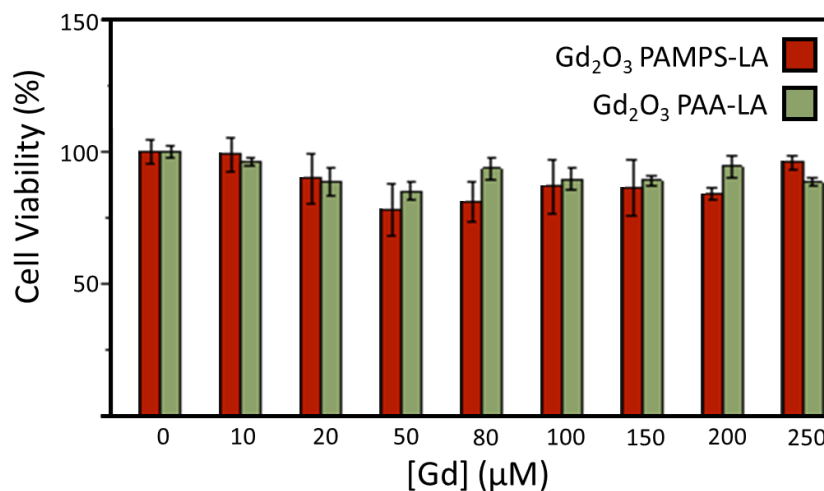


**Figure 4.7 Cell viability of PAMPS-LA and PAA-LA coated Gd<sub>2</sub>O<sub>3</sub> nanoplates.** (a) Percent of viable human dermal fibroblast (HDF) cells evaluated by MTS assay after incubation with PAMPS-LA and PAA-LA coated Gd<sub>2</sub>O<sub>3</sub> nanoplates (0 – 250 μM Gd) for 24 h.

– 5.5) – the coated nanocrystals exhibit more dissolution (< 30 %), but still not as much as the uncoated powder (> 90 %).<sup>129</sup> This is likely because our robust surface coatings prevent significant Gd dissolution even under acidic conditions (**Figure S4.15**). The marginal dissolution of these surface coated GONPs could help explain their relatively low cytotoxicity.

#### 4.4. Conclusion

In this study, Gd<sub>2</sub>O<sub>3</sub> nanoplates (GONP) were stabilized by highly charged amphiphilic copolymers (PAMPS-LA and PAA-LA) for high T<sub>1</sub> relaxivities. Their exceptional contrast performance can be attributed to their plate-like morphology and negatively charged surface coatings which together promote inner and second sphere relaxation processes. We sought to use these high performance T<sub>1</sub> contrast agents to examine the effects of serum conditions on relaxivity and how, or if, surface coating can be used to mitigate

those effects. The relaxivity of PAA-LA coated GONPs was generally unaffected by ionic strength or protein concentration, while PAMPS-LA coated GONPs were significantly affected. Ionic strength induced a dehydration effect by which water was removed from the inner and second spheres of GONPs, decreasing  $r_1$ . This effect was more pronounced for PAMPS-LA coated GONPs because of its greater zeta potential and H-bonding capacity compared to PAA-LA. SE-HPLC and protein-nanocrystal concentration ratio dependent data revealed that the differential effect of protein concentration on PAA-LA and PAMPS-LA coated nanocrystals has to do with differences in protein interactions. Compared to PAMPS-LA, PAA-LA coated GONPs have a lower affinity for proteins, resulting in the formation of hard and soft protein coronas, respectively. This makes PAA-LA coated GONPs about 4.2 times more resistant to excessive protein binding that can be detrimental to  $T_1$  relaxivity at very high, and physiologically relevant, protein-nanocrystal concentration ratios. Thus, supporting the use of low affinity coatings for high contrast performance in vivo. Additionally, while the remarkable chemical stability of the  $Gd_2O_3$  nanoplates and their favorable in vitro cytotoxicity profiles suggest a positive biosafety profile, in vivo toxicity remains to be fully characterized.

#### 4.5. Experimental Section

##### Materials

Ethanol (100%), acetone (Certified ACS), hexanes (Certified ACS), DMF (Certified ACS), DEE (Certified ACS), methanol (Certified ACS), methanol (HPLC grade), nitric acid (Certified ACS), glacial acetic acid (Certified ACS), sodium acetate anhydrous (Certified ACS), and water (HPLC grade) were purchased from Fisher Chemical and were used as received.

Gadolinium(III) nitrate hexahydrate ( $\text{Gd}(\text{NO}_3)_3 \cdot 6\text{H}_2\text{O}$ , 99.99%), 1-octadecene (ODE, 90%), oleylamine (OAm, 70%), oleic acid (OAc, 90%), 2,2'-azobis (2-methylpropionitrile) (AIBN, 98%), lauryl acrylate (LA, 90%), 2-acrylamido-2-methyl-1-propanesulfonic acid (AMPS, 99%), acrylic acid (AA, anhydrous),  $\alpha$ -cyano-4-hydroxycinnamic acid (MALDI-TOF MS), gadolinium standard for ICP (TraceCERT), bovine calf serum (BCS, SAFC USA sourced), and micronized  $\text{Gd}_2\text{O}_3$  ( $\geq 99.9\%$ ) were purchased from Sigma Aldrich. Deuterium oxide (99.9%) and d-chloroform (99.8%) were purchased from Cambridge Isotope Laboratories, Inc. For cell studies, Raw 264.7 cells, DMEM, FBS, PBS, and MTS reagents were purchased from ATCC (Manassas, Virginia). High purity Argon gas ( $>99\%$ ) for syntheses requiring inert atmosphere conditions was purchased from TechAir. For syntheses requiring photoinitiation, AIBN was further purified as follows: unpurified AIBN dissolved in methanol at  $50\text{ }^\circ\text{C}$ , solution filtered into ice bath cooled beaker until recrystallization, and AIBN precipitate vacuum filter dried. All other reagents were used without further purification.

#### Synthesis of Gadolinium Oxide Nanocrystals

In a three-neck flask (50 mL),  $\text{Gd}(\text{NO}_3)_3 \cdot 6\text{H}_2\text{O}$  (1.8 g, 4 mmol) was dissolved in oleic acid (1.25–3.75 mL, 4–12 mmol) and 1-octadecene (12.7 mL, 80 mmol). The reaction mixture was heated to  $100\text{--}110\text{ }^\circ\text{C}$  under inert argon atmosphere conditions and medium stir for 1–5 h to remove low boiling point impurities and generate the clear yellow to light brown gadolinium oleate precursor. After this period, oleylamine (0–4 mL, 0–12 mmol) was added, followed by raising the temperature to  $290\text{ }^\circ\text{C}$  for 3–18 h. At this temperature, the gadolinium oleate complexes decompose, initiating nucleation and nanocrystal growth,

generating an opaque brown solution. While still stirring and under argon, solution allowed to cool gradually to room temperature. After cooling, the following purification procedure was done three times: product dissolved in hexanes (5–10 mL), transferred into a centrifuge tube (50 mL) and filled with a solution of ethanol and acetone (1:5 vol%), and centrifuged for 10 min at 10 000 rpm. The final precipitate was resuspended in hexanes (10 mL).

### Synthesis of Amphiphilic polymers

Poly (2-acrylamido-2-methylpropane sulfonic acid-lauryl acrylate) or PAMPS-LA and poly (acrylic acid-lauryl acrylate) or PAA-LA polymers were formed through a reaction of AMPS and AA, respectively, with LA. For both polymers, the ratio of hydrophilic monomer (AMPS or AA) to hydrophobic monomer (LA) was 4:1 to 5:1 in 3 mL DMF. After all reagents were dissolved in a glass scintillation vial, AIBN (3.75 mg) was added to photoinitiate the radical polymerization of monomers for 1 – 4 hr in a UV reactor (Luzchem, 253 nm).

### Surface Modification of Gadolinium Oxide Nanocrystals

To achieve dispersion of the nanocrystals in an aqueous phase, PAMPS-LA or PAA-LA was used as a phase transfer agent. A 1:1 by volume mixture of a gadolinium oxide nanoplate solution in DEE (25 mg mL<sup>-1</sup>) and a solution of polymer in DMF (80–120 mg mL<sup>-1</sup>) were added to a glass scintillation vial (20 mL). Both solutions were probe sonicated (Hielscher, UP100H) for 5 min prior to preparing the 1:1 mixture. The mixture was stirred vigorously for 12 h (cap on) to allow encapsulation to occur. After that time, DI water (10 mL) was added to the mixture and stirred vigorously for another 12 h (cap off) to evaporate DMF

and DEE and allow the PAMPS-LA encapsulated GONP to transfer into water. After centrifuging the sample for 30 min at 6000 rpm and discarding the precipitate to remove uncoated GONP, the following purification procedure was done three times: separated sample equally between eight ultracentrifuge bottles (26 mL, polycarbonate, Beckman Coulter), filled each bottle with DI water, centrifuged for 1 h at 45000 rpm using an ultracentrifuge (Beckman Coulter, Optima L-90K), gently extracted supernatant liquid, and resuspended precipitate in DI water. Finally, purified GONP were probe sonicated for 5 min and filtered using 0.2  $\mu\text{m}$  polyethersulfone (PES) membrane filters (Watman, Pauradisk 25 mm syringe filter PES, nonsterile).

#### Relaxivity Measurement

The concentration of  $\text{Gd}^{3+}$  was measured using a Perkin Elmer Nexion 300 inductively coupled optical mass spectrometer (ICP-MS) equipped with an autosampler. The sample preparation started with digesting nanocrystals (100  $\mu\text{L}$ ) in nitric acid (70%, 500  $\mu\text{L}$ , trace metal basis) on a hotplate at  $\approx 90$   $^{\circ}\text{C}$  for 2 h. Acidified solutions were filtered and diluted to 10 mL with deionized water using a 0.2  $\mu\text{m}$  PES syringe filter. Calibration curve samples were prepared using dilutions of gadolinium standard solution (0.5, 1.0, 2.5, 5.0, and 10.0  $\text{mg mL}^{-1}$ ) for ICP (1002 ppm in 2% nitric acid) using nitric acid solution (2%). GONP sample solutions (0.5–2 mM  $\text{Gd}^{3+}$ ) were prepared for relaxometric analysis.  $T_1$  measurements were carried out on an MR relaxometer (NMR analyzer mq60, Bruker, Billerica, MA) at 1.4 T. The inverse of  $T_1$  relaxation time ( $1/T_1, \text{s}^{-1}$ ) was plotted as a function of GONP sample  $\text{Gd}^{3+}$  concentration (mM). A linear regression was made using the GONP sample



concentration data points and the ionic relaxivities per  $\text{Gd}^{3+}$  ( $\text{mM}^{-1} \text{ s}^{-1}$ ) were extracted from its slope.

#### Size-Exclusion High-Performance Liquid Chromatography (SE-HPLC)

Size-exclusion high-performance liquid chromatography (SE-HPLC) experiments used to analyze protein-nanocrystal interactions were performed using an Ultrahydrogel-200 7.8 × 300 mm column (Agilent 1100 series, bead size = 200 nm). Protein-nanocrystal solutions (0.5 mL) were added to autosampler vials (Kinesis SureStop, 9mm short tread) for analysis. A PBS buffer (pH 7.4) was used for the mobile phase, set to a flow rate of 0.5 mL  $\text{min}^{-1}$  for 30 min. The final chromatograms were obtained via UV-Vis detector at 250 and 275 nm. Depending on the experiment, protein solutions (FBS or HSA) were incubated with polymer coated gadolinium oxide nanoplates at room temperature for 1 – 24 hr. However, experiments with incubation times approaching 24 hr were done in a refrigerator (30 – 40 C).

#### Transmission Electron Microscopy (TEM)

For transmission electron microscopy (TEM) images, a JEOL 2100F (200 kV) and Phillips FEI CM 20 (200 kV) with single tilt holders were used. Samples were prepared by dropping diluted hexane solution of nanocrystals (nearly light brown solution) onto ultra-thin Formavar/Carbon coated copper grids (type-A, 400 mesh, grid holes ~ 42  $\mu\text{m}$ , Ted Pella Inc.). For each sample, at least 200 particles were analyzed in Image J to get their average dimensions.

#### Thermogravimetric Analysis (TGA)

A Mettler Toledo TG50 thermogravimetric analyzer was used to assess the efficiency of the pre-phase transfer hydrophobic gadolinium oxide nanoplates purification process. Concentrated nanoplate samples were placed in alumina crucibles for TGA measurements at a heating rate of 20 °C/min between 50 to 650°C. Measurements were done in triplicate and under air atmosphere with a flow rate of 80 ml/min.

Matrix-Assisted Laser Desorption Ionization-Time of Flight Mass Spectrometry (MALDI-TOF MS)

Polymer number averaged molecular weights were measured using a Bruker autoflex MALDI-TOF mass spectrometer with a 355 nm Nd:YAG SmartBeam laser. For MS analysis, a 1:1 by volume mixture was made with a solution of PAMPS-LA or PAA-LA in ethanol (30–50 mg mL<sup>-1</sup>) and a saturated solution of  $\alpha$ -cyano-4-hydroxycinnamic acid (MALDI matrix) in ethanol.

Fourier Transform Infrared Spectroscopy (FTIR)

Fourier transform infrared spectroscopy (FTIR) was performed on polymers (PAMPS-LA or PAA-LA) and nanocrystal coatings (before and after phase transfer) using a Thermo Nicolet NEXUS 670 spectrometer equipped with a Mercury Cadmium Telluride (MCT) detector cooled down with liquid nitrogen. In preparation for FTIR, samples were dried in a desiccator overnight on a calcium fluoride round window (12 mm diameter, 2 mm thick). The calcium fluoride window was used as a baseline with a resolution of 4 cm<sup>-1</sup> and 128 scans. Samples spectra were measured between 800 and 4000 cm<sup>-1</sup>.

Dynamic Light Scattering (DLS)

Dynamic light scattering (DLS) was used to measure the hydrodynamic diameter and zeta potential for nanoplate samples using a Malvern Zen6300 Zetasizer NanoS equipped with a 633 nm laser. Aqueous samples were filtered (0.45  $\mu\text{m}$  PES syringe filter) and placed in disposable plastic cuvettes. DLS measurements were performed in triplicate. Hydrodynamic size (based on intensity-weighted measurements; Z-average) and zeta potential are reported as the average with the standard deviation as error bars.

### Raman Spectroscopy

The Raman spectrum for gadolinium oxide nanoplates was recorded at 532 nm using a Witec Alpha 300 Confocal Raman Microscope. Spectra were acquired using between 5-20 accumulations for 30 s, a laser intensity of  $\sim 1\%$ , and a grating of 600.

### X-ray Diffraction (XRD)

X-ray diffraction patterns were measured using a Bruker D8 Discovery 2D X-ray diffractometer operating at 40 kV and 40 mA with a Cu tube ( $1.5413 \text{ \AA}$ ). Diffraction patterns were smoothed using Microsoft Excel. Samples were prepared for XRD by dropping highly concentrated solutions of materials onto glass slides and heat drying. Solid samples were fixed to glass slides using double sided tape.

### Cell Viability Assay

Cell viability assays are convenient, sensitive, and colorimetric methods for evaluating cell viability.<sup>130</sup> Here, an MTS cell viability assay was performed in a 96-well plate for human dermal fibroblasts (HDF), and each dataset was measured in triplicate. When preparing

the assay after detachment from the original culture flask, cells were plated in the first three rows of a 96-well plate (seeding density:  $2 \times 10^4$ /well, 100  $\mu$ L). The fourth 96 row was filled with 100  $\mu$ L media without cells to act as the blank. In rows 1–3, 20  $\mu$ L of nanocrystals (PAMPSS-LA- or PAA-LA-coated) with various concentrations (10 – 300  $\mu$ M Gd) was added from columns 3–11 (this step was repeated in exactly the same manner for the 2nd and 3rd rows). Instead of nanocrystals, the 1st column was filled with 20  $\mu$ L of media and the 2nd column was filled with 20  $\mu$ L of PBS (negative control). The last column (12th) was filled with 20  $\mu$ L of ethanol (positive control) to produce dead cells. Rows 5–9 were filled in the same way, but with different concentrations of nanocrystals. The prepared 96-well plates were placed in the incubator for 24 hr. After the incubation period, the solutions were removed from all wells using glass pipettes attached to the aspiration tube and fresh prewarmed media (100  $\mu$ L), and an MTS reagent (20  $\mu$ L) was subsequently added to all wells. After another 1 h incubation period, absorbance of each well at 490 nm was measured using a microplate reader (TECAN Infinite M1000).

To calculate cell viability, first the average absorbance of blank wells was subtracted from the negative control wells, nanocrystal-containing wells, and positive control wells to remove the absorbance of media or nanocrystals. Then the average absorbance of all wells (except the blank wells) was divided by the average absorbance of the negative control. In this study, all negative control cells were considered viable cells where cell viability is the percentage of the resulting value

Gadolinium Dissolution Studies

Dialysis experiments coupled with ICP-AES were used to determine the amount of  $Gd^{3+}$  leaching from Gd-containing samples (PAMPS-LA and PAA-LA GONPs, micro  $Gd_2O_3$  powder, or  $Gd(NO_3)_3$ ) dispersed in a variety of biologically relevant media (water and pH 4.5) over time (1, 4, 7, 11, 14, 18, and 21 days). Stock sample  $Gd^{3+}$  concentrations were approximately 0.5 – 4 mM for nanoplate samples, approximately 5 mM for gadolinium oxide powders (micro and nano), and 5 mM for gadolinium nitrate. For all experiments, 3 – 3.5 mL of sample was pipetted into a 7 – 10-inch section of dialysis tubing, sealed with clips, and placed in a beaker of water or acetate buffer (4.5). Dialysates were manually stirred twice daily for 30 seconds. Also, in the case of the micro and nano gadolinium oxide powders, homogeneous solutions could not be prepared, and micrograms of material weighed on an analytical balance were poured into the tubing and then water was added. A 1:100 volume ratio of sample inside tubing to the dialysate was used for all experiments. Spectra/Por 6 dialysis membranes (prewetted RC tubing, 1 kDa MWCO) were used in all dialysis experiments. A Thermo Scientific iCAP 7400 DUO inductively coupled plasma atomic emission spectrometer (ICP-AES) was used to measure  $Gd^{3+}$  concentrations of samples, tubing, and dialysate. Samples were digested with tubing in a Milestone Ultrawave SRC microwave digestion system in preparation for ICP analysis. Calibration curve standards were prepared using 0.050, 0.10, 0.25, 0.50, 1.0, 2.5, 5.0, 10, and 50 ppm dilutions of a gadolinium standard solution for ICP (1002 ppm  $Gd^{3+}$  in 2% nitric acid) using 2% nitric acid solution. The following experiments always had total mass recoveries of more than 70 % - with most were above 85 %.

#### 4.6. Supporting Information

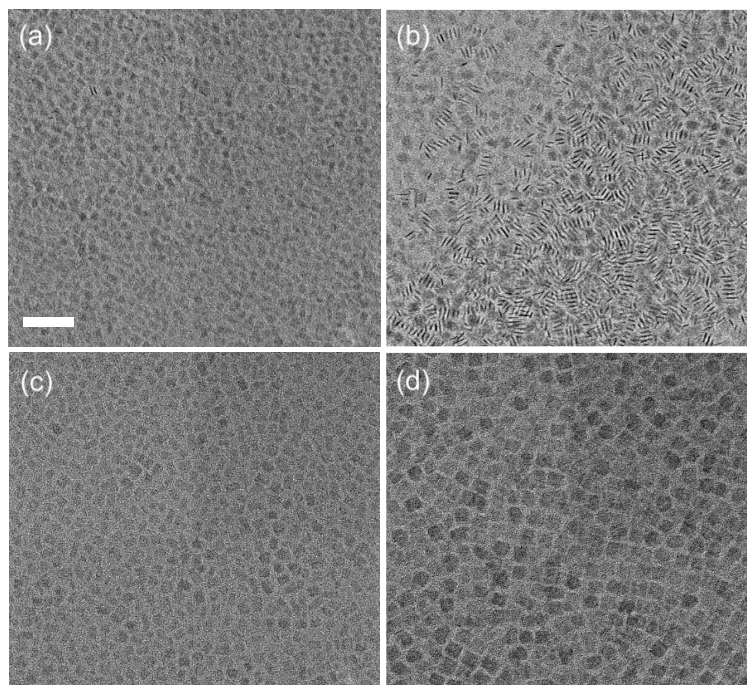


**Figure S4.1** Transmission electron microscopy (TEM) of  $\text{Gd}_2\text{O}_3$  nanoplates. TEM images of monodisperse  $\text{Gd}_2\text{O}_3$  nanoplates with dimensions of (a)  $5.7 \pm 0.06$ , (b)  $8.0 \pm 0.07$ , (c)  $9.7 \pm 1.3$ , and (d)  $12.0 \pm 1.3$  nm. The scale bar (white) for all images is 50 nm.

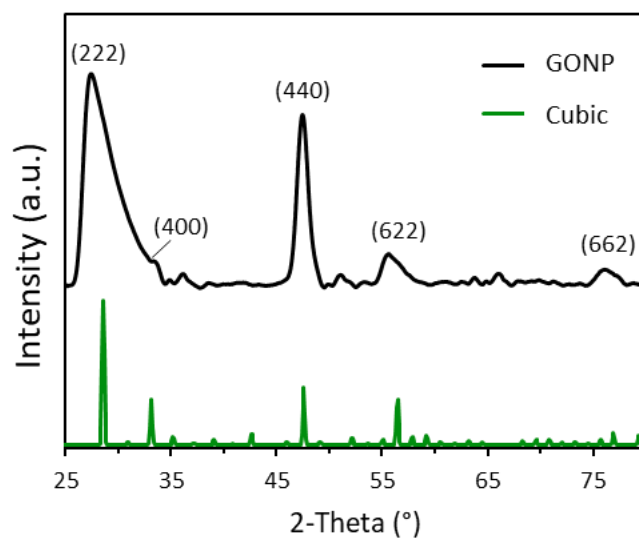


**Figure S4.2 X-ray diffraction pattern of  $Gd_2O_3$  nanoplates.** XRD patterns for as-synthesized  $Gd_2O_3$  nanoplates (black) and cubic  $Gd_2O_3$ .

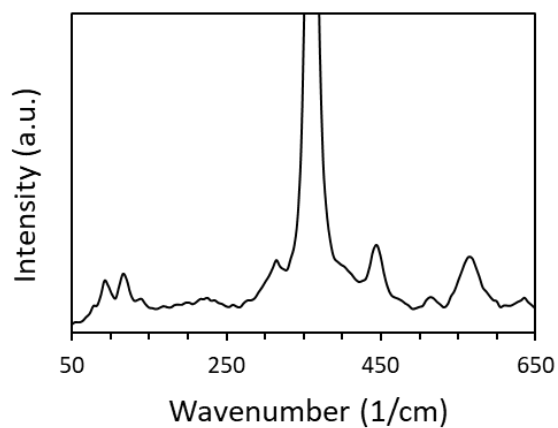


**Figure S4.3 Raman spectroscopy for  $Gd_2O_3$  nanoplates.** Raman spectrum of  $Gd_2O_3$  nanoplates ( $\lambda_{exc} = 532$  nm).

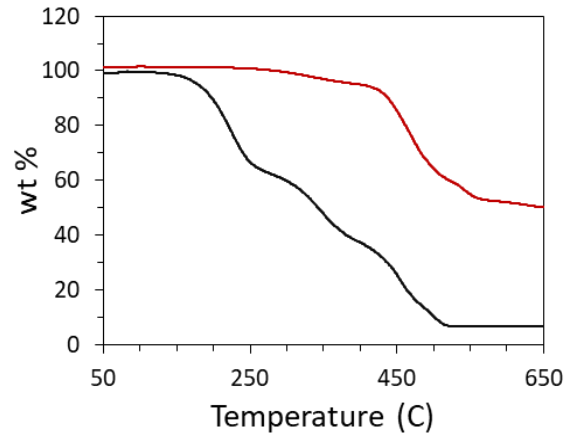


**Figure S4.4 Thermogravimetric analysis (TGA) of  $Gd_2O_3$  nanoplates.** TGA profile of hydrophobic  $Gd_2O_3$  nanoplates before (black) and after (red) purification via centrifugation.

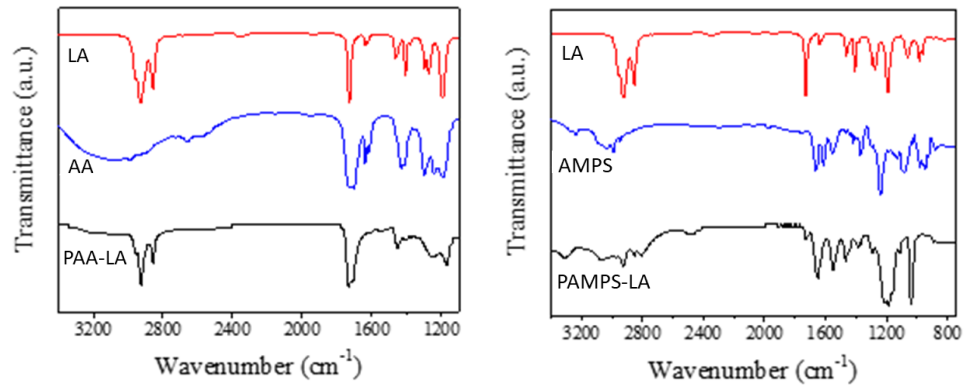


**Figure S4.5 Fourier transform infrared (FTIR) spectroscopy of polymer coatings.** FTIR spectra of (a) PAA-LA and (b) PAMPS-LA and their respective monomers before and after polymerization.



**Table S4.1** Hydrodynamic diameters (HD) and zeta potentials for coated GONPs in varying pH solution

pH	PAMPS-LA GONP		PAA-LA GONP	
	HD (nm)	Zeta potential (mV)	HD (nm)	Zeta potential (mV)
4	25.9 ± 0.4	-32.3 ± 6.3	11.1 ± 0.5	-48.6 ± 2.1
7	27.3 ± 3.1	-45.5 ± 1.0	37.8 ± 5.4	-33.0 ± 2.8
10	26.8 ± 1.6	-34.7 ± 2.5	32.0 ± 2.2	-36.7 ± 0.8

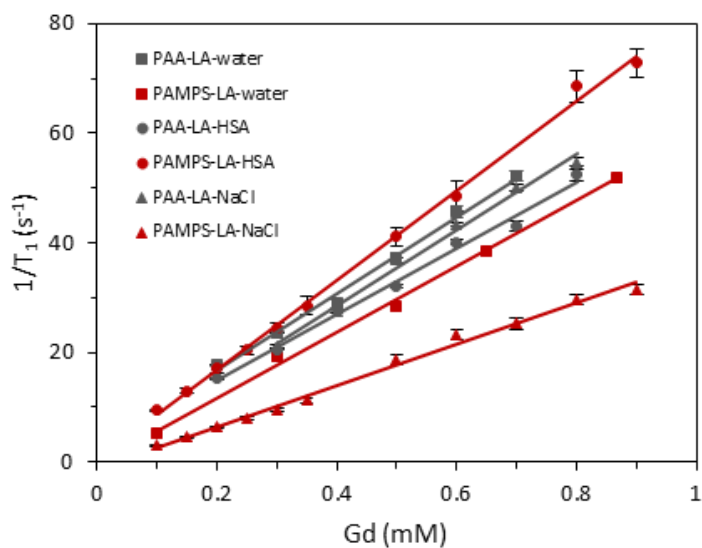


**Figure S4.6**  $T_1$  relaxation rates for  $Gd_2O_3$  samples in water, protein, and salt solution. Longitudinal relaxation rates ( $1/T_1$ ) of PAA-LA and PAMPS-LA coated  $Gd_2O_3$  nanoplates in 10 mg/mL HSA or 100 mM NaCl at 1.4 T.

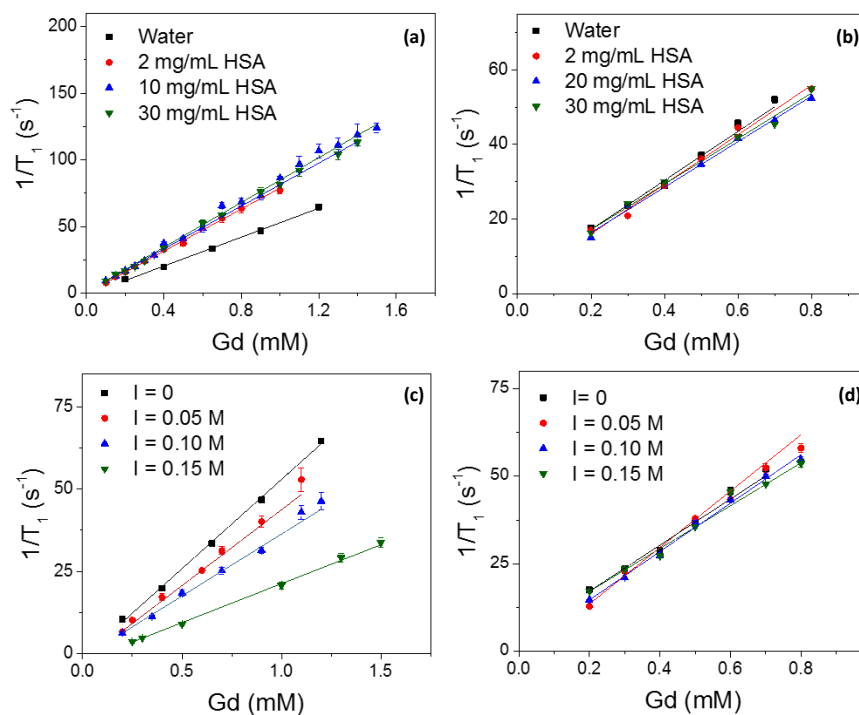


**Figure S4.7**  $T_1$  relaxation rates for Gd<sub>2</sub>O<sub>3</sub> samples in different concentration solutions of protein and salt. Longitudinal relaxation rates ( $1/T_1$ ) of (a) PAMPS-LA and (b) PAA-LA coated Gd<sub>2</sub>O<sub>3</sub> nanoplates in different protein concentration solutions (0 – 30 mg/mL HSA). Longitudinal relaxation rates ( $1/T_1$ ) of (c) PAMPS-LA and (d) PAA-LA coated Gd<sub>2</sub>O<sub>3</sub> nanoplates in different ionic strength solutions (0 – 150 mM NaCl). All measurements taken at 1.4 T.

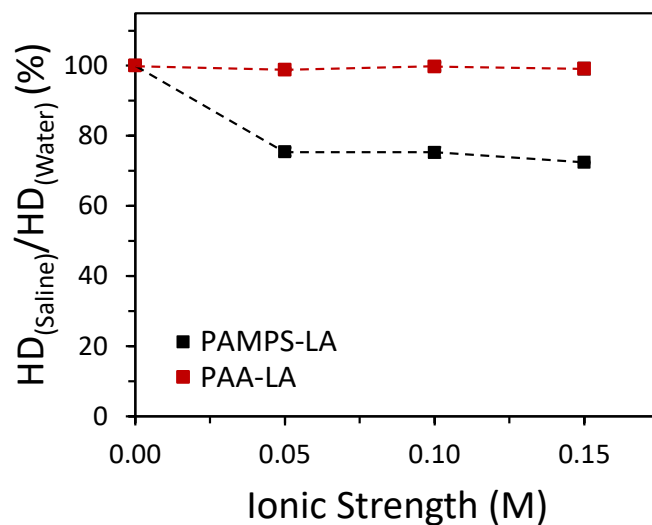


**Figure S4.8** Dependence of surface coated  $Gd_2O_3$  nanoplates hydrodynamic size on solution ionic strength. Effect of ionic strength (0 – 150 mM NaCl) on the hydrodynamic diameter (HD) of PAMPS-LA and PAA-LA coated  $Gd_2O_3$  nanoplates.

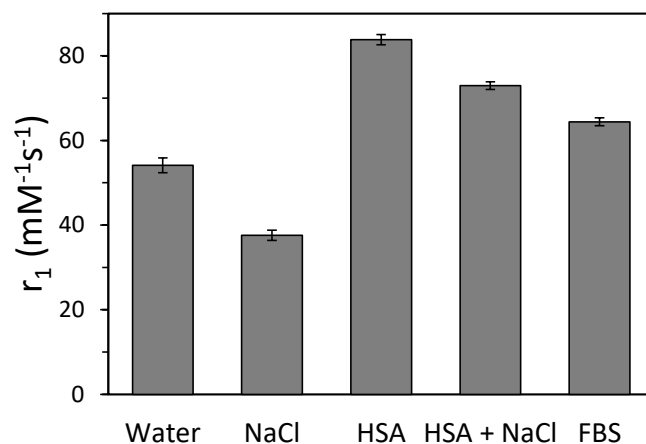


**Figure S4.9**  $T_1$  relaxivity ( $r_1$ ) of PAMPS-LA coated nanoplates in water, salt, protein, and serum solutions. PAMPS-LA coated  $Gd_2O_3$  nanoplates  $r_1$  in water, 100 mM NaCl, 10 mg/mL HSA, a solution of 100 mM NaCl and 10 mg/mL HSA, and 10 % FBS at 1.4 T.

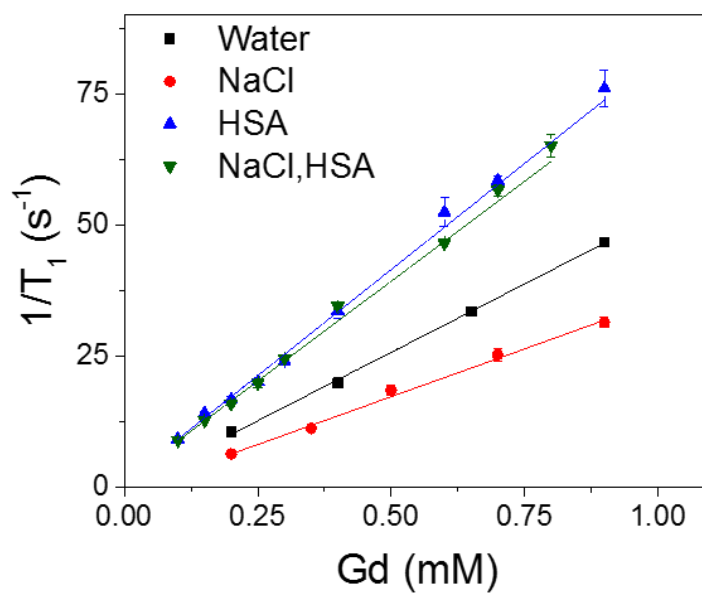


**Figure S4.10**  $T_1$  relaxation rates for PAMPS-LA coated  $Gd_2O_3$  nanoplates in water, salt, and protein solution. Longitudinal relaxation rates ( $1/T_1$ ) of PAMPS-LA coated  $Gd_2O_3$  nanoplates in water, 100 mM NaCl, 10 mg/mL HSA, and a solution of 100 mM NaCl and 10 mg/mL HSA at 1.4 T.

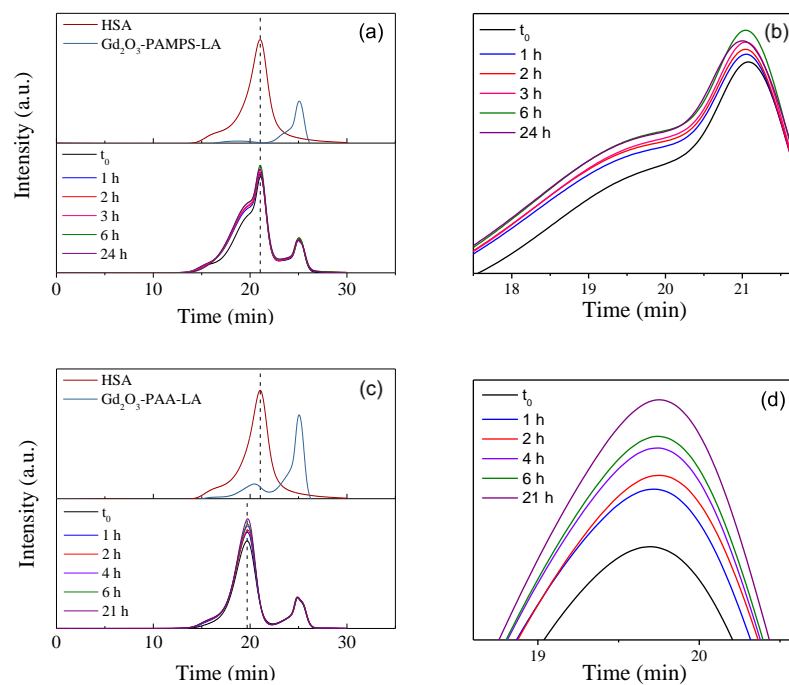


**Figure S4.11 Time-dependent size exclusion chromatograms for surface coated  $Gd_2O_3$  nanoplates in HSA solution.** Time-dependent SE-HPLC profile of (a,b) PAMPS-LA and (c,d) PAA-LA coated  $Gd_2O_3$  nanoplates after the addition of 10 mg/mL HSA.

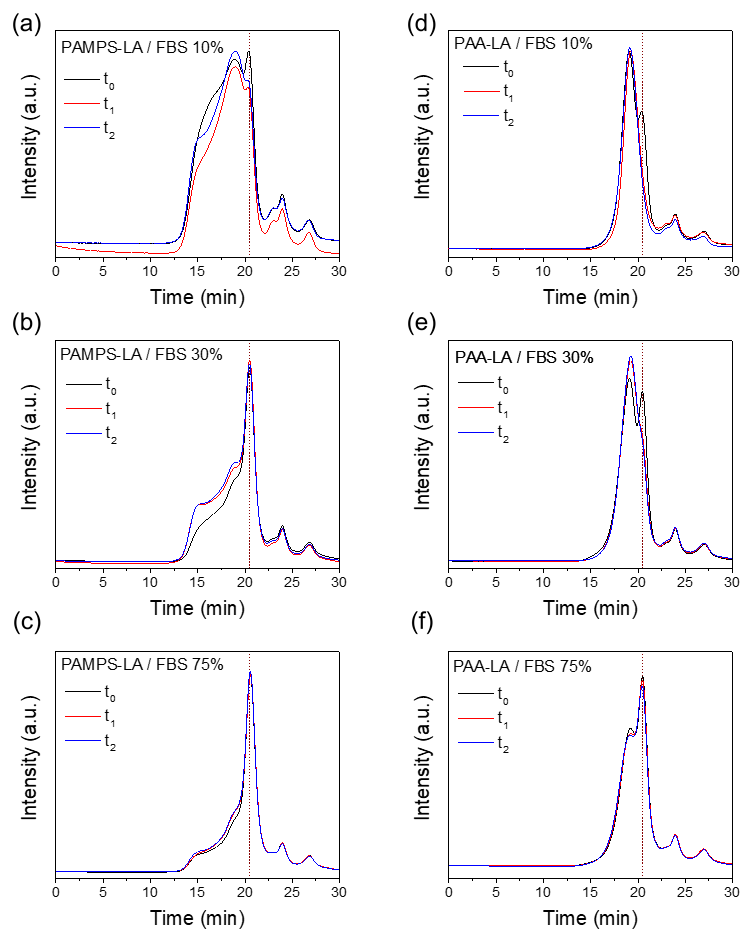


**Figure S4.12** Time-dependent size exclusion chromatograms for surface coated  $Gd_2O_3$  nanoplates in FBS solutions. Time-dependent SE-HPLC profile of PAMPS-LA and PAA-LA coated  $Gd_2O_3$  nanoplates after the addition of (a,d) 10, (b,e) 30, and (c,f) 75 % FBS.

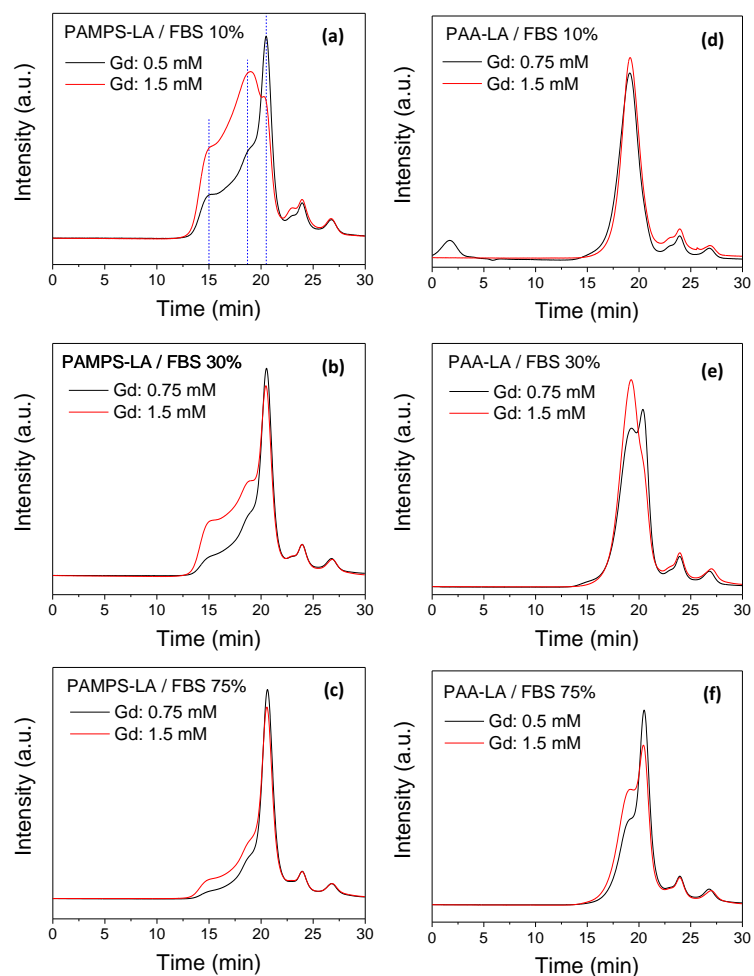


**Figure S4.13 Concentration-dependent size exclusion chromatograms for surface coated  $Gd_2O_3$  nanoplates in FBS solution.** Gd concentration-dependent SE-HPLC profile of (a-c) PAMPS-LA and (d-f) PAA-LA coated  $Gd_2O_3$  nanoplates after the addition (a,d) 10, (b,e) 30, and (c,f) 75 % FBS.

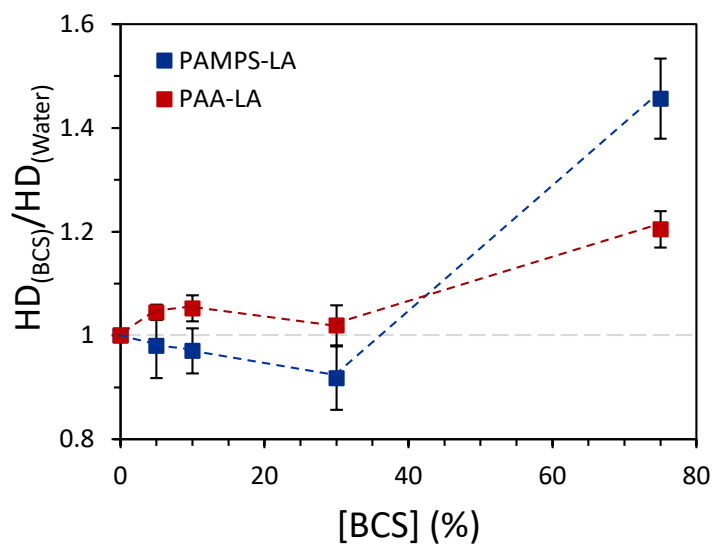


**Figure S4.14** Dependence of surface coated  $Gd_2O_3$  nanoplates hydrodynamic size on BCS solution concentration. Effect of bovine calf serum (0 – 75 % BCS) on the hydrodynamic diameter (HD) of PAMPS-LA (blue) and PAA-LA (red) coated  $Gd_2O_3$  nanoplates.



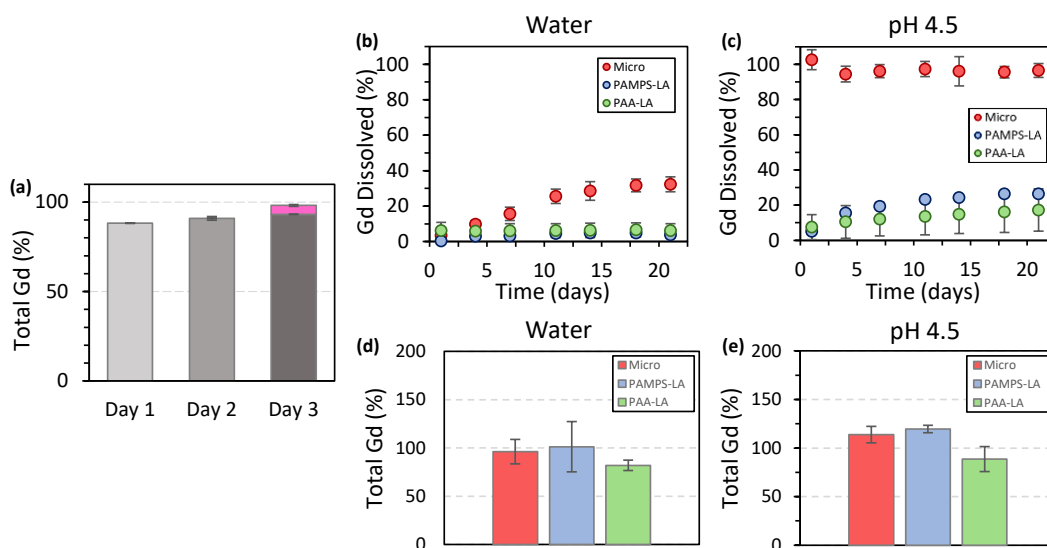


**Figure S4.15 Dissolution of gadolinium from coated and uncoated  $Gd_2O_3$  particles in water and pH 4.5 solution.** (a) Percent gadolinium released into dialysate (gray) from a water solution of  $Gd(NO_3)_3$  in dialysis tubing over 3 days. Percent gadolinium retained in dialysis tubing (pink) after 3 days. Percent gadolinium released into dialysate from (b) water and (c) acetate buffer (pH 4.5) solutions of micronized  $Gd_2O_3$  powder (red), and PAMPS-LA (blue) and PAA-LA (green) coated  $Gd_2O_3$  nanoplates in dialysis tubing over 21 days. Percent total gadolinium recovered from dialysate and dialysis tubing from (d) water and (e) acetate buffer (pH 4.5) solutions of micronized  $Gd_2O_3$  powder (red), and PAMPS-LA (blue) and PAA-LA (green) coated  $Gd_2O_3$  nanoplates in dialysis tubing after 21 days.

#### 4.7. References

1. Giljohann, D. A.; Seferos, D. S.; Daniel, W. L.; Massich, M. D.; Patel, P. C.; Mirkin, C. A., Gold Nanoparticles for Biology and Medicine. *Angewandte Chemie International Edition* 2010, 49 (19), 3280-3294.
2. Klein, J., Probing the interactions of proteins and nanoparticles. *Proceedings of the National Academy of Sciences* 2007, 104 (7), 2029-2030.
3. De, M.; Ghosh, P. S.; Rotello, V. M., Applications of Nanoparticles in Biology. *Advanced Materials* 2008, 20 (22), 4225-4241.
4. Smith, B. R.; Gambhir, S. S., Nanomaterials for In Vivo Imaging. *Chem Rev* 2017, 117 (3), 901-986.
5. Stueber, D. D.; Villanova, J.; Aponte, I.; Xiao, Z.; Colvin, V. L., Magnetic Nanoparticles in Biology and Medicine: Past, Present, and Future Trends. *Pharmaceutics* 2021, 13 (7), 943.
6. Colombo, M.; Carregal-Romero, S.; Casula, M. F.; Gutiérrez, L.; Morales, M. P.; Böhm, I. B.; Heverhagen, J. T.; Prosperi, D.; Parak, W. J., Biological applications of magnetic nanoparticles. *Chemical Society Reviews* 2012, 41 (11), 4306-4334.
7. Younis, M. A.; Tawfeek, H. M.; Abdellatif, A. A. H.; Abdel-Aleem, J. A.; Harashima, H., Clinical translation of nanomedicines: Challenges, opportunities, and keys. *Advanced Drug Delivery Reviews* 2022, 181, 114083.
8. Akçan, R.; Aydogan, H. C.; Yildirim, M.; Taştekin, B.; Sağlam, N., Nanotoxicity: a challenge for future medicine. *Turk J Med Sci* 2020, 50 (4), 1180-1196.
9. Zhang, X.-Q.; Xu, X.; Bertrand, N.; Pridgen, E.; Swami, A.; Farokhzad, O. C., Interactions of nanomaterials and biological systems: Implications to personalized nanomedicine. *Advanced drug delivery reviews* 2012, 64 (13), 1363-1384.
10. Lynch, I.; Dawson, K. A., Protein-nanoparticle interactions. *Nano Today* 2008, 3 (1), 40-47.
11. Mahmoudi, M.; Lynch, I.; Ejtehadi, M. R.; Monopoli, M. P.; Bombelli, F. B.; Laurent, S., Protein-nanoparticle interactions: opportunities and challenges. *Chem Rev* 2011, 111 (9), 5610-37.
12. Mahmoudi, M.; Shokrgozar, M. A.; Sardari, S.; Moghadam, M. K.; Vali, H.; Laurent, S.; Stroeve, P., Irreversible changes in protein conformation due to interaction with superparamagnetic iron oxide nanoparticles. *Nanoscale* 2011, 3 (3), 1127-38.
13. Yang, S. T.; Liu, Y.; Wang, Y. W.; Cao, A., Biosafety and bioapplication of nanomaterials by designing protein-nanoparticle interactions. *Small* 2013, 9 (9-10), 1635-53.
14. Nguyen, V. H.; Lee, B.-J., Protein corona: a new approach for nanomedicine design. *International journal of nanomedicine* 2017, 12, 3137-3151.

15. Park, S. J., Protein-Nanoparticle Interaction: Corona Formation and Conformational Changes in Proteins on Nanoparticles. *Int J Nanomedicine* 2020, 15, 5783-5802.
16. Pino, P. d.; Pelaz, B.; Zhang, Q.; Maffre, P.; Nienhaus, G. U.; Parak, W. J., Protein corona formation around nanoparticles – from the past to the future. *Materials Horizons* 2014, 1 (3), 301-313.
17. Cedervall, T.; Lynch, I.; Lindman, S.; Berggård, T.; Thulin, E.; Nilsson, H.; Dawson, K. A.; Linse, S., Understanding the nanoparticle-protein corona using methods to quantify exchange rates and affinities of proteins for nanoparticles. *Proc Natl Acad Sci U S A* 2007, 104 (7), 2050-5.
18. Monopoli, M. P.; Walczyk, D.; Campbell, A.; Elia, G.; Lynch, I.; Bombelli, F. B.; Dawson, K. A., Physical-chemical aspects of protein corona: relevance to in vitro and in vivo biological impacts of nanoparticles. *J Am Chem Soc* 2011, 133 (8), 2525-34.
19. Walkey, C. D.; Olsen, J. B.; Guo, H.; Emili, A.; Chan, W. C., Nanoparticle size and surface chemistry determine serum protein adsorption and macrophage uptake. *J Am Chem Soc* 2012, 134 (4), 2139-47.
20. Caravan, P., Protein-targeted gadolinium-based magnetic resonance imaging (MRI) contrast agents: design and mechanism of action. *Acc Chem Res* 2009, 42 (7), 851-62.
21. Caravan, P.; Cloutier, N. J.; Greenfield, M. T.; McDermid, S. A.; Dunham, S. U.; Bulte, J. W.; Amedio, J. C., Jr.; Looby, R. J.; Supkowski, R. M.; Horrocks, W. D., Jr.; McMurry, T. J.; Lauffer, R. B., The interaction of MS-325 with human serum albumin and its effect on proton relaxation rates. *J Am Chem Soc* 2002, 124 (12), 3152-62.
22. Zech, S. G.; Eldredge, H. B.; Lowe, M. P.; Caravan, P., Protein Binding to Lanthanide(III) Complexes Can Reduce the Water Exchange Rate at the Lanthanide. *Inorganic Chemistry* 2007, 46 (9), 3576-3584.
23. Caravan, P., Strategies for increasing the sensitivity of gadolinium based MRI contrast agents. *Chemical Society Reviews* 2006, 35 (6), 512-523.
24. Wahsner, J.; Gale, E. M.; Rodríguez-Rodríguez, A.; Caravan, P., Chemistry of MRI Contrast Agents: Current Challenges and New Frontiers. *Chem Rev* 2019, 119 (2), 957-1057.
25. Cao, Y.; Xu, L. J.; Kuang, Y.; Xiong, D. S.; Pei, R. J., Gadolinium-based nanoscale MRI contrast agents for tumor imaging. *Journal of Materials Chemistry B* 2017, 5 (19), 3431-3461.
26. Faucher, L.; Tremblay, M.; Lagueur, J.; Gossuin, Y.; Fortin, M. A., Rapid Synthesis of PEGylated Ultrasmall Gadolinium Oxide Nanoparticles for Cell Labeling and Tracking with MRI. *Acs Applied Materials & Interfaces* 2012, 4 (9), 4506-4515.

27. Wei, H.; Bruns, O. T.; Kaul, M. G.; Hansen, E. C.; Barch, M.; Wisniowska, A.; Chen, O.; Chen, Y.; Li, N.; Okada, S.; Cordero, J. M.; Heine, M.; Farrar, C. T.; Montana, D. M.; Adam, G.; Ittrich, H.; Jasanoff, A.; Nielsen, P.; Bawendi, M. G., Exceedingly small iron oxide nanoparticles as positive MRI contrast agents. *Proceedings of the National Academy of Sciences of the United States of America* 2017, 114 (9), 2325-2330.
28. Stinnett, G.; Taheri, N.; Villanova, J.; Bohloul, A.; Guo, X. T.; Esposito, E. P.; Xiao, Z.; Stueber, D.; Avendano, C.; Decuzzi, P.; Pautler, R. G.; Colvin, V. L., 2D Gadolinium Oxide Nanoplates as T-1 Magnetic Resonance Imaging Contrast Agents. *Advanced Healthcare Materials* 2021, 10 (11).
29. Caravan, P.; Farrar, C. T.; Frullano, L.; Uppal, R., Influence of molecular parameters and increasing magnetic field strength on relaxivity of gadolinium- and manganese-based T1 contrast agents. *Contrast Media Mol Imaging* 2009, 4 (2), 89-100.
30. Cao, Y. C., Synthesis of square gadolinium-oxide nanoplates. *J Am Chem Soc* 2004, 126 (24), 7456-7.
31. Jung, E.; Yu, T.; Kim, W. S., Synthesis of rare earth oxide nanoplates with single unit cell thickness using a thermal decomposition method. *Korean Journal of Chemical Engineering* 2016, 33 (2), 683-687.
32. Paik, T.; Gordon, T. R.; Prantner, A. M.; Yun, H.; Murray, C. B., Designing Tripodal and Triangular Gadolinium Oxide Nanoplates and Self-Assembled Nanofibrils as Potential Multimodal Bioimaging Probes. *Acs Nano* 2013, 7 (3), 2850-2859.
33. Seo, S.; Yang, H.; Holloway, P. H., Controlled shape growth of Eu- or Tb-doped luminescent Gd<sub>2</sub>O<sub>3</sub> colloidal nanocrystals. *Journal of Colloid and Interface Science* 2009, 331 (1), 236-242.
34. Si, R.; Zhang, Y. W.; You, L. P.; Yan, C. H., Rare-earth oxide nanopolyhedra, nanoplates, and nanodisks. *Angewandte Chemie International Edition* 2005, 44 (21), 3256-3260.
35. Si, R.; Zhang, Y. W.; Zhou, H. P.; Sun, L. D.; Yan, C. H., Controlled-synthesis, self-assembly behavior, and surface-dependent optical properties of high-quality rare-earth oxide nanocrystals. *Chemistry of Materials* 2007, 19 (1), 18-27.
36. Yuan, J. Q.; Peng, E. W.; Xue, J. M., Controlled loading of paramagnetic gadolinium oxide nanoplates in PMAO-g-PEG as effective T-1-weighted MRI contrast agents. *Journal of Materials Research* 2014, 29 (15), 1626-1634.
37. Liu, Y.; Dai, Y.; Li, H.; Duosiken, D.; Tang, N.; Sun, K.; Tao, K., Revisiting the factors influencing the magnetic resonance contrast of Gd<sub>2</sub>O<sub>3</sub> nanoparticles. *Nanoscale Advances* 2022, 4 (1), 95-101.
38. Singh, G.; McDonagh, B. H.; Hak, S.; Peddis, D.; Bandopadhyay, S.; Sandvig, I.; Sandvig, A.; Glomm, W. R., Synthesis of gadolinium oxide nanodisks and

- gadolinium doped iron oxide nanoparticles for MR contrast agents. *Journal of Materials Chemistry B* 2017, 5 (3), 418-422.
39. Cho, M. J.; Sethi, R.; Narayanan, J. S. A.; Lee, S. S.; Benoit, D. N.; Taheri, N.; Decuzzi, P.; Colvin, V. L., Gadolinium oxide nanoplates with high longitudinal relaxivity for magnetic resonance imaging. *Nanoscale* 2014, 6 (22), 13637-13645.
  40. Zhou, Z. J.; Hu, R.; Wang, L. R.; Sun, C. J.; Fu, G.; Gao, J. H., Water bridge coordination on the metal-rich facets of Gd<sub>2</sub>O<sub>3</sub> nanoplates confers high T-1 relaxivity. *Nanoscale* 2016, 8 (41), 17887-17894.
  41. Yu, W. W.; Chang, E.; Falkner, J. C.; Zhang, J.; Al-Somali, A. M.; Sayes, C. M.; Johns, J.; Drezek, R.; Colvin, V. L., Forming biocompatible and nonaggregated nanocrystals in water using amphiphilic polymers. *J Am Chem Soc* 2007, 129 (10), 2871-9.
  42. Stinnett, G.; Taheri, N.; Villanova, J.; Bohloul, A.; Guo, X.; Esposito, E. P.; Xiao, Z.; Stueber, D.; Avendano, C.; Decuzzi, P.; Pautler, R. G.; Colvin, V. L., 2D Gadolinium Oxide Nanoplates as T1 Magnetic Resonance Imaging Contrast Agents. *Advanced Healthcare Materials* 2021, 10 (11), 2001780.
  43. Ni, D. L.; Bu, W. B.; Ehlerding, E. B.; Cai, W. B.; Shi, J. L., Engineering of inorganic nanoparticles as magnetic resonance imaging contrast agents. *Chemical Society Reviews* 2017, 46 (23), 7438-7468.
  44. Zhou, Z. J.; Yang, L. J.; Gao, J. H.; Chen, X. Y., Structure-Relaxivity Relationships of Magnetic Nanoparticles for Magnetic Resonance Imaging. *Advanced Materials* 2019, 31 (8), 32.
  45. Alexis, F.; Pridgen, E.; Molnar, L. K.; Farokhzad, O. C., Factors affecting the clearance and biodistribution of polymeric nanoparticles. *Molecular Pharmaceutics* 2008, 5 (4), 505-515.
  46. Decuzzi, P.; Godin, B.; Tanaka, T.; Lee, S. Y.; Chiappini, C.; Liu, X.; Ferrari, M., Size and shape effects in the biodistribution of intravascularly injected particles. *Journal of Controlled Release* 2010, 141 (3), 320-327.
  47. He, C. B.; Hu, Y. P.; Yin, L. C.; Tang, C.; Yin, C. H., Effects of particle size and surface charge on cellular uptake and biodistribution of polymeric nanoparticles. *Biomaterials* 2010, 31 (13), 3657-3666.
  48. Machado, I. P.; Teixeira, V. C.; Pedroso, C. C. S.; Brito, H. F.; Rodrigues, L. C. V., X-ray scintillator Gd<sub>2</sub>O<sub>2</sub>S:Tb<sup>3+</sup> materials obtained by a rapid and cost-effective microwave-assisted solid-state synthesis. *Journal of Alloys and Compounds* 2019, 777, 638-645.
  49. Marasini, S.; Yue, H.; Ghazanfari, A.; Ho, S. L.; Park, J. A.; Kim, S.; Cha, H.; Liu, S.; Tegafaw, T.; Ahmad, M. Y.; Saidi, A. K. A. A.; Zhao, D.; Liu, Y.; Chae, K.-S.; Chang, Y.; Lee, G. H., Polyaspartic Acid-Coated Paramagnetic Gadolinium Oxide

- Nanoparticles as a Dual-Modal T1 and T2 Magnetic Resonance Imaging Contrast Agent. *Applied Sciences* 2021, 11 (17), 8222.
50. Luyer, C.; García Murillo, A.; Bernstein, E.; Mugnier, J., Waveguide Raman spectroscopy of sol–gel Gd<sub>2</sub>O<sub>3</sub> thin films. *Journal of Raman Spectroscopy* 2003, 34, 234-239.
  51. Fortin, M. A.; Petoral, R. M.; Soderlind, F.; Klasson, A.; Engstrom, M.; Veres, T.; Kall, P. O.; Uvdal, K., Polyethylene glycol-covered ultra-small Gd<sub>2</sub>O<sub>3</sub> nanoparticles for positive contrast at 1.5 T magnetic resonance clinical scanning. *Nanotechnology* 2007, 18 (39).
  52. Johnson, N. J. J.; Oakden, W.; Stanisz, G. J.; Prosser, R. S.; van Veggel, F., Size-Tunable, Ultrasmall NaGdF<sub>4</sub> Nanoparticles: Insights into Their T-1 MRI Contrast Enhancement. *Chem. Mater.* 2011, 23 (16), 3714-3722.
  53. Yang, G.; Phua, S. Z. F.; Bindra, A. K.; Zhao, Y., Degradability and Clearance of Inorganic Nanoparticles for Biomedical Applications. *Adv. Mater.* 2019, 31 (10), 1805730.
  54. Ahrén, M.; Selegård, L.; Klasson, A.; Söderlind, F.; Abrikossova, N.; Skoglund, C.; Bengtsson, T.; Engström, M.; Käll, P.-O.; Uvdal, K., Synthesis and Characterization of PEGylated Gd<sub>2</sub>O<sub>3</sub> Nanoparticles for MRI Contrast Enhancement. *Langmuir* 2010, 26 (8), 5753-5762.
  55. Zhou, Z.; Wu, C.; Liu, H.; Zhu, X.; Zhao, Z.; Wang, L.; Xu, Y.; Ai, H.; Gao, J., Surface and interfacial engineering of iron oxide nanoplates for highly efficient magnetic resonance angiography. *ACS Nano* 2015, 9 (3), 3012-22.
  56. Zhou, Z.; Zhu, X.; Wu, D.; Chen, Q.; Huang, D.; Sun, C.; Xin, J.; Ni, K.; Gao, J., Anisotropic Shaped Iron Oxide Nanostructures: Controlled Synthesis and Proton Relaxation Shortening Effects. *Chem. Mater.* 2015, 27 (9), 3505-3515.
  57. Botta, M., Second Coordination Sphere Water Molecules and Relaxivity of Gadolinium(III) Complexes: Implications for MRI Contrast Agents. *European Journal of Inorganic Chemistry* 2000, 2000 (3), 399-407.
  58. Hou, Y.; Qiao, R.; Fang, F.; Wang, X.; Dong, C.; Liu, K.; Liu, C.; Liu, Z.; Lei, H.; Wang, F.; Gao, M., NaGdF<sub>4</sub> nanoparticle-based molecular probes for magnetic resonance imaging of intraperitoneal tumor xenografts in vivo. *ACS Nano* 2013, 7 (1), 330-8.
  59. Laus, S.; Sitharaman, B.; Tóth, É.; Bolskar, R. D.; Helm, L.; Wilson, L. J.; Merbach, A. E., Understanding Paramagnetic Relaxation Phenomena for Water-Soluble Gadofullerenes. *The Journal of Physical Chemistry C* 2007, 111 (15), 5633-5639.
  60. Bloemen, M.; Brullot, W.; Luong, T. T.; Geukens, N.; Gils, A.; Verbiest, T., Improved functionalization of oleic acid-coated iron oxide nanoparticles for biomedical applications. *J Nanopart Res* 2012, 14 (9), 1100.

61. Chen, Z.; Yu, D.; Wang, S.; Zhang, N.; Ma, C.; Lu, Z., Biocompatible Nanocomplexes for Molecular Targeted MRI Contrast Agent. *Nanoscale Res Lett* 2009, 4 (7), 618-26.
62. Alcantar, N. A.; Aydil, E. S.; Israelachvili, J. N., Polyethylene glycol-coated biocompatible surfaces. *J Biomed Mater Res* 2000, 51 (3), 343-51.
63. El-Mahdy, G. A.; Atta, A. M.; Al-Lohedan, H. A., Synthesis and Evaluation of Poly(Sodium 2-Acrylamido-2-Methylpropane Sulfonate-co-Styrene)/Magnetite Nanoparticle Composites as Corrosion Inhibitors for Steel. *Molecules* 2014, 19 (2), 1713-1731.
64. Gad, Y. H., Preparation and characterization of poly(2-acrylamido-2-methylpropane-sulfonic acid)/Chitosan hydrogel using gamma irradiation and its application in wastewater treatment. *Radiation Physics and Chemistry* 2008, 77 (9), 1101-1107.
65. Zhang, X.; Zhang, Q.; Ma, T.; Liu, Q.; Wu, S.; Hua, K.; Zhang, C.; Chen, M.; Cui, Y., Enhanced Stability of Gold Magnetic Nanoparticles with Poly(4-styrenesulfonic acid-co-maleic acid): Tailored Optical Properties for Protein Detection. *Nanoscale Research Letters* 2017, 12 (1).
66. Xu, M.; Zhu, J.; Wang, F.; Xiong, Y.; Wu, Y.; Wang, Q.; Weng, J.; Zhang, Z.; Chen, W.; Liu, S., Improved In Vitro and In Vivo Biocompatibility of Graphene Oxide through Surface Modification: Poly(Acrylic Acid)-Functionalization is Superior to PEGylation. *ACS Nano* 2016, 10 (3), 3267-3281.
67. Dippon, U.; Pabst, S.; Klitzke, S., Colloidal stabilization of CeO<sub>2</sub> nanomaterials with polyacrylic acid, polyvinyl alcohol or natural organic matter. *Science of The Total Environment* 2018, 645, 1153-1158.
68. Arkaban, H.; Barani, M.; Akbarzadeh, M. R.; Pal Singh Chauhan, N.; Jadoun, S.; Dehghani Soltani, M.; Zarrintaj, P., Polyacrylic Acid Nanoplatforms: Antimicrobial, Tissue Engineering, and Cancer Theranostic Applications. *Polymers* 2022, 14 (6), 1259.
69. Sakai, Y.; Matsuguchi, M.; Yonesato, N., Humidity sensor based on alkali salts of poly(2-acrylamido-2-methylpropane sulfonic acid). *Electrochimica Acta* 2001, 46 (10), 1509-1514.
70. Cavus, S., Poly(methacrylamide-co-2-acrylamido-2-methyl-1-propanesulfonic acid) Hydrogels: Investigation of pH- and Temperature-Dependent Swelling Characteristics and Their Characterization. *Journal of Polymer Science Part B: Polymer Physics* 2010, 48 (23), 2497-2508.
71. Dey, R. E.; Wimpenny, I.; Gough, J. E.; Watts, D. C.; Budd, P. M., Poly(vinylphosphonic acid-co-acrylic acid) hydrogels: The effect of copolymer composition on osteoblast adhesion and proliferation. *J Biomed Mater Res A* 2018, 106 (1), 255-264.

72. Geyer, P. E.; Holdt, L. M.; Teupser, D.; Mann, M., Revisiting biomarker discovery by plasma proteomics. *Mol Syst Biol* 2017, 13 (9), 942.
73. Premaratne, W. A. P. J.; Priyadarshana, G.; Gunawardena, S.; de Alwis, A., Synthesis of Nanosilica from Paddy Husk Ash and Their Surface Functionalization. *J. Sci. Univ. Kelaniya* 2013, 8, 33-48.
74. Yoon, J.-Y.; Kim, J.-H.; Kim, W.-S., The relationship of interaction forces in the protein adsorption onto polymeric microspheres<sup>1</sup>This paper was presented in the 7th Iketani Conference — International Symposium on Advanced Technology of Fine Particles, October 1997, Yokohama Symposia, Japan.<sup>1</sup> *Colloids and Surfaces A: Physicochemical and Engineering Aspects* 1999, 153 (1), 413-419.
75. Çavuş, S., Poly(methacrylamide-co-2-acrylamido-2-methyl-1-propanesulfonic acid) hydrogels: Investigation of pH- and temperature-dependent swelling characteristics and their characterization. *Journal of Polymer Science Part B: Polymer Physics* 2010, 48 (23), 2497-2508.
76. Caravan, P.; Farrar, C. T.; Frullano, L.; Uppal, R., Influence of molecular parameters and increasing magnetic field strength on relaxivity of gadolinium- and manganese-based T(1) contrast agents. *Contrast Media Mol. Imaging* 2009, 4 (2), 89-100.
77. Johnson, N. J. J.; He, S.; Hun, V. A. N.; Almutairi, A., Compact Micellization: A Strategy for Ultrahigh T-1 Magnetic Resonance Contrast with Gadolinium-Based Nanocrystals. *Acs Nano* 2016, 10 (9), 8299-8307.
78. Kuang, Y.; Cao, Y.; Liu, M.; Zu, G. Y.; Zhang, Y. J.; Zhang, Y.; Pei, R. J., Geometrical Confinement of Gadolinium Oxide Nanoparticles in Poly(ethylene glycol)/Arginylglycylaspartic Acid-Modified Mesoporous Carbon Nanospheres as an Enhanced T-1 Magnetic Resonance Imaging Contrast Agent. *Acs Applied Materials & Interfaces* 2018, 10 (31), 26099-26107.
79. Lohrke, J.; Frenzel, T.; Endrikat, J.; Alves, F. C.; Grist, T. M.; Law, M.; Lee, J. M.; Leiner, T.; Li, K. C.; Nikolaou, K.; Prince, M. R.; Schild, H. H.; Weinreb, J. C.; Yoshikawa, K.; Pietsch, H., 25 Years of Contrast-Enhanced MRI: Developments, Current Challenges and Future Perspectives. *Adv. Ther.* 2016, 33 (1), 1-28.
80. Meenambal, R.; Poojar, P.; Geethanath, S.; Kannan, S., Substitutional limit of gadolinium in beta-tricalcium phosphate and its magnetic resonance imaging characteristics. *J. Biomed. Mater. Res. B Appl. Biomater.* 2017, 105 (8), 2545-2552.
81. Ni, D. L.; Zhang, J. W.; Wang, J.; Hu, P.; Jin, Y. Y.; Tang, Z. M.; Yao, Z. W.; Bu, W. B.; Shi, J. L., Oxygen Vacancy Enables Markedly Enhanced Magnetic Resonance Imaging-Guided Photothermal Therapy of a Gd<sup>3+</sup>-Doped Contrast Agent. *ACS Nano* 2017, 11 (4), 4256-4264.
82. Park, J. Y.; Baek, M. J.; Choi, E. S.; Woo, S.; Kim, J. H.; Kim, T. J.; Jung, J. C.; Chae, K. S.; Chang, Y.; Lee, G. H., Paramagnetic Ultrasmall Gadolinium Oxide Nanoparticles as Advanced T-1 MR1 Contrast Agent: Account for Large



- Longitudinal Relaxivity, Optimal Particle Diameter, and In Vivo T-1 MR Images. *ACS Nano* 2009, 3 (11), 3663-3669.
83. Sanchez, P.; Valero, E.; Galvez, N.; Dominguez-Vera, J. M.; Marinone, M.; Poletti, G.; Corti, M.; Lascialfari, A., MRI relaxation properties of water-soluble apoferritin-encapsulated gadolinium oxide-hydroxide nanoparticles. *Dalton Trans.* 2009, (5), 800-804.
  84. Shen, Z. Y.; Fan, W. P.; Yang, Z.; Liu, Y. J.; Bregadze, V. I.; Mandal, S. K.; Yung, B. C.; Lin, L. S.; Liu, T.; Tang, W.; Shan, L. L.; Liu, Y.; Zhu, S. J.; Wang, S.; Yang, W. J.; Bryant, L. H.; Nguyen, D. T.; Wu, A. G.; Chen, X. Y., Exceedingly Small Gadolinium Oxide Nanoparticles with Remarkable Relaxivities for Magnetic Resonance Imaging of Tumors. *Small* 2019, 15 (41), 9.
  85. Shen, Z. Y.; Liu, T.; Yang, Z.; Zhou, Z. J.; Tang, W.; Fan, W. P.; Liu, Y. J.; Mu, J.; Li, L.; Bregadze, V. I.; Mandal, S. K.; Druzina, A. A.; Wei, Z. N.; Qiu, X. Z.; Wu, A. G.; Chen, X. Y., Small-sized gadolinium oxide based nanoparticles for high-efficiency theranostics of orthotopic glioblastoma. *Biomaterials* 2020, 235, 12.
  86. Wahsner, J.; Gale, E. M.; Rodriguez-Rodriguez, A.; Caravan, P., Chemistry of MRI Contrast Agents: Current Challenges and New Frontiers. *Chemical Reviews* 2019, 119 (2), 957-1057.
  87. Xiao, N.; Gu, W.; Wang, H.; Deng, Y. L.; Shi, X.; Ye, L., T-1-T-2 dual-modal MRI of brain gliomas using PEGylated Gd-doped iron oxide nanoparticles. *J. Colloid Interface Sci.* 2014, 417, 159-165.
  88. Zeng, L. Y.; Wu, D.; Zou, R. F.; Chen, T. X.; Zhang, J. C.; Wu, A. G., Paramagnetic and Superparamagnetic Inorganic Nanoparticles for T-1-Weighted Magnetic Resonance Imaging. *Curr. Med. Chem.* 2018, 25 (25), 2970-2986.
  89. Zeng, Y.; Wang, L. Q.; Zhou, Z. J.; Wang, X. Y.; Zhang, Y.; Wang, J. Q.; Mi, P.; Liu, G.; Zhou, L. M., Gadolinium hybrid iron oxide nanocomposites for dual T-1- and T-2-weighted MR imaging of cell labeling. *Biomater. Sci.* 2017, 5 (1), 50-56.
  90. Zheng, X. Y. Z., K.; Tang, J.; Wang, X. Y.; Li, L. D.; Chen, N. X.; Wang, Y. J.; Shi, S.; Zhang, X.; Malaisamy, S.; Sun, L. D.; Wang, X.; Chen, C.; yan, C. H., Gd-Dots with Strong Ligand-Water Interaction for Ultrasensitive Magnetic Resonance Renography. *ACS Nano* 2017, 11, 3640-3650.
  91. Zhou, Z. J.; Huang, D. T.; Bao, J. F.; Chen, Q. L.; Liu, G.; Chen, Z.; Chen, X. Y.; Gao, J. H., A Synergistically Enhanced T-1-T-2 Dual-Modal Contrast Agent. *Adv. Mater.* 2012, 24 (46), 6223-6228.
  92. Caravan, P.; Ellison, J. J.; McMurry, T. J.; Lauffer, R. B., Gadolinium(III) Chelates as MRI Contrast Agents: Structure, Dynamics, and Applications. *Chemical reviews* 1999, 99 9, 2293-352.

93. Caravan, P.; Astashkin, A. V.; Raitsimring, A. M., The Gadolinium(III)–Water Hydrogen Distance in MRI Contrast Agents. *Inorganic Chemistry* 2003, 42 (13), 3972-3974.
94. Chen, J. W.; Belford, R. L.; Clarkson, R. B., Second-Sphere and Outer-Sphere Proton Relaxation of Paramagnetic Complexes: From EPR to NMRD. *The Journal of Physical Chemistry A* 1998, 102 (12), 2117-2130.
95. Ananta, J. S.; Godin, B.; Sethi, R.; Moriggi, L.; Liu, X.; Serda, R. E.; Krishnamurthy, R.; Muthupillai, R.; Bolskar, R. D.; Helm, L.; Ferrari, M.; Wilson, L. J.; Decuzzi, P., Geometrical confinement of gadolinium-based contrast agents in nanoporous particles enhances T1 contrast. *Nat. Nanotechnol.* 2010, 5 (11), 815-21.
96. Courant, T.; Roullin, V. G.; Cadiou, C.; Callewaert, M.; Andry, M. C.; Portefaix, C.; Hoeffel, C.; de Goltstein, M. C.; Port, M.; Laurent, S.; Elst, L. V.; Muller, R.; Molinari, M.; Chuburu, F., Hydrogels incorporating GdDOTA: towards highly efficient dual T1/T2 MRI contrast agents. *Angew. Chem. Int. Ed.* 2012, 51 (36), 9119-22.
97. Dash, A.; Blasiak, B.; Tomanek, B.; van Veggel, F., Validation of Inner, Second, and Outer Sphere Contributions to T-1 and T-2 Relaxation in Gd<sup>3+</sup>-Based Nanoparticles Using Eu<sup>3+</sup> Lifetime Decay as a Probe. *Journal of Physical Chemistry C* 2018, 122 (21), 11557-11569.
98. Jacques, V.; Dumas, S.; Sun, W. C.; Troughton, J. S.; Greenfield, M. T.; Caravan, P., High-relaxivity magnetic resonance imaging contrast agents. Part 2. Optimization of inner- and second-sphere relaxivity. *Invest. Radiol.* 2010, 45 (10), 613-24.
99. Ni, K.; Zhao, Z.; Zhang, Z.; Zhou, Z.; Yang, L.; Wang, L.; Ai, H.; Gao, J., Geometrically confined ultrasmall gadolinium oxide nanoparticles boost the T(1) contrast ability. *Nanoscale* 2016, 8 (6), 3768-74.
100. Pothayee, N.; Balasubramaniam, S.; Pothayee, N.; Jain, N.; Hu, N.; Lin, Y.; Davis, R. M.; Sriranganathan, N.; Koretsky, A. P.; Riffle, J. S., Magnetic nanoclusters with hydrophilic spacing for dual drug delivery and sensitive magnetic resonance imaging. *Journal of Materials Chemistry B* 2013, 1 (8), 1142-1149.
101. Rotz, M. W.; Culver, K. S.; Parigi, G.; MacRenaris, K. W.; Luchinat, C.; Odom, T. W.; Meade, T. J., High relaxivity Gd(III)-DNA gold nanostars: investigation of shape effects on proton relaxation. *ACS Nano* 2015, 9 (3), 3385-96.
102. Rowe, M.; Thamm, D.; Kraft, S.; Boyes, S., Polymer-Modified Gadolinium Metal-Organic Framework Nanoparticles Used as Multifunctional Nanomedicines for the Targeted Imaging and Treatment of Cancer. *Biomacromolecules* 2009, 10, 983-93.
103. Wartenberg, N.; Fries, P.; Raccurt, O.; Guillermo, A.; Imbert, D.; Mazzanti, M., A Gadolinium Complex Confined in Silica Nanoparticles as a Highly Efficient T1/T2 MRI Contrast Agent. *Chem. - Eur. J.* 2013, 19 (22), 6980-6983.

104. Gessner, A.; Lieske, A.; Paulke, B.; Müller, R., Influence of surface charge density on protein adsorption on polymeric nanoparticles: analysis by two-dimensional electrophoresis. *Eur J Pharm Biopharm* 2002, 54 (2), 165-70.
105. Bischel, H. N.; Macmanus-Spencer, L. A.; Zhang, C.; Luthy, R. G., Strong associations of short-chain perfluoroalkyl acids with serum albumin and investigation of binding mechanisms. *Environ Toxicol Chem* 2011, 30 (11), 2423-30.
106. Han, D. K.; Park, K. D.; Ryu, G. H.; Kim, U. Y.; Min, B. G.; Kim, Y. H., Plasma protein adsorption to sulfonated poly(ethylene oxide)-grafted polyurethane surface. *J Biomed Mater Res* 1996, 30 (1), 23-30.
107. Jackson, T. W.; Scheibly, C. M.; Polera, M. E.; Belcher, S. M., Rapid Characterization of Human Serum Albumin Binding for Per- And Polyfluoroalkyl Substances Using Differential Scanning Fluorimetry. *bioRxiv* 2021, 2021.06.13.448257.
108. Luebker, D. J.; Hansen, K. J.; Bass, N. M.; Butenhoff, J. L.; Seacat, A. M., Interactions of fluorochemicals with rat liver fatty acid-binding protein. *Toxicology* 2002, 176 (3), 175-185.
109. Matulis, D.; Lovrien, R., 1-Anilino-8-Naphthalene Sulfonate Anion-Protein Binding Depends Primarily on Ion Pair Formation. *Biophysical Journal* 1998, 74 (1), 422-429.
110. Salvalaglio, M.; Muscionico, I.; Cavallotti, C., Determination of Energies and Sites of Binding of PFOA and PFOS to Human Serum Albumin. *The journal of physical chemistry. B* 2010, 114, 14860-74.
111. Tang, M.; Xue, J.; Yan, K.; Xiang, T.; Sun, S.; Zhao, C., Heparin-like surface modification of polyethersulfone membrane and its biocompatibility. *Journal of Colloid and Interface Science* 2012, 386 (1), 428-440.
112. Xiang, T.; Lu, T.; Xie, Y.; Zhao, W.-F.; Sun, S.-D.; Zhao, C.-S., Zwitterionic polymer functionalization of polysulfone membrane with improved antifouling property and blood compatibility by combination of ATRP and click chemistry. *Acta Biomaterialia* 2016, 40, 162-171.
113. Zhang, A.; Sun, W.; Liang, X.; Chen, X.; Li, Y.; Liu, X.; Chen, H., The role of carboxylic groups in heparin-mimicking polymer-functionalized surfaces for blood compatibility: Enhanced vascular cell selectivity. *Colloids Surf B Biointerfaces* 2021, 201, 111653.
114. Zhang, L.; Ren, X. M.; Guo, L. H., Structure-based investigation on the interaction of perfluorinated compounds with human liver fatty acid binding protein. *Environ Sci Technol* 2013, 47 (19), 11293-301.
115. Zhong, W.; Zhang, L.; Cui, Y.; Chen, M.; Zhu, L., Probing mechanisms for bioaccumulation of perfluoroalkyl acids in carp (*Cyprinus carpio*): Impacts of

protein binding affinities and elimination pathways. *Science of The Total Environment* 2019, 647, 992-999.

116. Jia, B.; Cui, M.-J.; Yang, C.-C.; Hu, S.-Y.; Lv, Y.-K., Adsorption characteristics of monodisperse magnetic cation-exchange microspheres prepared based on swell-penetration method. *Journal of Applied Polymer Science* 2019, 136 (40), 48019.
117. Li, W.; Li, S., A study on the adsorption of bovine serum albumin onto electrostatic microspheres: Role of surface groups. *Colloids and Surfaces A-physicochemical and Engineering Aspects - COLLOID SURFACE A* 2007, 295, 159-164.
118. Lindl, T., *Zell- und gewebekultur : von den grundlagen zur laborbank*. Springer: [Place of publication not identified], 2008.
119. Zheng, X.; Baker, H.; Hancock, W. S.; Fawaz, F.; McCaman, M.; Pungor, E., Jr., Proteomic analysis for the assessment of different lots of fetal bovine serum as a raw material for cell culture. Part IV. Application of proteomics to the manufacture of biological drugs. *Biotechnol Prog* 2006, 22 (5), 1294-300.
120. Stevens, F. J., Analysis of protein-protein interaction by simulation of small-zone size exclusion chromatography. Stochastic formulation of kinetic rate contributions to observed high-performance liquid chromatography elution characteristics. *Biophysical Journal* 1989, 55 (6), 1155-1167.
121. Wiley, H. S.; Herbst, J. J.; Walsh, B. J.; Lauffenburger, D. A.; Rosenfeld, M. G.; Gill, G. N., The role of tyrosine kinase activity in endocytosis, compartmentation, and down-regulation of the epidermal growth factor receptor. *Journal of Biological Chemistry* 1991, 266 (17), 11083-11094.
122. Hanusch, U.; Mahmoudi, M.; Maurizi, L.; Coullerez, G.; Hofmann, M.; Rezaee, F.; Motazacker, M.; de vries, M.; Hofmann, H., Significance of surface charge and shell material of Superparamagnetic Iron Oxide Nanoparticles (SPIONs) based core/shell nanoparticles on the composition of the protein corona. *Biomaterials Science* 2015, 3, 265-278.
123. Kim, Y.; Ko, S. M.; Nam, J. M., Protein-Nanoparticle Interaction-Induced Changes in Protein Structure and Aggregation. *Chem Asian J* 2016, 11 (13), 1869-77.
124. Papini, E.; Tavano, R.; Mancin, F., Opsonins and Dysopsonins of Nanoparticles: Facts, Concepts, and Methodological Guidelines. *Front Immunol* 2020, 11, 567365.
125. Wang, H.; Lin, Y.; Nienhaus, K.; Nienhaus, G. U., The protein corona on nanoparticles as viewed from a nanoparticle-sizing perspective. *Wiley Interdiscip Rev Nanomed Nanobiotechnol* 2018, 10 (4), e1500.
126. Yoo, H.; Triandafillou, C.; Drummond, D. A., Cellular sensing by phase separation: Using the process, not just the products. *J Biol Chem* 2019, 294 (18), 7151-7159.

127. Kennedy, B.; Avdeev, M., The Structure of C -type Gd<sub>2</sub>O<sub>3</sub> . A Powder Neutron Diffraction Study using Enriched <sup>160</sup>Gd. Australian Journal of Chemistry 2011, 64, 119.
128. Huang, Y.-W.; Cambre, M.; Lee, H.-J., The Toxicity of Nanoparticles Depends on Multiple Molecular and Physicochemical Mechanisms. International journal of molecular sciences 2017, 18 (12), 2702.
129. Mazi, W.; Adhikari, R.; Zhang, Y.; Xia, S.; Fang, M.; Luck, R. L.; Tajiri, M.; Tiwari, A.; Tanasova, M.; Liu, H., Fluorescent probes with high pKa values based on traditional, near-infrared rhodamine, and hemicyanine fluorophores for sensitive detection of lysosomal pH variations. Methods 2019, 168, 40-50.
130. Ngen, E. J.; Artemov, D., Advances in Monitoring Cell-Based Therapies with Magnetic Resonance Imaging: Future Perspectives. International journal of molecular sciences 2017, 18 (1), 198.

## Chapter 5

### Clustered Magnetic Nanomaterials as MRI Contrast agents: Iron Oxide

#### Nanoworms and Ferrite Clusters<sup>†</sup>

<sup>†</sup> Reprinted (adapted) with permission from the following:

1) Xiao Z.; Zhang Q.; Guo X.; **Villanova J.**; Hu Y.; Kulaots I.; Garcia-Rojas D.; Guo W.; Colvin V. L., Libraries of Uniform Magnetic Multicore Nanoparticles with Tunable Dimensions for Biomedical and Photonic Applications, *ACS Applied Materials & Interfaces* **2020**, 12, 37, 41932–41941.

2) Xiao, Z.; **Villanova, J.**; Lee, M. J.; Stueber, D. D.; Zhang, Q.; Colvin, V. L., Magnetic Nanocrystal Chains with Large Magnetic Susceptibilities and Anisotropic Coercivity, *in preparation*.

3) Xiao, Z.; Guo, X.; **Villanova, J.**; Bi, Y.; Avidan, S.; Effman, S.; Zhang, Q.; Colvin, V. L., Portable Heating and Environmental Remediation Using the Giant Susceptibilities of Manganese-Doped Ferrite Clusters, *in preparation*.

## Chapter 5 Clustered Magnetic Nanomaterials as MRI Contrast agents: Iron Oxide Nanoworms and Ferrite Clusters

### 5.1. Abstract

Here, we present robust synthetic procedures allowing for the dimensional control of iron oxide clusters, manganese-ferrite clusters, and nanoworms for use as highly sensitive MRI contrast agents. Primary particle (4 – 10 nm) and cluster (20 – 200 nm) size of iron oxide and manganese ferrite clusters are reliably controlled with reaction temperature and concentration of water, respectively. The length of iron oxide nanoworms is reliably controlled between 0.8 and 4.7  $\mu\text{m}$  by applied magnetic field during silica deposition. The  $T_2$  relaxivity of these materials is exceptional (300 – 450  $\text{mM}^{-1}\text{s}^{-1}$ ) compared to commercial  $T_2$  MRI contrast agents (<200  $\text{mM}^{-1}\text{s}^{-1}$ ). Also, manganese ferrite clusters demonstrate exceptional  $T_1$  relaxivity ( $\sim 80 \text{mM}^{-1}\text{s}^{-1}$ ) and open the door to advanced applications in multimodal  $T_1/T_2$  imaging. In sum, with comprehensive dimensional control over clustered magnetic materials, their magnetic properties can be optimized for the efficient design of highly sensitive MRI contrast agents.

### 5.2. Introduction

Iron oxide nanocrystals (IONCs) have garnered considerable interest as gadolinium-free MRI contrast agents.<sup>1-3</sup> These materials generate localized inhomogeneous fields in the large magnetic fields of MRI scanners which accelerate transverse water  $^1\text{H}$  relaxation ( $T_2$ ) near their surface producing negative (dark) contrast in images. Due to their biocompatibility, hepatobiliary biodistribution, and clearance mechanisms, IONCs are the only gadolinium free nanoscale contrast agents approved by the US Food and Drug

Administration (FDA) for clinical use as MRI contrast agents.<sup>2</sup> Commercial IONCs like ferumoxytol (Feraheme) have been used for diverse applications including tumor imaging (e.g., liver, spleen, lymph nodes, brain), stem cell tracking, angiography, and perfusion imaging.<sup>4</sup> More advanced applications in molecular imaging require stable and biocompatible materials with enhanced contrast performance ( $T_2$  relaxivity) and specificity for greater sensitivity.<sup>1, 3-6</sup>

A major challenge to developing high performing  $T_2$  contrast agents for advanced MRI applications is understanding their physiochemical and magnetic properties in relation to their relaxation dynamics. A common trend reported is that IONC contrast performance ( $T_2$  relaxivity;  $r_2$ ) increases with core size due to increases in magnetization and water diffusion times.<sup>7-11</sup> Because of their larger magnetic moments and high surface energy, these materials also have the potential to aggregate – leading to acute toxicity, RES organ uptake, and shorter circulation times.<sup>12-14</sup> Robust surface coatings are therefore required for optimal colloidal stability, pharmacokinetics, biodistribution, and biocompatibility.<sup>1, 3, 13</sup> Surface coating, along with crystallinity, shape, and clustering, are also known to significantly impact  $r_2$ .<sup>15-28</sup> Clustering is a particularly interesting approach as it offers an enhanced magnetic properties and greater tunability than other types of magnetic materials.<sup>1, 3</sup> However, greater synthetic control of the dimensions of clustered materials is needed take advantage of their tunability for use as MRI contrast agents.<sup>1, 3, 29</sup>

Here, we present robust synthetic procedures allowing for the dimensional control of iron oxide clusters, manganese-ferrite clusters, and nanoworms for use as highly sensitive MRI contrast agents. Iron oxide nanocrystals are monodispersed and colloidally stable with



primary particle and cluster sizes controlled between 4 to 10 and 20 to 200 nm, respectively. Primary particle and cluster size are reliably controlled with reaction temperature and concentration of water, respectively. Consistent with contemporary relaxation theory,  $T_2$  relaxivity is cluster size dependent with optimal dimensions around 50 nm for a maximum  $r_2$  of approximately  $350 \text{ mM}^{-1}\text{s}^{-1}$ .<sup>3, 30, 31</sup> Silica-encapsulated iron oxide nanoworms are monodispersed and colloidally stable composed of 40 nm iron oxide cluster subunits with controllable length (0.8 – 4.7  $\mu\text{m}$ ). Length of nanoworms is reliably controlled by the linear external magnetic field strength applied during silica deposition.  $T_2$  relaxivity is nanoworm length dependent with optimal size around 2  $\mu\text{m}$  for a maximum  $r_2$  of approximately  $450 \text{ mM}^{-1}\text{s}^{-1}$ . Reaching maximum  $r_2$  at such a large size is unexpected but can be explained by the affect its impermeable silica surface coating has on the relaxation of water.<sup>3, 30-32</sup> The maximum  $r_2$  for these materials is also attributable to their large saturation magnetizations. Beyond clustering, another effective way is to increase saturation magnetization of the materials by doping other divalent metals such as Zn, Mn, Co, and Ni and forming ferrites ( $\text{M}_x\text{Fe}_{3-x}\text{O}_4$ ,  $\text{M} = \text{Zn, Mn, Co, Ni}$ ).<sup>1, 10, 18, 33-36</sup> We synthesize manganese ferrite clusters (MFCs) with the same range of dimensional control as iron oxide clusters, but with greater saturation magnetization and, as expected,  $T_2$  relaxivities much greater than their dimensionally similar counterparts ( $450 \text{ vs } 275 \text{ mM}^{-1}\text{s}^{-1}$ ). Manganese composition is easily controlled with the ratio of iron and manganese salts. Also, inclusion of paramagnetic ions like  $\text{Mn}^{2+}$  give MFCs exceptional  $T_1$  relaxivities ( $\sim 80 \text{ mM}^{-1}\text{s}^{-1}$ ), making them promising dual  $T_1/T_2$  contrast agents for advanced multimodal imaging applications.<sup>37-42</sup> In sum, with comprehensive

dimensional control over clustered magnetic materials, their magnetic properties can be optimized for the efficient design of highly sensitive MRI contrast agents.

### 5.3. Results and Discussion

#### 5.3.1. Iron Oxide Clusters

Here, we synthesize iron oxide nanoclusters with control of primary particle diameter ( $d_p$ ) and overall cluster diameter ( $D_c$ ) over a wide range of sizes. Iron salts hydrolyzed in alcohol at high temperatures form iron oxide nanocrystals that aggregate into individual clusters (**Figure 5.1a**). Studies have demonstrated that there are many steps during this process.<sup>43, 44</sup> Small amount of water in the alcohol solvents cause the formation of iron hydroxides, which form denser, crystalline iron oxides (primary particles) like magnetite at temperatures over 185°C (**Figure 5.1b**). Hundreds of these primary particles then aggregate into compact, and porous, clusters. These clusters can be characterized by both primary particle ( $d_p$ ) and cluster ( $D_c$ ) size (**Figure 5.1c**). Independently controlling these

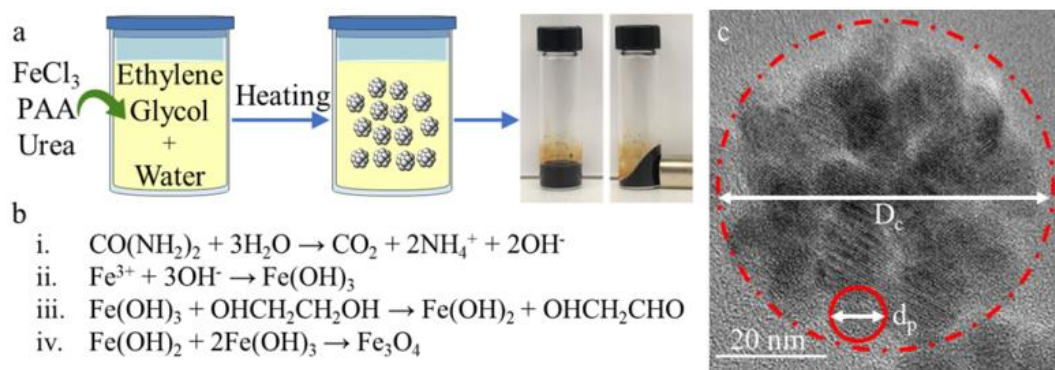


**Figure 5.1 Synthesis of the iron oxide nanoclusters.** (a) Schematic outlining reaction procedure. (b) Reaction pathway for the formation of  $\text{Fe}_3\text{O}_4$ . (c) Transmission electron microscopy (TEM) image outlining the dimensional parameters of iron oxide clusters: cluster ( $D_c$ , 50 nm) and primary particle ( $d_p$ , 10 nm) sizes outlined in red.

parameters, and over a wide range, has not been achieved. Attempts to make larger primary particles by increasing iron concentrations has also led to larger (> 100 nm) and more polydisperse clusters – with some smaller exceptions (30 nm).<sup>45-51</sup>

Temperature and volume of water added can more effectively control primary particle and cluster size, respectively. This approach yields a range of cluster (20 – 200 nm) and primary particle (4 – 10 nm) sizes. As a necessary reactant for hydrolyzing iron salts, water is critical in controlling cluster size; complete removal of water results in micron-sized clusters.<sup>52</sup> Here, increasing the molar concentration of water (0.3 – 6.2 M) effectively reduces cluster size (125 – 35 nm) with a constant primary particle size of about 4 nm (Figure 5.2a-e). We hypothesize that increased water not only increases iron salt hydrolysis, but also changes the solution viscosity, which promotes smaller and more

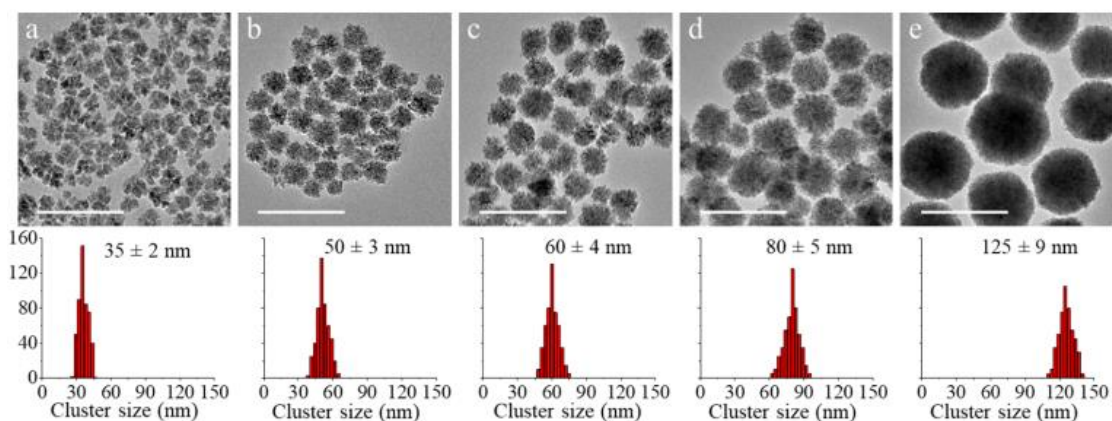


**Figure 5.2 Transmission electron microscopy (TEM) images and size distributions for iron oxide clusters of different size.** (bottom) Size distribution histograms and (top) are cluster samples of different cluster sizes. The molar concentrations of water for each synthesis are (a) 6.2, (b) 3.9, (c) 2.6, (d) 1.1, and (e) 0.3 M, respectively. The reported spread in diameter is the standard deviation from the measured diameters of the 500 clusters. Scale bar: 200 nm.

monodispersed clusters.<sup>32, 53</sup> On the other hand, reaction temperature is useful for tuning primary particle size. Reaction temperature both speeds up nucleation and facilitates Ostwald ripening and LaMer growth.<sup>44</sup> In agreement with the literature, we find that primary particle size increases with temperature.<sup>54, 55</sup> Limited by the maximum temperature of our reactor (275 °C), we achieve a maximum primary particle size of 10 nm (**Figure 5.1c**). Reducing the reaction temperature from 275 °C to the minimum temperature allowing crystallization (185 °C), we achieve a range of primary particle sizes (10 – 4 nm) with a constant cluster size of approximately 50 nm. Using these two parameters, water concentration and reaction temperature, we can form libraries of uniform iron oxide clusters with a range of cluster (25 – 90 nm) and primary particle (4 – 9 nm) sizes (**Figure S5.1, Table 5.1**).

Other reaction parameters like the reaction time and the concentrations of polyacrylate (PAA), urea, and iron chloride (FeCl<sub>3</sub>) could also be used to tune cluster and primary particle size, but with varied success (**Figure S5.2a-f**). Urea and PAA have little impact on either primary particle or cluster size compared to water and reaction temperature. As a surface coating, increasing concentration of PAA prevents aggregation, reducing cluster size (50 – 80 nm) but not over as wide a range as water.<sup>48, 56</sup> Used as a base in the reaction, urea is necessary to form the more dense, crystalline iron oxide and can therefore decrease cluster size (50 – 100 nm) with increased concentration but not over as wide a range as water.<sup>43</sup> Cluster size is pretty sensitive to FeCl<sub>3</sub> concentration (40 – 200 nm), but produced optimally uniform clusters at 100 mM. Increasing reaction time can increase primary particle size by Ostwald ripening, which in turn reduces sample uniformity.

The crystal phase of iron oxide nanocrystals is characterized by x-ray diffraction (XRD), Raman spectroscopy, and vibrating sample magnetometry (VSM) to be magnetite ( $\text{Fe}_3\text{O}_4$ ) iron oxide (**Figure S5.3 and Figure S5.4**). For XRD, patterns for a wide range of cluster and primary particle sizes are found to closely match the standard diffraction pattern for bulk magnetite iron oxide between  $10$  and  $95^\circ$  (**Figure S5.3a,b**). Close attention to higher order peaks ( $85 - 95^\circ$ ) help further confirm that these clusters are magnetite as opposed to maghemite iron oxide (**Figure S5.3c,d**). However, since distinguishing between these two phases is difficult in XRD, Raman spectroscopy shows that clusters have both Fe(II) and Fe(III), characteristic of magnetite (**Figure S5.4**).<sup>57</sup> As expected, samples smaller than  $50$  nm, VSM data show that clusters are superparamagnetic having no observable hysteresis at room temperature (**Figure S5.5**). The saturation magnetization for these clusters remains fairly constant ( $74 - 86$  emu/g  $\text{Fe}_3\text{O}_4$ ) no matter the cluster or primary particle size. This strong magnetization, similar to that of bulk magnetite, is another good indication the clusters are highly crystalline magnetite, rather than maghemite.<sup>58</sup>

As-synthesized PAA-coated iron oxide clusters have reasonable colloidal stability in water. After magnetic separation or centrifugation, clusters can be easily redispersed in water forming a transparent yellow-brown solution at low concentrations. The infrared spectrum for as-synthesized clusters shows that they have vibrational modes associated with PAA, thus helping to confirm that they are PAA-coated (**Figure S5.6**). Not only does PAA help bind primary particles in the clusters, but it also extends into solution and promotes colloidal stability – PAA-coated  $45$  nm clusters have a hydrodynamic diameter of about  $65$  nm (**Figure 5.3a**). However, PAA-coated clusters are not stable under

physiologically relevant acidic and ionic (PBS) conditions (**Figure 5.3b,c**). Further modification with a more colloidal stable polymeric surface coating is important for future biomedical applications.

Here, we modify our clusters with a sulfonated copolymer poly(AA-co-AMPS) surface coating to promote colloidal stability under harsher physiologically relevant conditions.<sup>59-</sup>

<sup>61</sup> The hydrodynamic diameter of copolymer-coated clusters increases to 100 nm (**Figure 5.3a**). Further, the copolymer-coated clusters have much greater colloidal stability, exhibiting no aggregation over a wide pH range and in PBS buffer solution (**Figure 5.3b,c**). Sulfonate-containing polymers have been shown to exhibit great charge stabilization, and therefore colloidal stability, over a wide range of harsh media conditions.<sup>59-61</sup> Further,

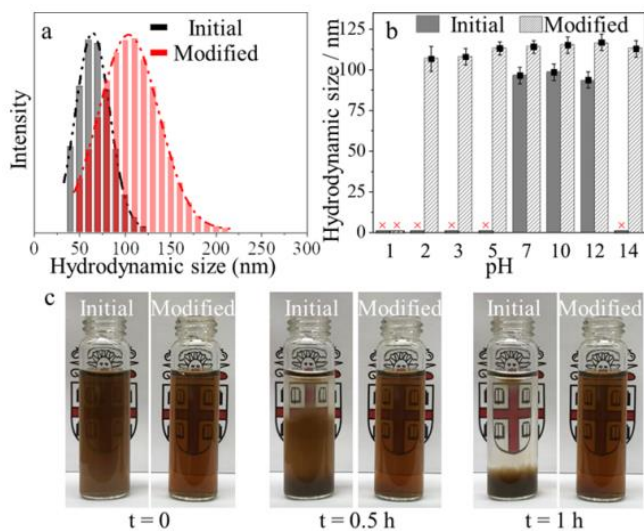


**Figure 5.3 Cluster surface functionalization and colloidal stability.** (a) DLS size distribution of a representative as-synthesized PAA-coated cluster and poly(AA-co-AMPS) modified cluster (PDI of 0.12 and 0.11, respectively). (b) Hydrodynamic size PAA- and poly(AA-co-AMPS)-modified clusters at different pH (× signifies visible aggregation). (c) Stability in phosphate buffered saline (PBS) solution of PAA- and poly(AA-co-AMPS)-modified clusters.

unlike the original carboxylate groups anchoring PAA to the clusters, poly(AA-co-AMPS) is linked to the clusters via a stronger, bidentate, catechol (nitro-dopamine) interaction – the nitro functionality further strengthening the bond.<sup>62-65</sup> The molecular weight (87 kDa) and composition of poly(AA-co-AMPS) are confirmed using HPLC and NMR, respectively (Figure S5.7a-c).

The high saturation magnetization and lower dimensional tunability of these clusters make them potentially useful for biomedical applications like contrast enhanced magnetic resonance imaging (MRI).<sup>2, 3, 31</sup> Magnetic nanoparticles inside the external field of an MRI system generate localized fields that facilitate the relaxation of water protons which, in the case of T<sub>2</sub> contrast agents like our clusters, generates dark signal enhancement.<sup>3, 31</sup> Phantom MR images demonstrate that these clusters do in fact affect contrast, and in a concentration- and cluster size-dependent fashion (Figure 5.4a). The ability of a contrast

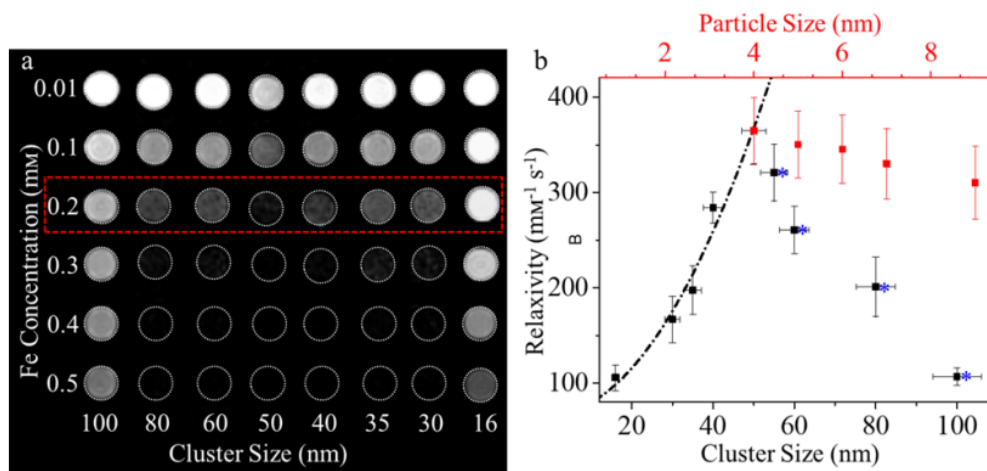


**Figure 5.4 T<sub>2</sub> weighted MR images and relaxivity of iron oxide clusters.** (a) Phantom images of the clusters as a function of cluster size and iron concentration (only 50 nm cluster are significantly dark at 0.2 mM). (b) T<sub>2</sub> relaxivity as a function of cluster ( $D_c$ ) and primary particle ( $d_p$ ) size. Black dashed line fits the universal scaling law proposed by Vuong et al.

agent to speed up relaxation, and therefore enhance contrast, is called its relaxivity. Plotting the  $T_2$  relaxivity ( $r_2$ ) as a function of cluster dimensions reveals that  $r_2$  is dependent on cluster and primary particle size (**Figure 5.4b**). Relaxivity decreases slightly with primary particle size but is significantly impacted by cluster size – a trend following the universal scaling law for clustered iron oxide  $T_2$  contrast agents proposed by Vuong et al.<sup>30</sup> Consistent with this law, for smaller cluster sizes (20 – 50 nm) relaxivity increases with size and for larger cluster sizes (50 – 100 nm) relaxivity decreases with size. Relaxivity is maximized at a mid-range cluster size (~50 nm) because that is the size at which freely diffusing water molecules spend the optimal amount of time being affected by the cluster's localized magnetic field – a similar cluster size trend (50 – 60 nm) found by others.<sup>29,30</sup> Notably, this maximal relaxivity is quite high ( $>350 \text{ mM}^{-1}\text{s}^{-1}$ ) – especially when compared to that of commercial  $T_2$  contrast agents ( $<200 \text{ mM}^{-1}\text{s}^{-1}$ ).<sup>4</sup> In fact, our clusters outperform similar clusters reported by Kratz et al. and Maity et al. ( $\sim 300 \text{ mM}^{-1}\text{s}^{-1}$ ).<sup>66, 67</sup>

### 5.3.2. Nanoworms

Magnetic nanoparticles colloidally stabilized with polymer coatings can experience three major interparticle forces in an external magnetic field: Van der Waals forces (attractive), magnetic dipolar forces between magnetized particles (attractive), and charge/steric-mediated forces (repulsive) (**Figure 5.5**). Magnetic nanoparticles are often coated with thick and/or charged polymers like PEG or PAA to induce charge/steric-mediate forces for greater colloidal stability.<sup>26</sup> Magnetic moments of magnetic nanoparticles can attract each other via dipolar forces and large enough magnetic nanoparticles can generate



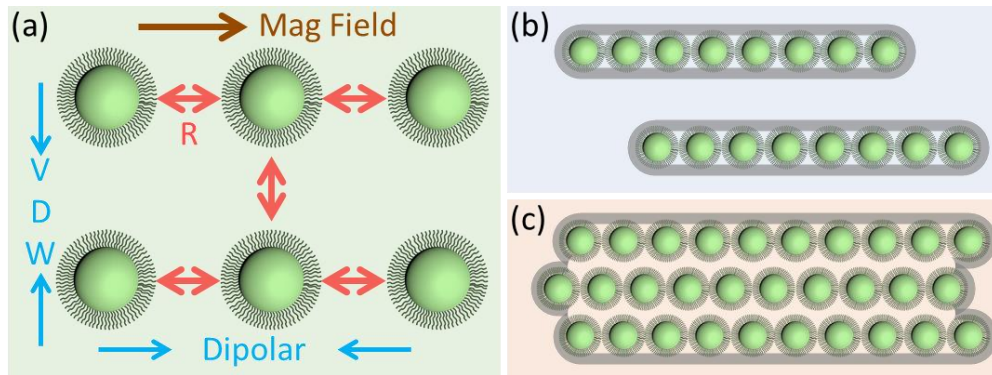


**Figure 5.5 Schematic of forces governing nanoworm formation.** (a) Attractive Van der Waals (VDW) and magnetic dipolar forces (blue) and repulsive charge/steric forces (red). (b) Individual chains (nanoworms) can be isolated with silica deposition (gray) when inter particle repulsion overcomes chain bundling. (c) Bundling occurs and is isolated with silica deposition (gray) when interparticle repulsion is weak.

motive forces in an external field – aligning parallel with field lines and forming one-dimensional chains.<sup>68</sup> If too concentrated, these one-dimensional chains can bundle into three-dimensional superstructures.<sup>26, 69</sup> Attractive, charge/steric-mediated forces from surface coatings can prevent this process.

One-dimensional nanoparticle assemblies could be fixed via silica deposition into self-contained chains that persist after the removal of the applied field (**Figure 5.5b**). Balancing the relevant attractive and repulsive forces could tailor the length of these chains – proportional to the number of nanoparticle subunits in the chain. Increasing the external field increases attractive magnetic forces, thus bringing nanoparticles together for greater chaining. However, decreasing repulsive forces can reduce interchain distances, resulting in the encapsulation of bundles (**Figure 5.5c**).

Isolated chains of magnetic nanoclusters ( $D_c = 40$  nm,  $d_p = 6$  nm) could be formed under the application of modest applied fields, and the structures captured permanently using a silica coating (**Figure 5.6**). Here, we use iron oxide nanoclusters (FNC) coated with a highly charged sulfonated copolymer as the links, or building blocks, for larger one-dimensional chains (nanoworms). These clusters have high susceptibilities, making them sensitive to modest external fields and are composed of a general class of magnetic materials used in a wide range of biomedical applications.<sup>4, 26</sup> Cluster chains are fixed into

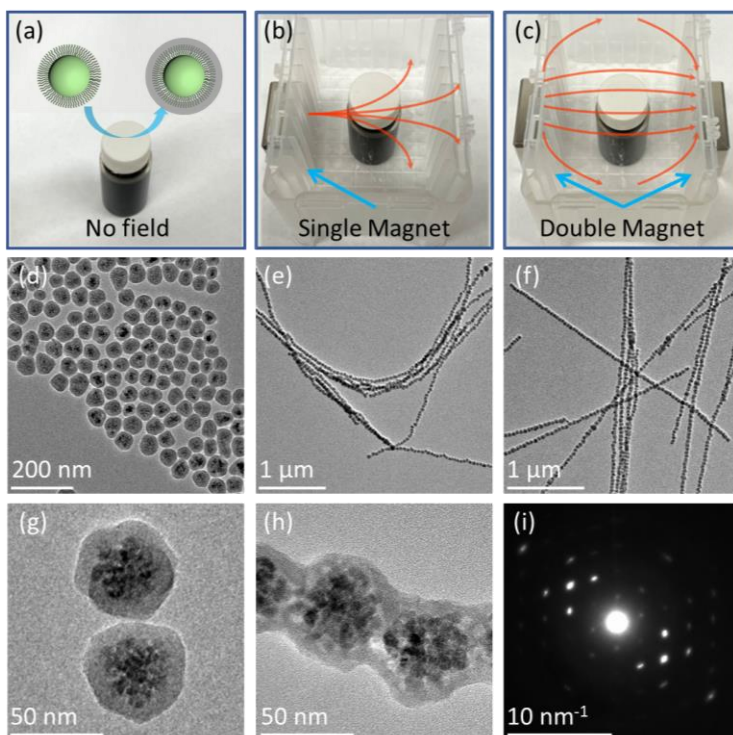


**Figure 5.6 Role of applied magnetic field in the formation of nanoworms.** (a, d, g) Without an external field, silica deposition coats individual clusters. (b, e) With a single applied magnetic field, non-linear nanoworms form because field is curved. (c, f) With two oppositely aligned magnets, generating a linear field, linear nanoworms form during silica deposition. (h) Nanoworms have a silica shell encapsulating cluster chains and in between individual clusters. (i) Selected area electron diffraction (SAED) showing primary particles have parallel crystallographic alignment.

isolatable nanoworms using tetraethoxysilane (TEOS) to coat field-assembled nanoclusters with a layer of silica. Ideally, TEOS is added before introduction of cluster samples to the external field so that the formed nanoworms have a layer of silica between each cluster.

**Figure 5.6** illustrates the central role that the field application geometry plays in defining the chain morphology. Under field-free conditions (**Figure 5.6 a, d, and g**) particles are merely coated with silica individually, generating uniformly coated core-shell silica-coated clusters (**Figure 5.6 d, g**). With a single permanent magnet next to the reaction vessel, non-linear worms are formed (**Figure 5.6 b,e**). Curved nanoworms are formed because of the non-linear field lines generated by the single magnet.<sup>70</sup> When the silica deposition is allowed to occur between two oppositely facing magnets, field lines are more uniformly linear and parallel, and the resultant worms are as well (**Figure 5.6c,f**).<sup>70</sup> Cluster subunits within nanoworms are approximately 10 nm apart (**Figure 5.6h**). The selected area electron diffraction (SAED) of two neighboring nanoclusters indicates their magnetocrystalline easy axes are aligned, which is crucial for dipolar interactions and the alignment of the magnetic spins of these magnetic nanoclusters (**Figure 5.6i**).<sup>26, 71, 72</sup> After purification, nanoworms are easily redispersed in water, forming stable colloidal solutions for up to 5 – 10 days (**Figure S5.8**). The larger size of nanoworms compared to free clusters makes them somewhat more prone to sedimentation and aggregation – especially if placed in a magnetic field.

Because of charge/steric mediate repulsive forces, cluster surface coating dictates whether nanoworms or bundles form during silica deposition. PAA and nitrodopa-PEG

coated clusters are well-dispersed prior to silica deposition, but end up forming small bundles afterwards (**Figure S5.9a,b**) – likely because of their smaller zeta potentials (-23.3 and -17.7 mV) and hydrodynamic size (61 and 75 nm) compared to sulfonated polymer (PAMPS, -45.5 mV and 90 nm). Therefore, dipolar forces are able to overcome charge/steric forces, causing worms to bundle together.<sup>26</sup> For the sulfonated coating (PAMPS), cluster size becomes important (**Figure S5.9c,d**). If clusters are too large (65 nm) or too small (25 nm), bundles and very short chains (2 – 3 clusters) form, respectively.<sup>73-75</sup> The 40 nm clusters provide the most consistent nanoworms with an assembly yield of 83 % compared to the 25 nm (< 20%) – so cluster size is not a good way to tune nanoworm

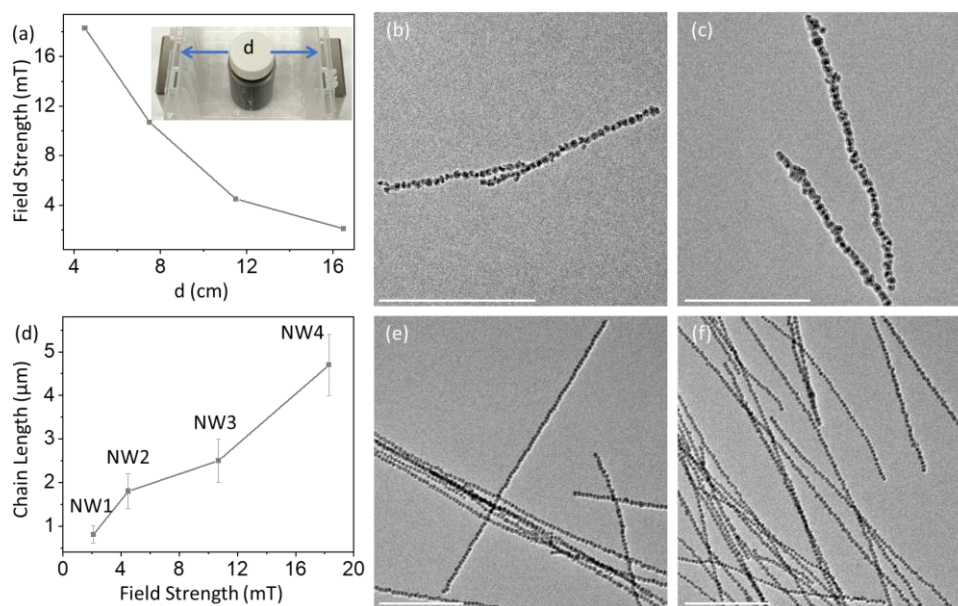


**Figure 5.7 Nanoworm length dependence on applied field strength.** (a) Field strength dependence on separation (d) between oppositely facing magnets. (b, c, e, f) Transmission electron microscopy (TEM) images of  $0.8 \pm 0.2$  (NW1),  $1.8 \pm 0.4$  (NW2),  $2.5 \pm 0.5$  (NW3), and  $4.7 \pm 0.7$  (NW4)  $\mu\text{m}$  nanoworm samples (scale bar = 1  $\mu\text{m}$ ). (d) Dependence of nanoworm length on applied field strength.

length. This decrease in efficiency is likely due to the lower magnetic moment of smaller clusters. To get similar yields would perhaps require a much larger external field.

This cluster size dependence would indicate that nanoworm length could be controlled by the applied field strength. With the polysulfonate coated 40 nm clusters, we adjust the external field strength by placing the oppositely facing magnets closer together around the reaction vessel. We find that nanoworm length can be controlled between 0.8 and 4.7  $\mu\text{m}$  by adjusting the distance between magnets (16.5 – 4.5 nm; 200 – 16 cluster links) and, consequently, the applied field (2.1 – 18.3 mT) (**Figure 5.7** and **Figure S5.10**). Nanoworms synthesized with these conditions are relatively monodispersed in terms of length (< 20 %; 100 nanoworms counted). Field strengths, and therefore distances between magnets, above or below this range are not ideal. Further separation drastically decreases nanoworm yield (forming silica coated single clusters) and more narrow distances cause motive forces to take over and pull particles to the sides of the reaction vessels resulting in aggregation (obstructing silica encapsulation).

With relatively high saturation magnetizations (**Table 5.1**, **Figure S5.11**), one-dimensional tunability, and larger sizes – leading to greater cellular retention – nanoworms may be

**Table 5.1** Summary nanoworm physical and magnetic properties.

Sample	Length ( $\mu\text{m}$ )	$M_{\text{sat}}$ (emu/g $\text{Fe}_3\text{O}_4$ )	$r_2$ ( $\text{s}^{-1} \text{mM}^{-1}$ )	$r_1$ ( $\text{s}^{-1} \text{mM}^{-1}$ )
FNC	$0.04 \pm 0.003$	79.1	350.0	2.2
NW1	$0.8 \pm 0.2$	78.9	524.5	1.5
NW2	$1.8 \pm 0.4$	78.7	549.5	1.8
NW3	$2.5 \pm 0.5$	78.9	453.8	2.4
NW4	$4.7 \pm 0.7$	78.9	459.5	2.1

promising magnetic resonance imaging (MRI) contrast agents for cellular tracking and labelling applications.<sup>2-4, 31, 76</sup> Magnetic nanoparticles inside the external field of an MRI system generate localized fields that facilitate the relaxation of water protons – the principle mechanism of signal production in MRI – which enhances contrast.<sup>3, 31</sup> The ability of a contrast agent to speed up this relaxation process and therefore enhance image contrast is called relaxivity ( $\text{mM}^{-1}\text{s}^{-1}$ ). We plot the longitudinal ( $1/T_1$ ) and transverse ( $1/T_2$ ) relaxation rates ( $\text{s}^{-1}$ ) for nanoworms and cluster solutions as a function of concentration ( $\text{mM Fe}$ ) to measure their  $T_1$  and  $T_2$  relaxivities –  $r_1$  and  $r_2$ , respectively. The  $r_1$  and  $r_2$  values for FNC and NW1 – NW4 are reported in **Table 5.1**. Because of their silica surface coating likely preventing inner sphere interactions with surface iron, nanoworms exhibit low, size-independent  $T_1$  relaxivity ( $\sim 2 \text{ mM}^{-1}\text{s}^{-1}$ ) comparable to the gadolinium chelate contrast agent used clinically ( $3 - 4 \text{ mM}^{-1}\text{s}^{-1}$ ) (**Figure 5.8b**).<sup>2</sup> However,  $T_2$  contrast agents generate contrast via indirect, outer sphere interactions and are preferred for cellular labelling and tracking MRI applications for their greater sensitivity.<sup>3, 4, 31</sup> Also, their relatively large sizes can obstruct rapid exocytosis, allowing for greater tracking duration.<sup>76, 77</sup> Fortunately, compared to clusters alone – which already exhibit relatively high  $T_2$  relaxivities ( $350 \text{ mM}^{-1}\text{s}^{-1}$ ) compared to commercial  $T_2$  contrast agents ( $< 200 \text{ mM}^{-1}\text{s}^{-1}$ ) – exhibit exceptionally high  $T_2$  relaxivities ( $450 - 550 \text{ mM}^{-1}\text{s}^{-1}$ ) (**Figure 5.8a**).<sup>4</sup> There is clearly a size dependent trend similar to the universal scaling law for clustered iron oxide  $T_2$  contrast agents proposed by Vuong et al.<sup>30</sup> However, maximal  $r_2$  is achieved at sizes much larger than  $50 - 60 \text{ nm}$  for nanoworms ( $\sim 2 \mu\text{m}$ ).<sup>29, 30</sup> This is likely because water-impermeable silica coating for nanoworms excludes water from a majority of its field, so even larger

materials are required for water to optimize their interactions with that field.<sup>24, 78</sup> Nanoscale contrast agents must also exhibit colloidal stability so they do not aggregate – which can cause acute toxicity.<sup>13, 79</sup> Because of the surface coating of these nanoworms, they exhibit good colloidal stability at a clinically relevant MRI field strength (3 T) over the course of the 15-minute measurements.<sup>26</sup>

### 5.3.3. Ferrite Clusters

Monodispersed manganese ferrite clusters (MFCs) are synthesized via a hydrothermal polyol synthetic approach similar to that of the iron oxide clusters. Visually, the product is a black ferrofluid after purification with a strong response to an external magnetic field (**Figure S5.12**). High resolution transmission electron microscopy (TEM), x-ray diffraction (XRD), selected area electron diffraction (SAED), and electron energy loss spectroscopy (EELS) are used to characterize the dimensions, morphology, and composition of MFCs. A

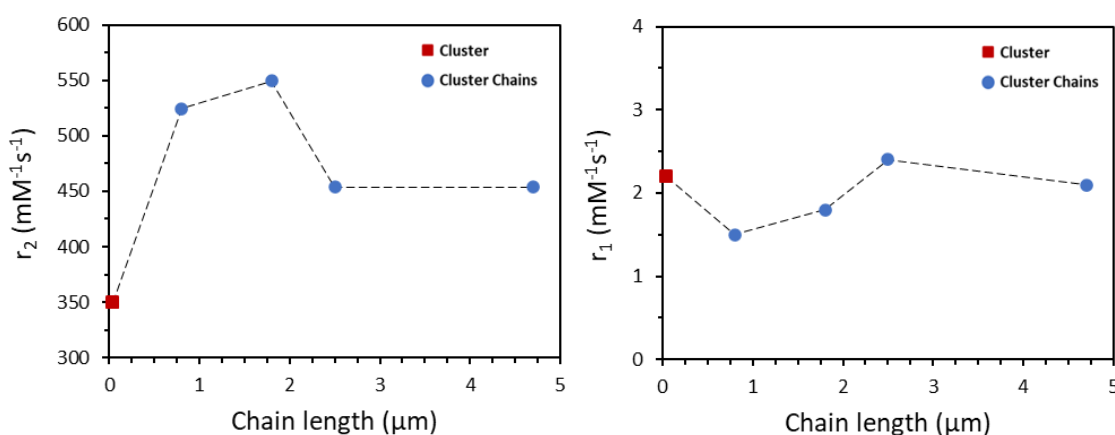


**Figure 5.8** T<sub>1</sub> and T<sub>2</sub> relaxivities of silica coated Fe<sub>3</sub>O<sub>4</sub> clusters nanoworms. (a) T<sub>2</sub> relaxivity and (b) T<sub>1</sub> relaxivity of Fe<sub>3</sub>O<sub>4</sub> clusters (red) and nanoworms (blue) as a function of chain length (3 T).

representative TEM images show that a representative MFC sample has uniform primary particle (5.5 nm) and cluster sizes ( $84 \pm 7$  nm) (**Figure 5.9a-c**). **Figure 5.10a** provides a useful schematic outlining the different dimensional parameters of MFCs: cluster size ( $D_c$ ) and primary particle size ( $d_p$ ). Notably, intracluster primary particle lattice fringes are parallel to one another, which is further supported by the SAED pattern with discrete scattered spots rather than the rings consistent with randomly oriented polycrystals (**Figure 5.9c,d**).<sup>80</sup> This is a good indication that when primary particles cluster during the synthesis, they form hard aggregates via oriented attachment.<sup>81,82</sup> This could help explain the high saturation magnetization of similar materials at low field strengths.<sup>83</sup> Elemental mapping with EELS shows that both iron and manganese are present and homogeneously distributed throughout the clusters – an indication of successful doping throughout the ferrite crystal structure (**Figure 5.9e,f**). Analysis with inductively coupled plasma



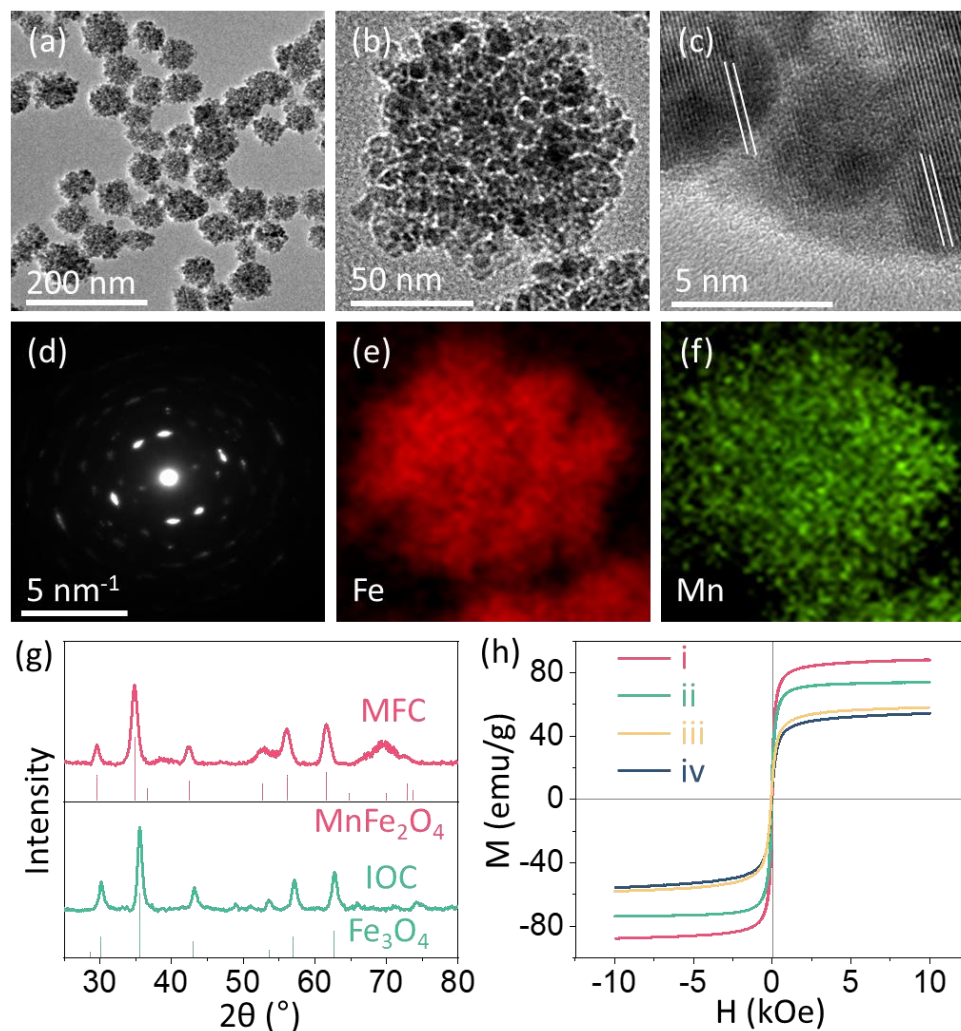


**Figure 5.9 Morphology, composition, and magnetic properties of MFCs.** (a, b) Transmission electron microscopy (TEM) images of representative samples of MFCs – (c) High resolution TEM image show lattice fringes. (d) Selected area electron diffraction (SAED) pattern for a single MFC. (e, f) Electron energy loss spectroscopy (EELS) elemental mapping of iron and manganese in MFCs. (g) X-ray diffraction (XRD) pattern for MFCs and iron oxide clusters compared to standard patterns for magnetite iron oxide and manganese ferrite. (h) The magnetization curves of MFCs (i), iron oxide clusters (ii), manganese ferrite nanoparticles (iii), and iron oxide nanoparticles (iv).

techniques provide a quantitative measure of the exact composition of the ferrite ( $\text{Mn}_{0.15}\text{Fe}_{2.85}\text{O}_4$ ). Low Mn concentration ensures that higher magnetic moment  $\text{Mn}^{2+}$  is doped into  $\text{Fe}_3\text{O}_4$  octahedral sites, thus replacing lower magnetic moment  $\text{Fe}^{2+}$  and

improving saturation magnetization.<sup>1, 18, 84, 85</sup> Excessive concentrations of manganese could result in the formation of manganese oxide, which would significantly reduce saturation magnetization.<sup>86</sup> Finally, XRD patterns of MFCs and iron oxide clusters confirm that they are both consistent with the standard diffraction patterns for different crystal structures,  $\text{MnFe}_2\text{O}_4$  and  $\text{Fe}_3\text{O}_4$ , respectively (**Figure 5.9g**).

The magnetic properties, namely saturation magnetization, are characterized for MFCs along with iron oxide clusters, iron oxide nanoparticles, and Mn-doped iron oxide nanoparticles for comparison (**Figure 5.9h**). All samples reach their peak saturation magnetization at about 1KOe. Notably, Manganese ferrite materials have higher saturation magnetizations than their iron oxide counterparts. For MFCs, iron oxide clusters, manganese ferrite nanoparticles, and iron oxide nanoparticles, their saturation magnetizations are about 90, 70, 55, and 50 emu/g. This is likely because  $\text{Fe}^{2+}$  is replaced by  $\text{Mn}^{2+}$ , which has a greater magnetic moment, in the octahedral site of  $\text{Fe}_3\text{O}_4$ , resulting in a greater overall saturation magnetization.<sup>1, 36</sup> The saturation magnetizations of the MFC samples are comparable to that of bulk magnetite (92 emu/g).<sup>58</sup>

Controlling the dimensions of MFCs is similar to that of the iron oxide nanoclusters – cluster and primary particle size can be independently and reliably controlled by the concentration of water and reaction temperature used for the synthesis, respectively.<sup>26</sup> For example, by reducing the concentration of water (1.95 – 0.2 mL), cluster size increases from 26 to 90 nm while maintaining a constant primary particle size of 5.5 nm (**Table S5.1**). Increased water not only increases iron salt hydrolysis, but also changes the solution viscosity, which promotes smaller and more monodispersed clusters.<sup>32, 53</sup>

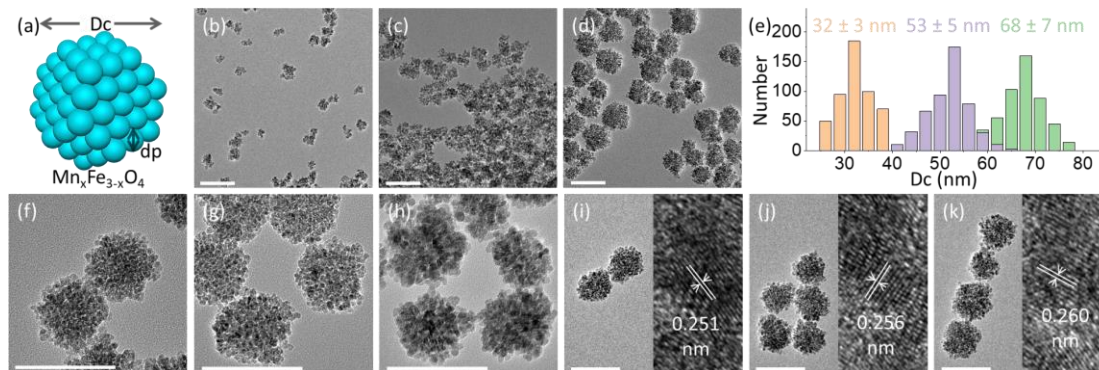


**Figure 5.10 Transmission electron microscopy (TEM) images of MFCs of different dimensions and composition.** (a) Schematic representation of the dimensions of an MFC. (b-d) MFC with increasing cluster diameter ( $32 \pm 3$ ,  $53 \pm 5$ , and  $68 \pm 7$  nm), (e) with their cluster size distribution histograms. (f-h) MFCs with increasing  $d_p$  (3.5, 5.5, and 10.5 nm). (h-j) MFC with increasing manganese content ( $Mn_{0.05}Fe_{2.95}O_4$ ,  $Mn_{0.15}Fe_{2.85}O_4$ ,  $Mn_{0.6}Fe_{2.4}O_4$ ). Scale bar = 100 nm.

Representative MFCs with cluster sizes of  $32 \pm 3$ ,  $53 \pm 5$ , and  $68 \pm 7$  nm were produced by altering the concentration of water (**Figure 5.10b-d**). By increasing the reaction temperature (170 – 260 °C), primary particle size increases from 2.5 to 10.5 nm while maintaining a constant cluster size of 53 nm (**Table S5.2**). Reaction temperature both speeds up nucleation and facilitates Ostwald ripening and LaMer growth.<sup>44</sup> Representative MFCs with primary particle sizes of 3.5, 5.5, and 10.5 nm were produced by altering the reaction time (**Figure 5.10f-h**). Also, the manganese content can be controlled by the ratio of iron and manganese salts used. By increasing the molar ratio of Mn/Fe salts (0 - 1), manganese content in MFCs increases from 0 to 20 % ( $Fe_3O_4$  to  $Mn_{0.6}Fe_{2.6}O_4$ ) while maintaining a constant cluster and primary particle size of 53 and 5.5 nm, respectively (**Table S5.3**). Representative MFCs with manganese content of

$\text{Mn}_{0.05}\text{Fe}_{2.95}\text{O}_4$ ,  $\text{Mn}_{0.15}\text{Fe}_{2.85}\text{O}_4$ ,  $\text{Mn}_{0.6}\text{Fe}_{2.4}\text{O}_4$  were produced by altering the molar ratio of Mn/Fe salts (**Figure 5.10i-k**).

The high saturation magnetization – compared to pure iron oxide clusters and Mn-ferrite nanoparticles alone – and lower dimensional tunability of MFCs make them potentially useful for biomedical applications like contrast enhanced magnetic resonance imaging (MRI).<sup>2, 3, 31</sup> Magnetic nanoparticles inside the external field of an MRI system generate localized fields that facilitate the relaxation of water protons – the principle mechanism of signal production in MRI – which enhances contrast.<sup>3, 31</sup> The ability of a contrast agent to speed up this relaxation process and therefore enhance image contrast is called relaxivity ( $\text{mM}^{-1}\text{s}^{-1}$ ). Typically, contrast agents are classified as either  $T_1$ - or  $T_2$ -type, meaning the different mechanisms by which they facilitate water proton relaxation produces positive or negative contrast enhancement.<sup>1-3</sup>  $T_1$  contrast agents (positive) are known to have better spatial resolution, while  $T_2$  contrast agents have better sensitivity – hence why the former are used in more quantitative applications (tumor volume assessment) while the latter are used more qualitatively (cell tracking and labeling).<sup>4</sup> However, with the recognition that both types of imaging can facilitate more accurate diagnoses, there is a need for multimodal  $T_1/T_2$  contrast agents with high  $T_1$  and  $T_2$  relaxivities.<sup>37-42</sup> The high saturation magnetization of MFCs ( $\sim 90$  emu/g) compared to similarly sized iron oxide clusters (70 emu/g) lends to a much greater outer sphere interactions with water, thus increasing  $T_2$  relaxivity by about 60 % (**Figure 5.11b**).<sup>1, 3, 31</sup> The  $T_2$  relaxivity of MFCs is about  $450 \text{ mM}^{-1}\text{s}^{-1}$  which is much greater than commercially available  $T_2$  contrast agents ( $<200 \text{ mM}^{-1}\text{s}^{-1}$ ).<sup>4</sup> On the other hand, replacing  $\text{Fe}^{2+}$  with a

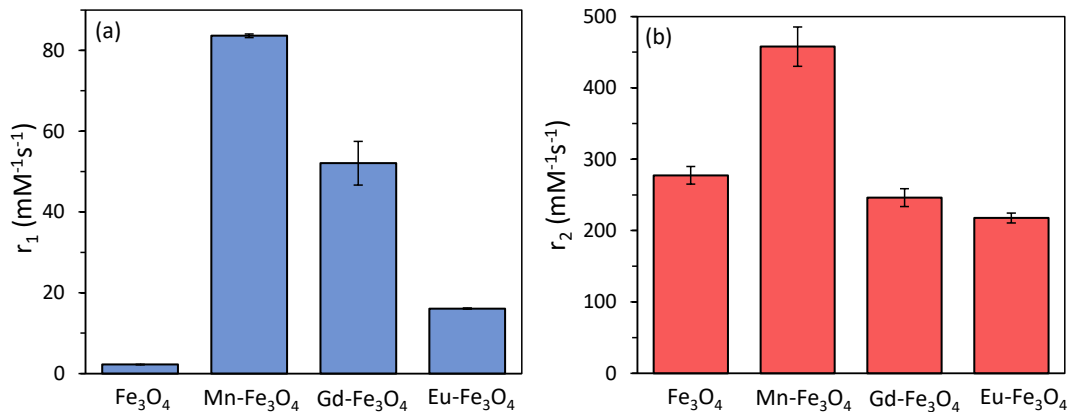


**Figure 5.11 T<sub>1</sub> and T<sub>2</sub> relaxivities of Fe<sub>3</sub>O<sub>4</sub> and ferrite clusters.** (a) T<sub>1</sub> relaxivity and (b) T<sub>2</sub> relaxivity of Fe<sub>3</sub>O<sub>4</sub>, Mn-Fe<sub>3</sub>O<sub>4</sub>, Gd-Fe<sub>3</sub>O<sub>4</sub>, and Eu-Fe<sub>3</sub>O<sub>4</sub> clusters at 3 T.

higher moment paramagnetic ion like Mn<sup>2+</sup> allows for greater inner sphere interactions with water, thus increasing T<sub>1</sub> relaxivity by a factor of about 40 (**Figure 5.11a**).<sup>1</sup> The  $r_1$  of MFCs is about 80 mM<sup>-1</sup>s<sup>-1</sup> which may be one of the highest recorded T<sub>1</sub> relaxivities for a nanocrystal contrast agent.<sup>1-3</sup> Interestingly, doping other strongly paramagnetic ions like Gd or Eu into similarly size iron oxide clusters (**Figure S5.13**) does not have the same effects on T<sub>1</sub> and T<sub>2</sub> relaxivity (**Figure 5.11**).<sup>1</sup> For Gd- and Eu-doped clusters, T<sub>2</sub> relaxivity slightly decreases and T<sub>1</sub> relaxivity does not increase as dramatically as it does for MFCs. This is because the ionic radii of Gd and Eu are larger than Mn<sup>2+</sup>, and likely occupy different positions within the crystal structure of Fe<sub>3</sub>O<sub>4</sub>.<sup>1, 36</sup> However, Eu-doped clusters still retain a relatively high T<sub>1</sub> and T<sub>2</sub> relaxivity and, because of its strong fluorescence emission peak at about 620 nm, offers an opportunity for fluorescence imaging along with MRI (**Figure S5.14**). Due to the intrinsically low sensitivity of MRI, combining it with a more sensitive modality like fluorescence imaging could be advantageous.<sup>91-93</sup>

## 5.4. Conclusion

Here, we introduce a systematic approach to the synthesis of dimensionally controlled clustered magnetic materials. With the ability to tune these dimensional parameters, we successfully optimize their magnetic properties for maximal performance as MRI contrast agents. Our optimized iron oxide clusters, nanoworms, and manganese ferrite clusters all have exceptional  $T_2$  relaxivities ( $300 - 450 \text{ mM}^{-1}\text{s}^{-1}$ ) compared to commercially available  $T_2$  MRI contrast agents ( $<200 \text{ mM}^{-1}\text{s}^{-1}$ ).<sup>4</sup> Also, manganese ferrite clusters demonstrate exceptional  $T_1$  relaxivity ( $\sim 80 \text{ mM}^{-1}\text{s}^{-1}$ ) and open the door to advanced applications in multimodal  $T_1/T_2$  imaging. In sum, with comprehensive dimensional control over clustered magnetic materials, their magnetic properties can be optimized for the efficient design of highly sensitive MRI contrast agents.

## 5.5. Experimental Section

### Materials

Ethylene glycol (anhydrous, 99.8%), tetraethyl orthosilicate (TEOS, 99%, GC), ethanol (ACS reagent,  $\geq 99.5\%$ ), ammonium hydroxide solution ( $\sim 30\%$ ), O-Methyl-O'-succinylpolyethylene glycol (PEG-COOH, Mw  $\sim 5,000$ ), 4-morpholineethanesulfonic acid, poly(ethylene glycol) methyl ether acrylate (Acryl-PEG, Mw  $\sim 480$ , contains 100 ppm BHT and 100 ppm MEHQ as inhibitor), 2-(N-morpholino)ethanesulfonic acid (MES, 99%), iron(III) chloride hexahydrate ( $\text{FeCl}_3 \cdot 6\text{H}_2\text{O}$ , ACS reagent, 97%), urea (ACS reagent, 99.0%), azobisisobutyronitrile (AIBN, 98%), acrylic acid (anhydrous, contains 200 ppm MEHQ as inhibitor, 99%), 2-acrylamido-2-methylpropane sulfonic acid (AMPS, 99%), dimethylformamide (DMF, anhydrous, 99.8%), dimethyl sulfoxide (DMSO, anhydrous,

≥99.9%), 3,4-dihydroxyphenethylamine hydrochloride (dopamine), rhodamine B (≥95%), 5-((2-aminoethyl)amino)naphthalene-1-sulfonic acid (EDANS), methoxypolyethylene glycol amine (PEG-NH<sub>2</sub>, M<sub>w</sub> = 5,000), poly(maleic anhydride-alt-1-octadecene) (PMAO, M<sub>w</sub> = 30,000), triethylamine, iron standard solution (Fe(NO<sub>3</sub>)<sub>3</sub> in HNO<sub>3</sub> 0.5 mol/L, 1000 mg/L Fe) Certipur®, 3-(2-Pyridyl)-5,6-diphenyl-1,2,4-triazine-*p,p'*-disulfonic acid monosodium salt hydrate (FerroZine™ Iron Reagent), ammonium acetate (for molecular biology, ≥98%), hydroxylamine hydrochloride (99.995% trace metals basis), europium(III) nitrate pentahydrate (99.9%), gadolinium nitrate hexahydrate (99.9 %), and sodium nitrite (ACS reagent, ≥97.0%) were obtained from Sigma Aldrich. Polyacrylic acid sodium salt (PAA, M<sub>w</sub>~6,000) was obtained from Polyscience Inc. 1-ethyl-3-(3-dimethylaminopropyl)carbodiimide hydrochloride (EDC), hydrochloric acid (ACS grade, 37%), sulfuric acid (ACS grade, 98%), and hydrogen peroxide (30%) were obtained from Fisher Scientific. All water was obtained from a Milli-Q purification system (specific resistance less than 18 mΩ).

#### Synthesis of poly(AA-co-AMPS) modified Fe<sub>3</sub>O<sub>4</sub> clusters

Clusters are synthesized via hydrothermal polyol method. First, FeCl<sub>3</sub>·6H<sub>2</sub>O (540 mg, 2 mmol) is dissolved in 20 mL ethylene glycol using magnetic stirring. Next, PAA (250 mg, 0.042 mmol; MW = 6000 Da) is added, then urea (1200 mg, 20 mmol) and water. This solution is stirred vigorously for 30 min, becoming a transparent yellow. This solution is transferred into a 40 mL Teflon-lined reactor (cleaned in 37% HCl for 30 min, washed several times with water, and dried at 60 °C), tightly sealed, and then heated at 185 °C for 6 hours with a temperature ramp of 20 °C/min in a stainless-steel autoclave. Once cooled

to room temperature, a black solution of 50 nm clusters is recovered. Clusters are precipitated magnetically and then washed by a water/acetone mixture three times. Final purified product is resuspended in water. Sample can be easily concentrated using a magnet to pull sample to bottom of container and slowly pouring out water. Cluster size ( $D_c$ ) can be controlled with the amount of water added to the synthesis (0 – 4 mL) and primary nanocrystal size ( $d_p$ ) is controlled by the reaction temperature (185 to 275 °C).

For poly(AA-co-AMPS) coating, 10 mL cluster solution (of 500 ppm  $Fe_3O_4$ ;  $D_c = 45$  nm,  $d_p = 4$  nm) was added to 2 mL of dopa-Poly(AA-co-AMPS) solution (10 mg/mL) at 1 drop/second. The solution was stirred for 30 min to replace PAA with dopa-Poly(AA-co-AMPS). Magnetic separation was used to remove excess polymer.

#### Synthesis of silica modified $Fe_3O_4$ cluster nanoworms

Clusters ( $D_c = 40$  nm) are synthesized via hydrothermal polyol method. First,  $FeCl_3 \cdot 6H_2O$  (540 mg, 2 mmol) is dissolved in 20 mL ethylene glycol using magnetic stirring. Next, PAA (250 mg, 0.042 mmol; MW = 6000 Da) is added, then urea (1200 mg, 20 mmol) and 2000 mg water. This solution is stirred vigorously for 30 min, becoming a transparent yellow. This solution is transferred into a 40 mL Teflon-lined reactor (cleaned in 37% HCl for 30 min, washed several times with water, and dried at 60 °C), tightly sealed, and then heated at 215 °C for 6 hours with a temperature ramp of 20 °C/min in a stainless-steel autoclave. Clusters are precipitated magnetically and then washed by a water/acetone mixture three times. Final purified product is resuspended in water.



For poly(AA-co-AMPS-co-PEG) coating, first add nitro-dopamine (10 mg) to a 10 mL solution of clusters (10 mg/mL). Magnetically separate particles after rapid aggregation and add EDC (20 mg), MES (100 mg), 60 mg of poly(AA-co-AMPS-co-PEG), and water (5 mL). Then, probe sonicate this mixture for about 30 min.

Next, add clusters (4 mg/mL) to a 20 mL glass scintillation vial with ethanol (10 mL), ammonium hydroxide solution (1 mL, 30 %), and TEOS (0.025 mL). For linear chain nanoworms (NW), immediately center the vial between two oppositely facing magnets (40 x 40 x 20mm strong neodymium cube magnets, N52) for 1 hour. Sample NW1, NW2, NW3, and NW4 are prepared with a distance between the magnets of 16.5, 11.5, 7.5, and 4.5 cm, respectively. Once finished, purify using magnetic separation, pouring out pale-yellow supernatant solution, adding water, and probe sonicating until the solution is homogeneous. Repeat purification process three times.

To make free non-chained silica coated clusters (FNC), place the vial in a mixer at a speed of 1000 rpm for 1 hour – instead of in between the two oppositely facing magnets. Use the same purification process as for the nanoworms.

#### Synthesis of Mn-ferrite clusters (MFC) and Gd- and Eu-ferrite clusters

To synthesize manganese ferrite clusters,  $\text{FeCl}_3$  and  $\text{MnCl}_2$  (combined total of 2 mmol) and PAA (250 mg,  $M_w \sim 6000$ ) are dissolved in ethylene glycol (20 mL), followed by urea (1.2 g), and water (0.2 – 2 mL). To change the concentration of metals in the MFC, the ratio of metal salts can be changed while maintaining the same total number of mmol. For Gadolinium or Europium ferrite clusters, the same synthesis can be done with

Gd(NO<sub>3</sub>)<sub>3</sub> or Eu(NO<sub>3</sub>)<sub>3</sub> instead of MnCl<sub>2</sub>. The solution is mixed well, transferred to a polyphenylene-lined reactor vessel (50 mL), sealed in a stainless-steel autoclave, and heated for 20 hr at 170 – 260 °C. Clusters are precipitated magnetically and then washed by a water/acetone mixture three times. Final purified product is resuspended in water.

For a Poly(AMPS-co-PEG) coating, add 10 mg nitro-dopamine in 10 mL MFC (10 mg/mL). Magnetically separate particles after rapid aggregation and add EDC (20 mg), MES (100 mg), 60 mg of Poly(AMPS-co-PEG), and water (5 mL). Probe sonicate this mixture for about 30 min until homogenous. Wash three times with magnetic separation and water.

#### Synthesis of nitro-dopamine functionalized Poly(AA-co-AMPS)

The copolymer Poly(AA-co-AMPS) is synthesized via free radical polymerization. A mixture of AIBN (50 mg), AMPS (1.5 g), and acrylic acid (500 mg) in 10 mL DMF is stirred for 30 min, then transferred to a UV reactor (LZC-4Xb photoreactor, UVA 350 nm, 36 W) for 1 hr. Next, 10 mL of water are added and the solution is dialyzed in water using a 3 kDa MWCO dialysis tubing (Cellulose Membrane, Sigma Aldrich) and then freeze-dried (LABCONCO FreeZone 6 Liter Freeze Dry Systems) for 2 days.

Nitrodopamine was synthesized as follows. Dopamine (5 g) is dissolved in water (150 mL) and stirred in an ice bath. Next, sodium nitrate (6.5 g) and sulfuric acid (50 mL, 20%, dropwise) are added. Since NO<sub>2</sub> is generated, make sure the reaction is vented. Reaction is removed from bath and allowed to cool to room temperature for 12 hr. This mixture is filtered and washed multiple times to recover nitrodopamine hydrogensulfate (nitrodopa), which was then freeze dried. Next, EDC (12 mg) and nitrodopa (20 mg) are

added to a solution of 200 mg of Poly(AA-co-AMPS) in 0.1 M MES buffer (10 mL) and are stirred for 2 hr at room temperature. Final sample are dialyzed in water using a 3 kDa MWCO dialysis tubing (Cellulose Membrane, Sigma Aldrich). After dialysis purification, the synthesized copolymer solution is about 10 mg/mL.

Synthesis of PEG-, sulfonate-, and carboxylate-containing copolymer Poly(AA-co-AMPS-co-PEG)

The copolymer Poly(AA-co-AMPS-co-PEG) is synthesized via free radical polymerization. A mixture of AIBN (200 mg), AMPS (750 mg), acrylic acid (250 mg), and acryl-PEG (1000 mg) in 10 mL DMF is heated for 1 hr at 70 °C in a water bath. Once cooled to room temperature, 10 mL of water are added, and the solution is dialyzed in water using a 3 kDa MWCO dialysis tubing (Cellulose Membrane, Sigma Aldrich). After dialysis purification, the synthesized copolymer is dissolved in water (40 mg/mL).

Synthesis of PEG- and sulfonate-containing copolymer Poly(AMPS-co-PEG)

The copolymer Poly(AMPS-co-PEG) is synthesized via free radical polymerization. A mixture of AIBN (200 mg), AMPS (750 mg), acrylic acid (250 mg), and acryl-PEG (1000 mg) in 10 mL DMF is heated for 1 hr at 70 °C in a water bath. Once cooled to room temperature, 10 mL of water are added and the solution is dialyzed in water using a 3 kDa MWCO dialysis tubing (Cellulose Membrane, Sigma Aldrich). After dialysis purification, the synthesized copolymer is dissolved in water (40 mg/mL).

Electron Microscopy

High-resolution transmission electron microscopy (HRTEM) and selected area electron diffraction (SAED) done with a JEOL 2100 field emission gun TEM at 200 kV. Scanning electron microscopy (SEM) was done with a Quattro Environmental SEM at 20 kV. Sample solutions (3 – 5  $\mu$ L, 300 ppm) were drop cast onto Carbon/Formvar coated copper TEM grids (200 mesh, Ted Pella). Material dimensions were analyzed using ImageJ software using at least 500 clusters or at least 100 nanoworms. Elemental mapping of Manganese and Iron in MFCs was done with electron energy loss spectroscopy (EELS).

#### X-Ray Diffraction (XRD)

X-ray diffraction patterns for samples were done using a Bruker D8 Discovery 2D X-ray Diffractometer (Cu  $K\alpha$ ,  $\lambda = 1.54056 \text{ \AA}$ ). Samples (1 mL, 3000 ppm) were drop cast onto single depression microscope slides (AmScope BS-C12). A small magnet was placed underneath the glass slide to assure a concentrated deposition. Once dried, XRD patterns were measured between 10 to 95° or 20 to 80° (depending on the sample). Grain sizes could be calculated based on the FWHM of the peak at 35.4° (311) measured using Origin Pro's peak analysis function. Grain size is finally calculated using the Debye-Scherrer equation:

$$\text{Grain size} = \frac{\lambda}{FWHM \cos(\theta)}$$

#### Dynamic Light Scattering (DLS)

A Zetasizer Nano S90 was used to measure the hydrodynamic diameter and zeta potential of cluster samples. A Zetasizer Nano ZS (Malvern Instruments Ltd, Malvern, UK) was used

measure the hydrodynamic diameter and zeta potential of nanoworm samples. All measurements taken at room temperature, and at a pH of 7. Error bars are from triplicate hydrodynamic diameter measurements (Z-average).

### Raman Spectroscopy

A Witec Alpha 300 confocal Raman microscope was used to obtain the Raman spectra of clusters. Samples (1 mL, 3000 ppm) were drop cast onto single depression microscope slides (AmScope BS-C12). A small magnet was placed underneath the glass slide to assure a concentrated deposition. Spectra were recorded with a two-laser source (532 and 785 nm) from 100 to 1500  $\text{cm}^{-1}$ .

### Relaxivity Measurements

A 3.4 T Tim Trio MRI scanner was used to measure the  $T_2$  relaxation times of iron oxide cluster samples. The following sequencing parameters were used for the measurements: 2280 ms repetition time (TR), 9 – 150 ms echo time (TE), 0.5 x 0.5 x 10.0 mm reference voxel size, 7 slices, and the second slice from the top was used. Clusters were diluted to 0.5, 0.4, 0.3, 0.2, 0.1, and 0.01 mM Fe and transferred to a 100-well plate.  $T_2$  relaxivity ( $r_2$ ) was calculated based on the slope of a line of the graph of  $1/T_2$  (1/s) as a function of concentration (mM). Error recorded for  $r_2$  was calculated from the regression used to fit that plot.

A Siemens 3 T PRISMA MR scanner equipped with 64 receive channels and high-performance XR 80/200 gradients was used to measure the  $T_2$  and  $T_1$  relaxation times for nanoworm and ferrite cluster samples. The following sequencing parameters were used

for the  $T_2$  measurements: 2280 ms repetition time (TR) and 16 echoes at 9.4 ms intervals. The following sequencing parameters were used for the  $T_1$  measurements: 15 ms repetition time (TR), 13 – 67° flip angles, and a 3 mm slice thickness (12 slices total). For  $T_1$  measurements for nanoworms, samples were diluted to 0.5, 0.185, 0.07, 0.026, and 0.01 mM Fe. For  $T_2$  measurements for nanoworms, samples were diluted to 0.185, 0.07, 0.026, and 0.01 mM Fe. For  $T_1$  measurements for ferrite clusters, samples were diluted to 0.5, 0.185, 0.07, 0.026, and 0.01 mM of the dopant (Mn, Gd, or Eu). For  $T_2$  measurements for nanoworms, samples were diluted to 0.185, 0.07, 0.026, and 0.01 mM total metal concentration (Fe + dopant). Relaxivities ( $r_2$  or  $r_1$ ) was calculated based on the slope of a line of the graph of  $1/(T_1$  or  $T_2)$  (1/s) as a function of concentration (mM). Error recorded for  $r_2$  and  $r_1$  were calculated from the regression used to fit that plot.

#### Nuclear Magnetic Resonance (NMR) Spectroscopy

Poly(AA-co-AMPS) was characterized via H-NMR using a Bruker Ascend™ 600 NMR spectrometer. As-synthesized sample (10 mg) was dissolved in  $D_2O$  (0.7 mL) and transferred into an NMR tube for measurement.

#### Fourier Transform Infrared Spectroscopy (FTIR)

A Shimadzu IRAffinity-1S FTIR spectrometer was used to record the IR spectra of cluster samples with and without polymer coating. The cluster solutions (1 mL, 500 ppm) were drop cast onto single depression microscope slides (AmScope BS-C12). A small magnet was placed underneath the glass slide to assure a concentrated deposition. Sample was

dried at 60°C and spectra were recorded at room temperature between 4000 and 400 cm<sup>-1</sup>.

#### Size Exclusion High Performance Liquid Chromatography (SE-HPLC)

Poly(AA-co-AMPS) molecular weight was characterized via size exclusion high performance liquid chromatography (SE-HPLC) using an Agilent HPLC 1100 series chromatogram equipped with a µL-aquagel-OH 40 and a µL-aquagel-OH 60 (25.0 x 300 mm, 15 µm) column and a refractive index detector (connected with a 3000 x 0.17 mm SS capillary tube). These columns are ideal for polymers of molecular weight between 10 – 200 kDa and 200 – 10000 kDa, respectively. All experiments were done at 30°C with minimal dead volumes. Sulfonate polystyrene beads of known molecular weight (1, 2, 4.5, 10, 30, 80, 140, 280, and 450 kDa; American Polymer Standards Corp.) were dissolved in 10 pH phosphate buffer and used as a standard curve. Poly(AA-co-AMPS) was ran under the same conditions and its elution time was used to get its molecular weight using this standard curve. The conditions used for all experiments are as follows: flow rate of 1 mL/min, 40 bar pressure, 25 µL injection volume, and column and detector temperature of 30 °C.

#### UV-Vis Absorption Spectroscopy

Cluster concentration can be determined via UV-Vis absorption spectroscopy. First, a calibration curve is made based on iron standards as follows: mix 0.2 mL iron nitrate (1, 5, 10, 25, and 50 ppm Fe), 0.15 mL ammonium acetate (7.5 M), 0.25 mL of hydroxylamine hydrochloride (5 %), 0.4 mL ferrozine (0.1 %), and 1 mL water in a 4 mL cuvette (quartz).

Fe(III)-ferrozine complex absorption peak could be found at 590 nm with intensity linearly dependent on Fe concentration. For cluster concentration, the following procedure is followed: dissolve 0.1 mL sample in 0.89 mL hydrochloric acid (37 %) and 0.01 mL H<sub>2</sub>O<sub>2</sub>, wait until transparent yellow, then take 0.1 mL of that solution and add 0.9 mL water; then take 0.2 mL of this dilute solution and add 0.15 mL ammonium acetate (7.5 M), 0.25 mL of hydroxylamine hydrochloride (5 %), 0.4 mL ferrozine (0.1 %), and 1 mL water in a 4 mL cuvette (quartz). The absorption spectrum of this solution is measured and the intensity at 590 nm is compared to the standard curve to get the Fe concentration.

Inductively Coupled Plasma Atomic Emission Spectroscopy (ICP-AES) and Mass Spectrometry (ICP-MS)

The relative concentration of different metals in ferrite clusters was measured using a Thermo Scientific iCAP 7400 DUO inductively coupled plasma atomic emission spectrometer (ICP-AES) and an Agilent 7900 inductively coupled plasma mass spectrometer (ICP-MS). To prepare the ICP samples, 0.1 mL of ferrite clusters are dissolved in 0.4 mL hydrochloric acid (37%) until transparent yellow. Then, 9.5 mL nitric acid (1%) is added to the solution. Prepare the Mn and Fe standard solutions with a concentration of 1 ppm, 5 ppm, 10 ppm, 20 ppm, 50 ppm, and 100 ppm, respectively, where 1,000 ppm is equivalent to 1 mg/mL. For ICP-MS, the same standards were prepared for Fe, Mn, Gd, and Eu and diluted by a factor of 10000.

Vibrating Sample Magnetometer



A Lake Shore 7400 Series vibrating sample magnetometer (VSM) was used to get the magnetization curves for dried samples (clusters and nanoworms). Sample preparation includes mixing 0.1 mL of sample (1000 ppm), mixing it with gypsum (10 mg), and drying at 60 °C. Measurement is recorded at room temperature from 10000 to -10000 Oe.

## 5.6. Supporting Information

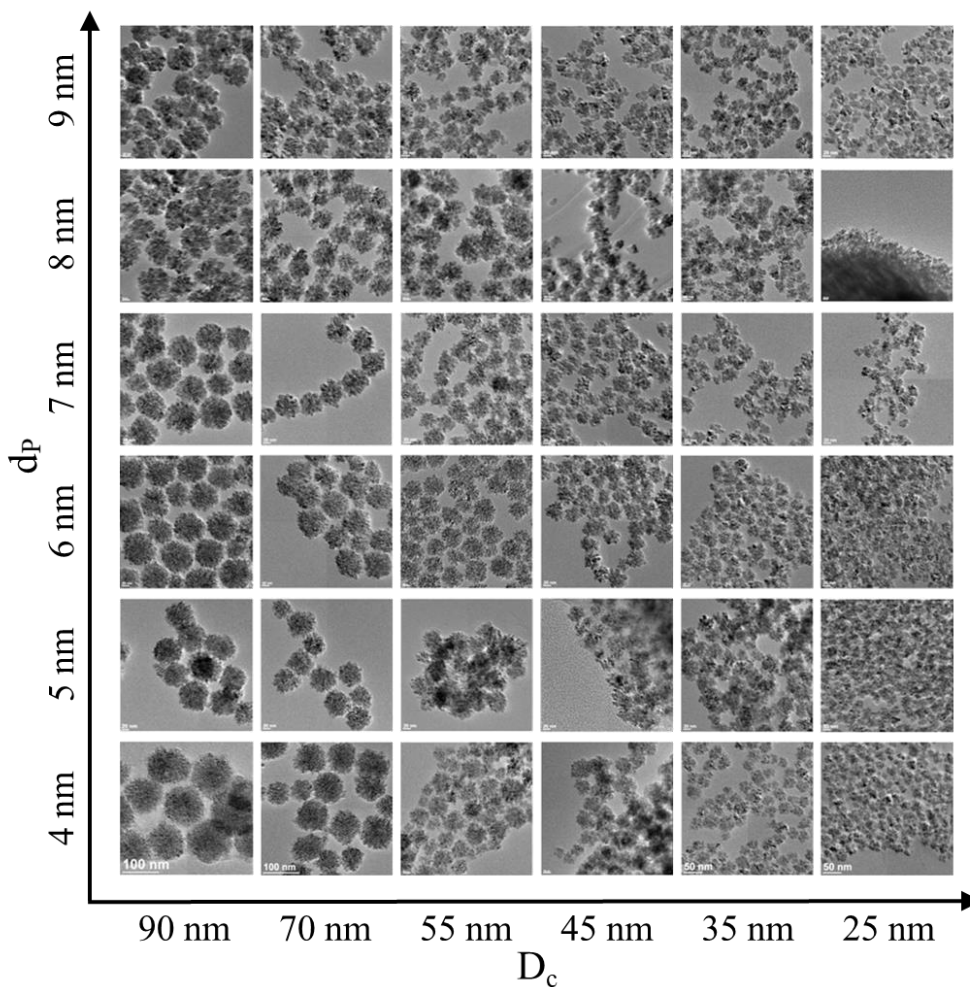


**Figure S5.1** Transmission electron microscopy (TEM) images iron oxide clusters with different cluster ( $D_c$ ) and primary particle ( $d_p$ ) sizes. TEM images of iron oxide nanoclusters with cluster and primary particle sizes of 25 to 90 nm and 4 to 9 nm, respectively.

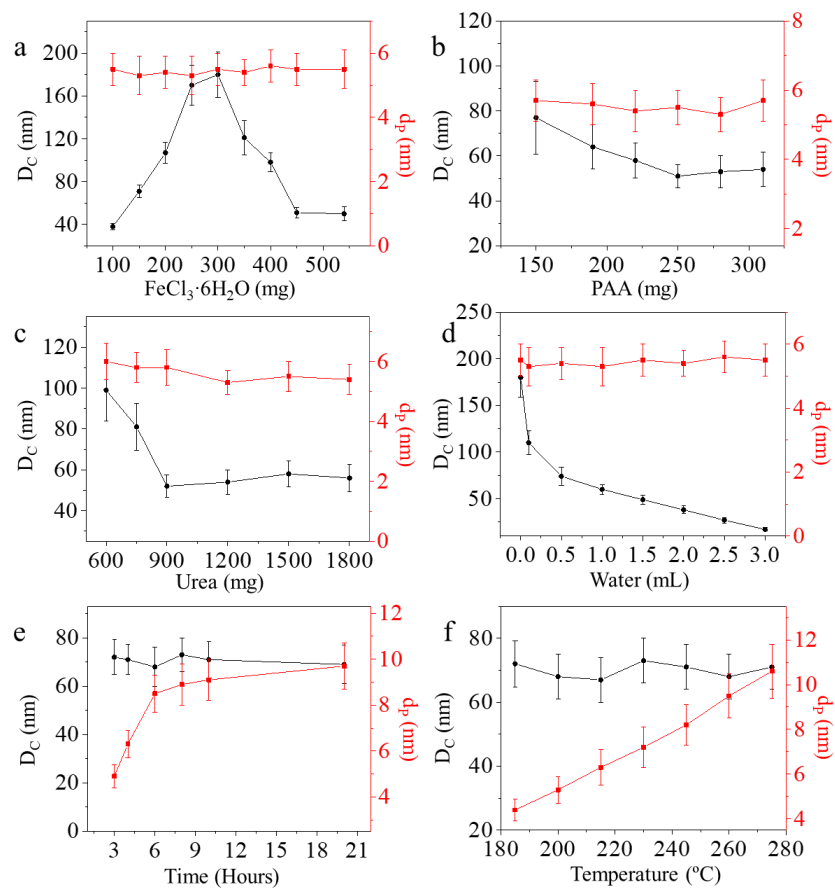


**Figure S5.2 Dependence of cluster dimensions on reaction conditions.** The dependence of cluster ( $D_c$ ) and primary particle ( $d_p$ ) size on the mass of (a)  $\text{FeCl}_3 \cdot 6\text{H}_2\text{O}$ , (b) polyacrylic acid (PAA), and (c) urea; (d) the volume water; and the reaction (e) time and (f) temperature. Unless stated in the figure, other reaction conditions are fixed at: 100 mM  $\text{FeCl}_3 \cdot 6\text{H}_2\text{O}$  3.9 M  $\text{H}_2\text{O}$ , 2.1 mM PAA, 1 M urea and 20 mL ethylene glycol and heated at heated at 185  $^{\circ}\text{C}$  for 6 h.

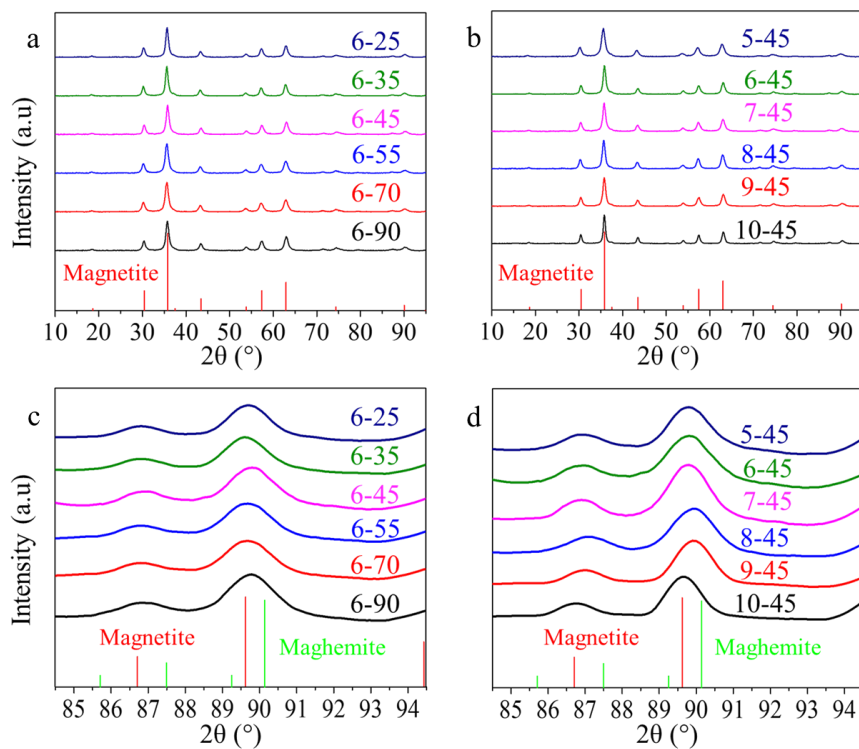


**Figure S5.3 X-ray diffraction (XRD) patterns of iron oxide clusters.** Clusters with different (a,c) cluster and (b,d) primary particle sizes. Standard diffraction patterns for bulk magnetite (PDF#19-0629, red) and maghemite (PDF#39-1346, green).

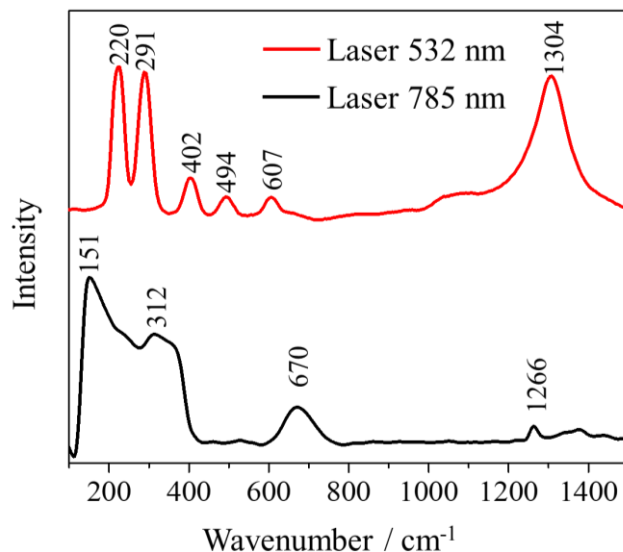


**Figure S5.4 Raman spectra of iron oxide clusters.** For a representative iron oxide cluster ( $D_c = 45$  nm,  $d_p = 4$  nm), characteristic peaks are located at 607, 402, and 291  $\text{cm}^{-1}$  (532 nm laser) and at 670 and 312  $\text{cm}^{-1}$  (785 nm laser), which are the characteristic bands for  $\text{Fe}_3\text{O}_4$ . Peaks at 1304 and 1266  $\text{cm}^{-1}$  indicate surface defects.

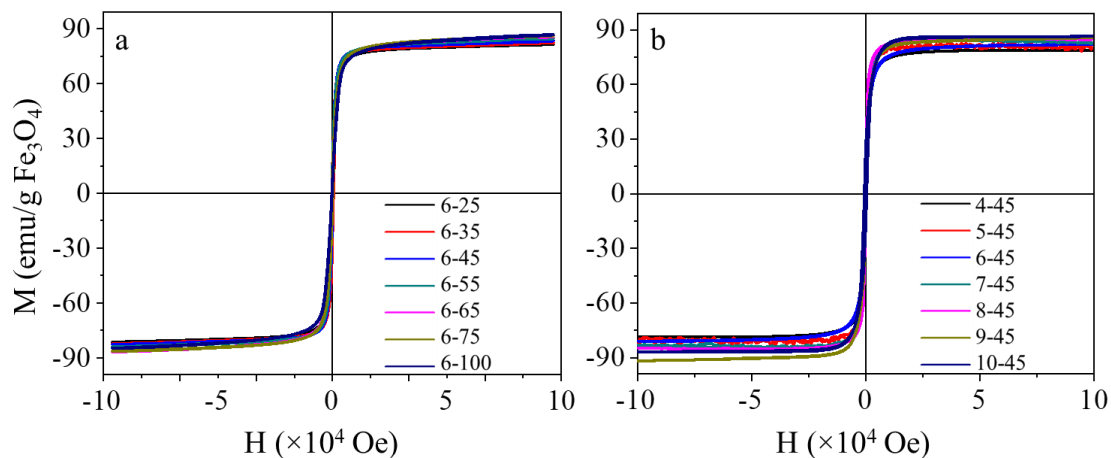


**Figure S5.5 Magnetization curves of iron oxide clusters.** Magnetization curves for clusters of different (a) cluster ( $D_c$ ) and (b) primary particle ( $d_p$ ) sizes. Hysteresis loops recorded from 10,000 to -10,000 oersted (Oe) at room temperature. Saturation magnetizations ranged from (a) 81.2 to 86.7  $\text{emu/g Fe}_3\text{O}_4$  and (b) from 78.7 to 86.7  $\text{emu/g Fe}_3\text{O}_4$ .

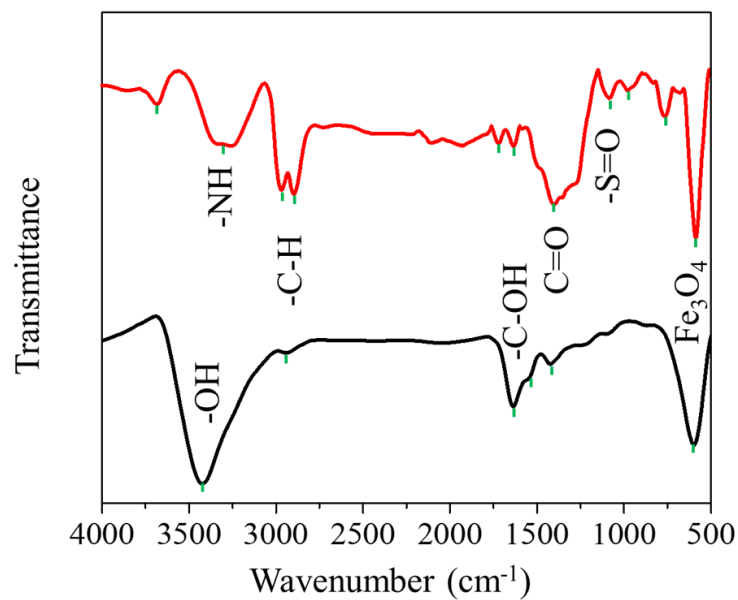


**Figure S5.6 Fourier transform infrared (FTIR) spectra of iron oxide clusters.** FTIR spectra of the clusters before (black) and after (red) surface modification. PAA-modified clusters (black) exhibit peaks characteristic of a carboxylic acid containing polymer, as expected. Poly(AA-co-AMPS)-modified clusters (red) exhibit peaks characteristic of a sulfonic acid containing polymer, as expected.

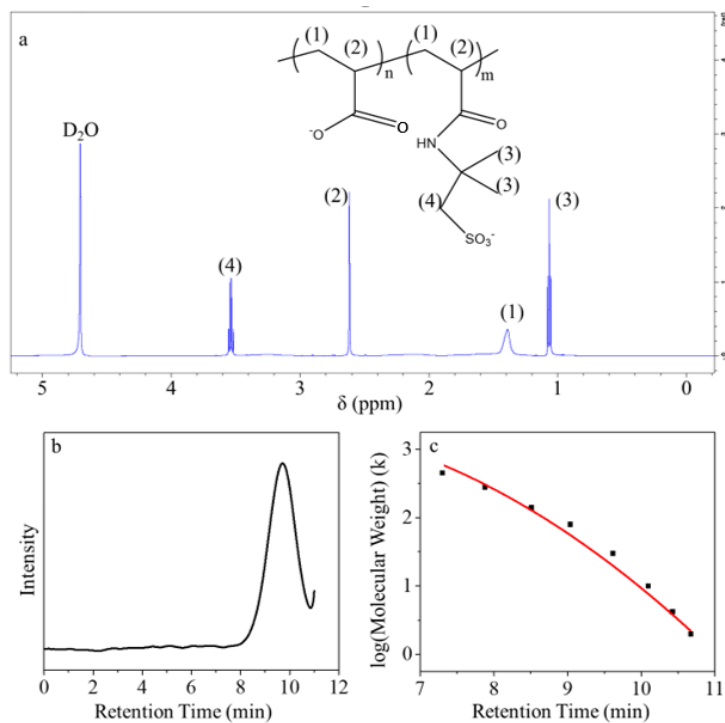


**Figure S5.7 Characterization of poly(AA-co-AMPS).** (a) NMR spectrum of as-synthesized Poly(AA-co-AMPS) – peak intensities suggest a 1:1 ratio of monomers. (b) HPLC elution profile for as-synthesized Poly(AA-co-AMPS). The 7 – 12 minute elution peak for Poly(AA-co-AMPS) can be compared to (c) the sulfonate polystyrene bead calibration curve to get the molecular weight (87 kDa).

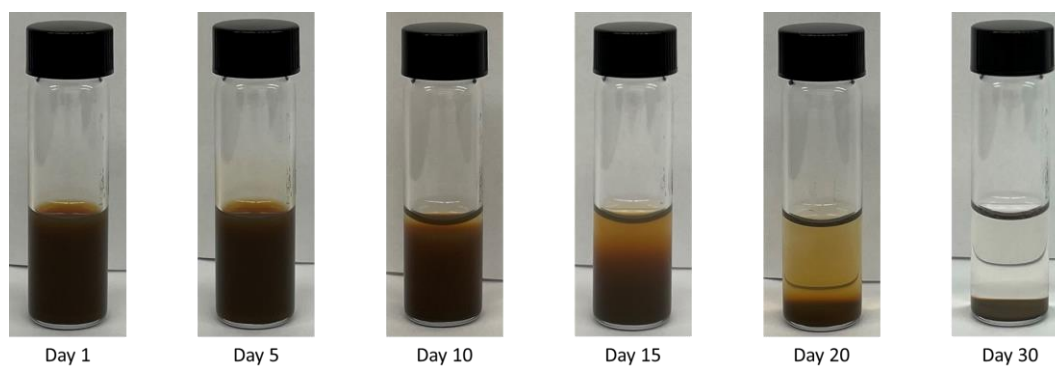


**Figure S5.8 Colloidal stability of nanoworms.** The solution (NW3, 1 mg/mL) was sonicated and left undisturbed for 1 month. Nanoworms remain homogeneously dispersed for 5 – 10 days.

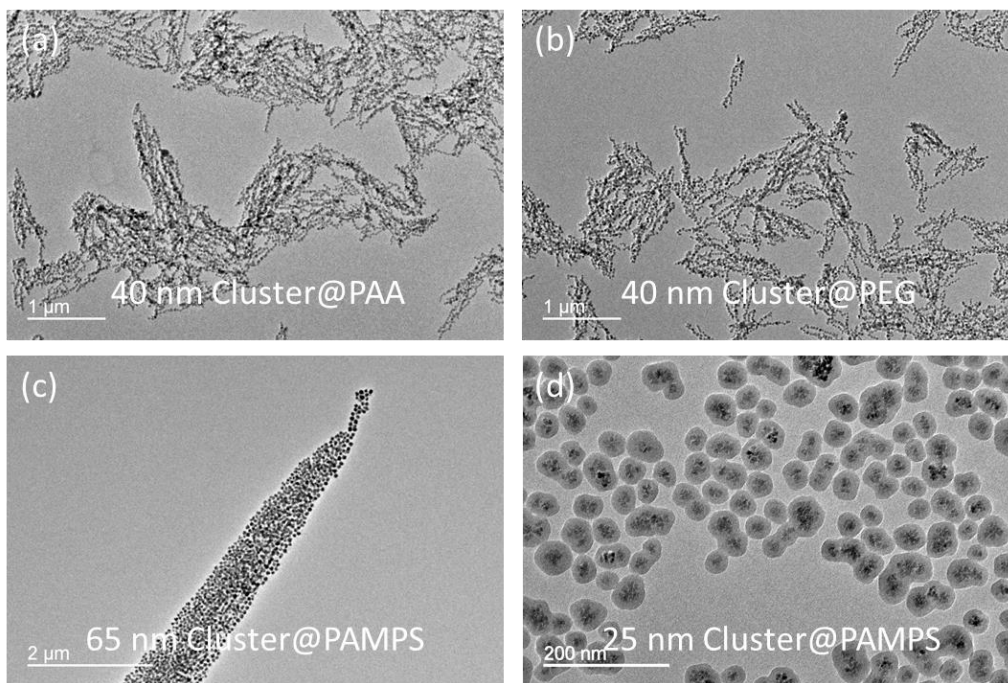


**Figure S5.9 Dependence of nanoworm formation on cluster size and surface coating.** Transmission electron microscopy (TEM) images of structures formed after silica deposition of (a) 40 nm PAA-coated clusters, (b) 40 nm PEG-coated clusters, (c) 65 nm PAMPS-coated clusters, and (d) 25 nm PAMPS-coated clusters. Field strength used for NW3 used throughout.

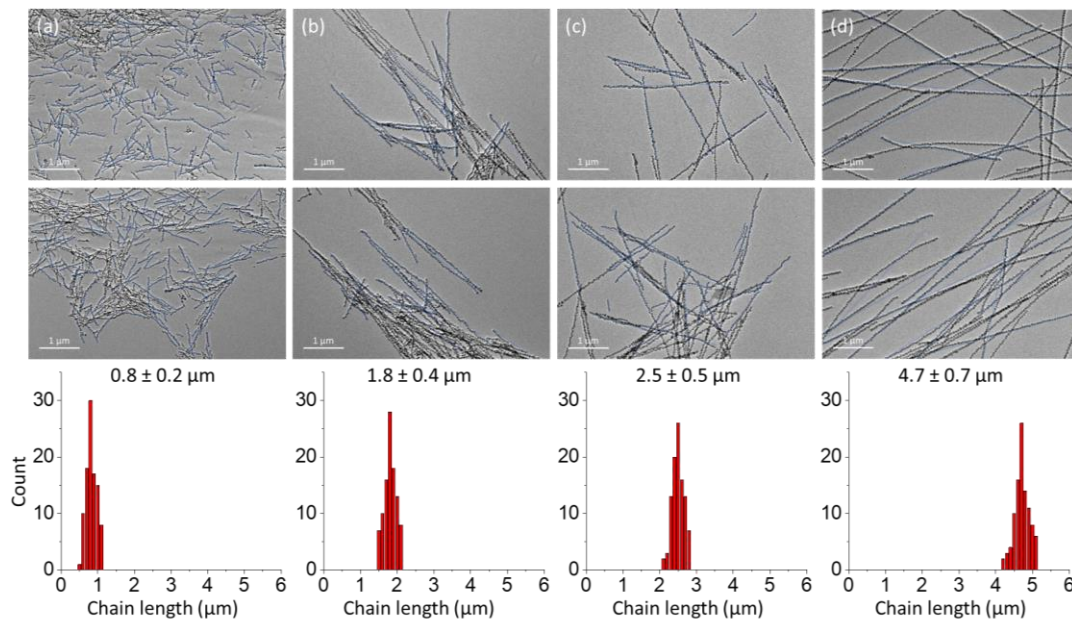


**Figure S5.10** The chain length distribution of the nano-worm samples. The average length for a-d is  $0.8 \pm 0.2 \mu\text{m}$ ,  $1.8 \pm 0.4 \mu\text{m}$ ,  $2.5 \pm 0.5 \mu\text{m}$ , and  $4.7 \pm 0.7 \mu\text{m}$ .

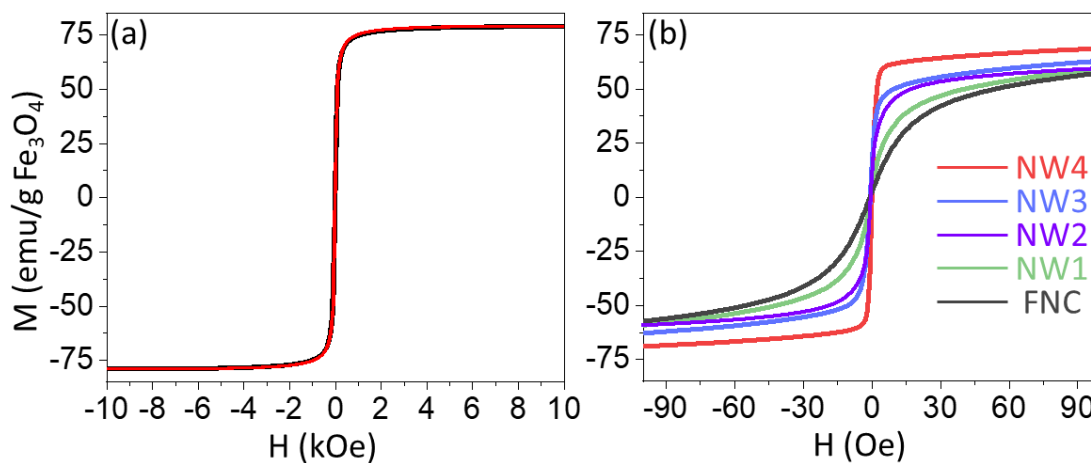


**Figure S5.11** Magnetization curves of nanoworms. (a-b) Magnetization curves of free nanoclusters (FNC) and the nanoworms of varying length (NW1 – NW4) all at 1 mg/mL. (a) At high field, saturation magnetizations are all about the same ( $\sim 80 \text{ emu/g}$ ). (b) At low field, saturation magnetizations can be more easily distinguished.



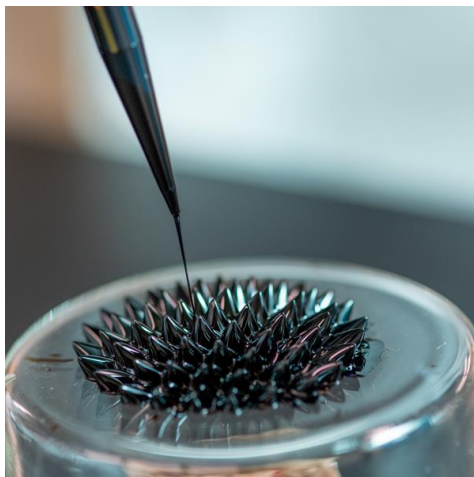


**Figure S5.12 Image of MFC ferrofluid.** An aqueous solution of MFCs (20 mg/mL,  $D_c = 53$  nm,  $d_p = 5.5$  nm,  $Mn_{0.15}Fe_{2.85}O_4$ ) is placed on an upside-down beaker over a handheld magnet.

**Table S5.1** MFC dimensions based on changing concentration of water.

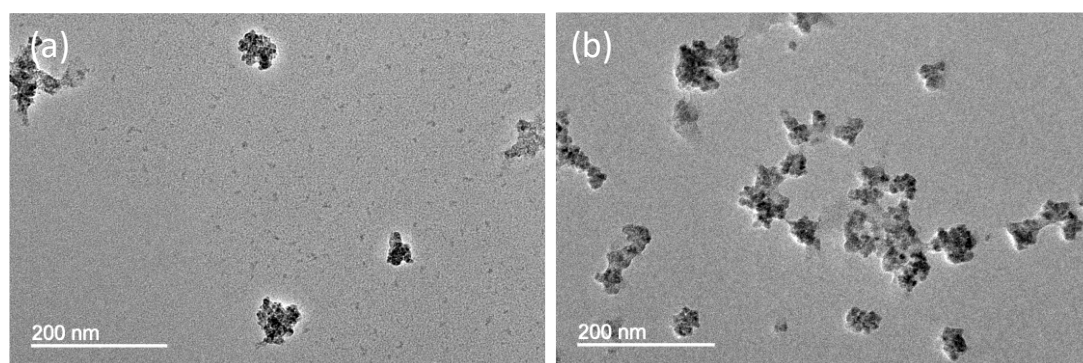
Composition	H <sub>2</sub> O (mL)	Temp (°C)	Mn/Fe	D <sub>c</sub> (nm)	d <sub>p</sub> (nm)	M <sub>sat</sub> (emu/g)
$Mn_{0.15}Fe_{2.85}O_4$	1.95	215	0.525	26	5.5	72
$Mn_{0.15}Fe_{2.85}O_4$	1.5	215	0.525	34	5.5	80
$Mn_{0.15}Fe_{2.85}O_4$	1.25	215	0.525	40	5.5	84
$Mn_{0.15}Fe_{2.85}O_4$	1	215	0.525	45	5.5	86
$Mn_{0.15}Fe_{2.85}O_4$	0.85	215	0.525	48	5.5	88
$Mn_{0.15}Fe_{2.85}O_4$	0.75	215	0.525	53	5.5	89
$Mn_{0.15}Fe_{2.85}O_4$	0.7	215	0.525	57	5.5	90
$Mn_{0.15}Fe_{2.85}O_4$	0.6	215	0.525	62	5.5	91
$Mn_{0.15}Fe_{2.85}O_4$	0.55	215	0.525	68	5.5	91
$Mn_{0.15}Fe_{2.85}O_4$	0.45	215	0.525	78	5.5	92
$Mn_{0.15}Fe_{2.85}O_4$	0.2	215	0.525	90	5.5	93

**Table S5.2** MFC dimensions based on changing reaction temperature.

Composition	H <sub>2</sub> O (mL)	Temp (°C)	Mn/Fe	D <sub>c</sub> (nm)	dp (nm)	Msat (emu/g)
Mn <sub>0.15</sub> Fe <sub>2.85</sub> O <sub>4</sub>	0.75	170	0.525	53	2.5	74
Mn <sub>0.15</sub> Fe <sub>2.85</sub> O <sub>4</sub>	0.75	185	0.525	53	3.5	80
Mn <sub>0.15</sub> Fe <sub>2.85</sub> O <sub>4</sub>	0.75	200	0.525	53	4.5	88
Mn <sub>0.15</sub> Fe <sub>2.85</sub> O <sub>4</sub>	0.75	215	0.525	53	5.5	89
Mn <sub>0.15</sub> Fe <sub>2.85</sub> O <sub>4</sub>	0.75	230	0.525	53	6.5	89
Mn <sub>0.15</sub> Fe <sub>2.85</sub> O <sub>4</sub>	0.75	245	0.525	53	8	90
Mn <sub>0.15</sub> Fe <sub>2.85</sub> O <sub>4</sub>	0.75	260	0.525	53	10.5	91

**Table S5.3** MFC composition based on changing Mn/Fe salt ratio.

Composition	H <sub>2</sub> O (mL)	Temp (°C)	Mn/Fe	D <sub>c</sub> (nm)	dp (nm)	Msat (emu/g)
Fe <sub>3</sub> O <sub>4</sub>	1.35	215	0	53	5.5	83
Mn <sub>0.06</sub> Fe <sub>2.94</sub> O <sub>4</sub>	0.6	215	0.333	53	5.5	84
Mn <sub>0.12</sub> Fe <sub>2.88</sub> O <sub>4</sub>	0.65	215	0.429	53	5.5	87
Mn <sub>0.15</sub> Fe <sub>2.85</sub> O <sub>4</sub>	0.75	215	0.525	53	5.5	88
Mn <sub>0.18</sub> Fe <sub>2.82</sub> O <sub>4</sub>	1.05	215	0.6	53	5.5	90
Mn <sub>0.24</sub> Fe <sub>2.76</sub> O <sub>4</sub>	1.3	215	0.667	53	5.5	92
Mn <sub>0.35</sub> Fe <sub>2.65</sub> O <sub>4</sub>	1.65	215	0.818	53	5.5	95
Mn <sub>0.6</sub> Fe <sub>2.4</sub> O <sub>4</sub>	2	215	1	53	5.5	102

**Figure S5.13** Transmission electron microscopy (TEM) images of Gd- and Eu-ferrite clusters.

Representative TEM images of (a) Gd-ferrite ( $D_c = 41 \pm 6$  nm) and (b) Eu-ferrite ( $D_c = 52 \pm 6$  nm) clusters.

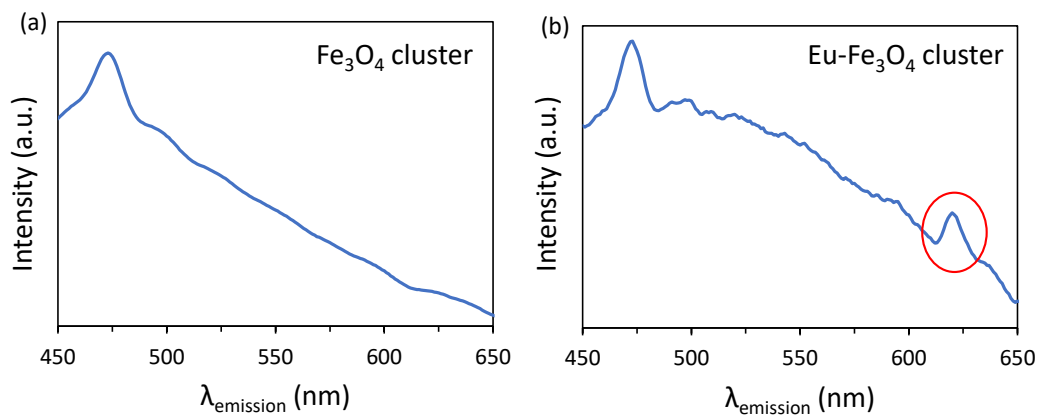


**Figure S5.14 Photoluminescence emission spectra of  $\text{Fe}_3\text{O}_4$  and  $\text{Eu-Fe}_3\text{O}_4$  clusters.** Photoluminescence emission spectra of (a)  $\text{Fe}_3\text{O}_4$  ( $\lambda_{\text{ex}} = 260$  nm) and (b)  $\text{Eu-Fe}_3\text{O}_4$  ( $\lambda_{\text{ex}} = 330$  nm).

## 5.7. References

1. Ni, D. L.; Bu, W. B.; Ehlerding, E. B.; Cai, W. B.; Shi, J. L., Engineering of inorganic nanoparticles as magnetic resonance imaging contrast agents. *Chemical Society Reviews* 2017, 46 (23), 7438-7468.
2. Wahsner, J.; Gale, E. M.; Rodríguez-Rodríguez, A.; Caravan, P., Chemistry of MRI Contrast Agents: Current Challenges and New Frontiers. *Chemical Reviews* 2019, 119 (2), 957-1057.
3. Zhou, Z. J.; Yang, L. J.; Gao, J. H.; Chen, X. Y., Structure-Relaxivity Relationships of Magnetic Nanoparticles for Magnetic Resonance Imaging. *Advanced Materials* 2019, 31 (8), 32.
4. Stueber, D. D.; Villanova, J.; Aponte, I.; Xiao, Z.; Colvin, V. L., Magnetic Nanoparticles in Biology and Medicine: Past, Present, and Future Trends. *Pharmaceutics* 2021, 13 (7), 943.
5. Danhier, F., To exploit the tumor microenvironment: Since the EPR effect fails in the clinic, what is the future of nanomedicine? *J. Control. Release* 2016, 244, 108-121.
6. Hingorani, D. V.; Bernstein, A. S.; Pagel, M. D., A review of responsive MRI contrast agents: 2005-2014. *Contrast Media & Molecular Imaging* 2015, 10 (4), 245-265.
7. Brooks, R. A.; Moiny, F.; Gillis, P., On T2-shortening by weakly magnetized particles: The chemical exchange model†. *Magnetic Resonance in Medicine* 2001, 45 (6), 1014-1020.
8. Gillis, P.; Moiny, F.; Brooks, R. A., On T(2)-shortening by strongly magnetized spheres: a partial refocusing model. *Magn Reson Med* 2002, 47 (2), 257-63.
9. Huang, J.; Bu, L.; Xie, J.; Chen, K.; Cheng, Z.; Li, X.; Chen, X., Effects of Nanoparticle Size on Cellular Uptake and Liver MRI with Polyvinylpyrrolidone-Coated Iron Oxide Nanoparticles. *ACS Nano* 2010, 4 (12), 7151-7160.
10. Jun, Y.-w.; Huh, Y.-M.; Choi, J.-s.; Lee, J.-H.; Song, H.-T.; Kim, S.; Yoon, S.; Kim, K.-S.; Shin, J.-S.; Suh, J.-S.; Cheon, J., Nanoscale Size Effect of Magnetic Nanocrystals and Their Utilization for Cancer Diagnosis via Magnetic Resonance Imaging. *Journal of the American Chemical Society* 2005, 127 (16), 5732-5733.
11. Kim, B. H.; Lee, N.; Kim, H.; An, K.; Park, Y. I.; Choi, Y.; Shin, K.; Lee, Y.; Kwon, S. G.; Na, H. B.; Park, J. G.; Ahn, T. Y.; Kim, Y. W.; Moon, W. K.; Choi, S. H.; Hyeon, T., Large-scale synthesis of uniform and extremely small-sized iron oxide nanoparticles for high-resolution T1 magnetic resonance imaging contrast agents. *J Am Chem Soc* 2011, 133 (32), 12624-31.
12. Arami, H.; Khandhar, A.; Liggitt, D.; Krishnan, K. M., In vivo delivery, pharmacokinetics, biodistribution and toxicity of iron oxide nanoparticles. *Chemical Society reviews* 2015, 44 (23), 8576-8607.

13. Malhotra, N.; Lee, J.-S.; Liman, R. A. D.; Ruallo, J. M. S.; Villaflores, O. B.; Ger, T.-R.; Hsiao, C.-D., Potential Toxicity of Iron Oxide Magnetic Nanoparticles: A Review. *Molecules* 2020, 25 (14), 3159.
14. Yeap, S. P.; Lim, J.; Ooi, B. S.; Ahmad, A. L., Agglomeration, colloidal stability, and magnetic separation of magnetic nanoparticles: collective influences on environmental engineering applications. *Journal of Nanoparticle Research* 2017, 19 (11), 368.
15. Choo, E. S. G.; Peng, E.; Rajendran, R.; Chandrasekharan, P.; Yang, C.-T.; Ding, J.; Chuang, K.-H.; Xue, J., Superparamagnetic Nanostructures for Off-Resonance Magnetic Resonance Spectroscopic Imaging. *Advanced Functional Materials* 2013, 23 (4), 496-505.
16. de Moura, C. L.; Gallo, J.; Garcia-Hevia, L.; Pessoa, O. D. L.; Ricardo, N.; Banobre-Lopez, M., Magnetic Hybrid Wax Nanocomposites as Externally Controlled Theranostic Vehicles: High MRI Enhancement and Synergistic Magnetically Assisted Thermo/Chemo Therapy. *Chemistry-a European Journal* 2020, 26 (20), 4531-4538.
17. He, J. P.; Liu, X. H.; Niu, D. C.; Chen, J. Z.; Qin, X.; Li, Y. S., Supramolecular-based PEGylated magnetic hybrid vesicles with ultra-high transverse relaxivity. *Applied Materials Today* 2018, 11, 238-245.
18. Jang, J. T.; Nah, H.; Lee, J. H.; Moon, S. H.; Kim, M. G.; Cheon, J., Critical Enhancements of MRI Contrast and Hyperthermic Effects by Dopant-Controlled Magnetic Nanoparticles. *Angewandte Chemie-International Edition* 2009, 48 (7), 1234-1238.
19. Kostevsek, N.; Cheung, C. C. L.; Sersa, I.; Kreft, M. E.; Monaco, I.; Franchini, M. C.; Vidmar, J.; Al-Jamal, W. T., Magneto-Liposomes as MRI Contrast Agents: A Systematic Study of Different Liposomal Formulations. *Nanomaterials* 2020, 10 (5).
20. LaConte, L. E.; Nitin, N.; Zurkiya, O.; Caruntu, D.; O'Connor, C. J.; Hu, X.; Bao, G., Coating thickness of magnetic iron oxide nanoparticles affects R2 relaxivity. *J Magn Reson Imaging* 2007, 26 (6), 1634-41.
21. Lee, N.; Choi, Y.; Lee, Y.; Park, M.; Moon, W. K.; Choi, S. H.; Hyeon, T., Water-Dispersible Ferrimagnetic Iron Oxide Nanocubes with Extremely High r2 Relaxivity for Highly Sensitive in Vivo MRI of Tumors. *Nano Letters* 2012, 12 (6), 3127-3131.
22. Lee, N.; Hyeon, T., Designed synthesis of uniformly sized iron oxide nanoparticles for efficient magnetic resonance imaging contrast agents. *Chem Soc Rev* 2012, 41 (7), 2575-89.
23. Mohapatra, J.; Mitra, A.; Tyagi, H.; Bahadur, D.; Aslam, M., Iron oxide nanorods as high-performance magnetic resonance imaging contrast agents. *Nanoscale* 2015, 7 (20), 9174-9184.

24. Tong, S.; Hou, S.; Zheng, Z.; Zhou, J.; Bao, G., Coating Optimization of Superparamagnetic Iron Oxide Nanoparticles for High T2 Relaxivity. *Nano Letters* 2010, 10 (11), 4607-4613.
25. Tromsdorf, U. I.; Bigall, N. C.; Kaul, M. G.; Bruns, O. T.; Nikolic, M. S.; Mollwitz, B.; Sperling, R. A.; Reimer, R.; Hohenberg, H.; Parak, W. J.; Forster, S.; Beisiegel, U.; Adam, G.; Weller, H., Size and surface effects on the MRI relaxivity of manganese ferrite nanoparticle contrast agents. *Nano Letters* 2007, 7 (8), 2422-2427.
26. Xiao, Z.; Zhang, Q.; Guo, X.; Villanova, J.; Hu, Y.; Külaots, I.; Garcia-Rojas, D.; Guo, W.; Colvin, V. L., Libraries of Uniform Magnetic Multicore Nanoparticles with Tunable Dimensions for Biomedical and Photonic Applications. *ACS Applied Materials & Interfaces* 2020, 12 (37), 41932-41941.
27. Yang, L.; Ma, L.; Xin, J.; Li, A.; Sun, C.; Wei, R.; Ren, B. W.; Chen, Z.; Lin, H.; Gao, J., Composition Tunable Manganese Ferrite Nanoparticles for Optimized T2 Contrast Ability. *Chemistry of Materials* 2017, 29 (7), 3038-3047.
28. Zhao, Z.; Zhou, Z.; Bao, J.; Wang, Z.; Hu, J.; Chi, X.; Ni, K.; Wang, R.; Chen, X.; Chen, Z.; Gao, J., Octapod iron oxide nanoparticles as high-performance T<sub>2</sub> contrast agents for magnetic resonance imaging. *Nat Commun* 2013, 4, 2266.
29. Pösel, E.; Kloust, H.; Tromsdorf, U.; Janschel, M.; Hahn, C.; Maßlo, C.; Weller, H., Relaxivity Optimization of a PEGylated Iron-Oxide-Based Negative Magnetic Resonance Contrast Agent for T2-Weighted Spin–Echo Imaging. *ACS Nano* 2012, 6 (2), 1619-1624.
30. Vuong, Q. L.; Berret, J.-F.; Fresnais, J.; Gossuin, Y.; Sandre, O., A Universal Scaling Law to Predict the Efficiency of Magnetic Nanoparticles as MRI T2-Contrast Agents. *Advanced Healthcare Materials* 2012, 1 (4), 502-512.
31. Xiao, Y.; Du, J., Superparamagnetic nanoparticles for biomedical applications. *J Mater Chem B* 2020, 8 (3), 354-367.
32. Tong, G.; Liu, Y.; Wu, T.; Tong, C.; Du, F., H<sub>2</sub>O-steered size/phase evolution and magnetic properties of large-scale, monodisperse Fe<sub>x</sub>O<sub>y</sub> nanomaterials. *Journal of Materials Chemistry C* 2015, 3 (21), 5506-5515.
33. Anandhi, J. S.; Jacob, G. A.; Joseyphus, R. J., Factors affecting the heating efficiency of Mn-doped Fe<sub>3</sub>O<sub>4</sub> nanoparticles. *Journal of Magnetism and Magnetic Materials* 2020, 512.
34. Del Sol-Fernandez, S.; Portilla-Tundidor, Y.; Gutierrez, L.; Odio, O. F.; Reguera, E.; Barber, D. F.; Morales, M. P., Flower-like Mn-Doped Magnetic Nanoparticles Functionalized with alpha(v)beta(3)-Integrin-Ligand to Efficiently Induce Intracellular Heat after Alternating Magnetic Field Exposition, Triggering Glioma Cell Death. *Acs Applied Materials & Interfaces* 2019, 11 (30), 26648-26663.

35. Qu, Y.; Li, J. B.; Ren, J.; Leng, J. Z.; Lin, C.; Shi, D. L., Enhanced Magnetic Fluid Hyperthermia by Micellar Magnetic Nanoclusters Composed of  $MnxZn_{1-x}Fe_2O_4$  Nanoparticles for Induced Tumor Cell Apoptosis. *ACS Applied Materials & Interfaces* 2014, 6 (19), 16867-16879.
36. Nandwana, V.; Ryoo, S.-R.; Kanthala, S.; De, M.; Chou, S. S.; Prasad, P. V.; Dravid, V. P., Engineered Theranostic Magnetic Nanostructures: Role of Composition and Surface Coating on Magnetic Resonance Imaging Contrast and Thermal Activation. *ACS Applied Materials & Interfaces* 2016, 8 (11), 6953-6961.
37. Chen, Y.; Ai, K.; Liu, J.; Ren, X.; Jiang, C.; Lu, L., Polydopamine-based coordination nanocomplex for T1/T2 dual mode magnetic resonance imaging-guided chemophotothermal synergistic therapy. *Biomaterials* 2016, 77, 198-206.
38. Choi, J. S.; Lee, J. H.; Shin, T. H.; Song, H. T.; Kim, E. Y.; Cheon, J., Self-confirming "AND" logic nanoparticles for fault-free MRI. *J Am Chem Soc* 2010, 132 (32), 11015-7.
39. Lee, N.; Yoo, D.; Ling, D.; Cho, M. H.; Hyeon, T.; Cheon, J., Iron Oxide Based Nanoparticles for Multimodal Imaging and Magnetoresponse Therapy. *Chemical Reviews* 2015, 115 (19), 10637-10689.
40. Shin, T.-H.; Choi, J.-s.; Yun, S.; Kim, I.-S.; Song, H.-T.; Kim, Y.; Park, K. I.; Cheon, J., T1 and T2 Dual-Mode MRI Contrast Agent for Enhancing Accuracy by Engineered Nanomaterials. *ACS Nano* 2014, 8 (4), 3393-3401.
41. Shin, T.-H.; Choi, Y.; Kim, S.; Cheon, J., Recent advances in magnetic nanoparticle-based multi-modal imaging. *Chemical Society Reviews* 2015, 44 (14), 4501-4516.
42. Zhou, Z.; Bai, R.; Munasinghe, J.; Shen, Z.; Nie, L.; Chen, X., T(1)-T(2) Dual-Modal Magnetic Resonance Imaging: From Molecular Basis to Contrast Agents. *ACS Nano* 2017, 11 (6), 5227-5232.
43. Cheng, C.; Wen, Y.; Xu, X.; Gu, H., Tunable synthesis of carboxyl-functionalized magnetite nanocrystal clusters with uniform size. *Journal of Materials Chemistry* 2009, 19 (46), 8782-8788.
44. Gerber, O.; Pichon, B.; Ihiawakrim, D.; Florea, I.; Moldovan, S.; Ersen, O.; Begin, D.; Grenèche, J.-M.; Lemonnier, S.; Barraud, E., Synthesis engineering of iron oxide raspberry-shaped nanostructures. *Nanoscale* 2017, 9 (1), 305-313.
45. Wang, L.; Bao, J.; Wang, L.; Zhang, F.; Li, Y., One-pot synthesis and bioapplication of amine-functionalized magnetite nanoparticles and hollow nanospheres. *Chemistry—A European Journal* 2006, 12 (24), 6341-6347.
46. Wang, T.; Zhang, L.; Wang, H.; Yang, W.; Fu, Y.; Zhou, W.; Yu, W.; Xiang, K.; Su, Z.; Dai, S., Controllable synthesis of hierarchical porous  $Fe_3O_4$  particles mediated by poly (diallyldimethylammonium chloride) and their application in arsenic removal. *ACS applied materials & interfaces* 2013, 5 (23), 12449-12459.

47. Zhu, M.; Diao, G., Synthesis of Porous Fe<sub>3</sub>O<sub>4</sub> Nanospheres and Its Application for the Catalytic Degradation of Xylenol Orange. *Journal of Physical Chemistry C* 2011, 115 (39), 18923-18934.
48. Liang, J.; Ma, H.; Luo, W.; Wang, S., Synthesis of magnetite submicrospheres with tunable size and superparamagnetism by a facile polyol process. *Materials Chemistry and Physics* 2013, 139 (2-3), 383-388.
49. Deng, H.; Li, X.; Peng, Q.; Wang, X.; Chen, J.; Li, Y., Monodisperse magnetic single-crystal ferrite microspheres. *Angewandte Chemie* 2005, 117 (18), 2842-2845.
50. Hemery, G.; Keyes Jr, A. C.; Garaio, E.; Rodrigo, I.; Garcia, J. A.; Plazaola, F.; Garanger, E.; Sandre, O., Tuning sizes, morphologies, and magnetic properties of monocoresh versus multicore iron oxide nanoparticles through the controlled addition of water in the polyol synthesis. *Inorganic chemistry* 2017, 56 (14), 8232-8243.
51. Wei, X.; Jing, L.; Liu, C.; Hou, Y.; Jiao, M.; Gao, M., Molecular mechanisms for delicately tuning the morphology and properties of Fe<sub>3</sub>O<sub>4</sub> nanoparticle clusters. *CrystEngComm* 2018, 20 (17), 2421-2429.
52. Kostopoulou, A.; Brintakis, K.; Vasilakaki, M.; Trohidou, K.; Douvalis, A.; Lascialfari, A.; Manna, L.; Lappas, A., Assembly-mediated interplay of dipolar interactions and surface spin disorder in colloidal maghemite nanoclusters. *Nanoscale* 2014, 6 (7), 3764-3776.
53. Tang, Y. X.; Liu, Y.; Li, W.; Xie, Y.; Li, Y. J.; Wu, J.; Wang, S. J.; Tian, Y.; Tian, W.; Teng, Z. G.; Lu, G. M., Synthesis of sub-100 nm biocompatible superparamagnetic Fe<sub>3</sub>O<sub>4</sub> colloidal nanocrystal clusters as contrast agents for magnetic resonance imaging. *Rsc Advances* 2016, 6 (67), 62550-62555.
54. Bunge, A.; Porav, A. S.; Borodi, G.; Radu, T.; Pîrnău, A.; Berghian-Grosan, C.; Turcu, R., Correlation between synthesis parameters and properties of magnetite clusters prepared by solvothermal polyol method. *Journal of Materials Science* 2019, 54 (4), 2853-2875.
55. Gavilán, H.; Sánchez, E. H.; Brollo, M. E.; Asín, L.; Moerner, K. K.; Frandsen, C.; Lázaro, F. J.; Serna, C. J.; Veintemillas-Verdaguer, S.; Morales, M. P., Formation mechanism of maghemite nanoflowers synthesized by a polyol-mediated process. *Acs Omega* 2017, 2 (10), 7172-7184.
56. Xuan, S.; Wang, Y.-X. J.; Yu, J. C.; Cham-Fai Leung, K., Tuning the grain size and particle size of superparamagnetic Fe<sub>3</sub>O<sub>4</sub> microparticles. *Chemistry of Materials* 2009, 21 (21), 5079-5087.
57. Otero-Lorenzo, R.; Ramos-Docampo, M. A.; Rodríguez-González, B.; Comesaña-Hermo, M.; Salgueiriño, V. n., Solvothermal clustering of magnetic spinel ferrite nanocrystals: a Raman perspective. *Chemistry of Materials* 2017, 29 (20), 8729-8736.



58. Cullity, B. D.; Frahm, C. D., Ferrimagnetism. In Introduction to Magnetic Materials, 2008; pp 175-195.
59. Cavus, S., Poly(methacrylamide-co-2-acrylamido-2-methyl-1-propanesulfonic acid) Hydrogels: Investigation of pH- and Temperature-Dependent Swelling Characteristics and Their Characterization. Journal of Polymer Science Part B: Polymer Physics 2010, 48 (23), 2497-2508.
60. El-Mahdy, G. A.; Atta, A. M.; Al-Lohedan, H. A., Synthesis and Evaluation of Poly(Sodium 2-Acrylamido-2-Methylpropane Sulfonate-co-Styrene)/Magnetite Nanoparticle Composites as Corrosion Inhibitors for Steel. Molecules 2014, 19 (2), 1713-1731.
61. Gad, Y. H., Preparation and characterization of poly(2-acrylamido-2-methylpropane-sulfonic acid)/Chitosan hydrogel using gamma irradiation and its application in wastewater treatment. Radiation Physics and Chemistry 2008, 77 (9), 1101-1107.
62. Amstad, E.; Gillich, T.; Bilecka, I.; Textor, M.; Reimhult, E., Ultrastable iron oxide nanoparticle colloidal suspensions using dispersants with catechol-derived anchor groups. Nano letters 2009, 9 (12), 4042-4048.
63. Thomas, G.; Demoisson, F.; Chassagnon, R.; Popova, E.; Millot, N., One-step continuous synthesis of functionalized magnetite nanoflowers. Nanotechnology 2016, 27 (13), 135604.
64. Ding, X.; Vegesna, G. K.; Meng, H.; Winter, A.; Lee, B. P., Nitro-Group Functionalization of Dopamine and its Contribution to the Viscoelastic Properties of Catechol-Containing Nanocomposite Hydrogels. Macromolecular chemistry and physics 2015, 216 (10), 1109-1119.
65. Zirbs, R.; Lassenberger, A.; Vonderhaid, I.; Kurzhals, S.; Reimhult, E., Melt-grafting for the synthesis of core-shell nanoparticles with ultra-high dispersant density. Nanoscale 2015, 7 (25), 11216-11225.
66. Kratz, H.; Taupitz, M.; de Schellenberger, A. A.; Kosch, O.; Eberbeck, D.; Wagner, S.; Trahms, L.; Hamm, B.; Schnorr, J., Novel magnetic multicore nanoparticles designed for MPI and other biomedical applications: From synthesis to first in vivo studies. Plos One 2018, 13 (1).
67. Maity, D.; Chandrasekharan, P.; Pradhan, P.; Chuang, K.-H.; Xue, J.-M.; Feng, S.-S.; Ding, J., Novel synthesis of superparamagnetic magnetite nanoclusters for biomedical applications. Journal of Materials Chemistry 2011, 21 (38), 14717-14724.
68. Xu, X.; Friedman, G.; Humfeld, K. D.; Majetich, S. A.; Asher, S. A., Synthesis and utilization of monodisperse superparamagnetic colloidal particles for magnetically controllable photonic crystals. Chemistry of Materials 2002, 14 (3), 1249-1256.

69. He, L.; Wang, M. S.; Ge, J. P.; Yin, Y. D., Magnetic Assembly Route to Colloidal Responsive Photonic Nanostructures. *Accounts Chem. Res.* 2012, 45 (9), 1431-1440.
70. Zhou, Z.; Shen, Z.; Chen, X., Tale of two magnets: An advanced magnetic targeting system. *ACS nano* 2019, 14 (1), 7-11.
71. Anand, M., Thermal and dipolar interaction effect on the relaxation in a linear chain of magnetic nanoparticles. *Journal of Magnetism and Magnetic Materials* 2021, 522, 167538.
72. Zhao, Z.; Rinaldi, C., Computational predictions of enhanced magnetic particle imaging performance by magnetic nanoparticle chains. *Physics in Medicine & Biology* 2020, 65 (18), 185013.
73. Krommenhoek, P. J.; Tracy, J. B., Magnetic Field-Directed Self-Assembly of Magnetic Nanoparticle Chains in Bulk Polymers. *Particle & Particle Systems Characterization* 2013, 30 (9), 759-763.
74. Corr, S. A.; Byrne, S. J.; Tekoriute, R.; Meledandri, C. J.; Brougham, D. F.; Lynch, M.; Kerskens, C.; O'Dwyer, L.; Gun'ko, Y. K., Linear assemblies of magnetic nanoparticles as MRI contrast agents. *Journal of the American Chemical Society* 2008, 130 (13), 4214-+.
75. Kralj, S.; Makovec, D., Magnetic Assembly of Superparamagnetic Iron Oxide Nanoparticle Clusters into Nano chains and Nanobundles. *Acs Nano* 2015, 9 (10), 9700-9707.
76. Taylor, A.; Herrmann, A.; Moss, D.; Sée, V.; Davies, K.; Williams, S. R.; Murray, P., Assessing the efficacy of nano- and micro-sized magnetic particles as contrast agents for MRI cell tracking. *PLoS one* 2014, 9 (6), e100259-e100259.
77. Xu, C.; Miranda-Nieves, D.; Ankrum, J. A.; Matthiesen, M. E.; Phillips, J. A.; Roes, I.; Wojtkiewicz, G. R.; Juneja, V.; Kultima, J. R.; Zhao, W.; Vemula, P. K.; Lin, C. P.; Nahrendorf, M.; Karp, J. M., Tracking mesenchymal stem cells with iron oxide nanoparticle loaded poly(lactide-co-glycolide) microparticles. *Nano Lett* 2012, 12 (8), 4131-9.
78. Joshi, H.; De, M.; Richter, F.; He, J.; Prasad, P.; Dravid, V., Effect of silica shell thickness of Fe<sub>3</sub>O<sub>4</sub> SiO<sub>x</sub> core-shell nanostructures on MRI contrast. *Journal of Nanoparticle Research* 2013, 15, 1-8.
79. Abakumov, M. A.; Semkina, A. S.; Skorikov, A. S.; Vishnevskiy, D. A.; Ivanova, A. V.; Mironova, E.; Davydova, G. A.; Majouga, A. G.; Chekhonin, V. P., Toxicity of iron oxide nanoparticles: Size and coating effects. *J Biochem Mol Toxicol* 2018, 32 (12), e22225.
80. Ge, J.; Hu, Y.; Biasini, M.; Beyermann, W. P.; Yin, Y., Superparamagnetic magnetite colloidal nanocrystal clusters. *Angewandte Chemie International Edition* 2007, 46 (23), 4342-4345.

81. Guo, P. Z.; Zhang, G. L.; Yu, J. Q.; Li, H. L.; Zhao, X. S., Controlled synthesis, magnetic and photocatalytic properties of hollow spheres and colloidal nanocrystal clusters of manganese ferrite. *Colloids and Surfaces a-Physicochemical and Engineering Aspects* 2012, 395, 168-174.
82. Xie, J.; Yan, C. Z.; Zhang, Y.; Gu, N., Shape Evolution of "Multibranched" Mn-Zn Ferrite Nanostructures with High Performance: A Transformation of Nanocrystals into Nanoclusters. *Chemistry of Materials* 2013, 25 (18), 3702-3709.
83. Lartigue, L.; Hugounenq, P.; Alloyeau, D.; Clarke, S. P.; Levy, M.; Bacri, J.-C.; Bazzi, R.; Brougham, D. F.; Wilhelm, C.; Gazeau, F., Cooperative organization in iron oxide multi-core nanoparticles potentiates their efficiency as heating mediators and MRI contrast agents. *ACS nano* 2012, 6 (12), 10935-10949.
84. Aslibeiki, B.; Kameli, P., Effect of ZnO on Structural and Magnetic Properties of MnFe<sub>2</sub>O<sub>4</sub>/ZnO Nanocomposite. *Journal of Superconductivity and Novel Magnetism* 2015, 28 (11), 3343-3350.
85. Casula, M. F.; Conca, E.; Bakaimi, I.; Sathya, A.; Materia, M. E.; Casu, A.; Falqui, A.; Sogne, E.; Pellegrino, T.; Kanaras, A. G., Manganese doped-iron oxide nanoparticle clusters and their potential as agents for magnetic resonance imaging and hyperthermia. *Physical Chemistry Chemical Physics* 2016, 18 (25), 16848-16855.
86. McDonagh, B. H.; Singh, G.; Hak, S.; Bandyopadhyay, S.; Augestad, I. L.; Peddis, D.; Sandvig, I.; Sandvig, A.; Glomm, W. R., L-DOPA-Coated Manganese Oxide Nanoparticles as Dual MRI Contrast Agents and Drug-Delivery Vehicles. *Small* 2016, 12 (3), 301-306.
87. Liu, X.; Liu, J.; Zhang, S. H.; Nan, Z. D.; Shi, Q., Structural, Magnetic, and Thermodynamic Evolutions of Zn-Doped Fe<sub>3</sub>O<sub>4</sub> Nanoparticles Synthesized Using a One-Step Solvothermal Method. *Journal of Physical Chemistry C* 2016, 120 (2), 1328-1341.
88. Choi, Y. S.; Yoon, H. Y.; Lee, J. S.; Wu, J. H.; Kim, Y. K., Synthesis and magnetic properties of size-tunable Mn<sub>x</sub>Fe<sub>3-x</sub>O<sub>4</sub> ferrite nanoclusters. *Journal of Applied Physics* 2014, 115 (17).
89. Qi, Y. Z.; Shao, C.; Gu, W.; Li, F. Y.; Deng, Y. L.; Li, H. S.; Ye, L., Carboxylic silane-exchanged manganese ferrite nanoclusters with high relaxivity for magnetic resonance imaging. *Journal of Materials Chemistry B* 2013, 1 (13), 1846-1851.
90. Gupta, R.; Sharma, D., Manganese-Doped Magnetic Nanoclusters for Hyperthermia and Photothermal Glioblastoma Therapy. *ACS Applied Nano Materials* 2020, 3 (2), 2026-2037.
91. Lartigue, L.; Coupeau, M.; Lesault, M., Luminophore and Magnetic Multicore Nanoassemblies for Dual-Mode MRI and Fluorescence Imaging. *Nanomaterials* 2020, 10 (1), 28.

92. Zhang, T.; Wang, Z.; Xiang, H.; Xu, X.; Zou, J.; Lu, C., Biocompatible Superparamagnetic Europium-Doped Iron Oxide Nanoparticle Clusters as Multifunctional Nanoprobes for Multimodal In Vivo Imaging. *ACS Applied Materials & Interfaces* 2021, 13 (29), 33850-33861.
93. Zhu, H.; Tao, J.; Wang, W.; Zhou, Y.; Li, P.; Li, Z.; Yan, K.; Wu, S.; Yeung, K. W. K.; Xu, Z.; Xu, H.; Chu, P. K., Magnetic, fluorescent, and thermo-responsive Fe<sub>3</sub>O<sub>4</sub>/rare earth incorporated poly(St-NIPAM) core-shell colloidal nanoparticles in multimodal optical/magnetic resonance imaging probes. *Biomaterials* 2013, 34 (9), 2296-2306.